Nonequilibrium signatures and phase transitions in active matter and beyond

David Martin

Université de Paris

École Doctorale PIF 564

Laboratoire Matières et Systèmes Complexes

Nonequilibrium signatures and phase transitions in active matter and beyond

Par David Martin

Thèse de doctorat de Physique

Dirigée par Julien Tailleur

Présentée et soutenue publiquement le 08/10/2021

Devant un jury composé de :

Francesco GINELLI, Associate Professor, Università degli Studi dell'Insubria, rapporteur

Davide MARENDUZZO, Professor, University of Edinburgh, rapporteur

Jean-Louis BARRAT, professeur des universités, Université Grenoble Alpes, examinateur

David DEAN, professeur des universités, Université Bordeaux 1, examinateur

Irene GIARDINA, Associate Professor, Sapienza University, examinatrice

Estelle PITARD, HDR, Université de Montpellier, examinatrice

Raphaël VOITURIEZ, DR, Sorbonne Université, examinateur

Cesare NARDINI, professeur associé, CEA, membre invité

Acknowledgement-Remerciements

Je tiens tout d'abord à remercier les personnes qui m'ont encadré durant ces quelques 3 années de thèse. Merci à Julien en premier lieu pour m'avoir patiemment supervisé tout au long de ce travail, mais aussi pour m'avoir initié aux arcanes du métier de chercheur et transmis sa passion de la physique statistique. J'espère que ce manuscrit portera la marque de son enseignement scientifique et de son infatiguable perfectionnisme. Merci à Frédéric pour ses explications patientes sur les questions théoriques ainsi que pour son aide administrative face à mon accident. Enfin, merci à Cesare pour son soutien continu depuis plus de 4 ans ainsi que pour toutes les discussions de physique pendant lesquelles j'ai beaucoup appris. Je réalise peu à peu que le jeune physicien que je suis a été particulièrement chanceux d'avoir pu puiser dans vos trois expériences conjointes.

Je souhaitais aussi remercier Hugues, Alex, Denis, Etienne, Thibaut, Jérémy et Delphine pour les collaborations très instructives que j'ai pu construire et partager avec eux. I also take this opportunity to thanks all the members of my PhD comittee for accepting to be part of my jury. In particular, I would like to thanks Francesco Ginelli and Davide Marenduzzo for having accepted the time-consuming task of reviewing this manuscript.

Je tiens aussi à remercier toute l'équipe de MSC, et particulièrement mes infortunés compagnons d'open space Jérémy, Ruben, Thibaut, Annette, Mourtaza, Mélina et Anouchka. Votre omniprésente complicité m'a été précieuse tout le long de cette thèse. Merci également à Marlène pour avoir organisé mes expéditions à droite et à gauche dans le monde ainsi que pour son délicieux punch coco. Merci à François et Olivier d'avoir accepté de m'accompagner durant ces trois années lors de mes comités de suivi de thèse. Vos conseils m'ont été précieux. Merci à tous les pensionnaires de la 777 pour m'avoir montré qu'il n'y a pas que la théorie dans la vie; il y a aussi les expériences.

Je tenais par ailleurs à remercier toute l'équipe enseignante de physique en PASS à l'université de Paris et en particulier Mohamed et Jean-François pour toutes ces heures passées en TP/TD avec eux auprès des élèves. Cette première expérience d'enseignement à l'université a été très enrichissante pour moi.

Merci à tous les membres de la SFJAP, et en particulier à Paul, Tony et Benjamin pour toutes ces après-midi passées à révolutionner la physique ensemble. Grâce à vous, j'ai tout compris à la mesure quantique. Merci à tous mes amis de la coloïde pour toutes ces soirées (ou était-ce des matinées ?) revigorantes passées à refaire le monde (et pas à faire des sevens). Un grand merci au mythique tryptique du 103 rue de la Glacière, Louise, Paul, et Antoine pour tous ces moments inoubliables sans lesquels ma vie aurait été bien plus morne.

Merci à ma famille, et particulièrement à mes parents, qui, bien qu'ils cherchent toujours à comprendre la physique de cette thèse, m'ont constamment épaulé tout au long de son avancée. Merci à mes frères Henri et Etienne; votre estime et votre soutien m'ont toujours été très précieux. Enfin, et non sans émotions, merci à Anaëlle de partager ma vie.

Résumé en Français

La matière active regroupe l'étude des systèmes comprenant un grand nombre d'agents capables d'exercer des forces d'autopropulsion sur leur environement. La motivation première de la matière active est de fournir un cadre théorique simplifié décrivant des ensembles d'entités vivantes en interaction. Cette approche spécifique est déjà à l'origine de plusieurs percées dans la compréhension des systèmes vivants, dans l'étude du mouvement bactérien et dans celle des nuées d'oiseaux par exemple. Les succès de la matière active se sont récemment étendus au delà du vivant. Le domaine a notamment inspiré toute une panoplie d'expériences basées sur des matériaux artificiels : des rollers de Quincke aux colloïdes de Janus en passant par les grains vibrés. Dans ces montages, les entités actives sont synthétiques et leur moyen de propulsion repose sur un mécanisme physique plutôt que biologique. Ces nouvelles expériences permettent notamment de sonder la matière active dans un environement bien mieux contrôlé que ce qui était auparavant possible en biologie. Par ailleurs, elles ouvrent de nouvelles possibilités pour répondre à un défi majeur du domaine : parvenir à contrôler les propriétés et les transitions de phases des milieux actifs. La réussite de ce dernier objectif serait un premier pas vers la conception d'une nouvelle classe de matériaux, les matériaux actifs.

Ce manuscrit de thèse contribue au développement de la matière active suivant 4 axes : l'étude exacte d'un modèle de dynamique active, la caractérisation de l'ordre dans la transition vers le mouvement collectif, l'étude de l'émergence d'embouteillages au sein d'un liquide polaire et l'apparition de corrélations longue portée dues à l'anisotropie.

Malgré ses succès, la matière active souffre des limitations inhérentes à la complexité de son objet d'étude. Parce qu'elle cherche à modéliser des entités du vivant, même le système actif le plus simple sera soumis à des fluctuations non Gaussiennes, éventuellement corrélées, qui sont responsables de son maintien hors d'équilibre. D'un point de vue théorique, l'utilisation de ces fluctuations inhabituelles a le désavantage technique de rendre les calculs analytiques beaucoup plus difficiles. Quantifier le caractère hors équilibre des particules actives est un champ de recherche entier en soi, mais les résultats exact dans ce domaine restent rares et limités à certains modèles spécifiques. En présentant une analyse perturbative exacte d'une particule active d'Ornstein-Uhlenbeck (AOUP), le chapitre 2 du présent manuscrit apporte une contribution aux résultats analytiques en matière active. Dans le modèle AOUP, on considère une dynamique colloïdale dont le bruit Brownian diffusif est remplacé par un processus d'Ornstein-Uhlenbeck de temps de persistence τ. Ce processus d'Ornstein-Uhlenbeck modélise une autopropulsion colorée et sa persistence τ contrôle le niveau d'activité dans la dynamique : à $\tau = 0$, l'autopropulsion devient Brownienne alors qu'à $\tau = \infty$ elle devient constante. En utilisant ce "levier" de contrôle, nous calculons dans un premier temps la distribution stationnaire d'une AOUP au voisinage de l'équilibre sous la forme d'une série en puissance de τ. Nous utilisons ensuite ce résultat pour quantifier analytiquement trois signatures de l'irréversibilité temporelle générée par l'activité : la déviation au poids de Boltzmann, le courant "de cliquet" et la production d'entropie. Dans un potentiel confinant, la distribution spatiale d'une AOUP montre une accumulation en dehors du minimum local, en fort contraste avec le poids de Boltzmann de l'équilibre. Dans un potentiel périodique, une AOUP peut acquérir une vitesse moyenne non nulle dans l'état stationnaire et ainsi présenter un courant "de cliquet". La conception d'un "cliquet" de Feynmann menant à un mouvement perpétuel, prohibé dans la physique d'équilibre, devient possible grâce à la dynamique active. Finalement, et de nouveau en opposition à la physique d'équilibre, nous calculons

une production d'entropie non nulle pour la dynamique AOUP. Nous vérifions nos résultats analytiques à l'aide de simulations numériques : l'accord est quantitatif sans aucun paramètre d'ajustement.

En matière active, la plupart des travaux sont menés dans des régimes d'activité forte tels que les fluctuations thermiques des colloïdes actifs peuvent être négligées. Malgré son importance pour de multiples expériences, l'interaction entre bruit actif et bruit passif a rarement été étudiée et son influence sur l'irréversibilité de la dynamique n'a pas été discutée. C'est pourquoi, dans un second temps, nous étudions l'effet de l'ajout d'un bruit Brownien à la dynamique AOUP. En généralisant notre analyse perturbative, nous retraçons les rôles respectifs des bruits actif et passif dans la distribution stationnaire de ce modèle spécifique. A l'aide de ce résultat, nous calculons les signatures de l'irréversibilité et nous montrons qu'elles peuvent avoir un comportement surprenant lorsque la température varie. Selon la nature du potentiel dans lequel la particule évolue, le courant "de cliquet" et la production d'entropie peuvent être des fonctions non monotones de T. Cette dernière peut même diverger pour des potentiels suffisamment abruptes. Ainsi, selon le contexte, la présence de bruit thermique peut rapprocher ou éloigner la particule active de l'équilibre. Une fois de plus, nous vérifions nos prédictions analytiques à l'aide de simulations numériques : le courant de "cliquet" tout comme la distribution stationnaire sont en accord quantitatifs avec nos résultats.

La transition vers le mouvement collectif est l'un des phénomènes les plus étudiés en matière active. Elle modélise l'émergence de nuées depuis un ensemble désordonné de particules autopropulsées soumises à un mécanisme d'alignement. Les spécificités de cette transition, et particulièrement son ordre, ont été longuement discutées dans la littérature. Une classification basée sur le type d'interactions microscopiques en jeu a émergé : l'émergence du mouvement collectif serait discontinue dans les modèles dits "métriques" et continue dans les modèles dits "topologiques". Dans le chapitre 3, nous montrons que cette classification fondée sur des approches de champ moyen ne survit pas à la prise en compte des fluctuations. Dans un premier temps, nous introduisons le mouvement collectif à l'aide d'une dynamique paradigmatique : le modèle de Vicsek. En s'appuyant sur son analyse théorique, nous montrons que l'émergence discontinue des nuées dans ce modèle est due à la dépendence en densité de sa température critique. Nous confirmons ensuite cette analyse pour tous les systèmes de particules autopropulsées en étudiant les équations de champs génériques de Toner-Tu : la dépendence en densité de la température critique entraîne génériquement une transition du premier ordre.

Dans un second temps, nous introduisons le modèle d'Ising actif (AIM) et décrivons la disparité entre les équations de champ moyen et les résultats des simulations numériques. Alors que le champ moyen prédit une transition continue, les simulations montrent au contraire que l'émergence du mouvement collectif est discontinue et mène à la formation de nuées ordonnées de particules. Afin de déterminer le mécanisme à l'origine de cette disparité, nous étudions la stabilité des équations de champ moyen par rapport au bruit microscopique à l'aide de la renormalisation quasi-linéaire. Il s'avère que les fluctuations de la dynamique des spins renormalisent directement la température critique du modèle en induisant une dépendance en la densité. In fine, les fluctuations sont donc à l'origine de la transition du premier ordre observée dans les simulations.

Dans un troisième temps, nous évaluons si ce phénomène, appelé transition de premier ordre induite par les fluctuations (FIFOT), est générique et s'applique également aux modèles dits "topologiques". Dans ces derniers, l'alignement entre les particules ne dépend pas de leur distance relative mais de règles topologiques construites par la tessella-

tion de Voronoi ou les plus proches voisins. Dans la littérature, ces modèles "topologiques" jouent un rôle important lorsque les indices visuels dominent les indices métriques; c'est le cas pour les études de groupes d'animaux ou de piétons par exemple. Si l'on prends l'exemple d'un alignement entre plus proches voisins, doubler la distance entre les particules est équivalent à diviser la densité par 2^d sans changer les voisins dans la dynamique d'alignement. Ainsi, on pourrait penser que les fluctuations locales de la densité n'ont pas d'impact sur la magnétisation et que donc la température critique ne dépends pas de la densité. Nous montrons cependant que ce n'est pas le cas; à l'instar du modèle d'Ising actif, la transition continue prédite par le champ moyen est également remplacé par une séparation de phase dans le cas "topologique" : le mécanisme de transition de premier ordre induite par les fluctuations s'applique également dans ce cas particulier. Afin de vérifier notre analyse, nous effectuons des simulations numériques du modèle de Vicsek et d'Ising actif avec alignement sur les trois plus proches voisins. Dans les deux cas, nous confirmons la présence d'un domaine de coexistence dans le diagramme des phases. A l'intérieur de ce domaine, nous observons des nuées ordonnées de particules qui coexistent avec un gaz désordonné et pouvons donc conclure que la transition vers le mouvement collectif est discontinue dans ces deux modèles. Après avoir démontré que les modèles de Vicsek et d'Ising actif topologiques étaient, eux aussi, instables aux fluctuations mésoscopiques, nous nous demandons si ce mécanisme se généralise à d'autre modèles topologiques.

Pour répondre à cette question, nous considérons un champ d'alignement générique que nous supposons être une fonctionnelle de la densité et de la magnétisation locale. A l'aide d'une analyse dimensionnelle et d'arguments de scalings, nous montrons qu'il n'est pas possible d'exclure une dépendance en la densité de la température critique. Nous nous attendons donc à ce que le mécanisme de transition de premier ordre induite par les fluctuations affecte la plupart des modèles dits "topologiques". Dans une vaste majorité de modèles, l'émergence du mouvement collectif prendra donc la forme d'une transition de phase où des nuées ordonnées se propagent au milieu d'un gaz désordonné.

Enfin, nous terminons ce chapitre en présentant un test numérique pour évaluer l'ordre de la transition dans les modèles de mouvement collectif. Nous proposons de mesurer la dépendence de la température critique par rapport à la densité : si elle n'en dépend pas, c'est que la transition est continue, sinon c'est qu'elle est discontinue. Afin de vérifier la pertinence de ce test, nous l'appliquons sur deux modèles de mouvement collectif en champ moyen ainsi qu'au modèle d'Ising actif topologique. Dans les deux premiers cas, la température critique reste inchangée quelque soit la densité tandis que dans le dernier cas nous mesurons qu'elle augmente avec la densité.

Aux côtés du mouvement collectif, il existe une autre transition de phase paradigmatique en matière active : la séparation de phase induite par la motilité (MIPS). Elle apparaît dans les systèmes de particules actives où l'autopropulsion décroît suffisamment rapidement lorsque la densité augmente. Ce comportement déclenche une boucle de rétroaction menant à la formation d'amas denses inertes qui coexistent avec une phase gazeuse. Si la transition vers le mouvement collectif et MIPS ont été largement étudiées séparément, leur interaction dans les systèmes actifs avec alignement et autopropulsion dépendant de la densité reste mal comprise. En particulier, la possible formation de MIPS dans un état plutôt que dans un gaz désordonné reste une question ouverte. Dans le chapitre 4, nous répondons à cette question en étudiant l'interaction de MIPS et du mouvement collectif. Dans ce but, nous rapportons qu'une nouvelle transition de phase a lieu dans les assemblées de rollers de Quincke à haute densité. A la transition, que nous

avons nommée solidification active, nous observons de denses embouteillages désordonnés qui remontent le flux collectif ordonné des rollers. Nous caractérisons expérimentalement la solidification active comme transition de premier ordre grâce à trois signatures : le respect de la règle du levier à la coexistence, la présence d'une dynamique lente de croissance de domaine, et l'existence de boucles d'hysteresis. Par ailleurs, les expériences montrent que les embouteillages constituent un solide amorphe, dans lequel les rollers sont arrêtés. La mesure de l'autopropulsion moyenne d'un roller de Quincke en fonction de la densité locale fournit un indice sur le mécanisme à l'origine de la solidification active : elle montre que l'autopropulsion décroît abruptement au delà d'une densité critique. En partant d'une description hydrodynamique générique des rollers autopropulsés, nous construisons une théorie phénoménologique prenant en compte ces résultat expérimentaux : nous imposons que la vitesse et l'alignement des rollers décroissent tous deux à haute densité. L'addition de ces deux ingrédients que l'on retrouve communément chez MIPS permet de reproduire la physique de la solidification active avec nos équations d'évolution. A haute densité, nous observons bien la formation de denses embouteillages désordonnés qui remontent le flux d'un liquide polaire ordonné. De plus, les équations de champ reproduisent qualitativement la même transition de premier ordre avec règle du levier, présence d'une dynamique lente de croissance de domaine et existence de boucles d'hysteresis. Ces similitudes avec l'expérience justifient l'utilisation de cette hydrodynamique généralisée pour éclairer le mécanisme à l'origine de la solidification active. Une analyse de stabilité linéaire montre directement que le critère de formation des embouteillages est mathématiquement similaire à celui de l'émergence de MIPS : ainsi, la solidification active peut être bien décrite comme une séparation de phase induite par la motilité entre un liquide polaire et un embouteillage. Jusqu'à présent, notre étude théorique se borne à une approche phénoménologique de la solidification active qui ne peut être directement reliée aux constantes physiques microscopiques : l'origine de la chute de l'autopropulsion à haute densité reste en effet à déterminer (répulsion stérique, lubrification ?). Pour clore ce chapitre, afin de mieux comprendre les ingrédients microscopiques nécessaires à la solidification active, nous étudions un modèle de gaz actif sur réseau. Dans un tel cadre théorique, nous savons calculer l'hydrodynamique macroscopique à partir de la dynamique microscopique de manière exacte à l'aide de techniques d'intégrales de chemin. Cette correspondance nous permet de mettre en lumière 2 mécanismes clés nécessaires à la solidification active : une autopropulsion et un alignement non nuls à basse densité qui chutent à haute densité. Par ailleurs, en faisant varier les paramètres de notre modèle, nous sommes en mesure de prédire l'existence d'une phase de coexistence triple où des nuées de taille finie cohabitent avec un gaz avant de s'échouer sur des embouteillages. Nos résultats théoriques sont tous confirmés par les simulations : l'accord avec l'hydrodynamique exacte est très bon.

En physique statistique, la fonction à deux points $\langle\phi(\mathbf{x})\phi(0)\rangle$ d'un champ scalaire $\phi(\mathbf{x})$ est dite "à longue portée", ou "invariante d'échelle", lorsque $\langle\phi(\mathbf{x})\phi(0)\rangle \underset{|\mathbf{x}|\to\infty}{\sim} |\mathbf{x}|^{-\alpha}$ avec α un coefficient positif mesurant le déclin algébrique. Ce type de corrélations reste peu étudié en matière active en dehors de la phase ordonnée du modèle de Vicsek. C'est pourquoi, dans le chapitre 5, nous présentons un modèle dont le comportement macroscopique est invariant d'échelle. Dans le système considéré, les particules sont soumises à des fluctuations anisotropiques à courte portée. Leurs dynamiques sont couplées par le biais d'interactions spatiales : les particules situées dans un même rayon de taille σ sont soumises à un bruit corrélé. Nous montrons que, à cause de l'anisotropie, des corrélations à longue portée émergent dans les fluctuations de la densité. Nous cherchons

ensuite les signatures induites par cette invariance d'échelle sur les observables physiques du système. A l'inverse des systèmes d'équilibres, la pression moyenne exercée par notre système sur des murs confinants ne présente pas de comportement de type Casimir : elle suit simplement la loi du gaz parfait. En revanche, nous montrons que les corrélations de la pression exercée sur deux murs opposés et séparés par une distance L déclinent en L^{-2}. Tous nos résultats théoriques sont en accord quantitatifs avec les simulations numériques de notre modèle.

Finalement, dans le dernier chapitre, nous concluons ce manuscrit en résumant les contributions développées dans les 4 chapitres précedents. Pour chacun de ces travaux, nous proposons une possible direction de recherche future.

Contents

1. Introduction

Statistical Physics aims at describing the emerging properties of macroscopic assemblies composed of microscopic entities. Historically, the framework of equilibrium statistical physics has been developed to link the state functions of thermodynamics, such as entropy or free energy, to the microscopic dynamics of atoms and molecules. The entropy, the free energy acquire a physical meaning thanks to the idea of partitioning the accessible states of the system. In particular, they can be formally expressed as weighted sums where the environment only enters through a few set of parameters. From these expressions, it is possible to deduce all the static macroscopic physical quantities measurable by an experimentalist: pressure, work, chemical potential... However, the existence of these state functions relies on the knowledge of the statistical weights one has to attribute to each state of the system. The determination of these weights is miraculously possible at the expanse of restrictive hypotheses: the underlying dynamics must be ergodic and it must lead to a time-reversible steady state where the principle of detailed balance is verified.

On the contrary, the study of generic systems dealing with assemblies of time-irreversible entities falls into the realm of nonequilibrium statistical physics. And this realm is far more extended than the equilibrium one. The overwhelming majority of daily phenomena around us can be studied through the lenses of out-of-equilibrium statistical physics. At the nanometric scale, molecular motors are consuming ATP to transport ions along actin filaments [1–4] (see Fig. 1.1b). At the micrometric scale, living cells exhibit rich nonequilibrium behaviours when they crawl on a substrate [5–7]. At the metric scale, flocks of birds coherently fly in a given direction, breaking rotational symmetry [8, 9] and leading to long-lived currents (see Fig. 1.1b). At the scale of society, financial trends can be modeled by considering agents who stochastically and imperfectly try to optimize their gains [10, 11]. Nonequilibrium systems have such a diverse field of application that

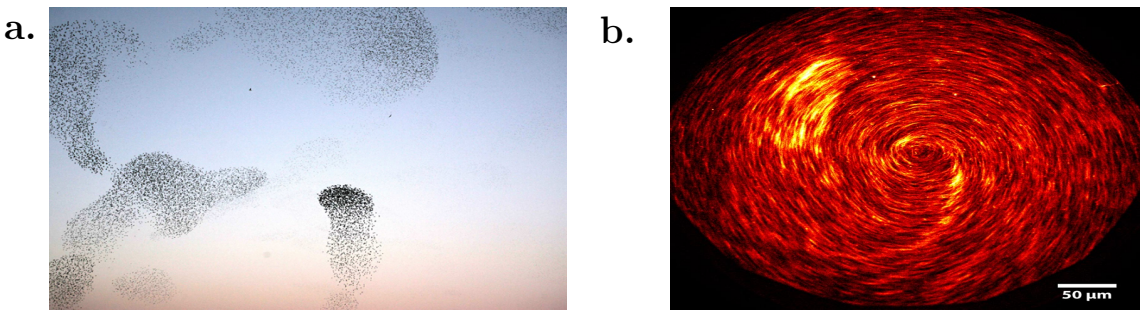

Figure 1.1 – **a.** Typical example of starling aerial display used for 3D reconstruction of the birds' dynamics in [9]. Figure adapted from [9]. **b.** Swirling pattern of actin filaments displaced by molecular motors. Figure adapted from [4].

it seems quite unfeasible to state general theorems about them. Surprisingly, generic results out of equilibrium have nonetheless been obtained, as exemplified by the Fluctuation Theorem [12, 13] or the Jarzynski's inequalities [14] among other results [15–18]. However, when a quantitative description of nonequilibrium systems is needed, it is often necessary to proceed to a case-by-case analysis. It is then difficult to extend the conclusions drawn on one specific model to other systems. In particular, the generic approach offered by equilibrium statistical mechanics collapses out of equilibrium.

During the last twenty years, some level of generality has been revealed in systems where the Brownian motion of colloids has been replaced by a persistent self-propulsion. Their study has been regrouped in a domain called active matter whose main motivation was first to provide a simple framework describing ensemble of living entities [19–21]. To this aim, active matter studies usually proceed in two key steps. The first one is the conception of simplified building blocks mimicking the behaviour of living automatons. The second step is the introduction of biologically-inspired interactions between these elementary building blocks. Such an approach has already fruitfully accounted for important features of bird flocks [8, 9], or bacterial dynamics [22, 23] among other works [5, 24–27]. But the successes of active matter extend beyond living systems. Recently, it has inspired a wealth of experiments dealing with artificial materials: Quincke rollers [28, 29], Janus colloids [30–33] (see Fig. 1.2b), shaken grains [34,35] (see Fig. 1.2a), hexbugs robots [36]... In most of these setups, the active entities are synthetic units whose self-propulsion relies on a physical rather than biological mechanism: electrohydrodynamic instability [37], Marangoni stress [38], built-in frictional asymmetry [39, 40], light-induced phoretic gradients [41]... These new experiments allow to probe active matter in a much more controlled environment than what was previously possible in biology.

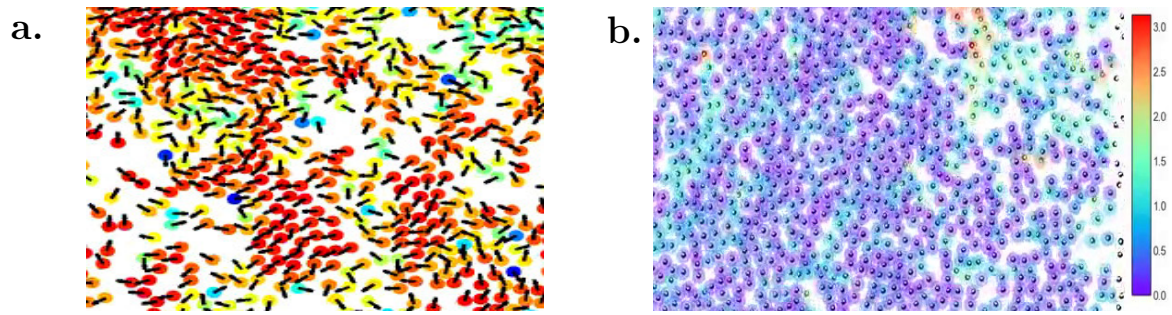

Figure 1.2 – **a.** Emergence of flocks in assemblies of vibrated asymmetric grains. The arrows indicate their orientation while the color account for local ordering: red indicates an almost perfect cohesion. Figure adapted from [34]. **b.** Collective motion in ensemble of Janus colloids. The color surrounding a particle indicate the absolute deviation of its orientation from the average direction $|\theta - \langle\theta\rangle|$. Figure adapted from [31]

Furthermore, they open up new opportunities to face one of the main challenge of active matter: bringing under control the properties and transitions of active media [42]. Achieving this last objective would be the first step on the path toward the engineering of active materials [43, 44]. In this manuscript, I contribute to the active matter roadmap along four axes: the exact study of a workhorse model of active dynamics, the characterization of the order in the flocking transition, the study of the interplay between flocks and jams, and the presentation of anisotropy-induced long-ranged correlations.

Despite its great sucesses, active matter suffers from limitations inherent to the complexity of its object of study [45]. As it aims at modelling living entities, even the simplest active system will feature non-Gaussian, possibly correlated fluctuations which are responsible for its nonequilibrium nature [46, 47]. From a theoretical standpoint, resorting to these unusual fluctuations has the technical disadvantage of making algebraic computations very challenging. Quantifying the departure of active particles from equilibrium physics is a whole research field *per se* [47–55] but exact results remain scarce and limited to specific models. Chapter 2 aims at filling this gap by presenting an exact perturbative analysis of Active Ornstein Uhlenbeck Particles (AOUPs). These results,

which generalize a previous work from the group [56], are summarized in our contributions [57, 58]. In section 2.1, I derive analytically the steady-state distribution of an AOUP and quantify its departure from equilibrium through the characterization of three signatures: the deviation from Boltzmann distribution, the ratchet current, and the entropy production rate. In section 2.2, I generalize my analytical results to the case of a particle experiencing both active and passive noise. The interplay between the two types of fluctuations is shown to lead to a rich phenomenology for the ratchet current and the entropy production rate when the temperature is varied: decline or non-monotonicity, divergence or decay at high T. Finally, in section 2.3, I discuss the extension of my derivations to the case of interacting active particles in arbitrary dimension.

The transition to collective motion [8, 9] is one of the most studied phenomena in active matter. It describes the emergence of flocks from a disordered assembly of aligning self-propelled units [59]. Its specificities, and particularly its order, have been discussed extensively in the literature [60–62]. A classification based on the type of microscopic interactions at play has emerged: the onset of flocking should be discontinuous in so-called metric models and continuous in so-called topological models. [63–65]. In Chapter 3, I show that such a classification does not survive the incorporation of microscopic noise. To this aim, I present a detailed account of our contribution [66]. In sections 3.1 and 3.2, I introduce the transition to collective motion and motivate my study. From sections 3.3 to 3.7, I present the notion of fluctuation-induced first-order transition and apply it to flocking models. Our work shows that the current classification of transition to collective motion must be revisited: there are strong evidences of a discontinuous scenario with phase-separation, no matter the type of microscopic alignment at play, as long as the orientational dynamics is not decoupled from the position of the agents.

Beside flocking, there is a second paradigmatic phase transition in active matter: Motility-Induced Phase Separation (MIPS) [67] (see Fig. 1.3). It occurs in systems of active particles where self-propulsion decreases sufficiently rapidly as the local density increases [68]. This dependency on the density triggers an unstable feedback loop leading to the formation of dense arrested clusters coexisting with a gas phase [67]. While the transition to collective motion and MIPS have been extensively studied on their own [69–74], there has been few studies about their interplay in active systems exhibiting both alignment and a density-dependent self-propulsion [75–78]. In particular, the possible occurrence of MIPS in an ordered state instead of in a disordered gas remains an open question. In Chapter 4, we tackle this problem by studying the interplay between the flocking transition and MIPS in dense assemblies of Quincke rollers. To this aim, I follow the presentation of our contribution [79], which I complement with unpublished results. This chapter corresponds to a joint work with Delphine Geyer and Denis Bartolo (ENS Lyon) who were in charge of all the experimental side of the collaboration. In sections 4.1 to 4.3, I unveil a new phase transition taking place in dense assemblies of colloidal rollers, which we dubbed active solidification. At the transition, disordered jams that propagate upstream a homogeneous flock of rollers are observed. In section 4.4, I show that active solidification is due to an extended MIPS scenario occurring between a polar liquid and an active solid. Finally, in section 4.5, I vary the parameters of our theoretical model to explore the rich phenomenology yielded by the interplay of MIPS and collective motion. By doing so, I predict the presence of an interesting phase where flocking bands coexist with active jams.

Chapter 5 lies slightly aside from the rest of this manuscript as it was started at the end of this PhD. It contains solely unpublished results obtained in collaboration with

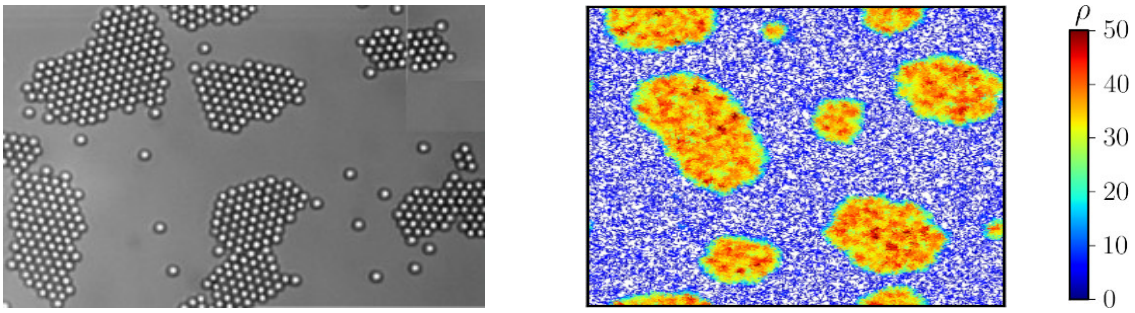

Figure 1.3 – **Left.** Snapshot of self-phoretic colloids spontaneously forming dense clusters of particles. Their self-propulsion mechanism is controlled by a homogeneous light shed on the system. Figure adapted from [80]. **Right.** Simulations of Active Brownian Particles with quorum sensing interaction: their self-propulsion decreases with the local density. They spontaneously form dense clusters of particles. Figure adapted from [67].

Yariv Kafri and Mehran Kardar. In statistical physics, whenever the two-point function of a quantity ϕ decays algebraically with the distance $|\mathbf{x}|$ as $\langle\phi(\mathbf{x})\phi(0)\rangle \propto |\mathbf{x}|^{-\alpha}$, it is said that correlations are long-ranged, or scale-free. Historically, there has been a large interest in long-ranged correlations, be it at the critical point in equilibrium systems [81–85] or in the steady state of out-of-equilibrium systems [86–94]. However, rather surprisingly, long-ranged correlations have rarely been discussed in active matter outside from the ordered phase of the Vicsek model [95–98]. As a first step in this direction, I present in Chapter 5 a particle-based model with emergent scale-free behaviour inspired by a field theoretical work of Lee, Grinstein and Sachdev [99]. Starting from a microscopic dynamics with anisotropic short-range interactions, I show the existence of macroscopic long-ranged density correlations in sections 5.3 to 5.3.2. In section 5.4, I assess the effect of this scale-free decay on the pressure exerted by the system in order to probe for a possible Casimir-like behaviour.

Finally, in chapter 6, I conclude this thesis by summarizing the contributions developed in the four chapters. For each one of my work, I propose a possible future research direction.

2. Active Ornstein Uhlenbeck Particle: departure from equilibrium

The present chapter details and contextualizes our contributions [57]- [58] on the AOUP model. Let us start with a paradigmatic equilibrium dynamics: we consider a particle evolving in a confining potential ϕ and submitted to a Gaussian white noise. Its position x obeys the following over-damped Langevin equation:

$$\dot{x} = -\mu\, \partial_x \phi + \sqrt{2T}\eta\,, \tag{2.1}$$

where μ is the mobility and η is a Gaussian thermal noise such that $\langle \eta(t)\eta(t')\rangle = \delta(t-t')$. In the remainder of this chapter, for clarity, we set the mobility coefficient μ to 1 in (2.1). The probability $P(x,t)$ to observe the particle at position x at time t evolves according to the Fokker-Planck equation

$$\partial_t P(x,t) = \partial_x \left[T\partial_x P(x,t) + \partial_x \phi P(x,t)\right]\ , \tag{2.2}$$

where ∂_x is a short-hand notation for $\partial/\partial x$. Thermal equilibrium imposes strong constaints on the steady state of dynamics (2.1):

CI. It enforces the Boltzmann weight, linking the stationary probability $P(x)$ to the local potential energy $\phi(x)$ as $P(x) \propto \exp(-\phi(x)/T)$.

CII. It prohibits the emergence of currents.

CIII. It prevents the existence of an arrow of time.

The first point stems from the Fokker-Planck equation (2.2), whose flux-free steady state satisfies $T\partial_x P + \partial_x \phi P = 0$ so that $P(x) \propto \exp(-\phi/T)$.

The second point is a consequence of the Boltzmann weight as the current J is the steady-state averaged velocity, *ie* $J = \langle \dot{x}\rangle$. Using expression (2.1) for $\dot{x}$, and noting that $\langle \eta\rangle = 0$, we obtain

$$J = \langle -\partial_x \phi\rangle = -\int_{-\infty}^{+\infty} \partial_x \phi P(x) dx = -\int_{-\infty}^{+\infty} \partial_x \phi \frac{e^{-\phi/T}}{Z} dx = 0\,, \tag{2.3}$$

where we have used that a confining potential satisfies $\phi(\pm\infty) = \infty$. Let us now demonstrate the last point by introducing the entropy production rate σ. It is defined as the long-time limit of the Kullback-Leibler divergence between the probability of a trajectory and its time-reversed counterpart (to which we refer as "forward" and "backward" trajectories) divided by the duration of the trajectory [100, 101]. In our case, a trajectory is defined by a set of positions $x(t)$ for $t \in [0, t_f]$ and its backward counterpart is given by the set of positions $\mathcal{R}x(t) = x(t_f - t)$. Mathematically, the entropy production rate reads

$$\sigma = \lim_{t_f\to\infty} \frac{1}{t_f} \int D[\{x(t)\}]\mathcal{P}[\{x(t)\}] \ln\left(\frac{\mathcal{P}[\{x(t)\}]}{\mathcal{P}[\{\mathcal{R}x(t)\}]}\right)\,, \tag{2.4}$$

where $\mathcal{P}[\cdot]$ is the probability to observe a given trajectory. If we define $\langle\cdot\rangle_{\mathcal{P}}$ as the ensemble average over all trajectories, we thus obtain σ as

$$\sigma = \lim_{t_f\to\infty} \left\langle \frac{1}{t_f} \ln\left(\frac{\mathcal{P}[\{x(t)\}]}{\mathcal{P}[\{\mathcal{R}x(t)\}]}\right)\right\rangle_{\mathcal{P}}\,. \tag{2.5}$$

In this chapter, we will assume that the dynamics of $x(t)$ is ergodic and has a steady-state density function $P(x)$. Under these two assumptions, the quantity $t_f^{-1}\Big[\ln(\mathcal{P}[\{x(t)\}]) - \ln(\mathcal{P}[\{\mathcal{R}x(t)\}])\Big]$ becomes trajectory-independent in the limit $t_f \to \infty$ and σ simplifies into

$$\sigma = \lim_{t_f\to\infty} \frac{1}{t_f} \ln\left(\frac{\mathcal{P}[\{x(t)\}]}{\mathcal{P}[\{\mathcal{R}x(t)\}]}\right) . \tag{2.6}$$

Using a path integral approach, we now compute $\mathcal{P}[\{x(t)\}]$ for (2.1) in Stratonovitch formalism as

$$\mathcal{P}[\{x(t)\}] \propto \exp\left[\int_0^{t_f} \frac{\partial_{xx}\phi}{2} dx\right] \exp\left[\int_0^{t_f} \frac{(\dot{x} + \partial_x\phi)^2}{4T} dt\right] . \tag{2.7}$$

The first factor on the right hand side of (2.7) is specific to the Stratonovitch convention: it stems from the determinant of the change of variable $\eta(t) \to x(t)$. Note that this factor will not contribute to the entropy production rate as it is not affected by the reversal operator $\mathcal{R}$. On the contrary, the second factor on the right hand side of (2.7) will change for a reversed trajectory through the transformation $\dot{x} \to -\dot{x}$. Note that the integral in this factor has to be understood in the Stratonovitch sense. Plugging (2.7) into (2.6), we thus obtain

$$\sigma = \lim_{t\to t_f} \frac{1}{t_f} \int_0^{t_f} \frac{\dot{x}\partial_x\phi}{T} dt = \lim_{t\to t_f} \frac{1}{t_f} \int_0^{t_f} \frac{1}{T}\frac{d\phi}{dt} dt = \lim_{t\to t_f} \frac{1}{t_f} \left[\frac{\phi\left[x(t_f)\right] - \phi\left[x(0)\right]}{T}\right] = 0 , \tag{2.8}$$

which shows that an observer cannot statistically distinguish between the forward and backward trajectories of the position $x(t)$. In layman's terms, movies recording the system's evolution played backward or forward cannot be distinguished: there is no arrow of time. I now study how a tiny addition of activity in dynamics (2.1) can circumvent the constraints CI-CII-CIII of thermal equilibrium, enabling the emergence of the three phenomena: deviation from Boltzmann, generation of currents and nonzero entropy production rate.

2.1 Exact perturbative results: non-interacting AOUPs in 1D

Let us consider one of the simplest model of active particles: the one-dimensional Active Ornstein Uhlenbeck Particle (AOUP). Its position x and self-propulsion speed v evolves according to the following over-damped langevin equations

$$\dot{x} = -\partial_x\phi + v \tag{2.9}$$

$$\dot{v} = -\frac{v}{\tau} + \frac{\sqrt{2D}}{\tau}\,\eta , \tag{2.10}$$

where τ is the persistence length, D is a constant, and η is a Gaussian white noise of unit variance. The system (2.9)-(2.10) differs from the Brownian case (2.1) because the Ornstein-Uhlenbeck noise v acting on the particle is colored: $\langle v(t)v(t')\rangle = D\exp(-|t - t'|/\tau)/\tau$. As the dissipation is memoryless in (2.9) ($\mu = 1$), the Stokes-Einstein relation between noise and friction is violated and the particle is driven out of thermal equilibrium.

Note that, for $\tau = 0$, the Gaussian noise v falls back onto a Wiener process of amplitude D since $\lim_{\tau\to 0}\langle v(t)v(t')\rangle = D\delta(t-t')$. In this particular case, the dynamics (2.9)-(2.10) is an equilibrium one with temperature D. Thus, intuitively, τ provides a continuous "handle" to set the level of activity in the dynamics. Despite the presence of this "handle", characterizing the departure from thermal equilibrium of (2.9)-(2.10) remains a challenge. Indeed, others active models such as RTPs and ABPs do have similar parameters ϵ controlling the intensity of activity but so far there are no analytic characterization of their behaviour when ϵ is small. In this section, I extend the approach of [56] and develop an exact perturbative expansion for the AOUP model (2.9)-(2.10). My main result is an analytical prediction of the steady-state distribution $\mathcal{P}_s(x,v)$ as a series in $\tau^{1/2}$ (see section 2.1.1). Building on it, I then make quantitative predictions about the three signatures of nonequilibrium CI-CII-CIII: I compute the marginal in space of the probability density in 2.1.2, the current in an asymmetric periodic ratchet in 2.1.4, and the entropy production rate in 2.1.5.

2.1.1 The stationary measure

In this section, I perform the derivation of the steady-state distribution $\mathcal{P}_s(x,v)$ as a series in powers of $\tau^{1/2}$. Historically, the density $\mathcal{P}_s$ was first derived to order τ in [56] for a confining potential. Herafter, I use a slightly different method and, most importantly, explain how to extend the expansion to arbitrary order.

The derivation proceeds in several steps. First, we conveniently rescale the Fokker-Planck operator. Then, we look for its stationary solution by expanding $\mathcal{P}_s$ on the basis of Hermite polynomials and we show how the Fokker-Planck equation imposes a recurrence relation between the coefficients of this expansion. Finally, we solve the recurrence by expanding these coefficients as power series in $\tau^{1/2}$. We now detail the derivation starting from the Fokker-Planck operator $\mathcal{L}$ corresponding to (2.9)-(2.10), which reads

$$\mathcal{L} = \partial_x(\partial_x\Phi) - v\partial_x + \partial_v\left(\frac{v}{\tau}\right) + \frac{D}{\tau^2}\partial_{vv} \ . \tag{2.11}$$

Because the steady-state distribution of (2.10) is proportional to $\exp(-\frac{\tau v^2}{2D})$, we rescale v as $\tilde{v} = \sqrt{\tau}v$ in order to expand $\mathcal{P}_s$ in series of $\tau^{1/2}$ around the equilibrium measure. Expressed in terms of the rescaled variable, $\mathcal{P}_s(x,\tilde{v})$ satisfies

$$\tilde{\mathcal{L}}\mathcal{P}_s(x,\tilde{v}) = 0 \tag{2.12}$$

with the operator $\tilde{\mathcal{L}}$ defined as :

$$\tilde{\mathcal{L}} = \partial_x(\partial_x\Phi) - \frac{\tilde{v}}{\sqrt{\tau}}\partial_x + \partial_{\tilde{v}}\left(\frac{\tilde{v}}{\tau}\right) + \frac{D}{\tau}\partial_{\tilde{v}\tilde{v}} \ . \tag{2.13}$$

In the remainder of this section, the tilde notation for v and $\mathcal{L}$ will be omitted for clarity. We first note that the Fokker-Planck operator (2.13) can be written as:

$$\mathcal{L} = \frac{1}{\tau}\mathcal{L}_1 + \frac{1}{\sqrt{\tau}}\mathcal{L}_2 + \mathcal{L}_3 \ . \tag{2.14}$$

Where $\mathcal{L}_1$, $\mathcal{L}_2$ and $\mathcal{L}_3$ are given by

$$\mathcal{L}_1 = D\frac{\partial^2}{\partial^2 v} + \frac{\partial}{\partial v}v \qquad \mathcal{L}_2 = -\frac{\partial}{\partial x}v \qquad \mathcal{L}_3 = \frac{\partial}{\partial x}\frac{\partial\phi}{\partial x} \ . \tag{2.15}$$

$\mathcal{L}_1$ is the Fokker-Planck generator of the Ornstein-Uhlenbeck process, and its n^{th} eigenfunction P_n is related to the n^{th} physicists' Hermite polynomial $H_n(v) = (-1)^n e^{v^2} \partial_v^n e^{-v^2}$ according to

$$P_n(v) = \frac{e^{-\frac{v^2}{2D}} H_n\left(\frac{v}{\sqrt{2D}}\right)}{\sqrt{2^n n! 2\pi D}} \ . \tag{2.16}$$

The family $\{P_n\}$ are eigenfunctions of the operator $\mathcal{L}_1$ satisfying

$$\mathcal{L}_1 P_n = -n P_n \tag{2.17}$$

and they form a family orthogonal to the set $\{H_n\}$:

$$\delta_{k,n} = \int_{-\infty}^{+\infty} \frac{H_k\left(\frac{v}{\sqrt{2D}}\right)}{\sqrt{2^k k!}} P_n(v) dv \ . \tag{2.18}$$

We use the P_n's to look for the solution of the stationnary distribution $\mathcal{P}_s$ under the form of:

$$\mathcal{P}_s(x,v) = \sum_{n \geq 0} P_n(v) A_n(x) \ . \tag{2.19}$$

Using the orthogonality property (2.18), the A_n's can be obtained as

$$A_n(x) = \int \mathcal{P}_s(x,v) \frac{H_n\left(\frac{v}{\sqrt{2D}}\right)}{\sqrt{2^n n!}} dv \ . \tag{2.20}$$

We further show in Appendix A.1.1 that they can be expanded in power of $\tau^{1/2}$ as

$$\begin{aligned} A_0 &= A_0^0(x) + \tau A_0^2(x) + \tau^2 A_0^4(x) + ... \\ A_1 &= \tau^{1/2} A_1^1(x) + \tau^{3/2} A_1^3(x) + \tau^{5/2} A_1^5(x) + ... \\ A_2 &= \tau A_2^2(x) + \tau^2 A_2^4(x) + \tau^3 A_2^6(x) + ... \\ &\vdots \end{aligned} \tag{2.21}$$

Note that A_{2k} contains only integer powers of τ and that its first nonzero contribution is of order τ^k. Likewise, A_{2k+1} contains only half-integer powers of τ and its first nonzero contribution is of order $\tau^{k+1/2}$. Thus, by definition, A_i^k is the term of order $\tau^{k/2}$ in A_i if $k \geq i$, and it vanishes otherwise. As explained in Appendix A.1.1, the A_i^k's can then be computed recursively and we report hereafter the expressions of A_0^0 and A_0^2 as an example:

$$A_0^0 = c_0 \ e^{-\frac{\phi}{D}} \ , \tag{2.22}$$

$$A_0^2 = c_0 \ e^{-\frac{\phi}{D}} \left(\partial_{xx}\phi - \frac{(\partial_x \phi)^2}{2D} \right) + c_2 \ e^{-\frac{\phi}{D}} - \frac{b_3}{\sqrt{D}} e^{-\frac{\phi}{D}} \int_0^x e^{\frac{\phi}{D}} dx \ . \tag{2.23}$$

As expected, A_0^0 corresponds to the equilibrium measure when $\tau = 0$ and c_0 is thus fixed by normalization, requiring $\int dx A_0^0 = 1$, which leads to

$$c_0 = \left(\int_{-\infty}^{+\infty} e^{-\frac{\phi}{D}} dx \right)^{-1} \ . \tag{2.24}$$

Equation (2.23) involves two additional integration constants: c_2 and b_3. While c_2 is found by normalization, requiring $\int_{-\infty}^{+\infty} A_0^2(x) dx = 0$, b_3 is fixed by the boundary conditions on

A_0^2 as we shall see in the next sections. As such, its value will differ when the system is infinite and confined by a diverging potential or is endowed with periodic boundary conditions. The recursion described in Appendix A.1.1 can be iterated up to an arbitrary order in τ to find all the A_i^k's for $i \geq 0$. In addition to the previous constants c_{2j} and b_{2j+1} for $j < k$, which were determined at order $\tau^{j/2}$, A_0^{2k} generically depends on two new integration constants: c_{2k} and b_{2k+1}. The former, c_{2k}, is found by requiring the normalization of A_0^{2k}, $\int A_0^{2k}(x)dx = 0$, while b_{2k+1} is fixed by the boundary conditions for A_0^{2k}.

For example, A_0^4 not only depends on c_2 and b_3, which were previously determined upon computing A_0^2, but also on two new integration constants : c_4 and b_5. The constant c_4 is found by requiring normalization $\int_{-\infty}^{+\infty} A_0^4(x)dx = 0$ and b_5 is fixed by enforcing the correct boundary conditions for A_0^4.

While the explicit expressions of the A_0^{2k} rapidly become cumbersome, their systematic derivation can be implemented with a software such as Mathematica [102]. For illustration purposes, we report the complete expression of $\mathcal{P}_s(x, v)$, with its integration constants, up to the order τ^2 in Appendix A.1.2.

2.1.2 Deviation from the Boltzmann distribution in a confining potential

The marginal in space of $\mathcal{P}_s(x, v)$ can be used to quantify how the steady-state distribution departs from the Boltzmann weight as τ increases. Integrating $\mathcal{P}_s(x, v)$ over v selects the term A_0 in the ansatz (2.19) through the use of the orthoganality relation (2.18):

$$\mathcal{P}_s(x) = \int_{-\infty}^{+\infty} \mathcal{P}_s(x, v)dv = A_0 = \sum_k A_0^{2k}\tau^k \ . \tag{2.25}$$

Here we consider the special case of a confining potential ϕ, and we require that, for all $k \geq 1$,

$$\lim_{x\to\pm\infty} A_0^{2k}(x) = 0 \tag{2.26}$$

$$\int_{-\infty}^{+\infty} A_0^{2k}(x) = 0 \ . \tag{2.27}$$

We remark that equation (2.26) imposes $b_{2k+1} = 0$ for all $k \geq 1$ while (2.27) fixes c_{2k} for all $k \geq 1$. The function A_0^{2k} is then uniquely determined. For example, using (2.23), A_0^2 reads

$$A_0^2 = \ c_0 \ e^{-\frac{\phi}{D}} \left(\partial_{xx}\phi - \frac{(\partial_x\phi)^2}{2D}\right) - \frac{3}{2}\frac{c_0^2}{} \ e^{-\frac{\phi}{D}} \int_{-\infty}^{+\infty} \partial_{xx}\phi \ e^{-\frac{\phi}{D}} dx \ , \tag{2.28}$$

where c_0 is given by (2.24). In expression (2.28), we can readily extract the first correction to the Gibbs-Boltzmann measure as

$$\frac{\mathcal{P}_s(x) - A_0^0}{A_0^0} = \tau \left[\partial_{xx}\phi - \frac{(\partial_x\phi)^2}{2D} - \frac{3\int_{-\infty}^{+\infty} \partial_{xx}\phi \ e^{-\frac{\phi}{D}} dx}{2\int_{-\infty}^{+\infty} e^{-\frac{\phi}{D}} dx}\right] + \mathcal{O}(\tau^2) \ . \tag{2.29}$$

Casting it into an effective potential ϕ_{eff}, we obtain

$$\mathcal{P}_s(x) \propto \exp\left(-\frac{\phi_{\text{eff}}}{D}\right) \quad \text{with} \quad \phi_{\text{eff}} = \phi + \tau\left(\frac{(\partial_x\phi)^2}{2} - D\partial_{xx}\phi\right) + \mathcal{O}(\tau^2) \ . \tag{2.30}$$

The cumbersome expression of the full marginal in space $\mathcal{P}_s(x)$ up to order τ^2 is reported in Appendix A.1.2.

Note that our ansatz (2.21) rests on the hypothesis that $\mathcal{P}_s(x)$ is an analytic function in $\tau^{1/2}$, which need not necessarily hold for an arbitrary potential. To check this hypothesis, we have to verify whether the series admits a finite radius of convergence.

2.1.3 Perturbative series: regularization process

In this section, I show that the convergence of our expansion (2.19) is only ensured for small values of τ. To formally extend our results beyond this regime, we have to resort to a regularization process described afterwards. We start by assessing numerically of convergence of our expansion for a potential $\phi(x) = x^4/4$, at fixed D, and for two different values of τ. For $\tau = 0.01$, we show in Fig. 2.1 truncations of (2.25) up to order τ^8. They are well-behaved and quantitatively agree with the stationary distribution obtained numerically. However, for $\tau = 0.2$, Fig. 2.1 shows the successive orders of the truncation to be typical of asymptotic series: adding one order in τ increases the series by a larger amount than the sum of the previous terms, leading to wild oscillations. While such a result seems disappointing, it does not mean that the full series fails in capturing the steady state. Mathematically speaking, it only entails that the finite truncation yields a poor approximation of the full series and that more work should be carried out to extract physical behaviours.

To regularize our diverging truncated sequence, we resort to a Padé-Borel summation method. We first introduce the Borel transform B_N associated to (2.25):

$$B_N(\tau) = \sum_{k=0}^{N} \frac{A_0^{2k}}{k!}\tau^k \ . \tag{2.31}$$

The finite-N truncation of the series (2.25) is exactly recovered from its N^{th}-Borel transform B_N by applying a Laplace inversion :

$$\sum_{k=0}^{N} A_0^{2k}\tau^k = \int_0^\infty B_N(\omega\tau)e^{-\omega}d\omega \ . \tag{2.32}$$

The Laplace inversion of expression (2.31) for B_N indeed leads back to the divergent finite truncation that we wanted to regularize. To avoid such a fate, one may use a nonpolynomial approximation of $B_N(\tau)$ whose Taylor expansion coincides with the known terms in (2.31). In the Padé-Borel method, it is achieved by approximating B_N with a rational fraction $F_N = Q_N/R_N$, where Q_N and R_N are polynomials in τ of order $N/2$ chosen such that $B_N(\tau) = Q_N(\tau)/R_N(\tau) + \mathcal{O}(\tau^{N+1})$. The Borel resummation to order N of (2.25), B_N^r, is defined by replacing B_N in (2.32) by its Padé approximant F_N :

$$B_N^r = \int_0^\infty \frac{Q_N(\omega\tau)}{R_N(\omega\tau)}e^{-\omega}d\omega \ . \tag{2.33}$$

Finally, the series (2.25) is formally obtained from the limit of B_N^r when $N \to \infty$. Hereafter, we estimate (2.25) while keeping N finite and we will not evaluate B_N^r beyond $N = 8$. Interestingly, for $\tau = 0.2$, while the truncated sequence of (2.25) is divergent, its Borel resummation B_8^r agrees quantitatively with numerical estimates of the steady-state distribution, as shown in the bottom right corner of Fig. 2.1. In Fig. 2.1, we plot

the Borel resummation B_8^r and the corresponding numerics for two different values of τ. When τ increases, the dynamics (2.9)-(2.10) departs more strongly from equilibrium and the probability density differs significantly from the Boltzmann weight with the presence of two humps. We have thus characterized how, when τ increases, AOUPs violate the equilibrium constraint CI described in introduction: their steady-state density $\mathcal{P}_s(x)$ is not enslaved to the local energy $\phi(x)$ through $\mathcal{P}_s(x) \propto \exp(-\phi(x)/D)$, and they can accumulate outside a local minima of ϕ.

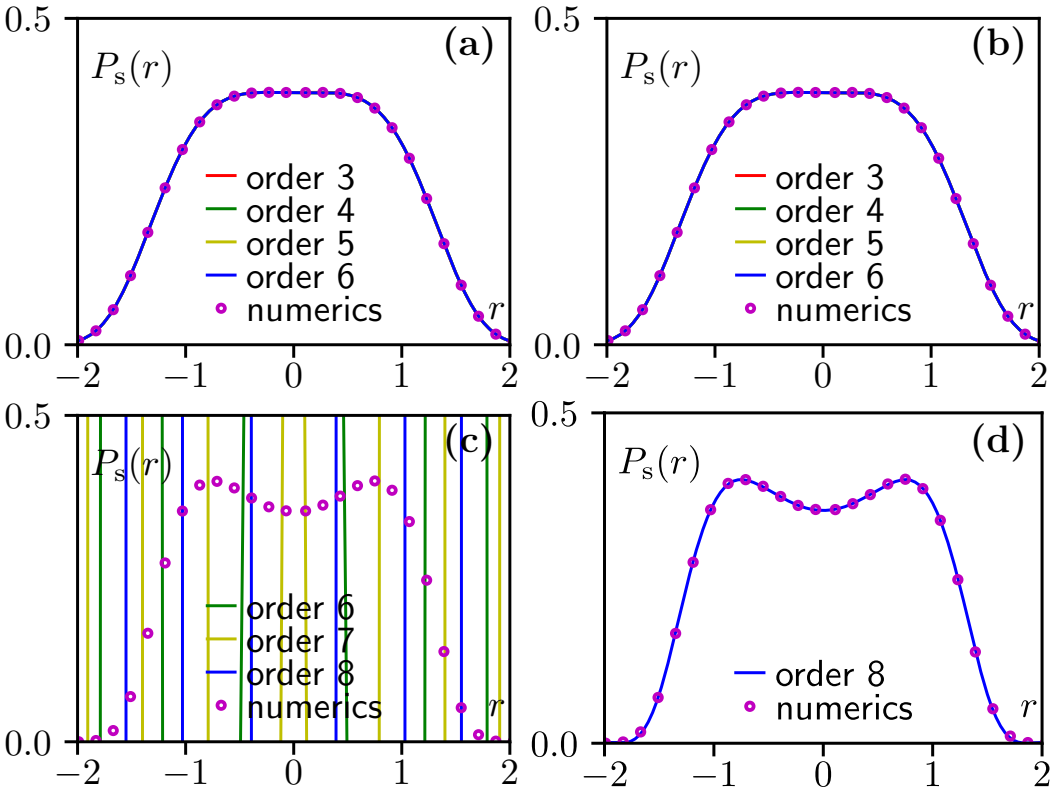

Figure 2.1 – Steady-state distribution of (2.9)-(2.10) in a confining potential $\phi(x) = x^4/4$ **Top: (a)** For $\tau = 0.01$, the finite truncation of (2.25) converges and agrees with the numerics. **(b)** Its corresponding Borel resummation B_8^r also coincides with simulation data. **Bottom: (c)** For $\tau = 0.2$, the finite truncation of (2.25) is rapidly diverging. **(d)** However, the Borel resummation B_8^r accurately follows the data. Parameters : $D = 1$, $dt = 10^{-4}$, time $= 10^8$. Figure adapted from [57].

2.1.4 The ratchet current

The second nonequilibrium signature CII described in the introduction is the ratchet mechanism by which asymmetric periodic potentials may lead to steady-state currents outside equilibrium [103–106]. In this section, we consider such a potential ϕ of period L and we use our perturbative expansion to compute the steady-state current $J = \langle \dot{x} \rangle$. Using $\dot{x} = -\partial_x \phi + v/\sqrt{\tau}$, J reads

$$J = -\int_0^L \int_{-\infty}^{\infty} \partial_x \phi \mathcal{P}_s(x,v) dx dv + \int_0^L \int_{-\infty}^{\infty} \frac{v}{\sqrt{\tau}} \mathcal{P}_s(x,v) dx dv \, . \tag{2.34}$$

We remark that the integral over v in (2.34) will select only specific terms in the ansatz (2.19) through the use of the orthogonality relation (2.18). For the first term on the right

hand side of (2.34), integrating v selects $A_0(x)$ while for the second term it selects $A_1(x)$. Using their expansion (2.21) in powers of τ, we thus obtain

$$J = -\sum_{k\geq 0} \tau^k \int_0^L \partial_x \phi A_0^{2k} dx + \frac{\sqrt{D}}{\sqrt{\tau}} \sum_{k\geq 0} \tau^{k+\frac{1}{2}} \int_0^L A_1^{2k+1} dx \tag{2.35}$$

Using expression (A.8) for A_1^{2k+1} given in Appendix A.1.1, we can further simplify J into

$$J = L\sqrt{D} \sum_{k>0} b_{2k+1} \tau^k \ . \tag{2.36}$$

While the $\{b_k\}$ all vanished in the previous section as a result of confinement (see (2.26)), they do not for a periodic potential. Here, instead, the value of b_k is fixed upon requiring the periodicity of A_0^{k-1}. We report the expression of the marginal in space $\mathcal{P}_s(x)$ for a periodic potential up to order τ^2 in (A.19)-(A.18) of Appendix A.1.2. Using it, we find that $Lb_5\tau^2$ is the first non-vanishing contribution to the current:

$$J = \frac{L\tau^2}{2} \frac{\int_0^L [\phi'(x)]^2 \phi^{(3)}(x) dx}{\int_0^L e^{\frac{\phi(x)}{D}} dx \int_0^L e^{-\frac{\phi(x)}{D}} dx} + \mathcal{O}(\tau^3) \ , \tag{2.37}$$

where $\phi^{(n)}(x)$ is the n-th derivative of the potential. In Fig. 2.2, we compare the above prediction with the results of numerical simulations of an AOUP experiencing a potential $\Phi(r) = \sin(\pi r/2) + \sin(\pi r)$.

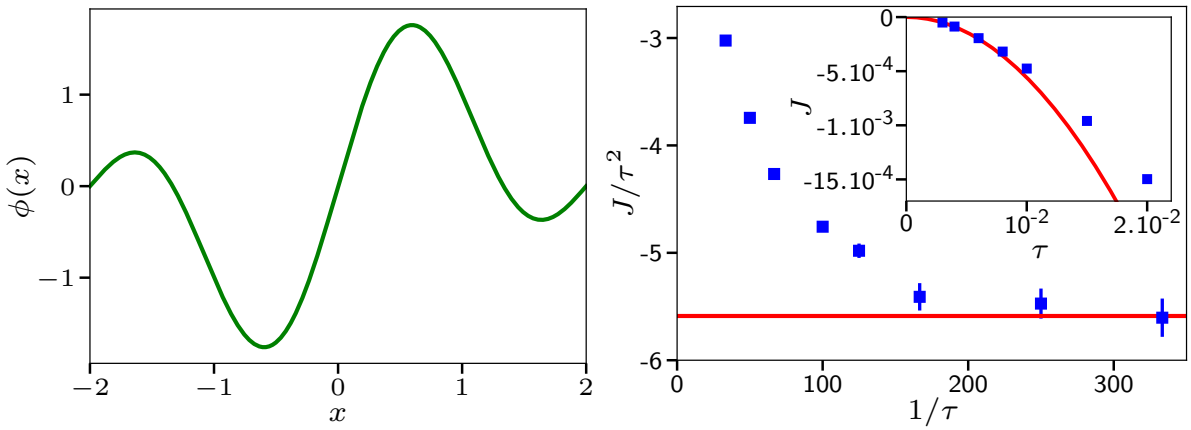

Figure 2.2 – **Left:** Plot of the ratchet potential $\phi(x) = \sin(\pi x/2) + \sin(\pi x)$ which is periodic of period 4. **Right:** Plot of the normalized current J/τ^2 induced by $\phi(x)$ as a function of the inverse of the persistence time τ^{-1}. The blue dots correspond to numerical simulations with error bars given by the standard deviation as described in Appendix A.3. The red line is the analytical prediction (2.37) in the small τ limit. In the inset, we plot J as a function of τ. Figure adapted from [57].

We find quantitative agreement at small τ for $\tau < 0.01$, which is consistent with the previous section for the radius of convergence of our ansatz (2.19). Note that J in (2.36) could also be regularized using Borel resummation to extend the quantitative range of agreement between theory and simulations to higher values of τ, but we leave such a regularization for future works.

2.1.5 The entropy production rate

In this section, I derive the entropy production rate defined in (2.6) for the AOUP dynamics (2.9)-(2.10). As shown in the introduction, σ measures the irreversibility of the dynamics and vanishes for a Brownian particle. It is thus a signature of nonequilibrium and we want to quantify its departure from zero when τ increases. The computation of σ for the AOUP dynamics (2.9)-(2.10) remains a debated topic [56, 107–109] as it has triggered a controversy about the parity of the self-propulsion v under time-reversal [110]. Following [56, 108], we choose here to focus instead on the non-Markovian process $x(t)$ obtained after integrating out the active degrees of freedom $v(t)$. In this case, a trajectory over the time interval $[0, t_f]$ is solely defined as a set of positions $x(t)$ for $t \in [0, t_f]$ and its backward counterpart is unambiguously given by the set of positions $\mathcal{R}x(t) = x(t_f - t)$. To derive σ, we use a path-integral formalism. Since the noise v is Gaussian, we obtain the probability of its realization as

$$\mathcal{P}[\{v(t)\}] \propto \exp\left(-\frac{1}{2}\int_0^{t_f}\int_0^{t_f} dt_1\, dt_2\, v(t_1)\Gamma^{-1}(t_1 - t_2)v(t_2)\right) , \tag{2.38}$$

where $\Gamma^{-1}(t)$ is the functional inverse of the noise time correlation $\Gamma(t) = \langle v(t)v(0)\rangle = De^{-|t|/\tau}/\tau$. Using the relation $\Gamma^{-1}(w)\Gamma(w) = 1$, valid in Fourier space, we obtain

$$\Gamma^{-1}(w) = \frac{1}{\Gamma(w)} = \frac{1}{2D} + w^2\frac{\tau^2}{2D} . \tag{2.39}$$

Transforming $\Gamma(w)$ back in real space gives

$$\Gamma^{-1}(t) = -\frac{\tau^2}{2D}\frac{d^2}{dt^2}\delta(t) + \frac{1}{2D}\delta(t) . \tag{2.40}$$

We now make the change of variable $v = \dot{x} + \partial_x\phi$ in (2.38) using the Stratonovitch convention. This change of variable will generate an extra factor invariant upon the reversal of trajectory $\mathcal{R}$ stemming from the determinant. As this extra factor will simplifies itself in the definition of the entropy production (2.6), we do not report it hereafter. We thus obtain the probability of a trajectory $\mathcal{P}[\{x(t)\}]$ as

$$\mathcal{P}[\{x(t)\}] \propto \exp\left(-\frac{1}{2}\int_0^{t_f}\int_0^{t_f} dt_1\, dt_2\, \mathcal{S}[\dot{x}, x]\right) , \tag{2.41}$$

with the action

$$\mathcal{S}[\dot{x}, x] = \left[\dot{x}(t_1) + \phi'(x(t_1))\right]\Gamma^{-1}(t_1 - t_2)\left[\dot{x}(t_2) + \phi'(x(t_2))\right] . \tag{2.42}$$

Inserting (2.41) into (2.6), we obtain the entropy production rate σ over a path $x(t)$ as

$$\sigma = \lim_{t_f\to\infty}\frac{1}{t_f}\int_0^{t_f}\int_0^{t_f} dt_1\, dt_2\, \frac{1}{2}\left(\mathcal{S}\left[\dot{\mathcal{R}}x, \mathcal{R}x\right] - \mathcal{S}\left[\dot{x}, x\right]\right) , \tag{2.43}$$

where $\mathcal{R}x = x(t_f - t)$ is the reverse path and $\dot{\mathcal{R}}x = -\dot{x}(t_f - t)$ the corresponding velocity. Note that, in (2.43), terms even under time reversal cancel, leading to

$$\sigma = \lim_{t_f\to\infty} -\frac{2}{t_f}\int_0^{t_f}\int_0^{t_f} dt_1\, dt_2\, \Gamma^{-1}(t_1 - t_2)\dot{x}(t_2)\phi'(x(t_1)) . \tag{2.44}$$

Inserting the definition (2.40) of Γ^{-1} into (2.44), we get

$$\sigma = \lim_{t_f\to\infty} -\frac{2}{t_f}\int_0^{t_f} dt\,\dot{x}(t)\left(-\frac{\tau^2}{2D}\frac{d^2}{dt^2}+\frac{1}{2D}\right)\phi'(x(t)) \tag{2.45}$$

$$\sigma = \lim_{t_f\to\infty} -\frac{1}{Dt_f}\int_0^{t_f} dt\,\dot{x}\left(-\tau^2\ddot{x}\dot{x}\phi^{(2)}(x)-\tau^2\dot{x}^2\phi^{(3)}(x)+\phi'(x)\right)\,, \tag{2.46}$$

where the integral is to be understood in the Stratonovitch sense. Performing an integration by part on the above expression, noting that exact derivatives yield no contribution to σ in the limit $t_f\to\infty$, we obtain

$$\sigma = \lim_{t_f\to\infty}\frac{\tau^2}{2Dt_f}\int_0^{t_f} dt\,\dot{x}^3\phi^{(3)}(x) \tag{2.47}$$

Finally, taking into account the ergodicity of the dynamics allows us to replace long-time averages by ensemble averages:

$$\sigma = \frac{\tau^2}{2D}\langle\dot{x}^3\phi^{(3)}\rangle = \frac{\tau^2}{2D}\langle(-\phi'+v)^3\phi^{(3)}\rangle\,, \tag{2.48}$$

where $\langle\cdot\rangle$ represents an average with respect to the steady-state measure. The last step consists in computing the ensemble averages by using the perturbative stationary measure (A.17) reported in Appendix A.1.2. After a lengthy but straightforward computation, we obtain σ up to order τ^2 as

$$\sigma = \frac{D\tau^2}{2}\frac{\int_{-\infty}^{+\infty}\phi^{(3)2}\,e^{-\frac{\phi}{D}}dx}{\int_{-\infty}^{+\infty}e^{-\frac{\phi}{D}}dx}+\mathcal{O}(\tau^{\frac{5}{2}})\,. \tag{2.49}$$

The derivation of (2.49) only requires the expression of $\mathcal{P}_s$ up to order $\tau^{3/2}$ and was first performed in [56] using a different approach. Importantly, we remark that σ is nonzero at order τ^2: activity breaks time-reversal symmetry and the observer can now distinguish between the forward and backward trajectory of an AOUP. The addition of the time-correlated self-propulsion v has thus lifted the equilibrium constraint CIII defined in the introduction. However, it is interesting to note that $\sigma = \mathcal{O}(\tau^2)$, which means that, to order τ, the AOUP dynamics is non-Boltzmann but time-reversible; breaking the Boltzmann weight does not necessarily entails violating time-irreversibility.

2.2 non-interacting AOUPs in 1D in the presence of a thermal noise

This section corresponds to the reference [58] and was developed in collaboration with Thibault Arnoulx De Pirey, who is currently finishing his PhD under the supervision of Frédéric Van Wijland at MSC. In the previous section, we have quantified how the active noise v drives an AOUP out of equilibrium through the derivation of three quantities

SI. The deviation of the spatial steady-state probability distribution $\mathcal{P}_s(x)$ from the Boltzmann weight

SII. The ratchet current J in a periodic potential

SIII. The entropy production rate σ

It would be interesting to ask how this picture survives the addition of a thermal white noise in the AOUP's dynamics. Indeed, in Active Matter, most works are carried out in the regime of large activity, where one can neglect the effect of thermal fluctuations on the self-propelled particle. Despite its relevance in multiple experiments (passive tracers in active mediums [5, 25, 111, 112], membrane fluctuations in red blood cells [24, 113]...), the interplay between active and passive noise sources has rarely been studied and its influence on the departure from equilibrium remains to be quantified. Would the three signatures of nonequilibrium SI-SII-SIII be mitigated or enhanced by the competition between the active and thermal noises ? To address this question, I now study an AOUP submitted to an additional white noise η_1

$$\dot{x}(t) = -\,\partial_x\phi\,(x(t)) + \sqrt{2T}\;\eta_1(t) + v(t) \tag{2.50}$$

$$\dot{v}(t) = -\,\frac{v(t)}{\tau} + \frac{\sqrt{2D}}{\tau}\;\eta_2(t)\;. \tag{2.51}$$

Once again, we note that, for $\tau = 0$, the dynamics (2.50)-(2.51) falls back to an equilibrium one with temperature $T + D$. Thus, τ remains the parameter controlling the departure from equilibrium and we show that our perturbative derivation of the steady-state distribution $\mathcal{P}_s(x, v)$ as a series in $\tau^{1/2}$ presented in 2.1.1 can be generalized to (2.50)-(2.51). This perturbative series disentangles the respective roles of passive and active noises on the steady-state of an AOUP, showing that the signatures of non-equilibrium SI-SII-SIII can display surprising behaviours as the temperature T is varied. Depending on the potential ϕ in which the particle evolves, I find that both the current J (see 2.2.3) and the entropy production rate σ (see 2.2.4) can be non-monotonic functions of T. The latter can even diverge at high temperature for steep enough confining potentials. Thus, depending on context, switching on translational diffusion may drive the AOUP closer to or further away from equilibrium.

2.2.1 The stationary measure

The derivation of the steady-state distribution $\mathcal{P}_s(x, v)$ as a series in powers of $\tau^{1/2}$ follows the same steps already described in section 2.1.1. Indeed, the Fokker-Planck operator $\mathcal{L}_T$ corresponding to (2.50)-(2.51) only differs from (2.11) by an additional term $T\partial_{xx}$

$$\mathcal{L}_T = \mathcal{L} + T\partial_{xx}\;. \tag{2.52}$$

Expressed in terms of the rescaled variable $\tilde{v} = \sqrt{\tau}v$, the operator $\tilde{\mathcal{L}}_T$ can still be decomposed into three terms:

$$\tilde{\mathcal{L}}_T = \frac{1}{\tau}\mathcal{L}_1 + \frac{1}{\sqrt{\tau}}\mathcal{L}_2 + \mathcal{L}_3^T\;. \tag{2.53}$$

where $\mathcal{L}_3^T$ differs from $\mathcal{L}_3$ only by the additional term due to thermal diffusion: $\mathcal{L}_3^T = \mathcal{L}_3 + T\partial_{xx}$. Since $\mathcal{L}_1$ and $\mathcal{L}_2$ are unaltered by the thermal noise, there is no need to change the basis of eigenfunctions used to expand $\mathcal{P}_s$ in section 2.1.1 and we still use the P_n's defined in (2.16) to look for the stationnary distribution under the form of

$$\mathcal{P}_s(x, v) = \sum_{n\geq 0} P_n(v)A_n(x)\;. \tag{2.54}$$

Similarly to the athermal case, the A_n's can also be expanded in power of $\tau^{1/2}$ as

$$\begin{aligned} A_0 &= A_0^0(x) + \tau A_0^2(x) + \tau^2 A_0^4(x) + ... \\ A_1 &= \tau^{1/2} A_1^1(x) + \tau^{3/2} A_1^3(x) + \tau^{5/2} A_1^5(x) + ... \\ A_2 &= \tau A_2^2(x) + \tau^2 A_2^4(x) + \tau^3 A_2^6(x) + ... \\ &\vdots \end{aligned} \tag{2.55}$$

As explained in Appendix A.1.1, the A_i^k's can then be computed recursively and we report hereafter the expressions of A_0^0 and A_0^2 as an example

$$A_0^0 = c_0\ e^{-\frac{\phi}{T+D}}\ , \tag{2.56}$$

$$A_0^2 = c_0\ e^{-\frac{\phi}{T+D}} \left(\frac{D\partial_{xx}\phi}{T+D} - \frac{D\left(\partial_x \phi\right)^2}{2(T+D)^2} \right) + c_2\ e^{-\frac{\phi}{T+D}} - \frac{b_3\sqrt{D}}{T+D} e^{-\frac{\phi}{T+D}} \int_0^x e^{\frac{\phi}{T+D}} dx\ , \tag{2.57}$$

Once again, A_0^0 is given by the Boltzmann weight with temperature $T+D$ and c_0 is determined by normalization. Requiring $\int A_0^0(x)dx = 1$ leads to

$$c_0 = \left(\int_{-\infty}^{+\infty} e^{-\frac{\phi}{T+D}} dx \right)^{-1} . \tag{2.58}$$

Equation (2.57) involves two additional integration constants: c_2 and b_3. While c_2 is found by normalization, requiring $\int_{-\infty}^{+\infty} A_0^2(x)dx = 0$, b_3 is fixed by the boundary conditions on A_0^2. The recursion described in Appendix A.1.1 can be iterated up to arbitrary order in τ to find the A_i^k's for $i \geq 0$. In addition to the previous constants c_{2j} and b_{2j+1} for $j < k$, which were determined to order $\tau^{j/2}$, A_0^{2k} generically depends on two new integration constants : c_{2k} and b_{2k+1}. The determination of these integration constants in the thermal case follows the same rules as in the athermal case: c_{2k}, is found by requiring the normalization of A_0^{2k} while b_{2k+1} is fixed by the boundary conditions for A_0^{2k} (see section 2.1.1). Similarly to the athermal case, the explicit expressions of the A_0^{2k} rapidly become cumbersome but their systematic derivation can be implemented with a software such as Mathematica [102]. For illustration purposes, I report the complete expression of $\mathcal{P}_s(x,v)$, with its integration constants, up to the order τ^2 in Appendix A.1.2.

2.2.2 Deviation from the Boltzmann distribution in a confining potential

In this section, I study the marginal in space $\mathcal{P}_s(x) = \sum_{k\geq 0} A_0^{2k}\tau^k$ in the case of a confining potential ϕ. Similarly to the athermal case, for all $k \geq 1$, the confinement imposes $b_{2k+1} = 0$ while c_{2k} is fixed by normalization $\int A_0^{2k}(x)dx = 0$ (see (2.26)-(2.27)). Using (2.57), A_0^2 then reads

$$A_0^2 = \ c_0\ e^{-\frac{\phi}{T+D}} \left(\frac{D\partial_{xx}\phi}{T+D} - \frac{D\left(\partial_x \phi\right)^2}{2(T+D)^2} \right) - \frac{3\ c_0^2\ D}{2(T+D)}\ e^{-\frac{\phi}{T+D}} \int_{-\infty}^{+\infty} \partial_{xx}\phi\ e^{-\frac{\phi}{T+D}} dx\ , \tag{2.59}$$

where c_0 is defined in (2.58). Thanks to (2.59), the first correction to the Gibbs-Boltzmann measure is readily expressed as

$$\frac{\mathcal{P}_s(x) - c_0 e^{-\frac{\phi}{T+D}}}{c_0 e^{-\frac{\phi}{T+D}}} = \tau \left[\frac{D}{T+D}\partial_{xx}\phi - \frac{D\left(\partial_x\phi\right)^2}{2(T+D)^2} - \frac{3D}{2(T+D)} \frac{\int_{-\infty}^{+\infty} \partial_{xx}\phi\ e^{-\frac{\phi}{T+D}} dx}{\int_{-\infty}^{+\infty} e^{-\frac{\phi}{T+D}} dx} \right] + \mathcal{O}(\tau^2)\ . \tag{2.60}$$

Note that the above expression falls back to the steady state of an athermal AOUP (2.29) when $T = 0$ to this order in τ. The cumbersome expression of the full marginal in space $\mathcal{P}_s(x)$ up to order τ^2, for generic D and T, is reported in Appendix A.1.2. Similarly to its athermal counterpart, the series $\sum_{k\geq 0} A_0^{2k}\tau^k$ has a small convergence radius in τ and we need to resort to a regularization process to extend its range of validity. For $\tau = 0.01$, we show in Fig. 2.3 that the truncation of $\sum_{k\geq 0} A_0^{2k}\tau^k$ to order τ^8 is well-behaved and quantitatively agrees with the stationary distribution obtained numerically. For $\tau = 0.2$, however, Fig. 2.3 shows that the same truncation is diverging away from the result of simulations. Fortunately, as described in section 2.1.3, we can resort to a Borel resummation and compute B_N^r to regularize $\mathcal{P}_s(x)$. As shown in the bottom right corner of Fig. 2.3, the Borel resummation B_8^r accurately fits the numerical steady-state distribution for $\tau = 0.2$: the domain of validity has been formally extended by the regularization process.

In Fig. 2.4, we plot the Borel resummations B_8^r and the corresponding numerics for different values of T. When $T \ll D$, the dynamics (2.50)-(2.51) is strongly out-of-equilibrium and the probability density differs significantly from the Boltzmann weight with the presence of two humps. When $T \gg D$, self-propulsion is washed out by thermal noise, the dynamics draws closer to equilibrium and the two humps of the distribution are smoothened out. Note that the Borel resummation B_8^r accurately fits the numerics without any free parameter.

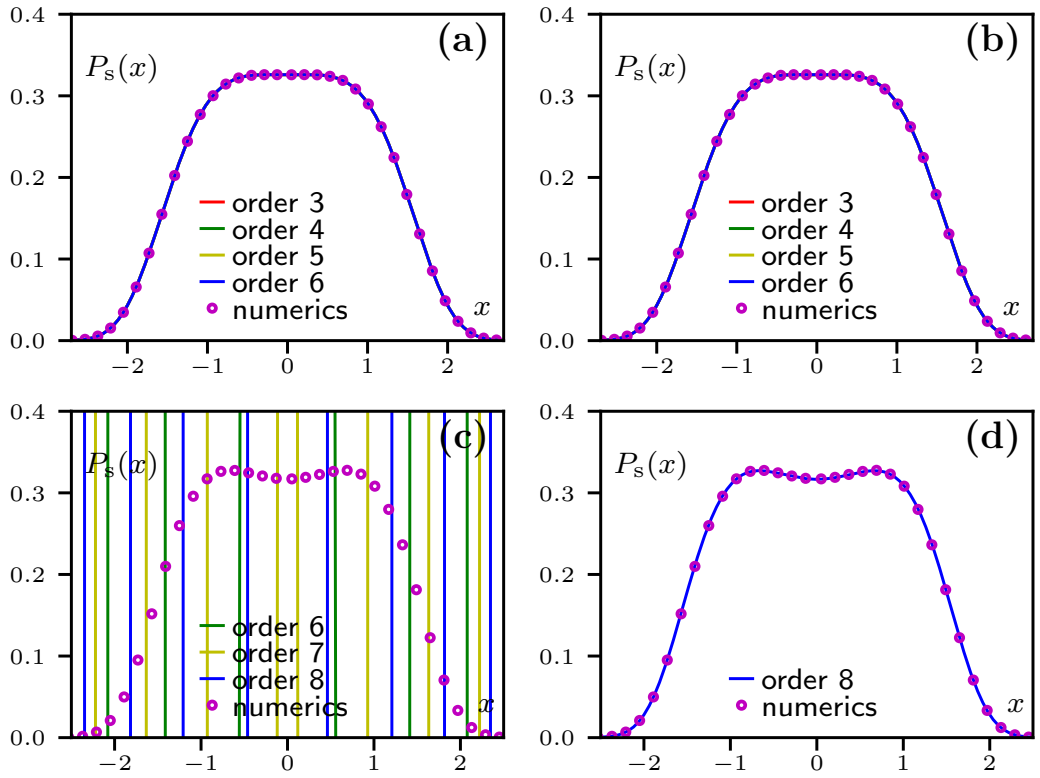

Figure 2.3 – Steady-state distribution of (2.50)-(2.51) in a confining potential $\phi(x) = x^4/4$ **Top:** **(a)** For $\tau = 0.01$, the finite truncation of (2.25) converges and agrees with the result of numerical simulations. **(b)** Its corresponding Borel resummation B_8^r also coincides with simulation data. **Bottom:** **(c)** For $\tau = 0.2$, the finite truncation of (2.25) is rapidly diverging. **(d)** However, the Borel resummation B_8^r accurately follows the data. Parameters : $D = T = 1$, $dt = 10^{-4}$, time $= 10^8$. Details of the numerical simulation are given in Appendix A.3. Figure adapted from [58].

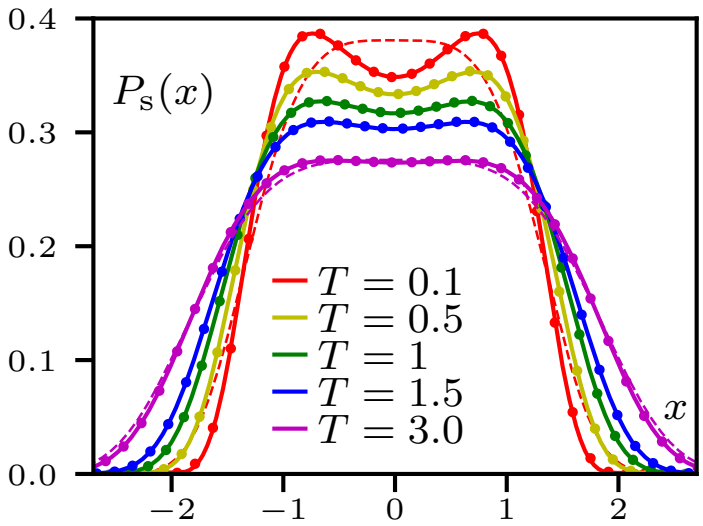

Figure 2.4 – Steady-state distributions of (2.50)-(2.51) in a confining potential $\phi(x) = x^4/4$ for different values of T. Plain curves correspond to Borel resummations B_8^r while symbols are obtained from numerical simulations of (2.50)-(2.51). In dashed lines, we plot the Gibbs-Boltzmann distributions for the two limiting cases $T = 0.1$ and $T = 3.0$ to highlight the activity-induced deviation from thermal equilibrium. The Borel resummation B_8^r always fits the data accurately without any free parameters. Parameters: $\tau = 0.2$, $D = 1$, $dt = 10^{-4}$, time $= 10^8$. Figure adapted from [58].

2.2.3 The ratchet current

In this section, I consider an asymmetric potential ϕ of period L and quantify how the thermal noise affects the ratchet current $J = \langle \dot{x} \rangle$. Using expression (2.50) for $\dot{x}$, J reads

$$J = \langle -\partial_x \phi + \frac{v}{\sqrt{\tau}} + \sqrt{2T}\eta \rangle = \int_0^L \int_{-\infty}^{\infty} \left(-\partial_x \phi + \frac{v}{\sqrt{\tau}} \right) \mathcal{P}_s(x, v) dx dv \tag{2.61}$$

From section 2.1.4, we know that the integral over v can be computed to yield

$$J = -\sum_{k \geq 0} \tau^k \int_0^L A_0^{2k}(x) \partial_x \phi(x) dx + \frac{\sqrt{D}}{\sqrt{\tau}} \sum_{k \geq 0} \tau^{k+\frac{1}{2}} \int_0^L A_1^{2k+1}(x) dx \, . \tag{2.62}$$

Using the expression (A.8) for A_1^{2k+1}, we simplify (2.62) into

$$J = \sum_{k \geq 0} \tau^k \, T \int_0^L \partial_x A_0^{2k}(x) dx + L\sqrt{D} \sum_{k>0} b_{2k+1} \tau^k \, . \tag{2.63}$$

Finally, we require the marginal in space $\mathcal{P}_s(x)$ to be periodic, which entails that A_0^{2k} is periodic for all $k \geq 0$. The current J then reduces to

$$J = L\sqrt{D} \sum_{k>0} b_{2k+1} \tau^k \, . \tag{2.64}$$

Similarly to the athermal case described in section 2.1.4, the value of b_k is fixed upon requiring the periodicity of A_0^{k-1}. We report the expression of the marginal in space $\mathcal{P}_s(x)$

for a periodic potential up to order τ^2 in (A.19) within Appendix A.1.2. Using it, we find that $Lb_5\tau^2$ is once again the first non-vanishing contribution to the current :

$$J = \frac{DL\tau^2}{2(T+D)} \frac{\int_0^L \phi^{(1)2}\phi^{(3)}dx}{\int_0^L e^{\frac{\phi}{T+D}}dx \int_0^L e^{-\frac{\phi}{T+D}}dx} + \mathcal{O}(\tau^3) \ . \tag{2.65}$$

The above formula reduces to the expression of J for an athermal AOUP (2.37) when $T = 0$. It is interesting to note that, as $T \to \infty$, J vanishes as $J \propto 1/T$. Physically, when the thermal noise is much stronger than the self-propulsion, the active dynamics becomes irrelevant and J dies out. However, as shown in the left part of Fig. 2.5, this intuitive picture is misleading at intermediate values of T. In this regime, the interplay between passive and active noises can, depending on the potential, make the current J non-monotonic: ramping up the temperature might drive the particle further away from equilibrium. In the right part of Fig. 2.5, we compare our quantitative prediction (2.65) with the results of numerical simulations for a potential $\phi(x) = \sin(\pi x/2) + \alpha \sin(\pi x)$ with α a constant. We find a quantitative agreement at small τ, for $\tau < 0.01$, which is consistent with the results of the previous sections regarding the radius of convergence. Note that J in (2.64) could also be regularized using Borel resummation to extend the quantitative range of agreement between theory and simulations to higher values of τ, but we leave such a regularization for future works.

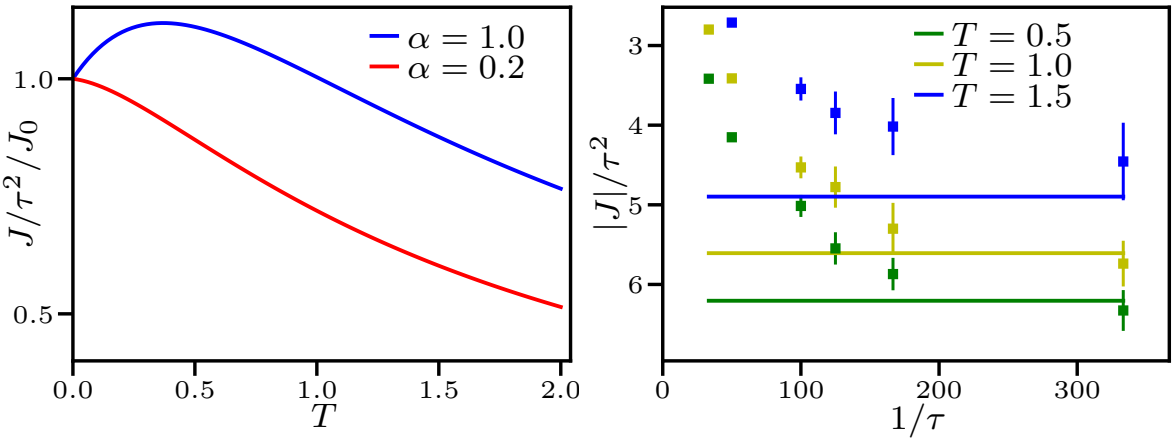

Figure 2.5 – Current J induced by a ratchet potential $\phi(x) = \sin(\pi x/2) + \alpha \sin(\pi x)$ for different values of T and α. Plain curves correspond to prediction (2.65) while dots are numerical simulations with error bars given by the standard deviation as described in Appendix A.3. **Left:** J/τ^2 normalized by $J_0 = J(T = 0)$ as a function of T for different values of α. **Right:** J/τ^2 as a function of $1/\tau$ for $\alpha = 1$. Parameters: $D = 1$, $dt = 15.10^{-4}$, time $= 5.10^8$. Figure adapted from [58].

2.2.4 The entropy production rate

In this part, I assess the dependency of the entropy production rate (2.6) on the temperature T and explore its possible behaviours in different contexts. We start from expression (2.44) for σ, which is valid for any additive SDE with Gaussian colored noise

$$\sigma = \lim_{t_f \to \infty} -\frac{2}{t_f} \int_0^{t_f} \int_0^{t_f} dt_1 \, dt_2 \, \Gamma^{-1}(t_1 - t_2)\dot{x}(t_2)\phi'\left[x(t_1)\right] \ , \tag{2.66}$$

and where $\Gamma^{-1}(t)$ is the functional inverse of the noise time correlation $\Gamma(t)$. Here, in addition to the Ornstein-Uhlenbeck noise v, the dynamics (2.50) also contains the thermal noise $\sqrt{2T}\eta_1$. Thus, the total Gaussian noise acting on the particle is $\tilde{\eta}(t) = v(t) + \sqrt{2T}\eta_2(t)$ and its correlation $\Gamma(t) = \langle\tilde{\eta}(t)\tilde{\eta}(0)\rangle$ reads

$$\Gamma(t) = \left\langle \left(v(t) + \sqrt{2T}\eta_1(t)\right)\left(v(0) + \sqrt{2T}\eta_1(0)\right)\right\rangle = \frac{D}{\tau}\exp\left(-\frac{|t|}{\tau}\right) + 2T\delta(t) \ . \tag{2.67}$$

Using the relation $\Gamma^{-1}(w)\Gamma(w) = 1$, valid in Fourier space, we obtain

$$\Gamma^{-1}(w) = \frac{1}{\Gamma(w)} = \frac{1}{2T + \frac{2D}{1+w^2\tau^2}} \ . \tag{2.68}$$

Transforming $\Gamma(w)$ back in real space then gives

$$\Gamma^{-1}(t) = \frac{1}{2T}\delta(t) - \frac{G(t)}{\tau} \ , \tag{2.69}$$

where $G(t)$ is given by

$$G(t) = \frac{D}{4T^2}\sqrt{\frac{T}{D+T}}\exp\left(-\sqrt{\frac{D+T}{T}}\frac{|t|}{\tau}\right) \ . \tag{2.70}$$

Inserting (2.69) into (2.66), we note that the term $\delta(t)/(2T)$ yields an exact derivative that will not contribute to the entropy production rate. We thus obtain

$$\sigma = \lim_{t_f\to\infty}\frac{2}{t_f\tau}\int_0^{t_f}\int_0^{t_f} dt_1\, dt_2\, G(t_1 - t_2)\dot{x}(t_2)\phi'\left[x(t_1)\right] \tag{2.71}$$

Finally, taking into account the ergodicity of the dynamics allows us to replace long-time averages by dynamical ensemble averages, and we get

$$\sigma = \frac{2}{\tau}\int_{-\infty}^{+\infty} G(t)\left\langle\dot{x}(0)\phi'(x(t))\right\rangle dt \ . \tag{2.72}$$

So far, the entropy production rate (2.72) involves two-time correlation functions, and our approach will be to reduce σ to averages taken from the steady-state distribution computed in Section 2.2.1. To this aim, we use the particle displacement as a small-τ expansion parameter. Indeed, over times of order τ, for which the kernel $G(t)$ is non-vanishing, we have $x(t) - x(0) \sim \sqrt{\tau}$. The details of this expansion are given in Appendix A.1.3. In particular, (2.72) leads to the following expansion of σ

$$\sigma = \frac{2}{\tau}\sum_{n=2}^{+\infty}\frac{1}{n!}\int_0^{+\infty} dt\, G(t)\left\langle\dot{x}(0)\phi^{(n+1)}(x(0))\left[x(-t) - x(0)\right]^n\right\rangle \ . \tag{2.73}$$

where the discretization is of the Stratonovich type and where $\phi^{(k)}$ is the k-th derivative of ϕ. In agreement with [45], (2.73) allows us to show that additive SDEs with Gaussian colored noise have vanishing entropy production rates when the potential is harmonic. Moreover, as shown in Appendix A.1.3, the equation of motion (2.50)-(2.51) can be integrated recursively in powers of τ to yield a series expansion in $\tau^{1/2}$ of σ. Our main result is the first non-vanishing order in τ of this expansion

$$\sigma = D\tau^2 H\left(\frac{T}{D}\right)\frac{\int_{-\infty}^{+\infty}\phi^{(3)2}\ e^{-\frac{\phi}{T+D}}dx}{\int_{-\infty}^{+\infty}e^{-\frac{\phi}{T+D}}dx} + \mathcal{O}(\tau^{\frac{5}{2}}) \ , \tag{2.74}$$

where the function H is given by

$$H(x) = \frac{4\sqrt{\frac{x}{x+1}} + x\left(4\sqrt{\frac{x}{x+1}} + 2\right) + 1}{8\sqrt{x(x+1)} + 2x\left(6x + 6\sqrt{x(x+1)} + 7\right) + 2} \,. \tag{2.75}$$

When $T \to 0$, the entropy production rate (2.74) brings us back to the athermal case of (2.49) and [56]. Furthermore, in a system endowed with periodic boundary conditions at $-L$ and $+L$, the entropy production rate vanishes as $1/T$ in the large temperature as

$$\sigma \simeq \frac{D^2\tau^2}{4T} \frac{\int_{-L}^{+L} \left[\phi^{(3)}(x)\right]^2 dx}{2L} \,. \tag{2.76}$$

Physically, this supports the idea that thermal noise is washing out activity and nonequilibrium signatures. However, this intuitive picture is challenged by the rich behaviour of $\sigma(T)$, which strongly depends on the nature of ϕ, and need not be a monotonically decreasing function. For an infinte system in a confining potential, the entropy production rate might even diverge at high temperature: increasing T might thus drive the system further away from equilibrium. In order to illustrate this idea, let us assume that $\phi(x) = \lambda x^{2p}/2p!$ with p an integer great than 1. For $T \gg D$,

$$\frac{\int_{-\infty}^{+\infty} \phi^{(3)2}\, e^{-\frac{\phi}{T+D}} dx}{\int_{-\infty}^{+\infty} e^{-\frac{\phi}{T+D}} dx} \sim \lambda \frac{(2p)!}{(2p-3)!} \frac{\int_{-\infty}^{+\infty} x^{4p-6}\, e^{-\lambda\frac{x^{2p}}{T}} dx}{\int_{-\infty}^{+\infty} e^{-\lambda\frac{x^{2p}}{T}} dx} \propto T^{2-3/p} \,, \tag{2.77}$$

which shows that the entropy production rate behaves at high T as $\sigma \propto T^{1-3/p}$. As $T \to \infty$, it thus goes to 0 for $p = 2$ and diverges for $p > 3$ as the particle explores steeper regions of the potential. In Fig. 2.6, we plot σ/τ^2 in the $\tau \to 0$ limit, as given by (2.74), as a function of temperature in the three potentials characterized by $p = 2$, $p = 3$ and $p = 4$, for $D = 1$ and $\lambda = 1$. Depending on the potential, Fig. 2.6 shows the rich phenomenology exhibited by σ when T is varied: monotonic decrease or non-monotonicity, divergence or decay at high temperature... Having detailed how a single AOUP can depart from equilibrium, I now review briefly the case of N interacting AOUPs and explain how the perturbative derivation of $\mathcal{P}_s$ can be generalized to the many-body dynamics.

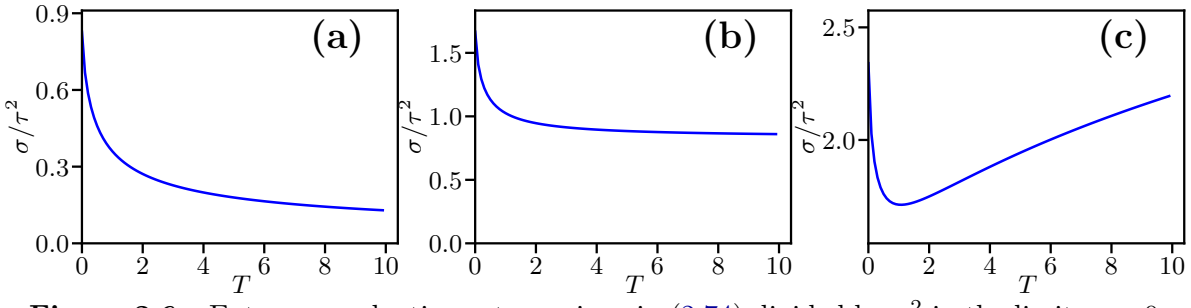

Figure 2.6 – Entropy production rate as given in (2.74) divided by τ^2 in the limit $\tau \to 0$ for different confining potential $\phi(x) = \lambda x^{2p}/2p!$ as a function of temperature at $D = 1$ and $\lambda = 1$. **(a)** For $p = 2$, the entropy production rate decreases as a function of T and converges to 0 at large T. **(b)** For $p = 3$, the entropy production rate decreases as a function of T and converges to a non vanishing constant at large T. **(c)** For $p = 4$, the entropy production rate is a non monotonous function of T and diverges at large T. Figure adapted from [58].

2.3 Interacting AOUPs in arbitrary dimension

In this section, I review the general case of N interacting AOUPs in any dimension d. The position of the i-th particle is given by $\mathbf{r}_i$ while $\mathbf{v}_i$ indicates its self-propulsion. These two vectors evolve according to the following Langevin system

$$\dot{\mathbf{r}}_i = -\boldsymbol{\nabla}_i \Phi + \mathbf{v}_i \tag{2.78}$$

$$\dot{\mathbf{v}}_i = -\frac{\mathbf{v}_i}{\tau} + \frac{\sqrt{2D}}{\tau}\boldsymbol{\eta}_i, \tag{2.79}$$

where $\Phi(\mathbf{r}_1, \ldots, \mathbf{r}_N)$ is the interaction potential which generically depends on the positions of all particles. The perturbative expansion developed in section 2.1.1 can be generalized to the N-body dynamics (2.78)-(2.79) to find the steady-state probability distribution $\mathcal{P}_s(\{\mathbf{r}_i, \mathbf{v}_i\})$ as a series in $\tau^{1/2}$. We show in Appendix A.2 that there is a general recurrence leading to an integrability condition for the τ^n correction to the Boltzmann measure.

We note that there is always an analytical solution whenever this integrability condition (A.58) depends on only one spatial variable. For example, in the case of 2 AOUPs interacting via a radial potential $\Phi(|\mathbf{r}_1 - \mathbf{r}_2|)$ in dimension d, (A.58) can be cast into a simple ODE on the variable $r = |\mathbf{r}_1 - \mathbf{r}_2|$ which can then be integrated to yield the τ^n correction.

Unfortunately, in the generic N-body case in dimension d, there is no symmetry constraining the integrability condition to depend on only one spatial variable and we could not find its generic analytic solution beyond order τ. However, the order n-th correction can still be obtained formally as the solution of a backward Fokker-Planck equation with a source term as shown in (A.58).

2.4 Conclusion

In this first chapter, I studied how Active Ornstein-Uhlenbeck particles depart from equilibrium. I devised perturbative schemes to derive the steady-state distribution of AOUPs as a series in the persistence time τ in the following three cases:

- a single AOUP evolving on a line (section 2.1)
- a single AOUP evolving on a line and submitted to an additional thermal noise (section 2.2)
- N-interacting AOUPs in any dimension d (section 2.3)

In the first two cases, I could derive $\mathcal{P}_s$ beyond the order $\tau^{3/2}$ and solve the integrability condition (A.58). Building on these analytical formulas for the stationary distribution, I derived quantitative expressions for three signatures of nonequilibrium: the deviation from Boltzmann weight SI, the ratchet current SII, and the entropy production rate SIII.

3. Fluctuation-induced first-order transition to collective motion

In the previous chapter, we have studied how active particles behave in the presence of an external potential. We now turn to the collective behaviours they exhibit when interactions are switched on. A self-propelled particles is characterized by two quantities; its position $\mathbf{r}$ and its orientation θ. While forces impact the dynamics of positions, torques control the fate of orientations.

Aligning torques arise naturally in models of collective motion, where a self-propelled unit usually aligns with its neighbouring fellows to maintain a common direction. Due to this aligning dynamics, two different phases are naturally expected.

When alignment is weak or density is low, rotational diffusion dominates and the assembly of self-propelled particles remains disordered. When alignment is strong and density is high, rotational noise becomes negligble, and the active units collectively move in the same direction. Between these two limit regimes, a phase transition must occur at a given alignment strength; this chapter is devoted to the characterization of the order of this transition to collective motion.

I will first review the most paradigmatic flocking model, namely the Vicsek Model, and show that its transition follows a first-order scenario with phase separation at the onset of order. In section 3.2, I discuss another type of models of collective motion, dubbed topological, and explain why they are believed to undergo a different, second-order phase transition. At odds with this statement, I report the existence of steady-state phase-separated solutions even in topological models close to the onset. In section 3.3 and 3.4, I propose a mechanism to explain this surprising instability and illustrate it on a simple flocking model: the Active Ising Model (AIM). I then show that this mechanism generically applies to a broad class of topological models in section 3.5, 3.6 and 3.7. Finally, in section 3.8, I propose a simple way to assess the order of the flocking transition through a measurement of the onset of order when the average density is varied.

3.1 A brief introduction to collective motion

In this section, I present my personal views on existing results about the transition to collective motion [59, 114–117]. The purpose of this section is to introduce established results that are particularly important for my own work, which is presented later in sections 3.4 to 3.8. I start by describing the phenomenology of flocking through the introduction of the Vicsek Model, focusing on the phase separation occurring at the onset of the transition. Through the use of the Boltzmann approach presented in [114], I then show that the Vicsek Model exhibits a density-dependent onset of order. Using the same symmetry argument as in [116], I explain in the last part that models of collective motion will generically exhibit phase-separated states at the transition whenever the onset of order is density-dependent.

3.1.1 The Vicsek Model

T. Vicsek and co-workers proposed in a seminal contribution [59] to replace the study of animals by the study of flying spins, hence attracting the attention of physicists and

giving birth to the field of active matter. The Vicsek Model successfully pinned down the minimal ingredients needed for the emergence of collective motion: self-propulsion and noisy aligning interactions. In the 2D Vicsek Model, point-like flying spins move in a domain $L_x \times L_y$ with periodic boundary conditions at constant speed v along their unitary spin direction $\mathbf{s}_i$. These spins further stochastically align their orientation $\mathbf{s}_i$ with the averaged magnetization of their local neighbours. The position $\mathbf{r}_i(t)$ of the i-th particle evolves according to (see [114])

$$\mathbf{r}_i(t+dt) = \mathbf{r}_i(t) + v dt\ \mathbf{s}_i \tag{3.1}$$

At every time step dt, the i-th particle aligns its spin with the averaged direction of its neighbours according to

$$\arg\left[\mathbf{s}_i(t+dt)\right] = \begin{cases} \arg\left[\sum_{j\in\mathcal{N}_i} \mathbf{s}_j(t)\right] + \sigma\eta_i & \text{if } \mathcal{N}_i \neq \{i\} \\ \arg\left[\mathbf{s}_i(t)\right] + \sigma\eta_i\,, \text{ with probability } Ddt & \text{if } \mathcal{N}_i = \{i\} \\ \arg\left[\mathbf{s}_i(t)\right]\,, \text{ with probability } 1 - Ddt & \text{if } \mathcal{N}_i = \{i\} \end{cases} \tag{3.2}$$

where $\mathcal{N}_i$ is the set of spins located within a radius r_0 around the i-th particle, η is a uniform noise in $[-\pi, \pi]$, σ plays the role of a temperature, and D controls the angular diffusion.

At low density, the i-th spin has no neighbour; $\mathcal{N}_i = \{i\}$ and it flies alone while $\mathbf{s}_i$ diffuses in the angular space. In this regime, the system remains in a disordered gas phase. On the opposite, at high density, $\mathcal{N}_i$ becomes a much larger set, the spins align with each others and the particles fly in a common direction. It has been shown that, unlike the equilibrium XY model, this phase corresponds to a polar liquid with true long-ranged order [118]. The existence of these two different regions at both end of the phase diagram raises the question of the nature of the transition occurring at intermediate densities. Does the polar liquid emerges continuously from the disordered gas phase or does it rather follow a discontinuous transition ? Historically, the emergence of the polar liquid was first believed to be continuous [59]: the homogeneous ordered liquid was thought to be stable at onset. However, careful numerical simulations of the Vicsek Model later revealed a landmark feature of first-order transitions: the presence of a coexistence region separating the gas and liquid phases [61, 62]. In this coexistence domain, one observes stationary profiles in which bands of polar liquid propagate in a disordered gaseous phase. As the width of these polar bands was shown to be invariant upon varying the system's size, this flocking transition was classified as first-order with micro-phase separation [61]. We report in Fig. 3.1 the full phase diagram of the Vicsek Model together with snapshots of the system taken in its three different phases. In the remainder of this manuscript, I will loosely qualify the flocking transition as first-order whenever we observe a phase-separation at onset of collective motion and as second order in the absence of such a scenario. In particular, I will not characterize the underlying phase-separated profiles and I will not discuss whether the system undergo a complete- or micro-phase separation.

Having detailed the microscopic dynamics of the Vicsek model as well as its macroscopic phenomenology, let us now present a theoretical approach that has been developed to predict the stochastic evolution of assemblies of flying spins. As our work in section 3.4 to 3.8 mostly implies phenomenological approaches, presenting such a coarse-graining method will ground our study by linking it to microscopic dynamics.

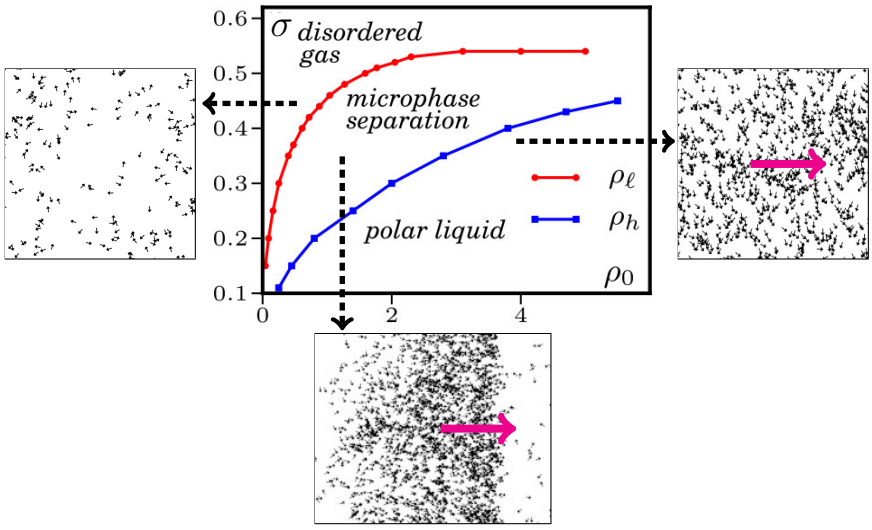

Figure 3.1 – **Center:** Phase diagram of the Vicsek Model in the temperature-density plane (σ, ρ_0). The red and blue lines delimit the coexistence region separating the polar liquid from the disordered gas. **Right, Left, Bottom:** Snapshots of the system corresponding to each phases. The magenta arrows indicate the average direction of the spins. Figure adapted from [119] for the phase diagram and from [61] for the snapshots.

3.1.2 Bottom-up approach for the Vicsek Model

In this subsection, I review the theoretical method developed in [114, 120] to compute the coarse-grained hydrodynamics of the Vicsek Model from its microscopic update rules (3.1)-(3.2). This hydrodynamic evolution allows us to draw an analogy between the flocking transition and ferromagnetism. Within this analogy, I will show that the critical temperature of the Vicsek Model is density-dependent: this is an established result that was first derived in [114, 120] and I will make use of it in section 3.1.3.

The first step of the Boltzmann approach in [120] is to write the evolution equation for $f(\mathbf{r}, \theta, t)$, the probability that a particle is at point $\mathbf{r}$ at time t with a velocity along the direction $\mathbf{e}(\theta)$. The Boltzmann equation relies on the assumption that the system is diluted, namely that the typical distance between particles is large compared to the interaction radius r_0. It gives the time-evolution of $f(\mathbf{r}, \theta, t)$ as

$$\frac{\partial f}{\partial t}(\mathbf{r}, \theta, t) + v\, \mathbf{e}(\theta) \cdot \nabla f(\mathbf{r}, \theta, t) = I_{\text{dif}}[f] + I_{\text{al}}[f]\,, \tag{3.3}$$

where the advective term accounts for ballistic motion between two stochastic events while I_{dif} and I_{al} accounts for angular diffusion and alignment respectively. According to (3.2), at each time-step dt, a particle has a probability Ddt to change direction so that I_{dif} reads

$$I_{\text{dif}}[f] = D \int_{-\pi}^{\pi} d\theta' \int_{-\sigma\pi}^{\sigma\pi} \frac{d\eta}{2\sigma\pi} \sum_{m=-\infty}^{\infty} \delta(\theta' + \eta - \theta + 2m\pi) f(\mathbf{r}, \theta', t) - D f(\mathbf{r}, \theta, t). \tag{3.4}$$

The first term on the right hand side of (3.4) represents the incoming probability flux of a particle at position $\mathbf{r}$ with orientation θ' which ends up with orientation θ after angular diffusion. The second term on the right hand side (3.4) describes the outgoing probability flux of a particle changing its orientation from θ to another direction after angular diffusion. Let us now derive I_{al}. We consider two interacting particles, referred

to as particle 1 and particle 2, and suppose that we can restrict our study to binary collisions. To align with particle 1 at time $t + dt$, particle 2 must lie in a parallelogram whose surface is given by $2r_0 v|\mathbf{e}(\theta_2) - \mathbf{e}(\theta_1)|dt$. The alignment term will thus reads

$$\begin{aligned} I_{\rm al}[f] = &- 2r_0 v f(\mathbf{r},\theta,t)\int_{-\pi}^{\pi} d\theta' \,|\mathbf{e}(\theta') - \mathbf{e}(\theta)| f(\mathbf{r},\theta',t) \\ &+ 2r_0 v \int_{-\pi}^{\pi} d\theta_1 \int_{-\pi}^{\pi} d\theta_2 \int_{-\sigma\pi}^{\sigma\pi} \frac{d\eta}{2\sigma\pi} |\mathbf{e}(\theta_2) - \mathbf{e}(\theta_1)| \\ &\times f(\mathbf{r},\theta_1,t) f(\mathbf{r},\theta_2,t) \sum_{m=-\infty}^{\infty} \delta(\bar{\theta} + \eta - \theta + 2m\pi), \end{aligned} \tag{3.5}$$

where $\bar{\theta} = \arg\left[e^{i\theta_1} + e^{i\theta_2}\right]$. The first term on the right hand side of (3.5) corresponds to an outgoing probability flux due to the collision of a particle of orientation θ with another particle. The second term on the right hand side of (3.5) corresponds to an incoming probability flux due to the realignment of two particles along the direction θ during a collision. The two hydrodynamic modes that are typically considered for this Boltzmann approach are the density and velocity fields, ρ and $\mathbf{W}$, where

$$\rho(\mathbf{r},t) = \int_{-\pi}^{\pi} d\theta\, f(\mathbf{r},\theta,t)\,, \qquad \mathbf{W}(\mathbf{r},t) = v\int_{-\pi}^{\pi} d\theta\, f(\mathbf{r},\theta,t)\,\mathbf{e}(\theta). \tag{3.6}$$

The time evolution of these two fields is derived by taking the successive angular moments of the Boltzmann equation (3.3). For example, a direct integration of (3.3) with respect to θ yields the evolution equation for ρ as

$$\frac{\partial \rho}{\partial t} + \nabla\cdot(\mathbf{W}) = 0, \tag{3.7}$$

which corresponds to the conservation of the number of particles. The evolution equation for $\mathbf{W}$ is obtained similarly by multiplying (3.3) by $\mathbf{e}(\theta)$, integrating over θ, and finally enforcing a closure approximation. Note that our derivation slightly differs from the original one performed in [120] as we considered a uniform noise η in the spins' dynamics (3.2) instead of a Gaussian noise. We detail this computation as well as the closure approximation in appendix B.1 and only report the resulting time evolution for $\mathbf{W}$ hereafter

$$\begin{aligned} \frac{\partial \mathbf{W}}{\partial t} + \gamma(\mathbf{W}\cdot\boldsymbol{\nabla})\mathbf{W} = &-\frac{v^2}{2}\boldsymbol{\nabla}\rho + \frac{\kappa}{2}\boldsymbol{\nabla}\mathbf{W}^2 + (\alpha - \xi\mathbf{W}^2)\mathbf{W} + \nu\boldsymbol{\nabla}^2\mathbf{W} \\ &- \kappa(\boldsymbol{\nabla}\cdot\mathbf{W})\mathbf{W} + 2\nu'\boldsymbol{\nabla}\rho\cdot\mathbf{M} - \nu'(\boldsymbol{\nabla}\cdot\mathbf{W})\boldsymbol{\nabla}\rho, \end{aligned} \tag{3.8}$$

where $\nu' = \partial\nu/\partial\rho$, $\mathbf{M} = \frac{1}{2}(\nabla\mathbf{W} + \nabla\mathbf{W}^{\mathbf{T}})$ is the symmetric part of the momentum gradient tensor and the different coefficients are given by

$$\nu = \frac{v^2}{4}\left[D\,(1 - \mathrm{sinc}(2\sigma\pi)) + \frac{16}{3\pi} r_0 v\rho\left(\frac{7}{5} + \mathrm{sinc}(2\sigma\pi)\right)\right]^{-1}, \tag{3.9}$$

$$\gamma = \frac{16\nu r_0}{\pi v}\left(\frac{16}{15} + 2\,\mathrm{sinc}(2\sigma\pi) - \mathrm{sinc}(\sigma\pi)\right), \tag{3.10}$$

$$\kappa = \frac{16\nu r_0}{\pi v}\left(\frac{4}{15} + 2\,\mathrm{sinc}(2\sigma\pi) + \mathrm{sinc}(\sigma\pi)\right), \tag{3.11}$$

$$\alpha = \frac{8}{\pi} r_0 v\rho\left(\mathrm{sinc}(\sigma\pi) - \frac{2}{3}\right) - D\,(1 - \mathrm{sinc}(\sigma\pi))\,, \tag{3.12}$$

$$\xi = \frac{256\nu r_0^2}{\pi^2 v^2}\left(\mathrm{sinc}(\sigma\pi) - \frac{2}{5}\right)\left(\frac{1}{3} + \mathrm{sinc}(2\sigma\pi)\right). \tag{3.13}$$

Note that in (3.8), higher order moments have been neglected to obtain a closed set of equations for $\mathbf{W}$ and ρ. Let us now sketch an analogy between (3.8) and the ϕ^4 theory for ferromagnetism. In the ϕ^4 field theory, the time evolution of the magnetization ϕ reads $\partial_t\phi = \nabla^2\phi + (\alpha - \xi\phi^2)\phi$, where $(\alpha - \xi\phi^2)\phi$ is the functional derivative of the Landau energy. α depends on T and changes sign at the critical temperature T_c while ξ is assumed to be a positive constant. In the high temperature phase $T > T_c$, $\alpha < 0$, and the only homogenous solution is $\phi = 0$. In the low temperature phase $T < T_c$, $\alpha > 0$, and a nonzero homogenous magnetization $\phi_0 = \pm\sqrt{\alpha/\xi}$ becomes a steady-state solution.

Comparing $\partial_t\phi = \nabla^2\phi + (\alpha - \xi\phi^2)\phi$ with (3.8), we remark that the time-evolution of $\mathbf{W}$ also contains a Landau-like term in the form of $(\alpha - \xi\mathbf{W}^2)\mathbf{W}$. Similarly to the ϕ^4 theory, this term can allow the development of a nonzero velocity $\mathbf{W}_0$ depending on the sign of α. We note that α in (3.8) depends on the noise strength σ and changes sign at a given σ_c. In the remainder of this chapter, we thus loosely adopt the language of magnetic phase transitions by analogy and speak about "temperature" to refer to noise strength and "critical temperature" to refer to the onset of order for the $q = 0$ mode.

As a final remark, we note that σ_c depends on the density ρ as it is defined by the implicit equation $\mathrm{sinc}(\sigma_c\pi)(24r_0v\rho + 3\pi D) = 16r_0v\rho - 2\pi D$. This last point will be important for the next section where we will assess the linear stability of the homogeneous phases in models of collective motion.

3.1.3 Phenomelogical description for models of collective motion

In this section, I review a generic description of flocking models: the Toner-Tu equations first established in [115–118]. Building on it, I study the linear stability of the homogeneous ordered phase and show that it is always unstable at onset whenever the critical temperature depends on the density.

The Toner-Tu equations aim at capturing the physics of collective motion in a continuous field description reproducing the large-scale and long-time properties of the flock. The motivation roots in the concept of universality class from renormalization group: microscopic models sharing similar symmetries and conservation laws should have the same large-scale behaviors. Instead of painfully coarse-graining models from their microscopic dynamics, and provided that there is no unexpected symmetries or conservation, one can write generic PDEs containing all the terms allowed by the constraints (symmetries, conservation) of the system.

Let us now apply this approach to a broad class of flocking models dealing with assemblies of flying spins, like in the Vicsek Model. The only symmetry is rotational invariance: the flying spins are not biased, all spatial directions are equivalent. This implies that the continuum field-description cannot have a privileged built-in direction: all terms must be invariant by rotation. We also remark that flying spins do not have Galilean invariance: adding a constant boost $\mathbf{v}_b$ to the velocities of the particles does not leave the system invariant. This exotic property is a landmark feature of flocking physics and is due to the surrounding resistive medium in which the organisms are evolving: air for birds, ground for sheeps, water for fish, etc. This resistive medium acts as a source of momentum which is used by the organisms to self-propel (sheeps push on the ground to move), ultimately breaking conservation of momentum and leading to the loss of Galilean invariance.

Having identified the symmetries, we now define the two hydrodynamic variables

relevant at the macroscopic level to characterize the flocks. The number of particles being conserved by the dynamics, we will retain the density field $\rho(\mathbf{r},t)$ as the first relevant macroscopic variable. As the velocity field $\mathbf{W}(\mathbf{r},t)$ will spontaneously break the rotational symmetry in the flocking phase, we retain it as the second relevant variable. While the density is given by the averaged number of particles in a mesoscopic volume centered around $\mathbf{r}$, the field $\mathbf{W}(\mathbf{r},t)$ is defined as the averaged self-propulsion of the particles located in the same volume. Mathematically, these two fields reads

$$\rho(\mathbf{r},t) = V^{-1} \sum_{i\in\mathcal{N}_\mathbf{r}} 1 \ , \quad \mathbf{W}(\mathbf{r},t) = V^{-1} \sum_{i\in\mathcal{N}_\mathbf{r}} v\, \mathbf{s}_i \ , \tag{3.14}$$

where $\mathcal{N}_\mathbf{r}$ is the set of particles located in the mesoscopic volume centered around $\mathbf{r}$ and V its volume. We are now ready to write the most general continuum evolution for $\mathbf{W}(\mathbf{r},t)$ and $\rho(\mathbf{r},t)$ consistent with the symmetries and conservation laws of flocks. As we are interested only in the large-scale properties of these fields, we perform a gradient expansion and only keep terms up to order 2 in gradients: this last constraint further simplifies the hydrodynamics and, following [115], we write

$$\begin{aligned}\partial_t \mathbf{W} = &-\lambda_1(\mathbf{W}\cdot\boldsymbol{\nabla})\mathbf{W} - \lambda_2(\boldsymbol{\nabla}\cdot\mathbf{W})\mathbf{W} - \lambda_3\boldsymbol{\nabla}(|\mathbf{W}|^2) + \alpha\mathbf{W} - a_4|\mathbf{W}|^2\mathbf{W} - \boldsymbol{\nabla}P_1 \\ &- \mathbf{W}\,(\mathbf{W}\cdot\boldsymbol{\nabla}P_2) + D_B\boldsymbol{\nabla}(\boldsymbol{\nabla}\cdot\mathbf{W}) + D_T\nabla^2\mathbf{W} + D_2(\mathbf{W}\cdot\boldsymbol{\nabla})^2\mathbf{W} \qquad (3.15)\\ \partial_t\rho = &-\nabla\cdot(\mathbf{W})\,. \qquad (3.16)\end{aligned}$$

where the coefficients λ_i, α, a_4, D_B , D_T, D_2, as well as the scalar functions P_1 and P_2, can depend, in general, on the local density $\rho(\mathbf{r})$ and norm $|\mathbf{W}(\mathbf{r})|$ of the velocity field. In the above continuum evolution (3.15)-(3.16), the microscopic details of the flocking model are buried away in a few set of phenomenological parameters. Note that there is no diffusion acting on the density field in (3.16) as we did not introduce a translational noise in the dynamics of the flying spins. However, such a diffusive term might well be generated on its own during a renormalization group analysis of (3.15)-(3.16).

Let us now compare the coarse-grained time evolution (3.15) with its counterpart (3.8) derived for the Vicsek Model in the previous subsection. We note that (3.8) contains two additional terms not present in (3.15): $2\nu'\boldsymbol{\nabla}\rho\cdot\mathbf{M}$ and $\nu'(\boldsymbol{\nabla}\cdot\mathbf{W})\boldsymbol{\nabla}\rho$. They are respectively of the form $\zeta_1\boldsymbol{\nabla}P_3\cdot\boldsymbol{\nabla}\mathbf{W}$ and $\zeta_2\boldsymbol{\nabla}P_4(\boldsymbol{\nabla}\cdot\mathbf{W})$, with ζ_1, ζ_2, P_3 and P_4 being scalar functions that generically depend on ρ and $|\mathbf{W}|$. While these two additional terms do transform as vectors, thus respecting the rotational symmetry of $\mathbf{W}$, they do not appear in the original Toner-Tu evolution [115]. However, we remark that these two gradient terms vanish at linear order around an homogeneous solution $\rho=\rho_0$, $\mathbf{W}=\mathbf{W}_0$: they will have no effect on the linear stability analysis of the homogeneous ordered profile that we now set up to perform.

Since we are interested in the propagation along the main direction of motion in the ordered phase, we will focus on a simplified one-dimensional version of (3.15)-(3.16) for this linear stability analysis. In 1D, $\mathbf{W}$ becomes a scalar and we note that some of the terms in (3.15) become redundants as $(\mathbf{W}\cdot\boldsymbol{\nabla})\mathbf{W} \propto (\boldsymbol{\nabla}\cdot\mathbf{W})\mathbf{W} \propto \boldsymbol{\nabla}(|\mathbf{W}|^2) \propto W\partial_x W$ and $\boldsymbol{\nabla}(\boldsymbol{\nabla}\cdot\mathbf{W}) \propto \nabla^2\mathbf{W} \propto \partial_{xx}W$. It thus implies that all the λ_i terms collapse in one term $\lambda W\partial_x W$ while the D_B and D_T terms collapse in a unique diffusive operator $D\partial_{xx}W$. Finally, we remark that $D_2(\mathbf{W}\cdot\boldsymbol{\nabla})^2\mathbf{W} \propto W^2\partial_{xx}W + W(\partial_x W)^2$, so this term can be partially absorbed into D as well. Taking into account all these simplifications in (3.15), we obtain the Toner-Tu equations in 1D as

$$\begin{aligned}\partial_t W + \lambda W\partial_x W &= \alpha W - a_4 W^3 - \partial_x P_1 - W^2\partial_x P_2 + D\partial_{xx}W + D_2 W(\partial_x W)^2 \qquad (3.17)\\ \partial_t\rho + \partial_x W &= 0\,, \qquad (3.18)\end{aligned}$$

where all the parameters, as well as the scalar functions P_1 and P_2 in (3.17), can depend, on general ground, on the density $\rho(x)$ and on $|W(x)|$. We now show that (3.17)-(3.18) are always unstable at onset of order whenever the linear Landau term α is density-dependent. In order to perform a linear stability analysis, we introduce a characteristic velocity scale v_0 such that $W = v_0\hat{W}$ In this new variable, the time-evolution reads

$$\partial_t\hat{W} + \hat{\lambda}\hat{W}\partial_x\hat{W} = \alpha\hat{W} - \hat{a_4}\hat{W}^3 - \partial_x\hat{P_1} - \hat{W}^2\partial_x\hat{P_2} + D\partial_{xx}\hat{W} + \hat{D_2}\hat{W}(\partial_x\hat{W})^2 \tag{3.19}$$

$$\partial_t\rho + v_0\partial_x\hat{W} = 0\,, \tag{3.20}$$

where $\hat{\lambda} = v_0\lambda$, $\hat{a_4} = v_0^2 a_4$, $\hat{P_1} = v_0^{-1}P_1$, $\hat{P_2} = v_0 P_2$ and $\hat{D_2} = v_0^2 D_2$. For clarity, we now drop the hat notation and consider the dynamics

$$\partial_t W + \lambda W\partial_x W = \alpha W - a_4 W^3 - \partial_x P_1 - W^2\partial_x P_2 + D\partial_{xx}W + D_2 W(\partial_x W)^2 \tag{3.21}$$

$$\partial_t\rho + v_0\partial_x W = 0\,, \tag{3.22}$$

where ρ and W now have the same dimension. We can therefore study the linear stability of perturbations $\delta\rho$ and δW around the homogeneous solution ρ_0, $W_0 = \sqrt{\alpha/a_4}$. The linearized dynamics of $\delta\rho$ and δW in Fourier space reads

$$\partial_t \begin{pmatrix} \delta\rho_q \\ \delta W_q \end{pmatrix} = \begin{pmatrix} 0 & -iv_0 q \\ \xi_1 - iq\xi_2 & \xi_3 - iq\xi_4 - \xi_5 q^2 \end{pmatrix} \begin{pmatrix} \delta\rho_q \\ \delta W_q \end{pmatrix}\,, \tag{3.23}$$

where the ξ_i's are all functions of ρ_0 and W_0. Their exact expressions can be directly deduced from a Taylor expansion around ρ_0 and W_0 of the parameters and scalar functions appearing in (3.21). Here, we are only interested in their scaling with W_0 near the transition when $W_0 \sim 0$, where we can write

$$\xi_1 = W_0\alpha' + \mathcal{O}(W_0^2)\,,\quad \xi_2 = \mathcal{O}(W_0)\,,\quad \xi_3 = -\gamma W_0^2 + \mathcal{O}(W_0^3)\,,\quad \xi_4 = \mathcal{O}(W_0)\,,\quad \xi_5 = \mathcal{O}(W_0)\,. \tag{3.24}$$

with α' and γ given by

$$\alpha' = \left.\frac{\partial\alpha}{\partial\rho}\right|_{\rho=\rho_0,\,|W|=0}\,,\quad \gamma = 2a_4(\rho=\rho_0, |W|=0)\,. \tag{3.25}$$

Note that, at this stage, the development (3.24) may seem inconsistent as the order retained in W_0 differs from ξ_1 to ξ_5. However, it will be sufficient to obtain the first nonzero order of (3.29) in later purposes. The growth rates of the perturbations are given by the two eigenvalues

$$\lambda_\pm = \frac{-\left(\xi_5 q^2 + i\xi_4 q - \xi_3\right) \pm \sqrt{\Delta}}{2}\,, \tag{3.26}$$

where Δ reads

$$\Delta = \left(\xi_5 q^2 + i\xi_4 q - \xi_3\right)^2 - 4v_0\left(iq\xi_1 + \xi_2 q^2\right)\,. \tag{3.27}$$

The stability of the homogeneous solution is determined by the sign of the real part of the eigenvalues $\lambda^\pm$. An unstable mode exists as soon as $|\Re(\xi_5 q^2 + i\xi_4 q - \xi_3)| < |\Re(\sqrt{\Delta})|$. We first note that

$$2\Re(\sqrt{\Delta})^2 - 2\Re\left(\xi_5 q^2 + i\xi_4 q - \xi_3\right)^2 = -a(q) + \sqrt{a^2(q) + b(q)}\,, \tag{3.28}$$

where $a(q)$ and $b(q)$ are real numbers given by

$$\begin{aligned} a(q) =& \xi_4 q^2 + (\xi_5 q^2 - \xi_3)^2 + 4 v_0 \xi_2 q^2 \\ b(q) =& 16 q^2 v_0 \left(\xi_1^2 v_0 + \xi_3 \xi_4 \xi_1 - \xi_2 \xi_3^2\right) + 16 q^4 v_0 \xi_5 \left(2 \xi_2\, \xi_3 - \xi_1\, \xi_4\right) - 16 q^6 \left(\xi_2\, \xi_5^2\, v_0\right) \ . \end{aligned}$$

Because $a(q)$ is always positive, the condition (3.28) shows that a homogeneous solution is unstable as soon as $b(q) > 0$. At low q, the stability is thus controlled by the quadratic term of $b(q)$. Close to the transition $|W_0| \ll 1$, and using (3.24) this quadratic term can be simplified as

$$16 q^2 v_0 \left(\xi_1^2 v_0 + \xi_3 \xi_4 \xi_1 - \xi_2 \xi_3^2\right) = 16 v_0 q^2 \left[(W_0 \alpha')^2 + \mathcal{O}(W_0^3)\right] \ . \tag{3.29}$$

Thus, in the limit $W_0 \sim 0$, (3.29) is always positive, whatever the sign of α': there exists a critical W_0^c below which the homogeneous ordered solution undergoes a low-q instability. Consequently, whenever α depends on the density, the emergence of collective motion has to be discontinuous as none of the homogeneous solutions are stable at onset. This result holds for the particular case of the Vicsek Model for which we have shown that the linear Landau term α is density-dependent in subsection 3.1.2.

Thus, the Toner-Tu equation shed light on the mechanism behind the emergence of propagating bands in the Vicsek Model: as established in [114, 120–122], their existence stems from a density-dependent critical temperature. The coexistence region in the phase diagram of the Vicsek Model (see Fig. 3.1) then corresponds to the region where the homogeneous solution $W_0 \in [0, W_0^c]$ is unstable.

Finally, (3.29) establishes a binary classification of the flocking transition in models of collective motion: a discontinuous emergence of order is characterized by a density-dependent α while a continuous onset must feature a density-independent α. Models of collective motion with 'metric-free' interactions are believed to fall in the latter category with a second-order scenario and we now present them in greater detail.

3.2 Topological alignment: a particular case in models of collective motion

In section 3.1, I reviewed the literature on the Vicsek Model and concluded that the emergence of collective motion follows a phase-separation scenario whenever the linear Landau term α in the hydrodynamics is density-dependent. Interestingly, when alignment between particles is not decided based on their relative distance [9, 123–127] , α is believed to be density-independent [63, 64, 128, 129]. In this specific case, often referred to as *topological* or *metric-free* [125], the transition to collective motion is believed to be continuous and travelling bands have not been reported so far.

Topological models play an important role thanks to their relevance to studies of groups of animals [9, 123, 124, 126] or pedestrians [130], where visual cues dominate metric ones. They are also the natural choice to model confluent tissues where topological neighbourhoods determine interactions [127, 131–134]. Existing numerical results on their transition are scarce and limited to particles aligning with their Voronoi neighbours [63] or their k-nearest neighbours [64, 65].

So far in this chapter, I have reviewed the work of others on the transition to collective motion. As a teaser to motivate the next sections, which present our contribution [66],

I now report our first important result: the existence of travelling waves at the onset of collective motion in a topological Vicsek model. We consider flying spins evolving in a domain $L_x \times L_y$ with periodic boundary conditions. As in section 3.1.1, the time-evolution of their position $\mathbf{r}_i$ reads

$$\mathbf{r}_i(t+dt) = \mathbf{r}_i(t) + v dt\ \mathbf{s}_i\ , \tag{3.30}$$

with v being the self-propulsion speed. In addition, at every time step, the spins align with the average direction of their k-nearest neighbours:

$$\arg\Big[\mathbf{s}_i\Big] \to \arg\Big[\frac{1}{k}\sum_{j\in\mathcal{N}_i}\mathbf{s}_j\Big] + \sigma\eta\ , \tag{3.31}$$

where η is uniformly drawn in $[-\pi,\pi]$ and $\mathcal{N}_i$ is the set of k-nearest neighbours of the i-th particle. Upon simulating microscopic dynamics (3.30)-(3.31) with parameters tuned at the onset of collective motion, we observed the propagating bands shown in Fig. 3.2, which correspond to a phase-separated profile. The remainder of this chapter is devoted to the description of the mechanism that can turn a deceptive continuous transition at the mean-field hydrodynamic level into the first-order scenario observed in the simulations.

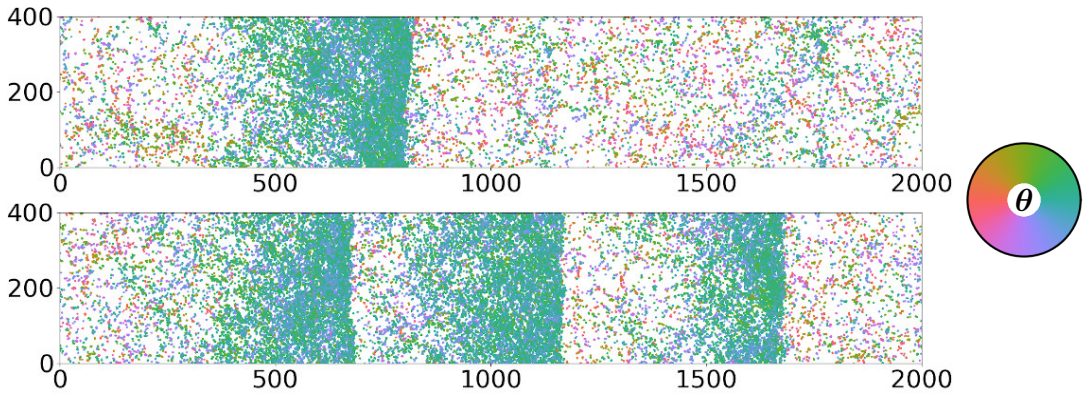

Figure 3.2 – Simulations of the topological Vicsek model (3.30)-(3.31) in 2D. At small noise, the system is disordered at low enough densities. Increasing the density then leads to an onset of order accompanied by propagating bands. Particles align with their $k = 3$ nearest neighbours. Parameters : $L_x = 2000$, $L_y = 400$, $\sigma = 0.08$, $k = 3$, $v = 0.2$, $\Delta t = 1$, $\rho_0 = 0.25$ (top) and $\rho_0 = 0.4$ (bottom). Figure adapted from [66].

3.3 A specific example: the 2D Active Ising Model

In this section, we present a minimalist lattice gas model for collective motion that was first introduced in [135, 136]: the Active Ising Model (AIM). We then show in sections 3.3.1 and 3.3.2 that the AIM suffers from the same defect already encountered in topological models: its mean-field hydrodynamics predicts a continuous onset of collective motion whereas its microscopic simulations instead exhibit a phase-separation scenario with travelling bands.

In the Active Ising Model, one consider N self-propelled particles carrying $\pm$ spins, moving on a 2D lattice $L_x \times L_y$, with lattice spacing a and periodic boundary conditions. We call $n_i^{\pm}$ the number of $\pm$ spins at site $i = (i_x, i_y)$ and we define the local density and magnetization as $\rho_i = n_i^+ + n_i^-$ and $m_i = n_i^+ - n_i^-$ respectively. Each spin undergoes a

biased diffusion according to its sign: + spins preferentially hop to the site on their right while − spins preferentially hop to the site on their left. Furthermore, spins align locally with flipping rates depending on the local density and magnetization. The microscopic update rules for a spin s at site i are the following (see also Fig. 3.3)

$$\begin{cases} \bullet \text{ it hops to site } j = (i_x + s, i_y) \text{ with rate } v/a \\ \bullet \text{ it diffuses isotropically with rate } D/a^2 \\ \bullet \text{ it flips into } -s \text{ with rate } \gamma \exp(-\beta s\, m_i/\rho_i) \end{cases} \tag{3.32}$$

We note that the minimal ingredients needed for a flocking transition are present: spins are endowed with a self-propulsion whose direction is coupled to a local aligning dynamics. The main difference with the Vicsek model described in section 3.1.1 lies in the direction of the self-propulsion, which is constrained to be $\pm\vec{e}_x$: the AIM has a discrete symmetry and it is biased solely along the x direction.

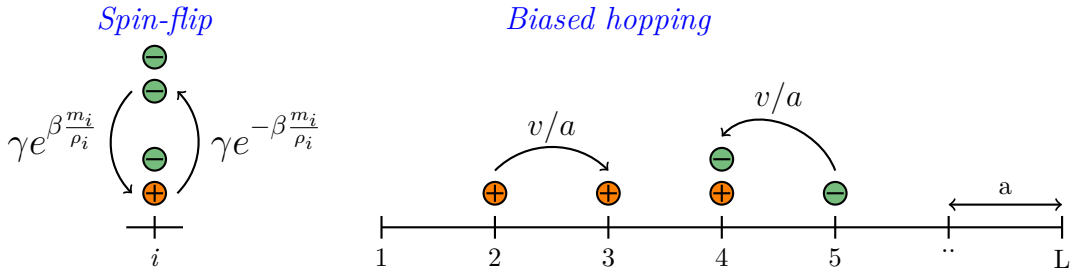

Figure 3.3 – Schematic representation of the dynamics (3.32). Spins align locally and hop asymetrically to their neighbouring sites in the x direction. In addition to the biased hops, the spins also diffuse freely in the x and y direction with rate D/a^2.

3.3.1 Mean-field hydrodynamics predicts a continuous transition

Following the approach established in [136], I now coarse-grain analytically the Active Ising Model to capture its phase diagram and assess the order of its transition to collective motion. The simplest way to derive a mean-field hydrodynamics for a non-equilibrium lattice gas is to perform a mean-field analysis. For clarity, we will first carry out the computation in 1D and then extend it to the 2D case. Starting from the master equation, we first derive the evolution of the mean number of ± spins at site i

$$\begin{aligned} \langle \dot{n}_i^{\pm} \rangle =& \frac{D}{a^2}\langle n_{i-1}^{\pm} \rangle + \frac{D}{a^2}\langle n_{i+1}^{\pm} \rangle - 2\frac{D}{a^2}\langle n_i^{\pm} \rangle \pm \frac{v}{a}\langle n_{i-1}^{\pm} \rangle \mp \frac{v}{a}\langle n_{i+1}^{\pm} \rangle \\ & \pm \left\langle n_i^{-} \exp\left(\beta \frac{m_i}{\rho_i}\right) \right\rangle \mp \left\langle n_i^{+} \exp\left(-\beta \frac{m_i}{\rho_i}\right) \right\rangle . \end{aligned} \tag{3.33}$$

Casting the above expressions into the local density ρ_i and magnetization m_i, we get

$$\langle \dot{\rho}_i \rangle = \frac{D}{a^2}(\langle \rho_{i+1} \rangle + \langle \rho_{i-1} \rangle - 2\langle \rho_i \rangle) - \frac{v}{a}(\langle m_{i+1} \rangle - \langle m_{i-1} \rangle) \tag{3.34}$$

$$\begin{aligned} \langle \dot{m}_i \rangle =& \frac{D}{a^2}(\langle m_{i+1} \rangle + \langle m_{i-1} \rangle - 2\langle m_i \rangle) - \frac{v}{a}(\langle \rho_{i+1} \rangle - \langle \rho_{i-1} \rangle) \\ & + 2\left\langle \rho_i \sinh\left(\beta \frac{m_i}{\rho_i}\right) \right\rangle - 2\left\langle m_i \cosh\left(\beta \frac{m_i}{\rho_i}\right) \right\rangle . \end{aligned} \tag{3.35}$$

The next step is to take the continuum limit by Taylor expanding the fields around i as $\rho_{i\pm1} = \rho(x)+a\partial_x\rho(x)+a^2/2\,\partial_{xx}\rho(x)+\mathcal{O}(a^3)$ and $m_{i\pm1} = m(x)+a\partial_x m(x)+a^2/2\,\partial_{xx}m(x)+\mathcal{O}(a^3)$. We thus obtain the hydrodynamics for the continuum fields $\rho(x)$ and $m(x)$ as

$$\partial_t\langle\rho\rangle = D\partial_{xx}\langle\rho\rangle - v\partial_x\langle m\rangle \tag{3.36}$$

$$\partial_t\langle m\rangle = D\partial_{xx}\langle m\rangle - v\partial_x\langle\rho\rangle + \left\langle 2\rho\sinh\frac{\beta m}{\rho} - 2m\cosh\frac{\beta m}{\rho}\right\rangle \ . \tag{3.37}$$

In higher dimensions, diffusion occurs in every direction instead of being restricted to the x-axis and generalizing (3.36)-(3.37) thus amounts to replacing $D\partial_{xx}$ by $D\boldsymbol{\nabla}^2$. So far, equations (3.36)-(3.37) are exact and couple the first moments $\langle\rho\rangle$ and $\langle m\rangle$ to higher ones through the hyperbolic cosine and sine functions. The mean-field approximation consists in neglecting this coupling between moments by replacing $\langle f(\rho,m)\rangle$ by $f(\langle\rho\rangle,\langle m\rangle)$. Performing this treatment into (3.36)-(3.37) and dropping the $\langle..\rangle$ notation, we obtain

$$\partial_t\rho = D\partial_{xx}\rho - v\partial_x m \tag{3.38}$$

$$\partial_t m = D\partial_{xx}m - v\partial_x\rho + 2\rho\sinh\left(\frac{\beta m}{\rho}\right) - 2m\cosh\left(\frac{\beta m}{\rho}\right) \ . \tag{3.39}$$

Because we are only interested in the onset of flocking, for which $m/\rho \ll 1$, we do not need the full dependency of the hyperbolic alignment term and we expand it up to order m^3/ρ^3 to get

$$\partial_t\rho = D\partial_{xx}\rho - v\partial_x m \tag{3.40}$$

$$\partial_t m = D\partial_{xx}m - v\partial_x\rho - \alpha m - \gamma m^3/\rho^2 \ , \tag{3.41}$$

with $\alpha = 2(1-\beta)$ and $\gamma = \beta^2(1-\beta/3)$. Note that α has the opposite sign convention with respect to the Vicsek model: $\alpha < 0$ promotes order whereas $\alpha > 0$ corresponds to the disordered phase. We are now in position to assess the order of the transition to collective motion through a linear stability analysis of (3.40)-(3.41) around the homogeneous ordered profile $\rho = \rho_0$ and $m = m_0$. To illustrate the effect of a putative dependency of α on the density, we will assume $\alpha = \alpha(\rho)$ throughout this stability analysis and eventually take $\alpha' = 0$ at the end of the derivation since $\alpha = 2(1-\beta)$ does not depend on the density at mean-field level.

We start by rescaling time and position in (3.40)-(3.41) as $x = \tilde{x}D/v$ and $t = \tilde{t}D/v^2$, which leads to

$$\partial_{\tilde{t}}\rho = \partial_{\tilde{x}\tilde{x}}\rho - \partial_{\tilde{x}}m \tag{3.42}$$

$$\partial_{\tilde{t}}m = \partial_{\tilde{x}\tilde{x}}m - \partial_{\tilde{x}}\rho - \tilde{\alpha}(\rho)m - \tilde{\gamma}\frac{m^3}{\rho^2} \ , \tag{3.43}$$

where $\tilde{\alpha}(\rho) = D\alpha(\rho)/v^2$ and $\tilde{\gamma} = D\gamma/v^2$. To lighten the notations, we now drop the tilde for the remainder of this section.

The linearized dynamics of the perturbations δm and $\delta\rho$ around the homogeneous solutions m_0 and ρ_0, are given, in Fourier space, by

$$\partial_t\begin{pmatrix}\delta\rho_q\\ \delta m_q\end{pmatrix} = \begin{pmatrix}-q^2 & -iq\\ -iq - \sqrt{\frac{|\alpha|}{\gamma}}\left(\alpha_0'\rho_0 + 2\alpha\right) & -q^2+2\alpha\end{pmatrix}\begin{pmatrix}\delta\rho_q\\ \delta m_q\end{pmatrix} \ , \tag{3.44}$$

where we used the relation $m_0 = \rho_0\sqrt{\frac{|\alpha|}{\gamma}}$ and defined $\alpha_0' = \alpha'(\rho_0)$. The growth rates of the perturbations are given by the two eigenvalues

$$\lambda_\pm = \frac{-\left(2q^2 - 2\alpha\right) \pm \sqrt{\Delta}}{2} \,, \tag{3.45}$$

where Δ reads

$$\Delta = \left(2q^2 - 2\alpha\right)^2 + 4iq\left(iq + \sqrt{\frac{|\alpha|}{\gamma}}\left(\alpha_0'\rho_0 + 2\alpha\right)\right) - q^2\left(q^2 - 2\alpha\right) \,. \tag{3.46}$$

The stability of the homogeneous solution is determined by the sign of the real part of the eigenvalues $\lambda^\pm$. An unstable mode exists as soon as $|2q^2 - 2\alpha| < |\Re(\sqrt{\Delta})|$. We first note that

$$2\Re(\sqrt{\Delta})^2 - 2\Re\left(2q^2 - 2\alpha\right)^2 = -a(q) + \sqrt{a^2(q) + b(q)} \,, \tag{3.47}$$

where $a(q)$ and $b(q)$ are real numbers given by

$$a(q) = 4(q^2+\alpha)^2 + 4v^2q^2 + 4q^2(q^2+2\alpha) \tag{3.48}$$

$$b(q) = -\frac{16\alpha q^2}{\gamma}\Big[\rho_0\alpha'\left(4\alpha + \rho_0\alpha'\right) - 4\alpha\Big(\alpha(2\gamma - 1) - \gamma\Big)\Big] - 64\alpha(5\alpha - 2)q^4 - 64(-4\alpha + 1)q^6 - 64q^8 \,. \tag{3.49}$$

Because $a(q)$ is always positive, the instability condition (3.47) amounts to $b(q) > 0$. Close to the transition $|\alpha| \ll 1$ and $b(q)$ can be simplified as

$$b(q) = -\frac{16\alpha q^2}{\gamma}\left[\rho_0^2\left(\alpha_0'\right)^2 + 4\gamma\alpha + \mathcal{O}(\alpha^2)\right] + 128\left[\alpha + \mathcal{O}(\alpha^2)\right]q^4 - 64\left[1 + \mathcal{O}(\alpha)\right]q^6 - 64q^8 \,. \tag{3.50}$$

At the onset of flocking, $\alpha \simeq 0^-$ and only the first term on the right hand side of (3.50) can be positive and trigger an instability at low q

$$b(q) \underset{q\to 0}{\sim} \begin{cases} \dfrac{16|\alpha|q^2\rho_0^2}{\gamma}(\alpha_0')^2 & \text{if } \alpha_0' \neq 0 \\ -64\alpha^2q^2 & \text{if } \alpha_0' = 0 \end{cases} \tag{3.51}$$

The sign of (3.51) finally gives the order of the transition. The homogeneous ordered solution remains stable close to the critical temperature when $\alpha'(\rho_0) = 0$, but it becomes unstable as soon $\alpha'(\rho_0) \neq 0$, regardless of the sign of $\alpha'(\rho_0)$. This implies that the AIM, for which we have a density-independent α at mean-field level, should exhibit a continuous emergence of collective motion. Let us now verify this statement in direct microscopic simulations.

3.3.2 Microscopic simulations show a discontinuous transition

The microscopic simulations performed in [136] stands at odd with a continuous transition and indicate instead a first order onset of flocking: they show the presence of a coexistence domain where ordered bands propagate in a disordered gas phase. We report in Fig. 3.4

the numerical phase diagram of the Active Ising Model in the temperature-density plane (T, ρ_0), with T being defined as $T = \beta^{-1}$.

At low densities (or high temperatures), the system exhibits a disordered gas phase while at high densities (or low temperatures) it forms a polar liquid. Between these two homogeneous phases, there is a coexistence region where steady-state phase-separated profiles are observed (see Fig. 3.4). In this domain, where one observes dense waves of spins propagating in a disordered gas phase, none of the homogeneous solutions are stable. Note also that the "critical" temperature of the onset of order depends on the density ρ. The presence of a coexistence region shows that the stability analysis developed in 3.3.1 is erroneous and, *a fortiori*, that the mean-field hydrodynamics (3.40)-(3.41) yields a poor description of the active spins.

Let us try to understand what mechanism lies at the origin of such a discrepancy between the mean-field limit and the numerical simulation. First, we know that mean-field approaches have a tendency to wipe out the fluctuations of the fields at play. Second, statistical field theory tells us that taking into account these fluctuations will generically renormalize all parameters entering (3.40)-(3.41). Especially, fluctuations will modify the linear Landau term α in (3.41). From our linear stability analysis, we know that the onset of flocking is very sensitive to modifications of α: as soon as α becomes density-dependent, the transition turns into a first-order scenario. We just digged out a possible mechanism explaining the discontinuous emergence of collective motion in the AIM: fluctuations may renormalize α by making it density-dependent, which in turn would destabilize the homogeneous phases at the critical temperature. Let us now show analytically that it is indeed the case.

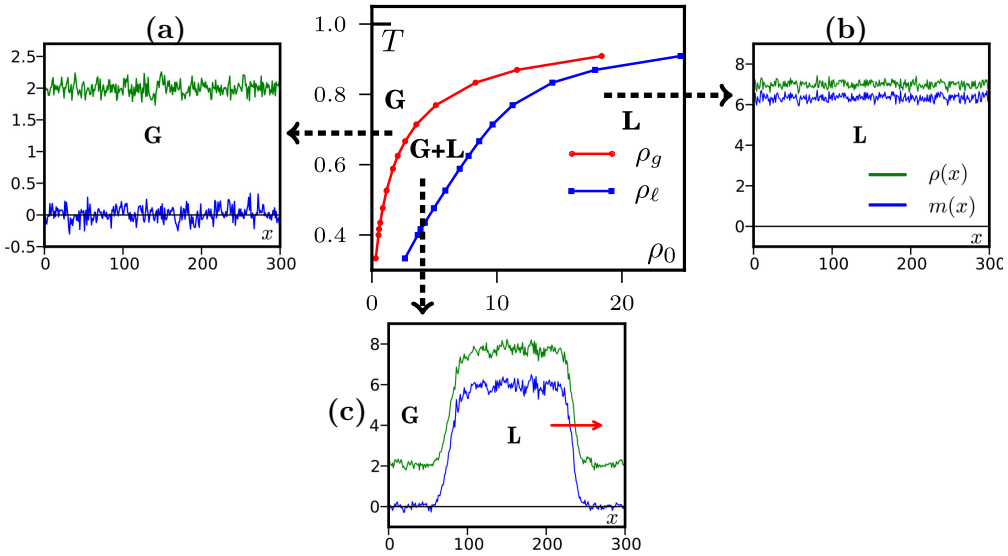

Figure 3.4 – **Center:** Phase diagram of the AIM in the Temperature-Density plane (T, ρ_0), with $T = \beta^{-1}$. Between the gaseous and liquid phases, indicated by **G** and **L** respectively, the red and blue lines delimit the coexistence domain in which propagating bands are reported. **Right, Left, Bottom:** examples of density profiles (green upper line) and magnetization profiles (blue lower line) averaged along the y direction for the three phases. (a) Disordered gas $T = 0.71$, $\rho_0 = 2$. (b) Polar liquid $T = 0.5$, $\rho_0 = 7$. (c) Liquid-gas coexistence $T = 0.62$, $\rho_0 = 5$. Figure adapted from [136].

3.4 Fluctuation-induced first-order transition in the Active Ising Model

In this section, we show that the hydrodynamic description of the AIM, derived in the mean-field limit in section 3.3.1, is unstable with respect to the addition of fluctuations. To this aim, we complement PDEs (3.40)-(3.41) with a noise term to obtain

$$\partial_t \rho = D\partial_{xx}\rho - v\partial_x m \tag{3.52}$$

$$\partial_t m = D\partial_{xx} m - v\partial_x \rho - \mathcal{F}(\rho, m) + \sqrt{2\sigma\rho}\,\eta\ , \tag{3.53}$$

where $\eta(x,t)$ is a zero-mean delta-correlated Gaussian white noise field and $\mathcal{F}(\rho,m) = \alpha m + \gamma m^3/\rho^2$. Note that, hereafter, $\rho(x,t)$ and $m(x,t)$ represent fluctuating fields. The order parameter $m(x,t)$ is the sum of the orientations of particles located around position x. The noise acting on $m(x,t)$ will thus be multiplicative; it describes the fluctuations of a sum over $\propto \rho$ particles and we take it proportional to $\sqrt{\rho}$.

We now construct the hydrodynamics of the average fields $\tilde{\rho}(x,t) = \langle \rho(x,t)\rangle$ and $\tilde{m}(x,t) = \langle m(x,t)\rangle$ to leading order in the noise strength σ. In principle, we could also complement (3.52) with a conserved noise. The latter is expected to be subdominant at large scales and we ignore it here, although our approach can be extended to this case, as shown later in section 3.7. Calling $\rho_0(x,t)$ and $m_0(x,t)$ the solution of (3.52)-(3.53) without noise (*ie* when $\sigma = 0$), we introduce the deviations $\Delta\rho$ and Δm from this mean-field solution as series in $\sigma^{1/2}$

$$\Delta\rho = \rho - \rho_0 = \sigma^{\frac{1}{2}}\delta\rho_1 + \sigma\delta\rho_2 + \dots\ , \qquad \Delta m = m - m_0 = \sigma^{\frac{1}{2}}\delta m_1 + \sigma\delta m_2 + \dots \tag{3.54}$$

Note that the $\delta\rho_k$ and δm_k are stochastic fields while ρ_0 and m_0 remain deterministic fields. Inserting the expansions (3.54) in (3.52)-(3.53) and equating terms of order $\sigma^{k/2}$ yields the evolution equation for $\delta\rho_k$ and δm_k. For $k = 1$, it gives

$$\partial_t \delta\rho_1 = D\partial_{xx}\delta\rho_1 - v\partial_x \delta m_1 \tag{3.55}$$

$$\partial_t \delta m_1 = D\partial_{xx}\delta m_1 - v\partial_x\delta\rho_1 - \frac{\partial\mathcal{F}}{\partial\rho}\delta\rho_1 - \frac{\partial\mathcal{F}}{\partial m}\delta m_1 + \sqrt{2\rho_0}\,\eta\ , \tag{3.56}$$

while for $k = 2$ we obtain

$$\partial_t \delta\rho_2 = D\partial_{xx}\delta\rho_2 - v\partial_x\delta m_2 \tag{3.57}$$

$$\begin{aligned}\partial_t \delta m_2 =& D\partial_{xx}\delta m_2 - v\partial_x\delta\rho_2 - \frac{\partial\mathcal{F}}{\partial\rho}\delta\rho_2 - \frac{\partial\mathcal{F}}{\partial m}\delta m_2 - \frac{\partial^2\mathcal{F}}{\partial m^2}\frac{\delta m_1^2}{2}\\ &- \frac{\partial^2\mathcal{F}}{\partial\rho^2}\frac{\delta\rho_1^2}{2} - \frac{\partial^2\mathcal{F}}{\partial m\partial\rho}\delta m_1\delta\rho_1 + \frac{\delta\rho_1}{\sqrt{2\rho_0}}\,\eta\ ,\end{aligned} \tag{3.58}$$

Averaging (3.55)-(3.56) over the noise with Itō prescription then gives

$$\partial_t\langle\delta\rho_1\rangle = D\partial_{xx}\delta\langle\rho_1\rangle - v\partial_x\langle\delta m_1\rangle \tag{3.59}$$

$$\partial_t\delta\langle m_1\rangle = D\partial_{xx}\delta\langle m_1\rangle - v\partial_x\langle\delta\rho_1\rangle - \frac{\partial\mathcal{F}}{\partial\rho}\langle\delta\rho_1\rangle - \frac{\partial\mathcal{F}}{\partial m}\langle\delta m_1\rangle\ , \tag{3.60}$$

while averaging equation (3.57)-(3.58) yields

$$\partial_t\langle\delta\rho_2\rangle = D\partial_{xx}\langle\delta\rho_2\rangle - v\partial_x\langle\delta m_2\rangle \tag{3.61}$$

$$\partial_t\langle\delta m_2\rangle = D\partial_{xx}\langle\delta m_2\rangle - v\partial_x\langle\delta\rho_2\rangle - \frac{\partial\mathcal{F}}{\partial\rho}\langle\delta\rho_2\rangle - \frac{\partial\mathcal{F}}{\partial m}\langle\delta m_2\rangle - \frac{\partial^2\mathcal{F}}{\partial m^2}\frac{\langle\delta m_1^2\rangle}{2} - \frac{\partial^2\mathcal{F}}{\partial\rho^2}\frac{\langle\delta\rho_1^2\rangle}{2} - \frac{\partial^2\mathcal{F}}{\partial m\partial\rho}\langle\delta m_1\delta\rho_1\rangle\ . \tag{3.62}$$

Summing together (3.40), (3.59) multiplied by $\sigma^{\frac{1}{2}}$ and (3.61) multiplied by σ gives the evolution of $\tilde{\rho}$ up to order σ as

$$\partial_t\tilde{\rho} = D\partial_{xx}\tilde{\rho} - v\partial_x\tilde{m}\ , \tag{3.63}$$

while summing together (3.41), (3.60) multiplied by $\sigma^{\frac{1}{2}}$ and (3.62) multiplied by σ yields the evolution of $\tilde{m}$ up to order σ

$$\partial_t\tilde{m} = D\partial_{xx}\tilde{m} - v\partial_x\tilde{\rho} - \mathcal{F}(\rho_0,m_0) - \sigma^{\frac{1}{2}}\frac{\partial\mathcal{F}}{\partial\rho}\langle\delta\rho_1\rangle - \sigma^{\frac{1}{2}}\frac{\partial\mathcal{F}}{\partial m}\langle\delta m_1\rangle - \sigma\frac{\partial\mathcal{F}}{\partial\rho}\langle\delta\rho_2\rangle - \sigma\frac{\partial\mathcal{F}}{\partial m}\langle\delta m_2\rangle - \sigma\frac{\partial^2\mathcal{F}}{\partial m^2}\frac{\langle\delta m_1^2\rangle}{2} - \sigma\frac{\partial^2\mathcal{F}}{\partial\rho^2}\frac{\langle\delta\rho_1^2\rangle}{2} - \sigma\frac{\partial^2\mathcal{F}}{\partial m\partial\rho}\langle\delta m_1\delta\rho_1\rangle\ . \tag{3.64}$$

To order σ, the Landau term $\mathcal{F}(\tilde{\rho},\tilde{m})$ taken at the averaged density and magnetization reads

$$\mathcal{F}(\tilde{\rho},\tilde{m}) = \mathcal{F}(\rho_0,m_0) + \sigma^{\frac{1}{2}}\frac{\partial\mathcal{F}}{\partial\rho}\langle\delta\rho_1\rangle + \sigma^{\frac{1}{2}}\frac{\partial\mathcal{F}}{\partial m}\langle\delta m_1\rangle + \sigma\frac{\partial\mathcal{F}}{\partial\rho}\langle\delta\rho_2\rangle + \sigma\frac{\partial\mathcal{F}}{\partial m}\langle\delta m_2\rangle + \frac{\sigma}{2}\frac{\partial^2\mathcal{F}}{\partial^2\rho}\langle\delta\rho_1\rangle^2 + \frac{\sigma}{2}\frac{\partial^2\mathcal{F}}{\partial^2 m}\langle\delta m_1\rangle^2 + \sigma\frac{\partial^2\mathcal{F}}{\partial\rho\partial m}\langle\delta\rho_1\rangle\langle\delta m_1\rangle + \mathcal{O}(\sigma^{\frac{3}{2}})\ . \tag{3.65}$$

Using expression (3.65) into (3.64) simplifies the time-evolution of $\tilde{m}$ as

$$\partial_t\tilde{m} = D\partial_{xx}\tilde{m} - v\partial_x\tilde{\rho} - \mathcal{F}(\tilde{\rho},\tilde{m}) - \sigma\frac{\partial^2\mathcal{F}}{\partial m^2}\left(\frac{\langle\delta m_1^2\rangle - \langle\delta m_1\rangle^2}{2}\right) - \sigma\frac{\partial^2\mathcal{F}}{\partial\rho^2}\left(\frac{\langle\delta\rho_1^2\rangle - \langle\delta\rho_1\rangle^2}{2}\right) - \sigma\frac{\partial^2\mathcal{F}}{\partial m\partial\rho}\left(\langle\delta m_1\delta\rho_1\rangle - \langle\delta m_1\rangle\langle\delta\rho_1\rangle\right)\ . \tag{3.66}$$

To close the above renormalized hydrodynamics (3.63)-(3.66), we only have to compute the correlators involving $\delta\rho_1$ and δm_1 by using their stochastic evolution given in (3.55)-(3.56). However, to perform such a derivation, we first need two crucial assumptions:

AI. We assume that $\delta\rho_1$ and δm_1 are fast modes varying on lengthscales and timescales much smaller than the ones relevant for ρ_0 and m_0. Under this assumption, $\rho_0(x,t)$ and $m_0(x,t)$ entering in the linearized evolution (3.55)-(3.56) can be considered as constants in both time and space. This adiabatic approximation allows us to compute the correlators in terms of ρ_0 and m_0 as parameters and to re-establish their dependency on x and t a posteriori.

AII. We assume that the fields $\delta\rho_1$ and δm_1 have a non-zero mass, which is equivalent to suppose that the real part of the eigenvalues of the system (3.55)-(3.56) are negative.

Note that the two asumptions AI-AII are related because a stochastic field with a high mass has a small correlation length and thus varies on smaller lengthscales. Using Fourier transform, we detail in Appendix B.2.1 the derivation of the correlators appearing in (3.66) under these approximations. Because we are only interested in the onset of collective motion where $m_0 \sim 0$, we hereafter report the result up to order m_0^2

$$\langle \delta m_1^2 \rangle = \rho_0 \frac{v^2\sqrt{\frac{2\alpha}{D}} + \alpha\sqrt{v^2+\alpha D}}{4\alpha v^2 + 2\alpha^2 D} - \rho_0 \frac{3\gamma D\left(\frac{\alpha D}{\sqrt{v^2+\alpha D}} + \frac{\sqrt{2}v^2\left(2v^2+3\alpha D\right)}{(\alpha D)^{3/2}}\right)}{4\left(\alpha D + 2v^2\right)^2}\frac{m_0^2}{\rho_0^2} + \mathcal{O}(m_0^3) \tag{3.67}$$

$$\langle \delta \rho_1^2 \rangle = \rho_0 \frac{v^2\left(\sqrt{\frac{2\alpha}{D}} - \frac{\alpha}{\sqrt{v^2+\alpha D}}\right)}{2\alpha\left(\alpha D + 2v^2\right)} + \mathcal{O}(m_0^2)\,, \qquad \langle \delta\rho_1 \delta m_1 \rangle = 0 + \mathcal{O}(m_0^2) \tag{3.68}$$

Plugging (3.67)-(3.68) into (3.66), discarding terms beyond order $\tilde{m}^3$, we obtain a closed hydrodynamics for $\tilde{m}$ which is valid up to order σ and reads

$$\partial_t \tilde{m} = D\partial_{xx}\tilde{m} - v\partial_x\tilde{\rho} - \hat{\alpha}(\tilde{\rho})\tilde{m} - \hat{\gamma}(\tilde{\rho})\frac{\tilde{m}^3}{\tilde{\rho}^2}\,, \tag{3.69}$$

with the renormalized Landau coefficients $\hat{\alpha}(\tilde{\rho})$ and $\hat{\gamma}(\tilde{\rho})$ given by

$$\hat{\gamma}(\tilde{\rho}) = \gamma + \frac{3\sigma\gamma}{2v\tilde{\rho}}\frac{\sqrt{\frac{2v^2}{D\alpha}} - \frac{1}{\sqrt{1+\frac{\alpha D}{v^2}}}}{\frac{\alpha D}{v^2}+2} - \frac{9\sigma\gamma^2 D}{4v^3\tilde{\rho}}\frac{\left(\frac{\alpha D}{v^2\sqrt{1+\frac{\alpha D}{v^2}}} + \frac{\sqrt{2}\left(2+3\frac{\alpha D}{v^2}\right)}{\left(\frac{\alpha D}{v^2}\right)^{3/2}}\right)}{\left(\frac{\alpha D}{v^2}+2\right)^2} \tag{3.70}$$

$$\hat{\alpha}(\tilde{\rho}) = \alpha + \frac{3\sigma\gamma}{2\tilde{\rho}v} f\left(\frac{\alpha D}{v^2}\right) \text{ with } f(u) = \frac{\sqrt{2/u}+\sqrt{1+u}}{2+u}\,, \tag{3.71}$$

Fluctuations have thus, to order σ, dressed α and γ into $\hat{\alpha}$ and $\hat{\gamma}$. Especially, we remark that the linear Landau term now depends explicitly on the density in (3.71). Note that, due to assumption AII, the renormalized hydrodynamics (3.69) is only valid in the high temperature phase, where $\alpha > 0$. We detail in Appendix B.2.2 how the renormalization process must be carried out in the low temperature phase when $\alpha < 0$ and we find that, even in this regime, fluctuations make $\hat{\alpha}$ density-dependent.

The mechanism by which $\hat{\alpha}$ becomes density dependent is thus robust and present in both the ordered and disordered phases. Note that higher orders in σ have no reason to cancel the dependence of $\hat{\alpha}$ on the density and we thus expect our conclusions to hold non-perturbatively in σ. According to the stability analysis performed in section 3.3.1, a density-dependent α should turn the continuous transition predicted by the mean-field evolution (3.40)-(3.41) into the standard liquid-gas separation.

To confirm our predictions, we carried out simulations of the scalar 2D generalization of the stochastic PDEs (3.52)-(3.53) where we substitute ∂_{xx} by the Laplacian operator:

$$\partial_t \rho = D\boldsymbol{\nabla}^2\rho - v\partial_x m \tag{3.72}$$

$$\partial_t m = D\boldsymbol{\nabla}^2 m - v\partial_x\rho - \mathcal{F}(\rho, m) + \sqrt{2\sigma\rho}\,\eta\,. \tag{3.73}$$

The continuous transition predicted in the case $\sigma = 0$ is indeed replaced by the standard liquid-gas framework [135, 136], as shown in Fig. 3.5 by the emergence of travelling-band solutions. Consistently with our result (3.71), the top-left panel of Fig. 3.5 also shows that

fluctuations have shifted the onset of order to a lower critical temperature compared to its mean-field value. Finally, as detailed in Appendix B.2.2, our renormalization procedure correctly forecast a noise-induced lowering of the magnetization compared to mean-field in the ordered phase (see the top-left panel of Fig. 3.5).

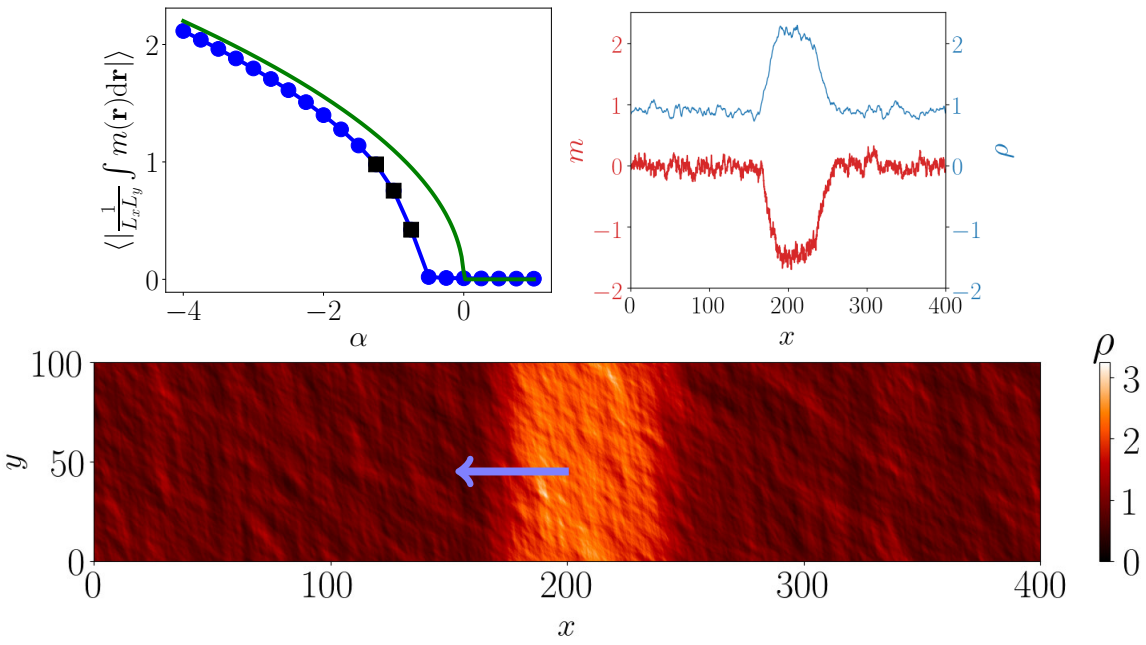

Figure 3.5 – Numerical simulations of (3.72)-(3.73). **Top left**: Average magnetization as α is varied. The transition occurs at $\alpha_c < 0$, shifted from the mean-field prediction (green line). At the onset of order, inhomogeneous profiles (black squares) separate homogeneous ordered and disordered phases (blue dots). Parameters: $D = v = \gamma = \sigma = 1$, $dx = 0.5$, $dt = 0.01$, $L_x = 400$, $L_y = 40$, $\rho_0 \equiv N/(L_xL_y) = 1.1$. **Bottom**: A snapshot close to the transition shows an ordered travelling band in a disordered background. **Top right**: The corresponding density and magnetization fields averaged along y. Parameters: same as before up to $L_y = 100$, $dx = 0.1$, $\alpha = -0.9$. Figure adapted from [66].

3.5 Fluctuation-induced first-order transition for k-nearest neighbours alignment

The study of the dynamics (3.52)-(3.53) in the previous section showed that fluctuations can turn a continuous transition at mean-field level into a discontinuous one. In this section, I assess whether the same mechanism applies to topological models. The common belief is that topological interactions protect the emergence of collective motion from density fluctuations. Indeed, if we take the example of k-nearest neighbours, doubling distances between all particles is equivalent to dividing the density by 2^{d}, but does not change the neighbours in the aligning dynamics. Thus, it can be argued that the local density should have no impact on the magnetization, and that the critical temperature should be density-independent. I hereafter refute this statement by studying a hydrodynamic description that preserves the topological nature of the interactions at the coarse-grained level. I show that the mean-field continuous transition is, once again, turned into a phase-separation scenario by a Gaussian noise.

3.5.1 Renormalization of the critical temperature

We introduce a generalization of the AIM's hydrodynamics (3.40)-(3.41) in which particles align with their k nearest neighbours. We first define the coarse-grained field $y(x)$, which measures the interaction range of a particle located at x, through the implicit equation:

$$\int_{x-y(x)}^{x+y(x)} \rho(z)\mathrm{d}z = k \ . \tag{3.74}$$

Particles at position x then align with a "topological" field $\bar{m}(x,t)$ computed over "their k nearest neighbours" through

$$\bar{m}(x) = \frac{1}{k}\int_{x-y(x)}^{x+y(x)} m(z)\mathrm{d}z \ . \tag{3.75}$$

Doubling the distance between particles does not alter the values of $\bar{m}(x)$, consistently with microscopic topological models [9,63]. We now construct the topological counterpart to the Landau term $\mathcal{F}(\rho,m) = \alpha m + \gamma m^3/\rho^2$ appearing in the hydrodynamics of the AIM (3.40)-(3.41). We have seen in section 3.3.1 that $\mathcal{F}$ is obtained as the small-magnetization expansion of a more complex function $\mathcal{F}_{\text{ferro}} = 2m\cosh(\beta p) - 2\rho\sinh(\beta p)$, where $p = m/\rho$ is the local magnetization per particle and β the inverse temperature. The fields ρ and m enter $\mathcal{F}_{\text{ferro}}$ through counting statistics, $(\rho \pm m)/2$, representing the local densities of particles with plus or minus spins. The field p, on the other hand, enters via the aligning rate at which a spins s flips, e.g. $W(s \to -s) = \Gamma\exp(-\beta s p)$. When particles align stochastically with a topological field $\bar{m}$, the Landau term thus simply becomes $\mathcal{F}_{\text{ferro}} = 2m\cosh(\beta\bar{m}) - 2\rho\sinh(\beta\bar{m})$. Expanding to third order in the fields then yields:

$$\mathcal{F}_{\text{topo}}\left(\bar{m},m,\rho\right) = \Gamma\Big(2m - 2\rho\beta\bar{m} - \frac{\rho\beta^3}{3}\bar{m}^3 + \beta^2 m\bar{m}^2\Big) \tag{3.76}$$

in which, for simplicity, we retain β as the sole control parameter. At mean-field level, our topological field theory is thus given by

$$\partial_t\rho = D\partial_{xx}\rho - v\partial_x m \,, \qquad \text{and} \qquad \partial_t m = D\partial_{xx}m - v\partial_x\rho - \mathcal{F}_{\text{topo}}(\bar{m},m,\rho) \ . \tag{3.77}$$

Homogeneous solutions ρ_0, m_0 correspond to $y(x) = y_0 = k/(2\rho_0)$ and $\bar{m} = m_0/\rho_0$. The linear term in $\mathcal{F}_{\text{topo}}$ then reduces to $2\Gamma(1-\beta)m_0$, leading to a density-independent critical temperature at $\beta_m = 1$. As described in Appendix B.3.1, linear stability analysis of the homogeneous solutions then shows that disordered and ordered solutions are linearly stable for $\beta < \beta_m$ and $\beta > \beta_m$, respectively. The topological field theory (3.77) thus predicts a continuous transition at the mean-field level.

Following section 3.4, we now assess the effect of dressing the topological hydrodynamics (3.77) with noise

$$\partial_t\rho = D\partial_{xx}\rho - v\partial_x m \tag{3.78}$$

$$\partial_t m = D\partial_{xx}m - v\partial_x\rho - \mathcal{F}_{\text{topo}}(\rho,m,\bar{m}) + \sqrt{2\sigma\rho}\,\eta \ . \tag{3.79}$$

Here again, the noise is multiplicative and proportional to $\sqrt{\rho(x,t)}$ since $m(x,t)$ is still the sum of the orientations of particles located around position x. To construct the dynamics of the averaged fields $\tilde{\rho} = \langle\rho(x,t)\rangle$ and $\tilde{m} = \langle m(x,t)\rangle$ to order σ, we first stress that (3.74) directly enslaves the field $y(x)$ to $\rho(x)$. There are thus, once again, only two independent

hydrodynamic fields, $\rho(x,t)$ and $m(x,t)$, so that our renormalization process presented in section 3.4 is still valid, up to $\mathcal{F} \to \mathcal{F}_{\rm topo}$. The expression of $\mathcal{F}_{\rm topo}$ being, however, more complicated than in the case of the AIM, the algebra is correspondingly more involved. Especially, beside assumptions AI-AII, we will need the additional approximation that

AIII. $\delta\rho_1$ and δm_1 are varying on lengthscales much smaller than the lengthscales over which $\bar{m}(x)$ and $y(x)$ vary.

I detail in Appendix B.3.2 the renormalization of the linear part of $\mathcal{F}_{\rm topo}$, which controls the nature of the transition. To first order in the noise strength σ, we find

$$\partial_t \tilde{\rho} = D\nabla^2\tilde{\rho} - v\nabla\tilde{m} \tag{3.80}$$

$$\partial_t \tilde{m} = D\nabla^2\tilde{m} - v\nabla\delta\tilde{\rho} - \mathcal{F}^R_{\rm topo}(\tilde{m},\tilde{\rho},\tilde{\bar{m}}) \ , \tag{3.81}$$

where $\tilde{\rho} = \langle\rho\rangle$, $\tilde{m} = \langle m\rangle$, $\tilde{\bar{m}} = \bar{m}(\tilde{\rho},\tilde{m})$ and where the renormalized $\mathcal{F}^R_{\rm topo}$ is given by

$$\mathcal{F}^R_{\rm topo}\left(\tilde{m},\tilde{\rho},\tilde{\bar{m}}\right) = \mathcal{F}_{\rm topo}\left(\tilde{m},\tilde{\rho},\tilde{\bar{m}}\right) + \tilde{m}\,\frac{2\sigma}{k}\,g\left(\beta,\frac{\Gamma k}{v\tilde{\rho}},\frac{\Gamma D}{v^2}\right) + \mathcal{O}(\tilde{m}^2\sigma) + \mathcal{O}(\sigma^{\frac{3}{2}}) \tag{3.82}$$

with g a positive function whose expression is provided as an integral in (B.135).

Importantly, the linear term in the aligning dynamics has again become density-dependent, hence inducing a phase-separation at the onset of order. This is confirmed by numerical simulations of (3.78) and (3.79), which again reveal the existence of inhomogeneous propagating bands in Fig. 3.6. Our results thus also predict a fluctuation-induced first-order transition to collective motion for k-nearest neighbours alignment.

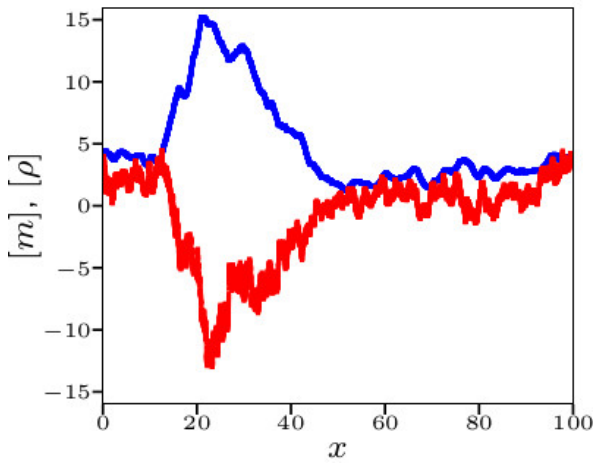

Figure 3.6 – Snapshot of a numerical integration of (3.78) and (3.79). The magnetization (red) and the density (blue) fields show a dense polar band propagating in a disordered gas. Parameters: $D = \Gamma = v = 1$, $k = 5$, $\rho_0 = 5$, $L = 100$, $\beta = 1.1$, $dx = 0.01$, $dt = 0.01$, $\sigma = 0.4$. Figure adapted from [66].

3.5.2 Microscopic simulations of topological models

We have shown in section 3.5.1 that an AIM endowed with k-nearest neighbours aligning interactions should also exhibit a first-order transition to collective motion. In this section, we test this prediction against microscopic simulations of this topological flocking

model. We consider an off-lattice topological Active Ising Model in which N particles move in an $L_x \times L_y$ domain with periodic boundary conditions. Each particle carries a spin $s_i = \pm 1$ and evolves according to the Langevin dynamics

$$\dot{\mathbf{r}}_i = s_i \, v \, \mathbf{e}_x + \sqrt{2D}\boldsymbol{\eta}_i \, , \tag{3.83}$$

where v_0 sets the self-propulsion speed, $\mathbf{e}_x$ is the unitary vector along the x direction, and D sets the strength of the unit-variance Gaussian white noise $\boldsymbol{\eta}_i$. Spins flip from s_i to $-s_i$ with rates $W(s_i)$ given by

$$W(s_i) = \Gamma e^{-\beta s_i \bar{m}_i}, \quad \text{with} \quad \bar{m}_i = \frac{1}{k} \sum_{j \in \mathcal{N}_i} s_j \, , \tag{3.84}$$

where $\mathcal{N}_i$ is the set of the k-nearest neighbours of particle i and $\bar{m}_i$ is their average magnetization. Note that, by construction, a mean-field treatment of the aligning dynamics (3.84) indeed leads to (3.76) and would predict a continuous transition. On the contrary, in agreement with our predictions, this model exhibits a first order transition to collective motion, akin to a liquid-gas phase separation: the onset of order at $\beta \gtrsim \beta_c(\rho_0)$ occurs through the emergence of an ordered propagating band (see Fig. 3.7). Unlike the mean-field critical temperature, the boundaries of the coexistence region show a clear dependence on the mean density ρ_0.

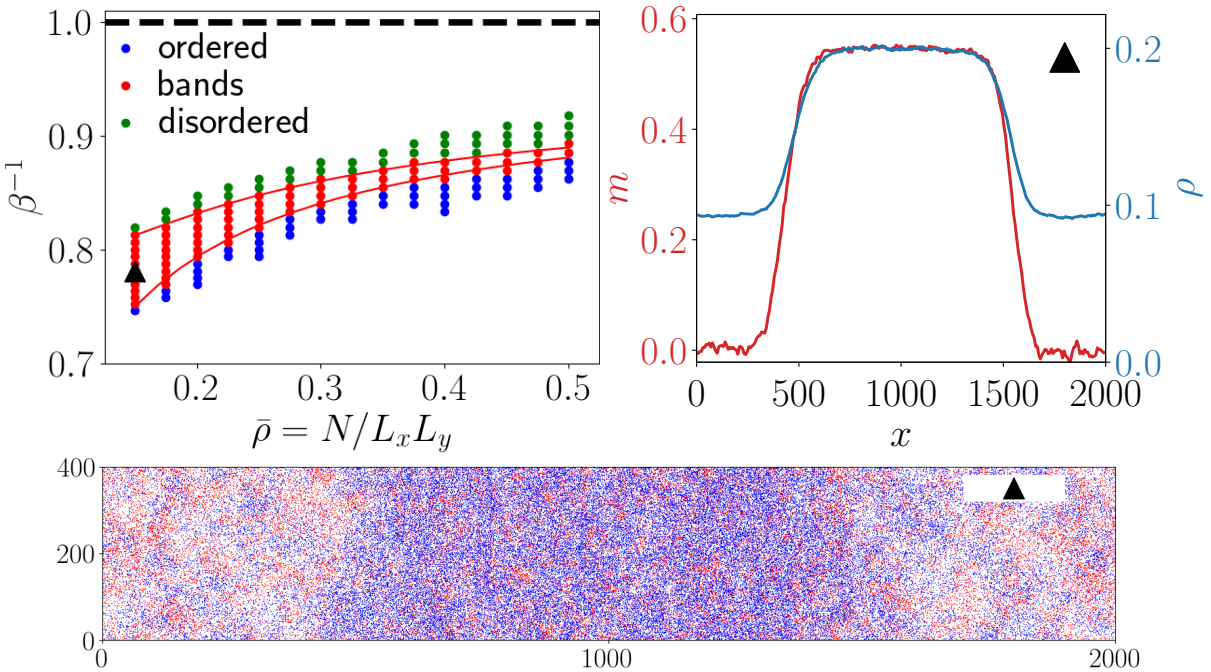

Figure 3.7 – **Top Left:** Phase diagram of the microscopic topological model defined in Eqs. (3.83) and (3.84). The homogeneous ordered (blue) and disordered (green) regions are separated by a coexistence phase (red). The mean-field critical temperature is $\beta = 1$ (dashed-lined). The red lines are guide to the eyes which show how the transitions shift as the mean density varies. **Bottom:** Snapshot of a propagating band corresponding to the black triangle in the phase diagram. Blue and red particles correspond to positive and negative spin respectively. The corresponding density and magnetization fields, averaged over y and time, are shown in the top-right panel. Parameters: $D = 8$, $L_y = 400$, $L_x = 2000$, $k = 3$, $\Gamma = 0.5$, $v = 0.9$. Figure adapted from [66].

3.6 Generalization to a broad class of aligning interactions

In flocking models, particles generically align with a local field $\bar{m}(x)$ which can be constructed in different ways. For instance, it can follow metric rules, be built on the k-nearest neighbours, or derived from a Voronoi tessellation.

While we provided a topological field theory consistent with the k-nearest-neighbours alignment rule in section 3.5.1, the question as to whether our results extend to other type of topological models remains open. In this section, we consider a more general case where $\bar{m}$ is an intensive field taking the form of an unspecified functional of ρ and m given by

$$\bar{m}(x) = \mathcal{G}(x, [\rho, m]) \, . \tag{3.85}$$

Using scalings and dimensional arguments, we show that, without having to specify $\mathcal{G}$, our methodology developed in 3.4 and 3.5 suggests a density-dependent renormalization of the linear Landau term. This result hints at a discontinuous emergence of collective motion for very generic functional $\mathcal{G}$.

As an example, $\mathcal{G}$ defined in (3.85) may encompass the case of k-nearest neighbours interactions described in (3.75). In this case:

$$\mathcal{G}(x, [\rho, m]) = \int_{x-y(x)}^{x+y(x)} \frac{m(z)}{k} dz; \quad \text{with} \quad k = \int_{x-y(x)}^{x+y(x)} \rho(z) dz \, . \tag{3.86}$$

The starting point of our analysis is the stochastic evolution for ρ and m given in (3.78)-(3.79) that we recall here

$$\partial_t \rho = D\partial_{xx}\rho - v\partial_x m \, , \qquad \partial_t m = D\partial_{xx} m - v\partial_x \rho - \mathcal{F}_{\text{topo}}(m, \rho, \bar{m}) + \sqrt{2\sigma\rho}\, \eta \, , \tag{3.87}$$

where $\mathcal{F}_{\text{topo}}(m, \rho, \bar{m}) = \Gamma(2m - 2\rho\beta\bar{m} - \frac{\rho\beta^3}{3}\bar{m}^3 + \beta^2 m\bar{m}^2)$, $\bar{m} = \mathcal{G}(x, [\rho, m])$ and η is a Gaussian white noise such that $\langle \eta(x,t)\eta(x',t')\rangle = \delta(t-t')\delta(x-x')$. As described in section 3.4, the mean-field approximation for the dynamics of $\tilde{\rho} = \langle \rho \rangle$ and $\tilde{m} = \langle m \rangle$ must be corrected by an additional term $\Delta\mathcal{F}_{\text{topo}}$ due to the noise:

$$\partial_t \tilde{\rho} = D\partial_{xx}\tilde{\rho} - v\partial_x \tilde{m} \, , \qquad \partial_t \tilde{m} = D\partial_{xx}\tilde{m} - v\partial_x \tilde{\rho} - \mathcal{F}_{\text{topo}}(\tilde{m}, \tilde{\rho}, \tilde{\bar{m}}) - \sigma\Delta\mathcal{F}_{\text{topo}} \, . \tag{3.88}$$

As shown in appendix B.4, we can use scaling arguments and dimensional analysis in the renormalization procedure to determine the generic dependency of $\Delta\mathcal{F}_{\text{topo}}$ on the parameters of the model. To leading order in σ, we obtain

$$\Delta\mathcal{F}_{\text{topo}} = \tilde{m}\, \bar{\mathcal{F}}\left(\frac{\Gamma D}{v^2}, \frac{\Gamma}{v\tilde{\rho}}, \beta\right) + \mathcal{O}(\tilde{m}^2) \, , \tag{3.89}$$

where $\bar{\mathcal{F}}$ is a dimensionless function depending on the specifities of the aliging functional $\mathcal{G}$. For generic models, (3.89) shows that fluctuations lead to a correction of the linear Landau term that depends on the local density $\tilde{\rho}$: we cannot rule out such a dependency. This result suggests that the vast majority of flocking models will exhibit a phase-separation at the onset of flocking. Especially, a broad class of topological models should exhibit a fluctuation-induced first-order transition.

It is interesting to ask whether one can find a case, within this formalism, in which the dependency of $\bar{\mathcal{F}}$ on the density cancels out. This can indeed happen when considering a fully-connected version of the topological AIM in which

$$\bar{m} = \frac{\int_0^L m(z)dz}{N}; \qquad \text{where} \qquad N = \int_0^L \rho(z)dz \; . \tag{3.90}$$

In this case, we show in appendix B.5 that, to leading order in σ, $\Delta\mathcal{F}_{\text{topo}}$ reads

$$\Delta\mathcal{F}_{\text{topo}} = \frac{\tilde{m}}{N}\left(\frac{\beta^2}{2} + \frac{\beta^2}{1-\beta}\right) + \mathcal{O}(\tilde{m}^2) \; . \tag{3.91}$$

Comparing (3.91) with (3.89), we remark that $\bar{\mathcal{F}}$ does not depend on $\Gamma D/v^2$ nor on $\Gamma/(v\tilde{\rho})$ for the fully connected AIM. For this specific kind of alignment, fluctuations leads to a density-independent correction of the linear Landau term and, consistently with the results of [137], renormalization points toward a continuous onset of collective motion.

3.7 Generalization to a mean-field description of the Vicsek model with Voronoi-based aligning interactions

In this section, we demonstrate that the scenario of a fluctuation-induced first-order transition applies to a broad class of dynamics and especially to Toner-Tu-like equations for flying spins. To this aim, we consider the evolution of the density and velocity fields derived in [128] for a Vicsek model with Voronoi alignment and show that it is unstable with respect to the addition of fluctuations. We now report the topological hydrodynamics used in [128]

$$\partial_t\rho + \nabla\cdot\mathbf{w} = 0 \tag{3.92}$$

$$\partial_t\mathbf{w} + \frac{\lambda}{\rho}(\mathbf{w}\cdot\nabla)\mathbf{w} = -\frac{1}{2}\nabla\rho + \frac{\kappa}{2\rho}\nabla\mathbf{w}^2 + \left(\alpha - \frac{\gamma}{\rho^2}\mathbf{w}^2\right)\mathbf{w} + D\nabla^2\mathbf{w} - \frac{\kappa}{\rho}(\nabla\cdot\mathbf{w})\mathbf{w} \; . \tag{3.93}$$

To keep the derivation tractable, we focus on a simplified one-dimensional version of (3.92)-(3.93) where $\mathbf{W}$ becomes a scalar. In this case, $(\mathbf{W}\cdot\nabla)\mathbf{W} \propto (\nabla\cdot\mathbf{W})\mathbf{W} \propto \nabla\mathbf{W}^2 \propto W\partial_x W$ and we obtain

$$\partial_t\rho + \partial_x W = 0 \tag{3.94}$$

$$\partial_t W + \frac{\lambda}{\rho}W\partial_x W = -\frac{v^2}{2}\partial_x\rho + D\partial_{xx}W + \alpha W - \frac{\gamma}{\rho^2}W^3 \; , \tag{3.95}$$

where D, α, λ, γ as well as v are assumed to be density-independent. Note that, in (3.95), we have kept a self-propulsion speed v whereas in (3.93) the authors of [128] had set it to unity by using a proper rescaling of time and space. In order to perform a renormalization analysis of (3.94)-(3.95), we use this velocity v to define the field $\hat{W} = v^{-1}W$. In this new variable, the dynamics reads

$$\partial_t\rho + v\partial_x\hat{W} = 0 \tag{3.96}$$

$$\partial_t\hat{W} + \frac{\hat{\lambda}}{\rho}\hat{W}\partial_x\hat{W} = -\frac{v}{2}\partial_x\rho + D\partial_{xx}\hat{W} + \alpha\hat{W} - \frac{\hat{\gamma}}{\rho^2}\hat{W}^3 \; , \tag{3.97}$$

where $\hat{\lambda} = v\lambda$ and $\hat{\gamma} = v^2\gamma$. For clarity, we now drop the hat notation and consider the time-evolution

$$\partial_t \rho + v\partial_x W = 0 \tag{3.98}$$

$$\partial_t W + \frac{\lambda}{\rho} W \partial_x W = -\frac{v}{2}\partial_x \rho + D\partial_{xx} W + \alpha W - \frac{\gamma}{\rho^2} W^3 \,, \tag{3.99}$$

where ρ and W now have the same dimension. Consistently with the scheme developed in section 3.4, we endow the dynamics (3.98)-(3.99) with fluctuations. To stay as general as possible, we further add a conservative Gaussian white noise to the evolution of the density

$$\partial_t \rho + v\partial_x W = \partial_x \left(\sqrt{2\sigma\epsilon\rho}\, \eta_1 \right) \tag{3.100}$$

$$\partial_t W + \frac{\lambda}{\rho} W \partial_x W = -\frac{v}{2}\nabla \rho + D\partial_{xx} W + \alpha W - \frac{\gamma}{\rho^2} W^3 + \sqrt{2\sigma\rho}\, \eta_2 \,, \tag{3.101}$$

Following the derivation performed in section 3.4, and using assumptions similar to AI-AII, we show in Appendix B.6 that the averaged fields $\tilde{\rho} = \langle \rho \rangle$ and $\tilde{W} = \langle W \rangle$ are solutions, up to order σ, of the renormalized hydrodynamics

$$\partial_t \tilde{\rho} + v\partial_x \tilde{W} = 0 \tag{3.102}$$

$$\partial_t \tilde{W} + \frac{\hat{\lambda}}{\tilde{\rho}} \tilde{W} \partial_x \tilde{W} = -\frac{v}{2}\nabla \tilde{\rho} + D\partial_{xx} \tilde{W} + \hat{\alpha} \tilde{W} - \frac{\hat{\gamma}}{\tilde{\rho}^2} \tilde{W}^3 \,, \tag{3.103}$$

where $\hat{\alpha}$, $\hat{\gamma}$ and $\hat{\lambda}$ are the renormalized coefficients up to order σ. Focusing on $\hat{\alpha}$, we show in Appendix B.6 that

$$\hat{\alpha} = \alpha - \sigma \frac{3\gamma}{\tilde{\rho}} \frac{2D - \alpha\epsilon}{4D\sqrt{D|\alpha|}} \tag{3.104}$$

Interestingly, fluctuations have, once again, made α density-dependent through the renormalization process. From the linear stability analysis of section 3.1.3, we conclude that (3.102)-(3.103) are exhibiting a first-order emergence of collective motion. Similarly to the AIM's, the mean-field hydrodynamics (3.94)-(3.95) for the Vicsek Model with Voronoi alignment should thus undergoes a fluctuation-induced first-order transition.

3.8 Testing the order of the transition through the density-dependence of the critical temperature

Since the introduction of the Vicsek model, determining numerically the nature of the transition to collective motion has proven itself a difficult task [62]. Its weakly first-order nature indeed challenges standard methods: in finite systems, the variations of the order parameter as a function of control parameters (noise, density, etc.) often misleadlingly suggests a second order scenario [63, 64].

Our results suggest an easier alternative: measuring the dependency of the onset of order on the average density. We illustrate this method by contrasting our topological model (3.83)-(3.84) with simpler ones in which the aligning dynamics is disconnected from spatial positions, hence trivially ensuring that the transition remains continuous.

We once again consider N scalar spins moving in a $L_x \times L_y$ domain with periodic boundary conditions according to the Langevin equation (3.83), which we recall here

$$\dot{\mathbf{r}}_i = s_i \; v \; \mathbf{e}_x + \sqrt{2D} \; \boldsymbol{\eta}_i \; . \tag{3.105}$$

We focus on two different aligning dynamics for the spins. In the Random Alignment Model (RAM), the flipping rate $W(s_i)$ of the i-th spin is given by

$$W(s_i) = \Gamma e^{-\beta s_i \bar{m}_i}, \quad \text{where} \quad \bar{m}_i = \frac{1}{k} \sum_{j \in \mathcal{N}_i} s_j \; , \tag{3.106}$$

with $\mathcal{N}_i$ a set of k spins chosen at random at every time step.

In the Loyal Alignment Model (LAM), on the contrary, alignment occurs with the same set $\mathcal{N}_i$ of k neighbours throughout the simulations, irrespectively of the particles' positions. In our simulations, we chose $k = 4$ and assigned to each particle its nearest neighbours on an initial square lattice. As expected, simulations of both systems lead to continuous transitions, without the emergence of phase-separated profiles. Fig. 3.8 shows that the behaviours of the global magnetization as the temperature is varied are hard to distinguish between LAM, RAM and our model (3.83)-(3.84). Repeating these measurements at different densities however reveals a density-dependence of the onset of order in the latter case, but not in LAM & RAM. Measuring β_c as ρ_0 varies thus constitutes a simple and robust test to assess the nature of the transition.

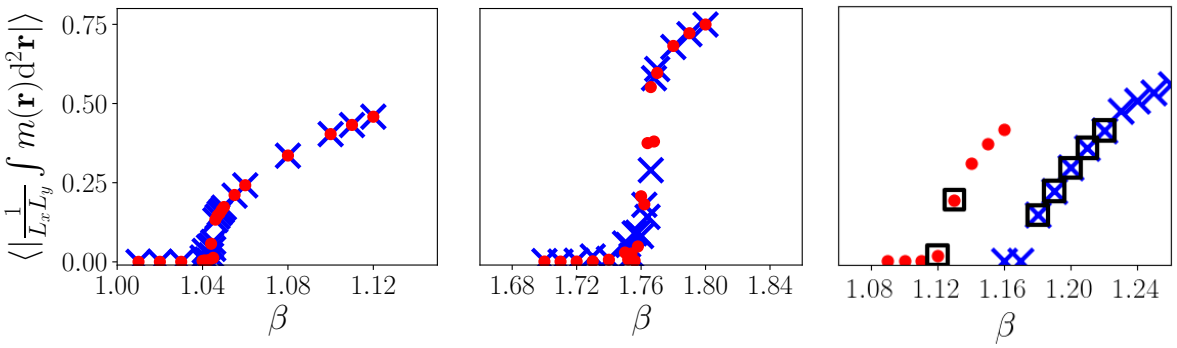

Figure 3.8 – Magnetization vs inverse temperature β for the RAM (left), the LAM (center), and the topological model (3.83)-(3.84) (right). Only the latter exhibits traveling bands (black squares). Blue crosses and red dots correspond to mean densities $\rho_0 = 0.25$ and $\rho_0 = 0.5$, respectively. Parameters: $L_x = 2000$, $L_y = 400$, $D = 8$, $v = 0.9$, $\Gamma = 0.5$, $k = 3$. For LAM, $k = 4$. Figure adapted from [66]

3.9 Conclusion

In this second chapter, I explained how fluctuations can turn a deceptive continuous transition at mean-field level into a phase-coexistence scenario in flocking models. I first reviewed why models of collective motion are sensitive to modifications of their linear Landau term α: as soon as α depends on the density, homogeneous solutions become unstable at onset of order. I then showed how noise generically dress α to make it density-dependent through a quasi-linear renormalization analysis.

In turn, this triggers the linear instability of the homogeneous ordered profile at the onset of collective motion. I have shown that such a mechanism applies independently of the specific underlying alignment, be it "metric" or "topological", and further generalizes to different mean-field hydrodynamics.

I illustrated our results with the microscopic simulations of an off-lattice topological Active Ising Model in which particles align with their k-nearest neighbours. For this specific model, I measured a clear dependency of the critical temperature on the density and located a coexistence region with phase-separated profiles in the phase diagram.

Finally, I compared the onset of flocking between models with different kind of alignment and showed that a measurement of the critical temperature as a function of the density could provide a robust evaluation of the order of the transition.

Having now reviewed the emergence of collective motion in detail, we turn to study how flocking physics can interplay with another active phase transition, namely Motility-Induced Phase Separation, to produce a novel phenomenology in dense assemblies of colloidal rollers.

4. Motility-Induced Phase Separation and flocks: an interplay at high density

Most flocking models focus on the two minimal ingredients needed to observe collective motion : self-propulsion and alignment between the agents. However, most physical systems are also submitted to other kind of interactions such as pairwise forces or external potentials.

For experimental assemblies of self-propelled particles, an important feature, which is not accounted for in the Vicsek model, might affect the dynamics: steric hindrance. Indeed, upon increasing the packing fraction, one expects the finite-size active particles to experience short range repulsive forces. In this chapter, I present recent results, obtained with the group of D. Bartolo, which show that such a repulsion leads to a novel phase transition between a polar flock and a dense arrested active solid in experimental assemblies of Quincke rollers: we dubbed this phenomena active solidification.

I start by briefly describing the experimental setup and previous results [28, 29] of the Bartolo group which explain why Quincke rollers are an experimental realization of the flying spins presented in section 3.1.1. As Motility-Induced Phase Separation (MIPS) will be frequently alluded to in this chapter, I dedicate a brief introductive section to this paradigmatic phenomenon in section 4.2. In section 4.3, I describe the experimental evidences of active solidification in dense assemblies of Quincke rollers and characterize the structure of the active solids as well as the order of the transition. In section 4.4, I show that active solidification can be phenomenologically described as a first-order scenario driven by Motility-Induced Phase Separation. Finally, in section 4.5, I introduce a microscopic model whose hydrodynamic equations can be constructed exactly, and which encompasses both the flocking transition and the active solidification. This approach confirms the ingredients sufficient for the emergence of active solidification and allows for probing a novel state yet to be observed in the experiments: the coexistence between travelling bands and an arrested solid.

4.1 Assemblies of colloidal rollers

This section is devoted to the experimental setup built in the Bartolo group that we have studied for elucidating active solidification in [79]. Note that all the experimental work was carried out by Delphine Geyer; this section does not aim at establishing a rigorous description of the setup but rather at giving a rough picture of the physics at play. The interested reader might refer to [28, 37, 79, 138] for a more exhaustive treatment.

In the experimental setup, colloidal beads of radius $a \sim 2.4\mu$m are confined in a racetrack of width $W \sim 1$mm, height $H \sim 220\mu$m and curvilinear length $L \sim 10$cm. The colloids are self-propelled thanks to an electrohydrodynamic phenomenon called the Quincke rotation [37, 138]. When an electric field $\mathbf{E}_0$ is applied to an insulated sphere immersed in a conducting fluid, charges accumulate at the liquid-sphere interface leading to a polarisation $\mathbf{p}$ which is anti parallel to $\mathbf{E}_0$ (see Fig. 4.1a). This configuration is mechanically unstable and the colloid tends to rotate to align $\mathbf{p}$ with $\mathbf{E}_0$. The ohmic current however tends to restore a dipole pointing downwards. Above a certain threshold,

these two effects balance to select an electric dipole that makes a constant angle with $\mathbf{E}_0$ and is accompanied by a rotation of the colloid at constant angular speed $\mathbf{\Omega}$ (see Fig. 4.1a). If the sphere sediments on the bottom electrod, this angular velocity will turn into a self-propulsion $\mathbf{v}$ thanks to the friction with the substrate. It is precisely this mechanism which is used by an isolated bead in the racetrack to roll along a random direction. The velocity v_0 acquired by the rollers through this Quincke mechanism scales as $\sqrt{E_0^2/E_Q^2 - 1}$. It can thus be tuned by varying the amplitude of the applied electric field $\mathbf{E}_0$ as shown in Fig. 4.1.

Alignment between the rollers' direction of motion is provided through both electrostatic and hydrodynamic interactions [28]. As colloids develop a surface charge through the Quincke phenomenon, they acquire a dipolar moment $\mathbf{p}$ whose projection $p_\parallel$ on the bottom electrod is colinear to the direction of their self-propulsion $\mathbf{v}$. A pair of rollers thus feel a dipole-dipole interaction $U \propto -\mathbf{p} \cdot \mathbf{p}'$ which promotes the alignment of their dipoles, and hence of their respective velocities.

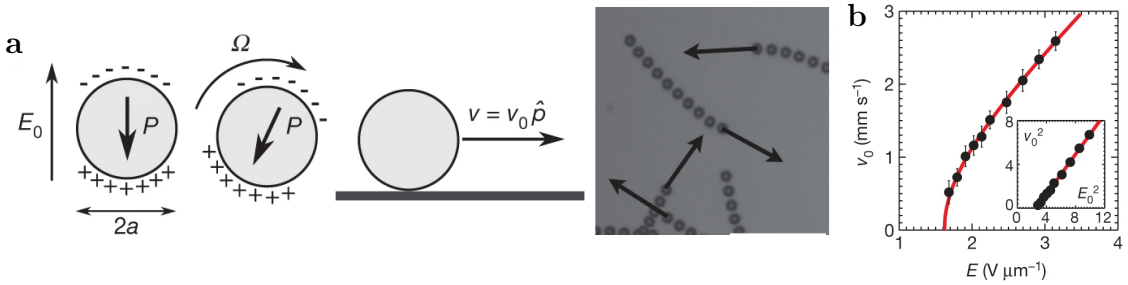

Figure 4.1 – **a.** Quincke rotation and self-propulsion mechanism of a colloid. Superposition of ten successive snapshots of self-propelled rollers. Time interval 5.6 ms. **b.** Roller velocity v_0 plotted against the field amplitude E_0. Inset, v_0^2 versus E_0^2. Figure adapted from [28].

Now that we have detailed the similarities between the Quincke rollers and the flying spins of the Vicsek Model, let us describe the experimental phenomenology observed in the racetrack. At low packing fraction ϕ_0, the rollers exhibit a disordered gaseous phase: they move independently in random directions. On the contrary, at high packing fraction, when $\phi_0 > \phi_c$, the colloidal assembly self-organize into a polar liquid state where all the rollers coherently cruise in the same direction. The order parameter $\Pi_0 = v_0^{-1}\langle \mathbf{v} \rangle$ quantifying this transition is close to one in the flocking phase while it vanishes in the isotropic gaseous phase (see Fig. 4.2). For packing fractions $\phi_0 \sim \phi_c$, the system phase-separates to form a single macroscopic band propagating at constant velocity through a disordered gaseous phase. Close-ups of the racetrack in the three differents phases are displayed on Fig. 4.2.

The onset of flocking observed in assemblies of Quincke rollers thus shares the same phase-separation scenario as the Vicsek Model near the critical temperature. Though we only detailed one experimental setup in this introduction, there exists other experiments closely related to the Vicsek Model such as shaken asymmetric grains [34] or Janus rollers [31,139]. Consistently with Vicsek phenomenology, they all confirm a discontinuous flocking transition with phase-separation. Having detailed the experimental setup that we will study in section 4.3 at high packing fraction, we now briefly introduce Motility-Induced Phase Separation for a futur use in section 4.4.

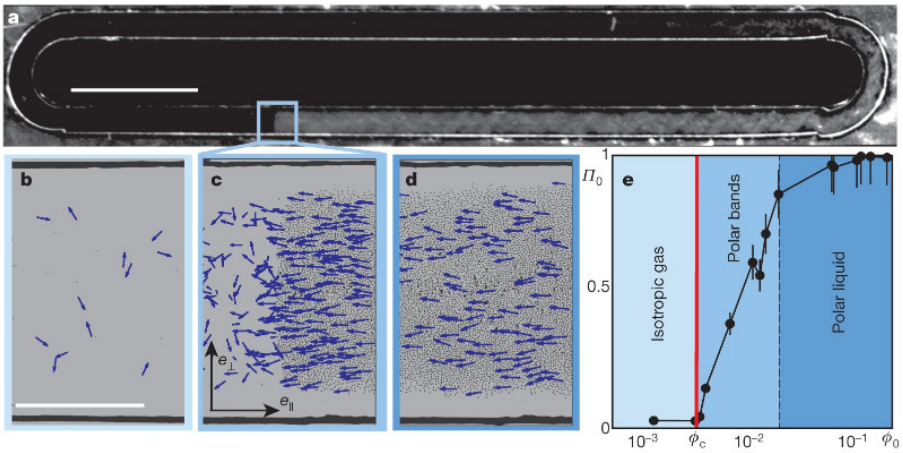

Figure 4.2 – **a** Snapshot of Quincke rollers spontaneously forming a macroscopic band revolving around the racetrack. $E_0/E_Q = 1.39$, $\phi_0 = 10^{-2}$, scale bar = 5mm. **b-d** Close-up. The arrows correspond to the roller displacement between two time-frame separated by 5.10^{-3} sec. **b** Isotropic gas, $\phi_0 = 6.10^{-4}$. **c** Propagating bands, $\phi_0 = 10^{-2}$. **d** Homogeneous polar liquid, $\phi_0 = 18.10^{-2}$. Scale bar = 500μm. **e** Norm of the order parameter Π_0 as a function of the packing fraction ϕ_0. Collective motion occurs as soon ϕ_0 exceeds $\phi_c = 3.10^{-3}$. Figure adapted from [28].

4.2 Introduction to Motility-Induced Phase Separation (MIPS)

In this section, we present the physics of Motility-Induced Phase Separation (MIPS). MIPS is a common transition occurring in assemblies of interacting self-propelled particles, be it Active Brownian Particles (ABPs) [67], Run and Tumble Particles (RTPs) [140] or AOUPs [57]. It leads to the formation of macroscopic, arrested clusters of particles which coexist with a dilute gas phase. MIPS resembles closely an equilibrium phase separation with interesting differences such as bubbly phase separation [141] or entropy production at the interfaces [57, 142]. These particularities will not be discussed in this manuscript. The mechanism behind MIPS stems from the interplay between two ingredients

MI The accumulation of active particles where the self-propulsion is small, as $\rho \sim 1/v(\mathbf{r})$, with $v(\mathbf{r})$ being the position-dependent speed of the active particles [68,140]. Particles spend more time where their motility is small, and so it is more likely to find them in such places [143].

MII A self-propulsion v decreasing with the local density $\rho(\mathbf{r})$, *i.e.* $v'(\rho(\mathbf{r})) < 0$. This slowing down of motility may arise from a variety of interactions between the particles, from crowding and repulsive forces [144, 145], to quorum-sensing [22].

When MI-MII are verified, particles slow down in denser regions (MII), which in turns triggers an accumulation making these regions even denser (MI). This feedback loop generates a linear instability leading to the formation of dense and arrested clusters as shown in Fig. 4.3. The steady-state attained at non-linear level has been the topic of many articles, and the interested reader might refer to [69] for recent accounts.

Let us now show the first point MI for an ABP with spatially varying self-propulsion in 2D. The position $\mathbf{r}$ of the particle and the orientational angle θ of its speed follow the

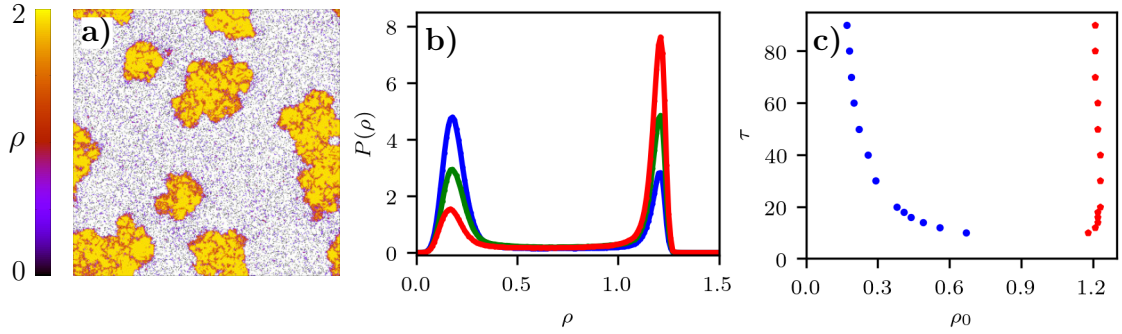

Figure 4.3 – Simulations of N AOUPs evolving with dynamics (2.78)-(2.79) and interacting via a pairwise radial potential $\Phi(r) = \epsilon\left[(r_0/r)^{12} - (r_0/r)^6\right] + \epsilon/4$ in a 400x400 domain with periodic boundary conditions. Parameters: $D = 10$, $\epsilon = r_0 = 1$. **a)** snapshot taken after a time $t = 10\,000$ shows the occurence of motility-induced phase separation for $\tau = 90$. The average densities are $\rho_0 = 0.5$ and $\rho_0 = 0.9$, respectively. Varying the overall density alters the size of the dense and dilute phases, but leaves their respective density unchanged. This can be seen from panel **b)**, which presents histograms of the local density measured in boxes of size 10x10. The three curves correspond to $\rho_0 = 0.50, 0.70, 0.90$. Finally, the phase diagram shown in panel **c)** is obtained by measuring the densities of the dilute and dense phases in simulations with an average density 0.9 and different values of τ. The densities are estimated from the maxima of histograms obtained as in **b)**. Figure adapted from [57].

Langevin dynamics

$$\dot{\mathbf{r}}(t) = v(\mathbf{r}(t))\mathbf{u}(\theta(t)), \qquad \dot{\theta}(t) = \sqrt{2D_\theta}\,\eta(t)\,, \tag{4.1}$$

where η is a Gaussian white noise, D_θ is the angular diffusion and $\mathbf{u}(\theta)$ is the unitary vector with orientation θ. The corresponding Fokker-Planck equation for the probability distribution $P(\mathbf{r}, \theta)$ reads

$$\partial_t P(\mathbf{r}, \theta) = -\mathbf{u}(\theta) \cdot \boldsymbol{\nabla}\left[v(\mathbf{r})P(\mathbf{r}, \theta)\right] + D_\theta \partial_{\theta\theta} P(\mathbf{r}, \theta)\,. \tag{4.2}$$

While we could directly conclude here as $P(\mathbf{r}, \theta) \propto 1/v(\mathbf{r})$ is a stationary solution of (4.2), we choose an alternative route, more easily generalized to the interacting case. We define the density $\rho(\mathbf{r}, t)$ and magnetization $\mathbf{w}(\mathbf{r}, t)$ as the first and second moment of the probability distribution: $\rho(\mathbf{r}, t) = \int P(\mathbf{r}, \theta) d\theta$ and $\mathbf{w}(\mathbf{r}, t) = \int \mathbf{u}(\theta) P(\mathbf{r}, \theta) d\theta$. Integrating (4.2) over θ then gives the conservation equation

$$\partial_t \rho(\mathbf{r}, t) + \boldsymbol{\nabla} \cdot \left[v(\mathbf{r})\mathbf{w}(\mathbf{r}, t)\right] = 0\,, \tag{4.3}$$

while multiplying (4.2) by $\mathbf{u}(\theta)$ and integrating over θ yields

$$\partial_t \mathbf{w}(\mathbf{r}, t) = -D_\theta \mathbf{w}(\mathbf{r}, t) - \frac{1}{2}\boldsymbol{\nabla}\left[v(\mathbf{r})\rho(\mathbf{r}, t)\right] + \mathbf{B}\,. \tag{4.4}$$

Note that, in $\mathbf{B}$, we hide terms of higher moments in θ depending on $\int \cos(2\theta) P(\mathbf{r}, \theta) d\theta$ and $\int \sin(2\theta) P(\mathbf{r}, \theta) d\theta$. Indeed, we will neglect these terms as we truncate the hierarchy of equations here, keeping only ρ and $\mathbf{w}$ as the hydrodynamic fields. We thus obtain

$$\partial_t \mathbf{w}(\mathbf{r}, t) = -D_\theta \mathbf{w}(\mathbf{r}, t) - \frac{1}{2}\boldsymbol{\nabla}\left[v(\mathbf{r})\rho(\mathbf{r}, t)\right] \tag{4.5}$$

Noting that the polarization $\mathbf{w}$ relaxes on a time scale $\tau_{\mathbf{w}} = D_\theta^{-1}$ much smaller than the relaxation time of the density $\tau_\rho \propto q^{-1}$ at low wave-vector q, we can enslave $\mathbf{w}$ as

$$\mathbf{w}(\mathbf{r},t) = -\frac{1}{2D_\theta}\boldsymbol{\nabla}\left[v(\mathbf{r})\rho(\mathbf{r},t)\right] \ . \tag{4.6}$$

Injecting the above equation into the mass conservation finally yields a closed equation for the density $\rho(\mathbf{r},t)$

$$\partial_t\rho(\mathbf{r},t) = \frac{1}{2D_\theta}\boldsymbol{\nabla}\cdot\Big[v(\mathbf{r})\boldsymbol{\nabla}\left(v(\mathbf{r})\rho(\mathbf{r},t)\right)\Big] \tag{4.7}$$

We note that $\rho(\mathbf{r}) = 1/v(\mathbf{r})$ is a solution of (4.7), which demonstrate the accumulation of ABPs in slower regions.

Let us now show how MII may emerge from purely repulsive forces for ABPs in 2D. For clarity, we consider a pairwise repulsive potential $U(\mathbf{r})$ with a finite interaction range σ. The dynamics (4.2) is thus modified according to

$$\dot{\mathbf{r}}_i(t) = v_0\mathbf{u}(\theta_i(t)) - \sum_{j\in\mathcal{N}_i}\boldsymbol{\nabla}U(\mathbf{r}_j(t)-\mathbf{r}_i(t)), \qquad \dot{\theta}_i(t) = \sqrt{2D_\theta}\,\eta_i(t) \ , \tag{4.8}$$

where $\mathcal{N}_i$ is the set of particles in the disk $\mathcal{D}_i$ of radius σ centered at $\mathbf{r}_i$. The velocity $\dot{\mathbf{r}}_i$ of (4.8) can be decomposed into parallel and orthogonal components with respect to $\mathbf{u}(\theta)$

$$\dot{\mathbf{r}}_i = v\mathbf{u}(\theta_i) - \sum_{j\in\mathcal{N}_i}\Big(\mathbf{u}(\theta_i)\cdot\boldsymbol{\nabla}U(\mathbf{r}_j-\mathbf{r}_i)\Big)\mathbf{u}(\theta_i) - \sum_{j\in\mathcal{N}_i}\Big(\mathbf{u}(\theta_i+\tfrac{\pi}{2})\cdot\boldsymbol{\nabla}U(\mathbf{r}_j-\mathbf{r}_i)\Big)\,\mathbf{u}(\theta_i+\tfrac{\pi}{2}) \ . \tag{4.9}$$

We now average (4.9) over all the remaining degrees of freedom r_j with $j \neq i$. Because the dynamics of the θ_i's is decoupled, the line defined by the unitary vector $\mathbf{u}(\theta_i)$ is an axis of symmetry which cuts in two halves the disk $\mathcal{D}_i$. As the distribution of particles is similar in these two half-disks, the component of the velocity orthogonal to $\mathbf{u}(\theta)$ vanishes and the third term on the right hand side of (4.9) is zero on average. Once averaged (4.9), we thus obtain the mean-field formula

$$\langle\dot{\mathbf{r}}_i\rangle = v_{\text{eff}}(\rho)\mathbf{u}(\theta_i) \ , \tag{4.10}$$

where the effective velocity $v_{\text{eff}}(\rho)$ reads

$$v_{\text{eff}}(\rho) = v - \sum_{j\in\mathcal{N}_i}\langle\mathbf{u}(\theta_i)\cdot\boldsymbol{\nabla}U(\mathbf{r}_j-\mathbf{r}_i)\rangle \ . \tag{4.11}$$

Note that, on the opposite, no symmetry arguments grants that the densities in the two half-disks obtained when cutting $\mathcal{D}_i$ along the axis $\mathbf{u}(\theta+\frac{\pi}{2})$ are similar. In fact, as shown in [146], it is more probable to find a neighbouring particle in the direction $\mathbf{u}(\theta)$ than in the opposite direction $-\mathbf{u}(\theta)$. This is why $\langle\mathbf{u}(\theta_i)\cdot\boldsymbol{\nabla}U(\mathbf{r}_j-\mathbf{r}_i)\rangle$ is positive and contributes to a density-dependent decrease of the self-propulsion. However, determining its precise analytical form as a function of ρ from the dynamics (4.8) is a difficult task which has been carried out only in specific conditions [147, 148].

We now mix the two ingredients MI and MII together to shed light on the instability behind MIPS. To this aim, in addition to the crude mean-field approximation leading

from (4.8) to (4.10), we make an adiabatic approximation and replace $v(\mathbf{r})$ in (4.7) by $v(\rho(\mathbf{r},t))$:

$$\partial_t \rho(\mathbf{r},t) = \frac{1}{2D_\theta} \boldsymbol{\nabla} \cdot \left[v(\rho(\mathbf{r},t)) \boldsymbol{\nabla} \left(v(\rho(\mathbf{r},t)) \rho(\mathbf{r},t) \right) \right] . \tag{4.12}$$

While it is possible to derive (4.12) from the dynamics (4.10), such a computation lies beyond the scope of this manuscript and can already be found in the literature [47,68,149].

We now analyze the linear stability of (4.12) around a homogeneous solution ρ_0 and introduce the perturbation $\delta\rho(\mathbf{r},t) = \rho(\mathbf{r},t) - \rho_0$. To first order in $\delta\rho$, we obtain the linearized dynamics

$$\partial_t \delta\rho(\mathbf{r},t) = \frac{v(\rho_0)}{2D_\theta} \left[v(\rho_0) + v'(\rho_0)\rho_0 \right] \boldsymbol{\nabla}^2 \delta\rho(\mathbf{r},t) . \tag{4.13}$$

As $v(\rho_0)$ and D_θ are positive, this dynamics is unstable as soon as

$$v(\rho_0) + v'(\rho_0)\rho_0 < 0, \tag{4.14}$$

which is nothing else than the linear instability criterion for the onset of MIPS [67]. Having introduced Motility-Induced Phase Separation, we now turn back to the experimental assemblies of Quincke rollers described in section 4.1 and study their behaviour at high density, where repulsion comes into play.

4.3 Solidification of flocks in assemblies of Quincke rollers

It is possible to ramp up the packing fraction ϕ_0 of colloids within the racetrack of the experiment presented in section 4.1. By doing so, we aim at probing a regime where short-range repulsion between the rollers comes into play.

When ϕ_0 exceeds $\phi_S \simeq 0.55$, D. Geyer and D. Bartolo observed that collective motion is locally suppressed, which leads to a dynamical arrest that cannot be explained using standard flocking models like the Vicsek model. In this high density regime, rollers stop their collective motion and jam as illustrated in Fig. 4.4. The traffic jams are active solids that continuously melt at one end while growing at the other end. This lively dynamics hence preserves the shape and length L_S of the solid which propagates at constant speed upstream the polar-liquid flow, as shown in the kymograph of Fig. 4.5a. Further increasing ϕ_0, the solid region grows and eventually spans the entire system. The phase diagram of Quincke rollers assemblies presented in Fig. 4.2 must thus be updated according to Fig. 4.4 to include this new jamming phase transition occuring at high packing fraction. We now characterize the structure of these traffic jams as well as the order of the transition leading to active solidfication.

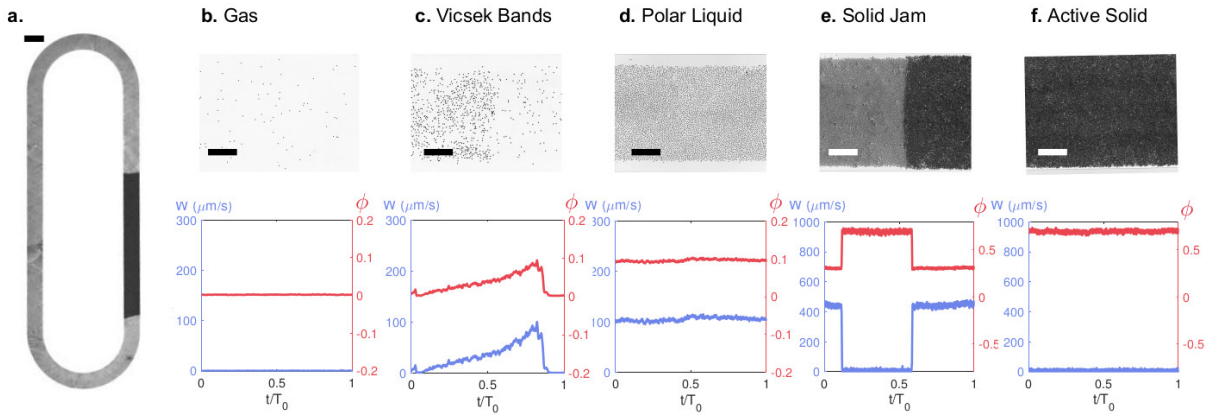

Figure 4.4 – The dynamical phases of Quincke rollers. a. Picture of a microfluidic racetrack where $\sim 3{\times}10^6$ Quincke rollers interact. An active solid (dark grey) propagates though a polar liquid (light grey). Scale bar: 2 mm. **b–f.** Top panel: close-up pictures of Quincke rollers in the racetrack. Scale bars: 250 μm. Bottom panel: longitudinal component of the particle current W and density plotted as a function of a normalized time. Both W and ϕ are averaged over an observation window of size $56\,\mu\text{m} \times 1120\,\mu\text{m}$. T_0 is arbitrarily chosen to be the time taken by an active solid to circle around the racetrack. **b.** Gas phase ($\phi_0 = 0.002$). **c.** Coexistence between a disordered gas and a denser polar band ($\phi_0 = 0.033$). **d.** Polar-liquid phase ($\phi_0 = 0.096$). **e.** Coexistence between a polar liquid and an amorphous active solid ($\phi_0 = 0.49$). **f.** Homogeneous active solid phase ($\phi_0 = 0.70$). Figure adapted from [79].

4.3.1 Characterization of active solids

Active solids form an amorphous phase. The pair correlation function shown in Fig. 4.5b and 4.5c indicates that they are more spatially ordered than the polar liquid they coexist with, but do not display any sign of long-range translational order. We note that the location of the first peak of $g(r)$ drops from a value that is larger than a colloid diameter in the liquid to one particle diameter in the solid phase. The large value of the typical interparticle distance in the polar liquid phase reflects the repulsive dipolar interactions acting on neighbouring Quincke rollers [28, 150–152]. But the most striking difference between the two phases is dynamical. While the rollers continuously move at constant speed in the polar liquid, they spend most of their time at rest in the solid phase, thereby suppressing any form of long-range orientational order of their velocity as shown in Fig. 4.5d and 4.5e.

We stress that the onset of active solidification corresponds to an area fraction $\phi_S \simeq 0.55$ which is much smaller than the random close packing limit ($\phi_0 = 0.84$) and than the crystalization point of self-propelled hard disks ($\phi_0 \sim 0.71$) reported in [153]. This marked difference hints towards different physics which we characterize and elucidate in the sections below.

As a last experimental result, we show in Fig. 4.9a how the roller speed $\nu_0(\phi)$ varies with the local density $\phi(\mathbf{r}, t)$ evaluated in square regions of size $12a \sim 29\,\mu$m. These measurements correspond to an experiment where a solid jam coexists with a homogeneous polar liquid. $\nu_0(\phi)$ hardly varies at the smallest densities and sharply drops towards $\nu_0(\phi) = 0$ when the local fraction $\phi(\mathbf{r}, t)$ exceeds ~ 0.35. Although the precise microscopic origin of this abrupt slowing down is difficult to identify, we expect near-field hydrodynamic interactions to frustrate self-propulsion.

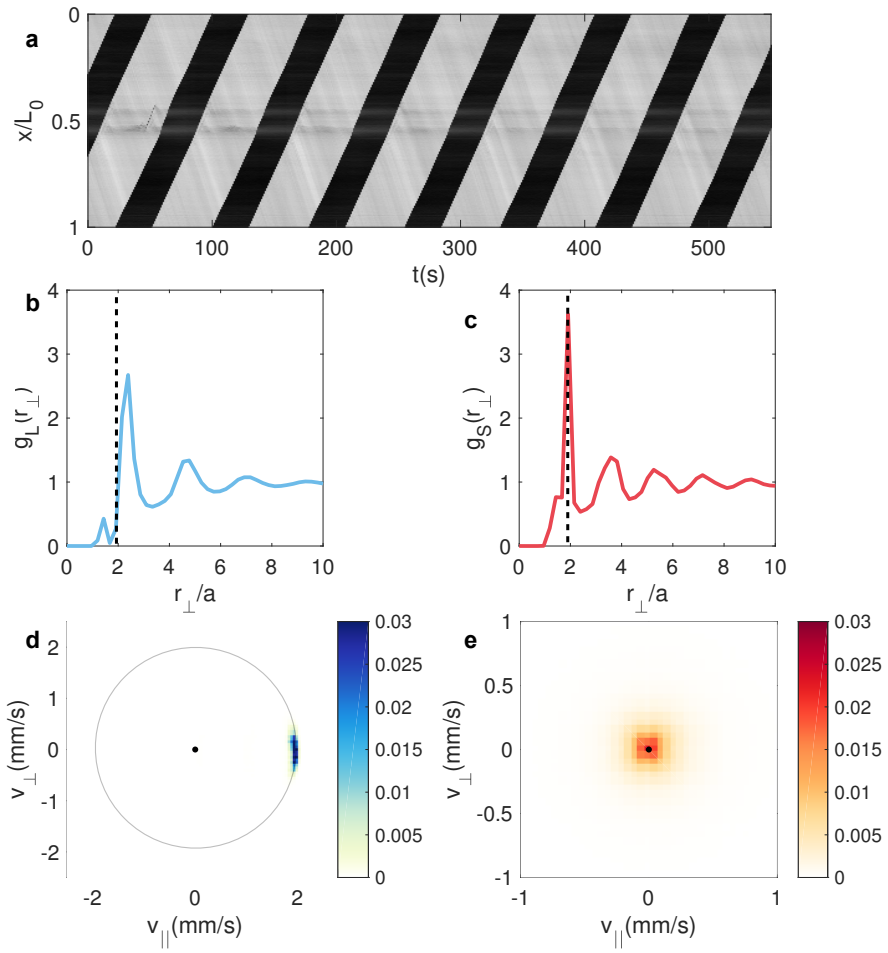

Figure 4.5 – Structure and dynamics of active jams. a. Kymograph of an active solid (dark region) propagating backward at constant speed in a homogeneous polar liquid (light region). **b and c.** Pair-correlation functions measured in the polar liquid (g_{L}) and in the coexisting active-solid phase (g_{S}) as a function of $r_\perp$, the direction transverse to the mean polar-liquid flow. The dashed lines indicate the distance corresponding to one particle diameter. **d**. Probability density functions of the roller velocities in the polar liquid region. The distribution is peaked around $\nu_0\hat{\mathbf{x}}_\parallel$, where $\hat{\mathbf{x}}_\parallel$ is the vector tangent to the racetrack. **e**. Probability density functions of the roller velocities in the active jam region. **b**, **c**, **d**, and **e**: average area fraction $\phi_0 = 0.58$. Figure adapted from [79].

4.3.2 Characterization of the transition

We now establish that the formation of active solids occurs according to a first order phase-separation scenario. Firstly, Fig. 4.6a and b indicate that, upon increasing ϕ_0, the extent of the solid phase has a lower bound: starting from a homogeneous polar liquid, the solid length L_{S} discontinuously jumps to a finite value before increasing linearly with $\phi_0 - \phi_L^{\mathrm{b}}$, where $\phi_L^{\mathrm{b}} = 0.55$, see Fig. 4.6b. The smallest solid observed in a stationary state is as large as $L_{\mathrm{S}} \sim 1.4\,\mathrm{cm}$. Smaller transient solid jams do form at local heterogeneities, but they merely propagate over a finite distance before rapidly melting. This observation suggests the existence of a critical nucleation radius for the solid phase.

Secondly, while the packing fraction of a polar liquid obviously increases with ϕ_0, its value saturates as it coexists with an active solid as shown in Fig. 4.6c. At coexistence,

the local packing fractions in the bulk of the liquid and solid phases are independent of the average fraction ϕ_0: $\phi_S^b = 0.75$ and $\phi_L^b = 0.55$, which again supports a phase-separation scenario. Note that ϕ_L^b is hardly distinguishable from the packing fraction at the onset of solidification ϕ_S in the experiments, because the system size is much larger than the size of the nucleated active solids. Increasing ϕ_0 leaves the inner structure of both phases unchanged and solely increases the fraction of solid L_S/L_0 in the racetrack. We find that, as in equilibrium phase separation, the length of the solid region is accurately predicted using a lever rule constructed from the stationary bulk densities ϕ_S^b and ϕ_L^b as exemplified in Fig. 4.6b.

Thirdly, we stress that when multiple jams nucleate in the device, they propagate nearly at the same speed. Therefore, they cannot catch up and coalesce. The system in fact reaches a stationary state thanks to a slow coarsening dynamics illustrated in Fig. 4.6d where we show the temporal evolution of the length of two macroscopic active solids (red symbols) and of the overall solid fraction (dark line). This experiment corresponds to a situation where the smallest solid jam grows at the expense of the larger. The converse situation is also possible and in both cases coarsening operates leaving the overall fraction of solid constant. All experiments end with complete phase separation: a single macroscopic active solid coexists with a single active liquid phase. The final state of the system is therefore uniquely determined by two macroscopic control parameters: the average packing fraction ϕ_0 and the magnitude E_0 of the electric field used to power the rollers.

Finally, the most compelling argument in favour of a genuine first-order phase separation is the bistability of the two phases. Fig. 4.6b shows that, at the onset of solidification, depending on the (uncontrolled) initial conditions, the system is either observed in a homogeneous polar liquid or at liquid-solid coexistence. The bistability of the active material is even better evidenced when cycling the magnitude E_0 of the electric field that powers the rollers' motion (cycling the average density is not experimentally feasible). Fig. 4.6e shows the temporal variations of the active-solid fraction upon triangular modulation of E_0. When E_0 increases an active-solid nucleates and quickly grows. When E_0 decreases, the solid continuously shrinks and eventually vanishes at a field value smaller than the nucleation point. Note that varying E_0 changes the speed of the particles as well as their interactions. These microscopic changes explain the variations of the packing fractions of the two coexisting phases which in turn account for the variation of the domain sizes at fixed average density. The asymmetric dynamics of L_S/L_0 demonstrates the existence of a metastable region in the phase diagram. As shown in Fig. 4.6f, the metastability of the active solid results in the hysteretic response of L_S, the hallmark of a first-order phase transition. We also observed that the continuous interfacial melting observed when E_0 smoothly decreases contrasts with the response to a rapid field quench. Starting with a stationary active solid, a rapid quench deep in the coexistence region results in a destabilization of the solid bulk akin to a spinodal decomposition dynamics. Finally, when repeating the same experiments in isotropic 6 mm-wide circular chambers, we observe the same macroscopic phase separation into active solids and polar liquids (see Fig. 4.7). This observation confirms that solidification is a bulk phenomenon which does not rely on specific geometrical parameters.

Altogether, these measurements and observations establish that the emergence of active solids results from a first-order phase transition which is embodied by

PI Constant binodals at coexistence and lever-rule (Fig. 4.6b-c)

PII The existence of a slow coarsening dynamics (Fig. 4.6d)

PIII The presence of hysteresis loops (Fig. 4.6e-f)

In the next section, we theoretically elucidate active solidification as an extended MIPS scenario.

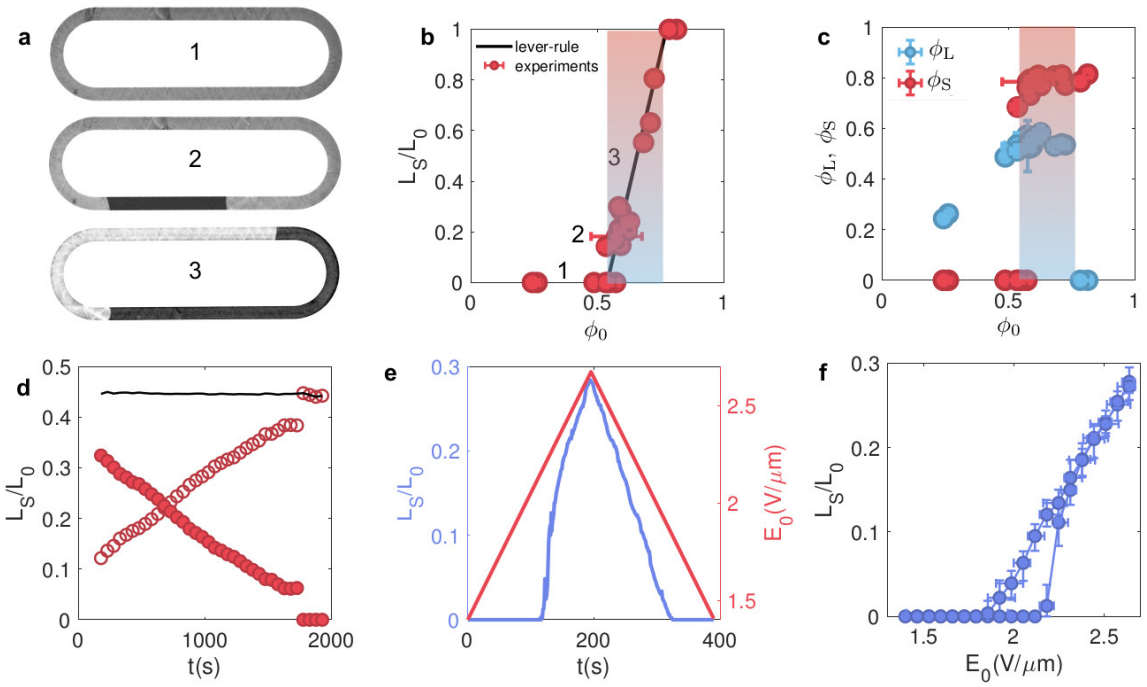

Figure 4.6 – **a.** Solid jams in a racetrack at $\phi_0 = 0.38, 0.58, 0.65$. **b.** Solid fraction plotted versus the average packing fraction ϕ_0. **c.** Density of the polar-liquid phase (blue circles) and of the active-solid phase (red circles) plotted versus ϕ_0. In **b.** and **c.** the shaded regions indicate the coexistence between the polar liquid and active solid phases. **d.** Fraction of two solid jams undergoing coarsening as a function of time. The total fraction of solid phase in the racetrack is represented by the black line. **e.** Solid fraction (blue line) and magnitude of the electric field (red line) plotted versus time. **f.** Variation of the solid fraction upon cycling the electric field amplitude. Figure adapted from [79].

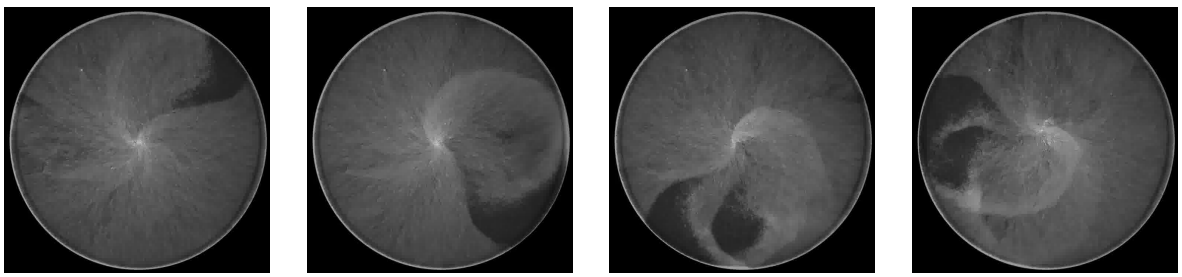

Figure 4.7 – Successive snapshots of Quincke rollers undergoing active solidification in a circular chamber. Time increases from left to right: the spiral rotates clockwise. Figure adapted from [79].

4.4 A phenomelogical approach to active solidification

Having established and characterized active solidification, we now build up a corresponding minimalist phenomenological theory. The aim is to pin down the minimal ingredients required to account for all the experimental findings. First, the theory must contain Vicsek physics to describe the formation of flocks at low density: an ordered phase must arise from a disordered gas due to aligning interactions. Second, it must take into account the drop of both velocity and local order when the density is increased that results from short-range interactions.

Elaborating a microscopic theory working at all density scale for colloidal rollers seems very challenging. Indeed, while the dependency of the self-propulsion ν_0 and local order W on the density is experimentally accessible (see Fig. 4.9a), the physical mechanism lying at its origin remains to be precisely determined (lubrication, steric hindrance ?). In this section, we instead adopt a generic hydrodynamic description of roller flocks which can be tuned phenomenologically to take into account high-density experimental features.

4.4.1 Nonlinear hydrodynamic theory

We start with the minimal version of the Toner-Tu equations introduced in section 3.1.3, which proved to correctly capture the coexistence of active gas and polar-liquid bands at the onset of collective motion [116,121,122]. For clarity, we ignore fluctuations transverse to the mean-flow direction and write the hydrodynamic equations for the one-dimensional longitudinal current $W(x,t)$ and number-density field $\rho(x,t)$:

$$\partial_t \rho + \partial_x W = D_\rho \partial_{xx} \rho, \tag{4.15}$$

$$\partial_t W + \lambda W \partial_x W = D_W \partial_{xx} W - \partial_x \left[p(\rho)\right] + a_2(\rho) W - a_4 W^3 \ , \tag{4.16}$$

where D_ρ, λ, D_W, a_4 are constant hydrodynamic coefficients. We can draw a parallel between (4.15)-(4.16) and the hydrodynamic equations (3.7)-(3.8) obtained using a bottom-up approach for the Vicsek model in section 3.1.2. On the one hand, we note that, for the Vicsek model, $a_2(\rho)$ is a function of ρ which changes sign and becomes positive as ρ exceeds a critical value ρ_c. It thus allows for a flocking transition upon increasing the particle density [114, 121, 122]. On the other hand, we note that the pressure term $p(\rho)$ in (3.8) is proportional to the density times the square of the particle's speed for the Vicsek Model. These two behaviours for $a_2(\rho)$ and $p(\rho)$ as a function of the density are summarized in Fig. 4.8a-b. Interestingly, the slowing down of the rollers at high density can be accounted for through a specific fine-tuning of $a_2(\rho)$ and $p(\rho)$, which we detail below.

Firstly, coarse-graining microscopic flocking models typically leads to a pressure term depending on the particle speed [19, 68, 76, 120]. We therefore expect $p(\rho)$ to follow the dependence of the self-propulsion ν_0 on the density and thus to sharply drop above a critical density $\bar{\rho}$ (see Fig. 4.9a). Second, given the loss of the orientational order in the solid phase, $a_2(\rho)$ is also expected to decay and change sign around $\bar{\rho}$.

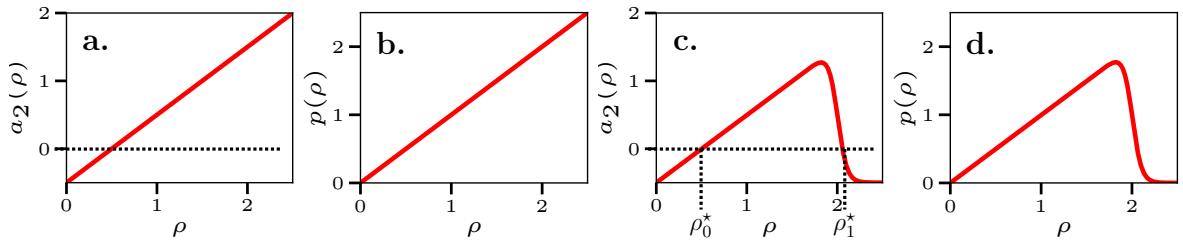

Figure 4.8 – **a**. Alignment term $a_2(\rho) = \alpha(\rho - \rho_c)$ for the Vicsek model with $\alpha = 1$ and $\rho_c = 0.5$. **b.** Pressure term $p(\rho) = \sigma\rho$ for the Vicsek model with $\sigma = 1$ (corresponding to a self-propulsion $v = \sqrt{2}$). **c.** Phenomelogical alignment term $a_2(\rho) = \alpha(\rho\epsilon(\rho) - \rho_c)$ for the Quincke rollers with $\alpha = 1$, $\rho_c = 0.5$, $\bar{\rho} = 2$ and $\xi = 0.1$. **d.** Phenomelogical pressure term $p(\rho) = \sigma\rho\epsilon(\rho)$ for the Quincke rollers with $\sigma = 1$, $\bar{\rho} = 2$ and $\xi = 0.1$.

As the slowing down of rollers and the suppression of orientational order happen concomitantly, in all that follows, we choose

$$a_2(\rho) = \alpha(\rho\epsilon(\rho) - \rho_c) \qquad \text{and} \qquad p(\rho) = \sigma\rho\epsilon(\rho) \ , \tag{4.17}$$

where the function $\epsilon(\rho)$ decreases from 1 in the low-density phases to a vanishing value deep in the solid phase, and where α and σ are two positive constants. In practice, the functional form of $\epsilon(\rho)$ is postulated on phenomenological grounds and we take

$$\epsilon(\rho) = \frac{1 - \tanh\left[(\rho - \bar{\rho})/\xi\right]}{2} \ . \tag{4.18}$$

The behaviours of $a_2(\rho)$ and $p(\rho)$ are displayed in Fig. 4.8c-d. Compared to their Vicsek's counterparts, they both present a sharp drop down at high densities around $\bar{\rho}$, which reflects the abrupt slowing down of the rollers. Note that, at densities larger than $\bar{\rho}$, we expect the repulsion and contact interactions between the particles to result in a pressure increase with the particle density [28, 154]. Our description (4.17)-(4.18) disregards this second regime which is not essential to the nucleation and propagation of active solids. We now turn to the discussion of numerical results obtained by solving (4.15) and (4.16) with spectral methods and semi-implicit time-stepping. As shown in Fig. 4.9, numerical

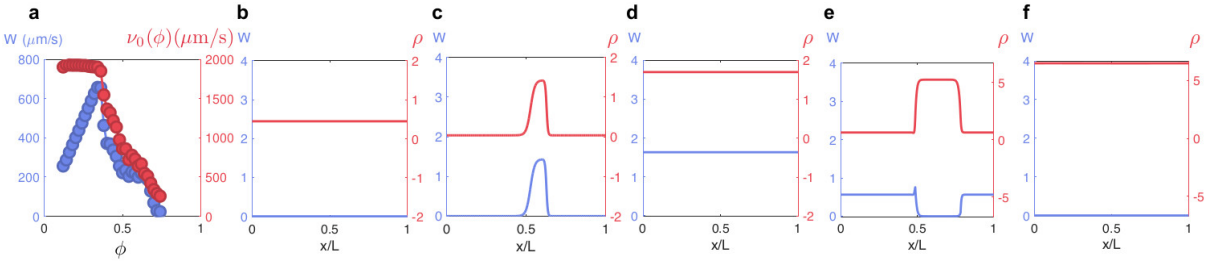

Figure 4.9 – **a.** Average velocity $\nu_0(\mathbf{r}, t)$ of the colloids (red) and local magnitude of the longitudinal current $W(\mathbf{r}, t)$ (blue) plotted as a function of the local packing fraction $\phi(\mathbf{r}, t)$. **b-e.** Successive phases observed in the numerical resolution of (4.15) and (4.16) at increasing average densities $\rho_0 = (0.10, 0.18, 1.7, 1.96, 6.5)$. The position x is normalized by the system size L. **Simulation parameters:** $D_\rho = 0.2$, $D_W = 1$, $\lambda = 1$, $a_4 = 0.45$, $\sigma = 0.2$, $\bar{\rho} = 2$, $\xi = 0.01$, $\alpha = 1$, $\rho_c = 0.5$, $L = 200$, $dx = 0.05$, $dt = 0.005$. Figure adapted from [79].

resolutions of (4.15) and (4.16) at increasing densities faithfully account for the five

successive phases observed in the experiments. At low densities, we first observe the standard Vicsek transition: a disordered gas phase is separated from a homogeneous polar liquid phase by a coexistence region where ordered bands propagate through a disordered background [62]. This phase transition occurs at very low densities ($\rho_0 \sim \rho_c \ll \bar{\rho}$), in a regime where the colloidal rollers experience no form of kinetic hindrance as they interact, therefore where $\epsilon(\rho) \simeq 1$. In agreement with the experiments, a second transition leads to the coexistence between a polar liquid of constant density ρ_L^b and an apolar dense phase of constant density ρ_S^b. This jammed phase propagates backwards with respect to the flow of the polar liquid as reported experimentally for the active solids in section 4.3. This second transition shares all the experimental signatures of the first-order phase separation reported in Fig. 4.6 for assemblies of Quincke rollers: constant binodals PI, slow coarsening PII and hysteresis PIII.

PI The bulk density in the active solid ρ_S^b and in the polar liquid ρ_L^b remains constant during the transition (see Fig. 4.10a). Consequently, the jammed phase obeys a lever rule: its width increases linearly with $\rho_0 - \rho_L^b$ as shown in Fig. 4.10b.

PII Fig. 4.10c indicates the existence of a coarsening dynamics leading to complete phase separation: small active solids tend to melt into bigger ones. During the process, the total fraction of solid jams remains constant.

PIII Upon ramping up and down the average density, the fraction of solid jam goes through an hysteresis loop as shown in Fig. 4.10d. Note that the active solid melt at a density lower than the one needed for its onset.

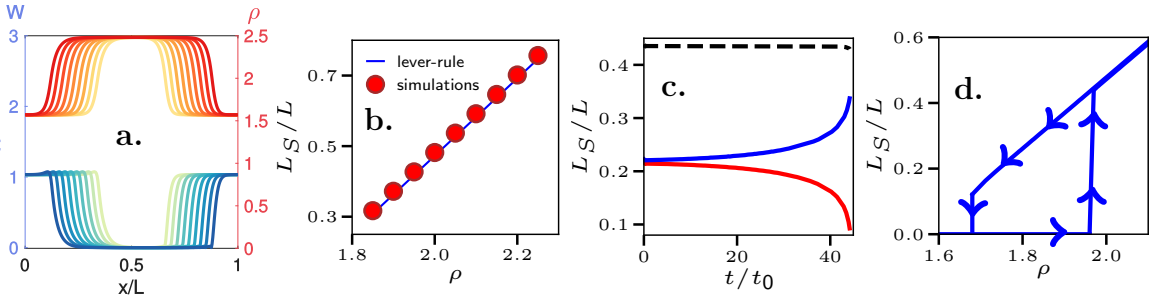

Figure 4.10 – Numerical resolution of (4.15) and (4.16). a. The density and magnetization profiles are computed for different values of ρ : from 1.85 (light colors) to 2.25 (dark colors). **b.** Fraction of the solid jam L_S/L plotted versus ρ (symbols) and lever rule (solid line). Same parameters as in **a**. **c.** Fraction of two solid jams undergoing coarsening as a function of a normalized time t/t_0. The total fraction of active solids is represented by the black dashed line. t_0 is arbitrarily chosen to be the time taken by an active solid to circle around the system. **d.** Variation of the fraction of solid jam upon cycling the density. **Parameters:** $D_\rho = 5$, $D_W = 10$, $\lambda = 1$, $a_4 = 1$, $\sigma = 1$, $\bar{\rho} = 2$, $\xi = 0.1$, $\alpha = 1$, $\rho_c = 0.5$, $L = 200$, $dx = 0.01$, $dt = 0.001$. Figure partially adapted from [79].

4.4.2 Spinodal instability of polar liquids and domain wall propagation

Having established the qualitative agreement between our hydrodynamic model and the experiments, we now use the former to gain physical insight into the origin of active solidification. In this section, we show how the succession of instabilities of the homogeneous solutions of Eqs. (4.15) and (4.16) correctly predict the full phase behaviour observed in the experiments and numerical simulations. We focus on the experimentally relevant situation where the slowing down of the particle occurs at packing fractions much larger than that of the onset of collective motion, namely $\bar{\rho} \gg \rho_c$.

Stability of the disordered phases

We start by considering a homogeneous disordered phase where $\rho = \rho_0$, $W = 0$. The linearized dynamics of a small perturbation $\delta X \equiv (\delta\rho, \delta W)$ is given, in Fourier space, by $\delta\dot{X}_k = M_k \delta X_k$, where the dynamical matrix M_k reads

$$M_k = \begin{pmatrix} -D_\rho k^2 & -ik \\ -(\epsilon + \epsilon'\rho_0)ik\sigma & a_2(\rho_0) - D_W k^2 \end{pmatrix} . \tag{4.19}$$

The eigenvalues $\lambda_\pm$ of M_k determines the stability of the disordered phases. We find

$$\begin{aligned} 2\lambda_\pm = \pm \sqrt{\Big[(D_\rho + D_W)k^2 - a_2(\rho_0)\Big]^2 - 4k^2\sigma(\epsilon + \rho_0\epsilon') - 4\Big[D_W k^2 - a_2(\rho_0)\Big]D_\rho k^2} \\ - \Big[(D_\rho + D_W)k^2 - a_2(\rho_0)\Big] \ . \end{aligned} \tag{4.20}$$

The disordered phases are unstable whenever there exists a $\lambda_\pm$ with a positive real part, ie $\Re(\lambda_\pm) > 0$, which is realized when either one of the following conditions is satisfied

$$a_2(\rho_0) > 0 \Leftrightarrow \rho_0\epsilon(\rho_0) - \rho_c > 0 \tag{4.21}$$

$$\sigma\left[\epsilon(\rho_0) + \rho_0\epsilon'(\rho_0)\right] < -(D_W k^2 - a_2(\rho_0))D_\rho \ . \tag{4.22}$$

For the case at hand, the second condition is never met in the low density regime $\rho_0 \lesssim \rho_c$ as $\rho_c \ll \bar{\rho}$. In this low density regime, Fig. 4.8c shows that the criterion (4.21) is first met at $\rho_0^\star \simeq \rho_c$: we recover the standard spinodal instability leading to the emergence of flocking motion [122]. As density increases, the system thus undergoes a first linear instability at $\rho_0 \simeq \rho_c$, which corresponds to the transition reported in Fig. 4.9, panels b to c.

At the other end of the density spectrum, deep in the active solid phase where $\rho_0 \gg \bar{\rho}$, the criterion (4.21) cannot be realized since $a_2(\rho) = -\alpha\rho_c < 0$. The condition given in (4.22) is not realized either because $\epsilon' \simeq 0$. As the density decreases, both (4.21) and (4.22) could lead to a linear instability of the active solid. Looking at Fig. 4.8c, condition (4.21) is realized at a second density $\rho_1^\star > \rho_0^\star$ such that $\rho_1^\star\epsilon(\rho_1^\star) = \rho_c$ and $a_2'(\rho_1^\star) < 0$. As $a_2'(\rho) = (\rho\epsilon(\rho))'$, it implies that $\rho\epsilon(\rho)$ is a decreasing function at $\rho_1^\star$. Since, for $k = 0$, (4.22) reduces to $(\rho_0\epsilon(\rho_0))' < -D_\rho\alpha(\rho_c - \rho_0\epsilon(\rho_0))/\sigma$, the criterion of (4.22) is already realized at $\rho_1^\star$: the linear instability of the active solid is always given by (4.22). We recognize in (4.22) the standard form of a MIPS spinodal instability derived in (4.14) $\epsilon + \rho\epsilon' \ll -K_1 D_\rho$, with K_1 a positive constant [67]. The linear instability of the active solid leading to the transition illustrated by the panels e and f of Fig. 4.9 is thus consistent with a MIPS scenario.

Stability of the ordered phase

Let us now consider a polar liquid where $\rho = \rho_0$, and $W = W_0$, with $a_4 W_0^2 = a_2(\rho_0)$. Following the same procedure as above, the linearized dynamics of a small perturbation $\delta X = (\delta\rho, \delta W)$ is given by $\delta\dot{X} = M\delta X$ where the dynamical matrix M reads

$$M_k = \begin{pmatrix} M_{\rho\rho} & M_{\rho W} \\ M_{W\rho} & M_{WW} \end{pmatrix} , \tag{4.23}$$

with the coefficients given by

$$M_{\rho\rho}(k) = -D_\rho k^2, \qquad M_{\rho W}(k) = -ik, \tag{4.24}$$

$$M_{W\rho}(k) = -(\epsilon + \epsilon'\rho_0)(ik\sigma - W_0\alpha), \quad M_{WW}(k) = -D_W k^2 - \lambda ikW_0 - 2a_4 W_0^2 . \tag{4.25}$$

The linear stability of the polar liquid is determined by the sign of the real parts of the eigenvalues of M_k, $\Re(\lambda^\pm(k))$. To be consistent with our modified Toner-Tu equations (4.15) and (4.16) that are truncated at the second order in gradients, we only consider $\lambda^\pm(k)$ up to order k^2. Only $\Re(\lambda^-(k))$ can become positive and lead to an instability. At order k^2, it reads

$$\Re\left(\lambda^-(k)\right) = -\frac{k^2}{8a_4^3 W_0^4}\left[(\epsilon + \rho\epsilon')2a_4 W_0^2(2a_4\sigma + \alpha\lambda) - \alpha^2(\epsilon + \rho\epsilon')^2 + 8a_4^3 D_\rho W_0^4\right] + o(k^2) .$$

This is a second order polynomial in $\epsilon + \rho\epsilon'$ and the polar liquid is linearly unstable whenever one of the two following conditions is satisfied

$$\epsilon + \rho\epsilon' < \frac{a_4 W_0^2}{\alpha^2}(\alpha\lambda + 2a_4\sigma)\left(1 - \sqrt{1 + \frac{8a_4 D_\rho \alpha^2}{(\alpha\lambda + 2a_4\sigma)^2}}\right) \tag{4.26}$$

$$\epsilon + \rho\epsilon' > \frac{a_4 W_0^2}{\alpha^2}(\alpha\lambda + 2a_4\sigma)\left(1 + \sqrt{1 + \frac{8a_4 D_\rho \alpha^2}{(\alpha\lambda + 2a_4\sigma)^2}}\right) . \tag{4.27}$$

The first inequality (4.26) can only be satisfied at high densities, when $\rho \sim \bar{\rho}$. It is again of a standard MIPS form similar to (4.14), *i.e.* $\epsilon + \rho\epsilon' < -W_0^2 K_2$ with $K_2 > 0$, and corresponds to the solidification transition from panel d to panel e on figure Fig. 4.9. Both the melting of the active solid and the solidification of the polar liquid thus correspond to standard MIPS instability criteria. It is interesting to note that the local order of the polar liquid merely alters the MIPS instability scenario although orientational order makes it harder to phase separate through the factor W_0^2 in (4.26). This result is consistent with recent results on the large deviations of active-matter systems that show collective motion to be an optimal strategy to avoid MIPS [155].

On the contrary, the second inequality (4.27) is realized at much lower densities, close to $\rho_0 = \rho_c$, when W_0^2 is small enough. It corresponds to the standard linear instability of the polar liquid leading to the formation of Vicsek bands, as shown on panels c and d in Fig. 4.9. Using $W_0^2 = \alpha(\rho_0 - \rho_c)/a_4$ and that $\epsilon = 1$ when $\rho_0 \ll \bar{\rho}$, (4.27) becomes

$$\frac{\alpha}{\alpha\lambda + 2a_4\sigma}\left(1 + \sqrt{1 + \frac{8a_4 D_\rho \alpha^2}{(\alpha\lambda + 2a_4\sigma)^2}}\right)^{-1} + \rho_c < \rho_0 \tag{4.28}$$

In the limit of small D_ρ relevant for our experiments [29], we recover the usual instability criterion of a homogeneous polar liquid discussed in [121] :

$$\rho_c + \frac{\alpha}{2\lambda\alpha + 4a_4\sigma} < \rho_0 \ . \tag{4.29}$$

All in all, we have determined all the spinodal lines governing the two phase transitions found numerically.

- Flocking transitions between a disordered gas and a polar liquid. The transition from:
  - panel b to c in Fig. 4.9 corresponds to (4.21)
  - panel d to c in Fig. 4.9 corresponds to (4.27)
- MIPS-like transitions between a polar liquid and an active solid. The transition from
  - panels d to e in Fig. 4.9 corresponds to (4.26)
  - panels f to e in Fig. 4.9 corresponds to (4.22)

At low densities, when $\rho_0 \ll \bar{\rho}$, the hydrodynamics (4.15)-(4.16) corresponds to that thoroughly studied in [121, 122, 156]. It correctly predicts a first order transition from an isotropic gas to a polar-liquid phase with a spinodal decomposition into Vicsek bands whenever (4.28) is verified. However, at high density, the stability of the polar liquid is limited by the formation of active-solid jams, a phenomenon that is not captured by classical flocking models. We learn from the stability analysis that this active solidification ultimately relies on the decrease of the effective pressure with density in (4.16) as a result of the slowing down of the colloids in dense environments. Criterion (4.26) is exactly analogous to the spinodal decomposition condition in MIPS physics (see (4.14) in section 4.2): the formation of active-solid jams results from a Motility-Induced Phase Separation.

4.5 A microscopic approach to active solidification

Because we could not coarse-grain explicitly the rollers' microscopic dynamics in the previous part, we had to resort to phenomenological modifications directly at the hydrodynamic level in (4.15)-(4.16). Especially, we postulated that the macroscopic slowing down and the loss of order should happen concomitantly at $\bar{\rho}$ with a specific dependency given by $\epsilon(\rho)$ in (4.18). Here, instead, I want to explore more generally the minimal microscopic ingredients sufficient to produce both collective motion and active jams at the coarse-grained scale. To this aim, I use a controlled framework in which the coarse-grained evolution of the fields ρ and W can be obtained from the underlying microscopic dynamics. Such a framework has been developped for active lattice gases, where one can specify the microscopic update rule of the spins and determine exactly the associated macroscopic hydrodynamics [148, 157]. This section contains recent results that go beyond the physics reported in [79] and will be published in a separate contribution. The experimental observations of section 4.3 points toward four key mechanisms necessary for the physics of active solidification

- non-zero self-propulsion speed at low density.
- alignment at low density.
- Loss of orientational order at high density.
- Drop of self-propulsion at high density.

For simplicity, we work in one space dimension and consider a lattice with periodic boundary conditions and lattice spacing a. Particles carry plus and minus spins and evolve on the lattice. The density ρ_j and the magnetization m_j at site j are given by

$$\rho_j = \eta_j^+ + \eta_j^- \qquad m_j = \eta_j^+ - \eta_j^- \ , \tag{4.30}$$

where η_j^+ and η_j^- are the number of plus and minus spins at site j respectively. Echoing the four mechanisms cited above, the dynamics is as follows:

RI Particles diffuse isotropically with rate Da^{-2}

RII Spin $\pm$ at site j hop to site $j \pm 1$ with rate $va^{-1}\exp(-\lambda\rho_j)$

RIII Spin $\pm$ at site j flips into a $\mp$ spin with rate $\gamma W_\pm$ with

$$W_\pm = \begin{cases} \exp(\mp\beta m_j) & \text{if } \rho_j \leq 3 \\ 1 & \text{if } \rho_j \geq 4 \end{cases} \tag{4.31}$$

Using the Heaviside function $\Theta(u)$, which is equal to 1 if $u \geq 0$ and zero otherwise, we obtain a more compact formulation for the $W_\pm$

$$W_\pm = \Theta(3-\rho_j)\exp(\mp\beta m_j) + \Theta(\rho_j - 4) \ . \tag{4.32}$$

In the above microscopic rules, we note that alignment is switched off at site j when $\rho_j \geq 4$: spins flips to $+$ or $-$ with equal probability at high density. Furthermore, self-propulsion drops down with the local density as $\exp(-\lambda\rho_j)$: spins are arrested in the high density regime. We now derive the coarse-grained hydrodynamics corresponding to the microscopic rules RI, RII and RIII.

4.5.1 Exact coarse-grained evolution

We consider a lattice with L different sites and a discretized time t_j with $j \in \{1,..,N\}$. In a time $dt = t_{j+1} - t_j$, a unique spin makes one of the three moves described in RI, RII and RIII. A trajectory of the spins is completely determined by the set $\{\eta\}$ containing all the $\eta_i^\pm(t_j)$'s

$$\{\eta\} = \left\{\eta_i^\pm(t_j) \quad \text{for} \quad i \in \{1,..,L\},\ j \in \{1,..,N\}\right\} \ . \tag{4.33}$$

Using path integral technics, we derive in appendix C.1 the probability $P(\{\eta\})$ to observe a given trajectory of the spins. Building on it, we change variables from the $\eta_i^\pm$ to the averaged density $\langle\rho_i\rangle$ and magnetization $\langle m_i\rangle$. Finally, as shown in appendix C.1,

taking the saddle point of the action in the limit of small lattice size $a \to 0$ yields the hydrodynamic evolution as

$$\partial_t \rho = D\nabla^2 \rho - \nabla \left[v_{\text{eff}}(\rho)\ m \right] \tag{4.34}$$

$$\partial_t m = D\nabla^2 m - \nabla \left[v_{\text{eff}}(\rho)\ \rho \right] + a_2(\rho) m - a_4(\rho)\ m^3\ , \tag{4.35}$$

where $v_{\text{eff}}(\rho)$, $a_2(\rho)$ and $a_4(\rho)$ are given by

$$v_{\text{eff}}(\rho) = \rho\ e^{-\rho(1-e^{-\lambda})-\lambda}\ , \qquad a_4(\rho) = \gamma\ m^3 \frac{e^{-3\beta}}{8} \left(e^{2\beta} - 1\right)^2 \tag{4.36}$$

$$a_2(\rho) = -\gamma e^{-\rho} \left[\left(e^{-\beta} - 1\right) + \left(e^{-2\beta} - 1\right) \rho + \left(3e^{-3\beta} + 2e^{-\beta} - e^{\beta} - 4\right) \frac{\rho^2}{8} \right] - \gamma \tag{4.37}$$

We can compare the evolution of the magnetization (4.35) with the phenomelogical Toner-Tu (4.16) in section 4.4.1 which was derived for the assemblies of Quincke rollers. Through coarse-graining, we obtained exact expressions for $a_2(\rho)$ in (4.37) as well as for $p(\rho)$ which reads

$$p(\rho) = \rho\ v_{\text{eff}}(\rho)\ . \tag{4.38}$$

Let us now compare these exact formulas with the phenomelogical ones previously postulated in (4.17). Consistently with its counterpart plotted in Fig. 4.8d, we note that $p(\rho)$ in (4.38) first increases linearly at low density before decaying to zero. However, as shown in Fig. 4.11b, it does not sharply drop around a critical value $\bar{\rho}$ but constantly decays exponentially from its maximum value at low density. Interestingly, the exact $a_2(\rho)$ in (4.37) shares all the characteristic features of its phenomelogical counterpart postulated in section 4.4.1 and plotted in Fig. 4.8c. First, it is negative at both low and high densities, so that the system remains disordered in these two regimes. Second, for sufficiently large β, it becomes positive at intermediate densities to foster an ordered phase (see Fig. 4.11a). Given these similarities between (4.35) and (4.16), we expect our microscopic model to produce a rich macroscopic physics similar to the one discussed in section 4.4.1. Let us now verify this statement by looking for active solidification and collective motion in the numerical simulations.

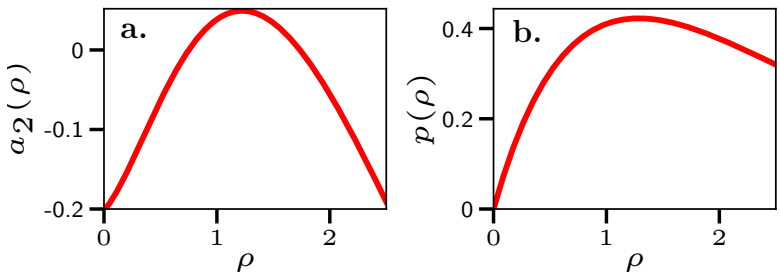

Figure 4.11 – **a.** Alignment term $a_2(\rho)$ given by (4.37). **b.** Pressure term $p(\rho)$ as in (4.38). **Parameters:** $\beta = 1.6$, $v = 4$, $\lambda = 1.5$, $\gamma = 1$.

4.5.2 Phase diagram and triple coexistence state

We first perform numerical simulations of the hydrodynamic equations (4.34)-(4.35) using a spectral method with semi-implicit Euler scheme. We find a phase diagram similar to

the one encountered for our phenomelogical Toner-Tu (4.15)-(4.16) in Fig. 4.9. Upon increasing the density, the system successively goes from a disordered gas phase to a phase-separated state with travelling bands. It then displays a flocking phase with non-zero homogeneous magnetization before once again exhibiting a coexistence state between a polar liquid and a jammed solid. Finally, at very high density, this jammed solid ends up spanning the entire length of the system. The whole phase diagram as a function of density is summarized in Fig. 4.12.

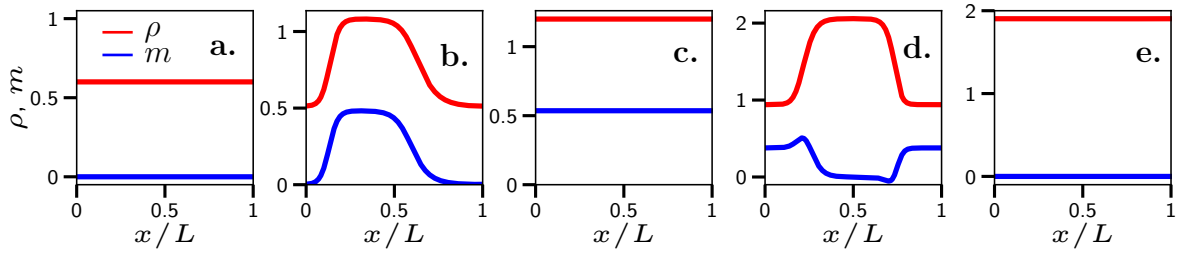

Figure 4.12 – Successive phases observed in the numerical resolution of (4.34)-(4.35) at increasing average densities $\rho_0 = (0.6, 0.8, 1.2, 1.5, 1, 9)$ from left to right. The position x is normalized by the system size. **a.** Gas phase. **b.** Coexistence of gas and flock. **c.** Flocking phase. **d.** Coexistence of jam and flock. **e.** Solid phase. **Parameters:** $D = 0.5$, $\beta = 1.6$, $v = 4$, $\lambda = 1.5$, $\gamma = 1$, $L = 80$.

So far, here and in section 4.3, we always observed systems where the two transitions, namely active solidification and the emergence of collective motion, were occurring at very distinct regimes of densities without affecting each others. It would be interesting to study how both transitions would interplay if their respective spinodals were brought within the same density range. While it is practically difficult to control the onset of the different phases in the experiments, here we can easily vary the parameters in (4.34)-(4.35) to bring the onset of collective motion close to the emergence of jams.

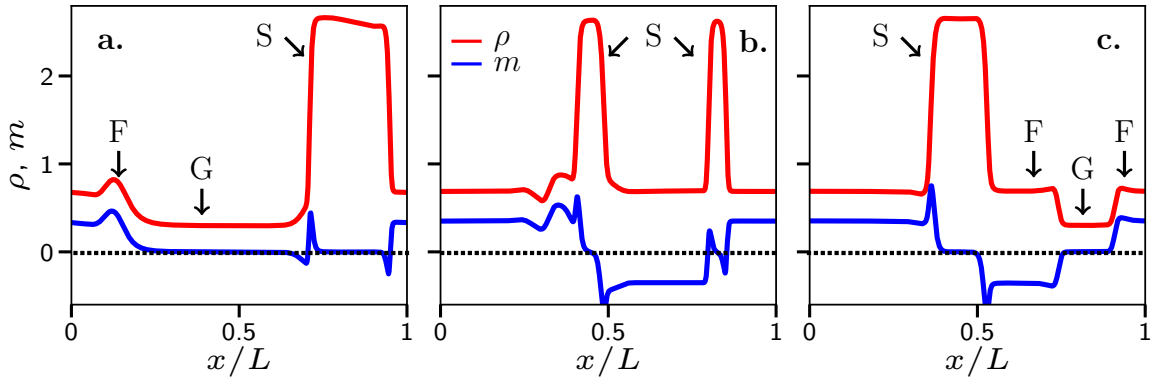

Figure 4.13 – Successive snapshots of the steady-state presenting a triple coexistence between gaseous (G), flocking (F) and solid (S) phases at increasing simulation time $t = (194, 344, 408)$ from left to right. The position x is normalized by the system size. **a.** Travelling band crashing into a jam. **b.** Nucleation of a new jam while the older one melts. **c.** Formation of two bands travelling in opposite directions after melting. **Parameters:** $D = 1$, $\beta = 1.8$, $v = 8$, $\lambda = 1.25$, $\gamma = 1$, $L = 400$, $\rho_0 = 0.95$.

By doing so, we can find an exotic steady-state where the flocking, gaseous and

jammed phases coexists together in a rather chaotic dynamics. The latter takes the form of travelling flocks propagating in a gaseous medium which eventually collide on the active solid (see Fig. 4.13a.). The active solid moves upstream the travelling bands by increments occurring after each collision with a flock. In Fig. 4.13, we present a few snapshots of the system in this triple coexistence regime. The phenomenology observed is in fact even richer than a mere steady-state between flocks and jammed phase. At triple coexistence, active solids can also completely melt into two flocks, one going rightward and the other going leftward (see Fig. 4.13b. and c.). These two travelling flocks then propagates in the system until they meet one another due to the periodic boundary conditions; their collision then nucleates a new jam at the location of their encounter. Consequently, the stationary state at triple coexistence can exhibit a complicated phenomenology with traffic jams appearing and melting chaotically.

Having exploited (4.34)-(4.35) to unveil the phase diagram in Fig. 4.12 as well as this new exotic steady-state with triple coexistence, we now confront our predictions to microscopic simulations of active spins.

4.5.3 Microscopic simulations: triple coexistence is confirmed

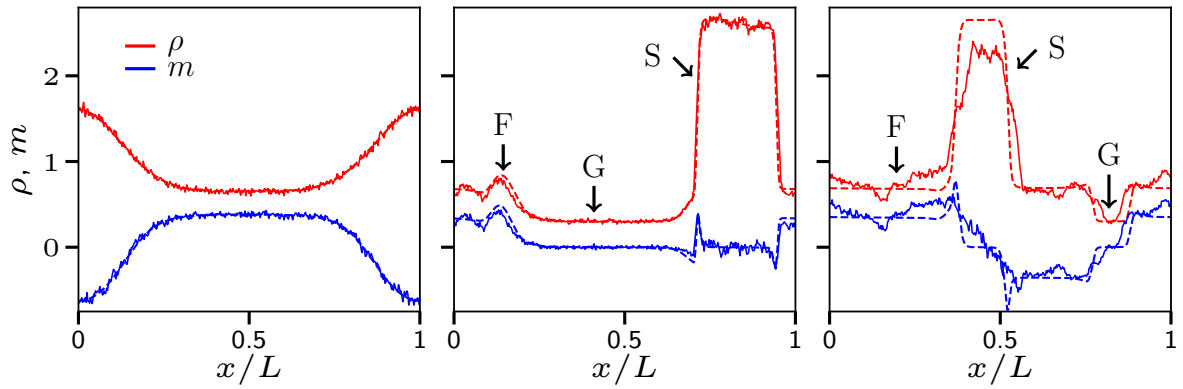

Figure 4.14 – **a-c.** Successive snapshots confronting the hydrodynamics (4.34)-(4.35) (dashed lines) with microscopic lattice gas dynamics RI-RII-RIII (plain lines) at increasing simulation time $t = (1, 200, 400)$ from left to right. The position x is normalized by the system size. Gaseous, flocking, and solid phases are indicated by G, F, and S respectively. **Parameters:** $D = 1$, $\beta = 1.8$, $v = 8$, $\lambda = 1.25$, $\gamma = 1$, $L = 400$ and $\rho_0 = 0.95$. For the on-lattice dynamics, $a = 0.0025$ and $dt = 3.125 \times 10^{-6}$.

In this section, we perform microscopic simulations of active spins obeying dynamics RI-RII-RIII in order to check the consistency of our coarse-grained hydrodynamics (4.34)-(4.35). As the limit of small lattice size $a \to 0$ is computationally costly, we will only confront (4.34)-(4.35) with its corresponding spin-based dynamics for a specific set of parameters for which the hydrodynamics exhibits a triple coexistence between gaseous, flocking and jammed phases.

Starting from the same initial conditions, and without any fitting parameters, the coarse-grained PDE accurately predicts the microscopic evolution up to a time of order $t \sim 1000$ for a lattice size of order $a \sim 0.0025$ as shown in Fig. 4.14. Note that the simulation of the lattice gas is very costly due to the high number of lattice sites $N \sim 2 \times 10^5$ as well as to the very small time-step increment $dt \sim 10^{-6}$ which is needed to keep

the stochastic rate RI of order 1. We report in appendix C.2 the details of the algorithm used and the difficulties that we encountered.

Having demonstrated the relevance of our hydrodynamic equations (4.34)-(4.35) to describe active lattice gases evolving according to RI-RII-RIII, we can affirm that the triple coexistence between gaseous, flocking and jammed phases is not an artifact of our coarse-grained procedure performed in section 4.5.1. However, we have only reported this triple coexistence state for on-lattice dynamics so far, and we now assess whether this exotic phase could also be present in continuous models.

4.5.4 Off-lattice generalization: triple coexistence remains robust

In this section, I show that the triple coexistence region is not an artifact of lattice-based models but a generic feature observed in systems endowed with alignment and slowing down at high density. To this aim, we study N active particles moving in a rectangular domain $L_x \times L_y$ endowed with periodic boundary conditions. Each particles carries a spin $s_i = \pm$ and evolves according to the stochastic dynamics

$$\dot{\mathbf{r}}_i = s_i v\, \mathbf{e}_x + \sqrt{2D}\, \boldsymbol{\eta}_i \,, \tag{4.39}$$

where v is the self-propulsion speed, D is the diffusion coefficient, $\boldsymbol{\eta}_i$ is a Gaussian white noise, and $\mathbf{e}_x$ is the unitary vector in the x direction. Spins flip from s_i to $-s_i$ at rate $W(s_i)$ given by

$$W(s_i) = \gamma \exp(-\beta s_i\, \tilde{m}_i) \,, \quad \text{with} \quad \tilde{m}_i = \frac{1}{N_i} \sum_{\ell \in \mathcal{N}_i} s_\ell \tag{4.40}$$

where β is the alignment strength, $\mathcal{N}_i$ is the set of neighbors in the disk $\mathcal{D}_i$ of radius r_0 centered at $\mathbf{r}_i$ and $N_i = \mathrm{card}(\mathcal{N}_i)$.

We now need to include the two keys features that were necessary to produce solid jams in the previous sections: slowing down and loss of orientational order at high densities. To this aim, we introduce two threeshold N_s and N_a such that when the number of neighbors N_i exceeds N_s (N_a), the speed v (the field $\tilde{m}_i$) drop to zero respectively. We thus have

$$\tilde{m}_i = \begin{cases} \dfrac{1}{N_i} \displaystyle\sum_{\ell \in \mathcal{N}_i} s_\ell & \text{if} \quad N_i < N_a \\ 0 & \text{if} \quad N_i \geq N_a \end{cases} \,, \qquad v = \begin{cases} v_0 & \text{if} \quad N_i < N_s \\ 0 & \text{if} \quad N_i \geq N_s \end{cases} \,. \tag{4.41}$$

The consequence of these threesholds on the dynamics is twofold

- Particles do not align at high density when $N_i > N_a$
- Particles do not self-propel at high density $N_i > N_s$

Having included the ingredients sufficient for active solidification, we can now perform numerical simulation of (4.39)-(4.40) with (4.41). In Fig. 4.15, we report the presence of a triple coexistence steady-state where flocks, jams and disordered gas cohabit together.

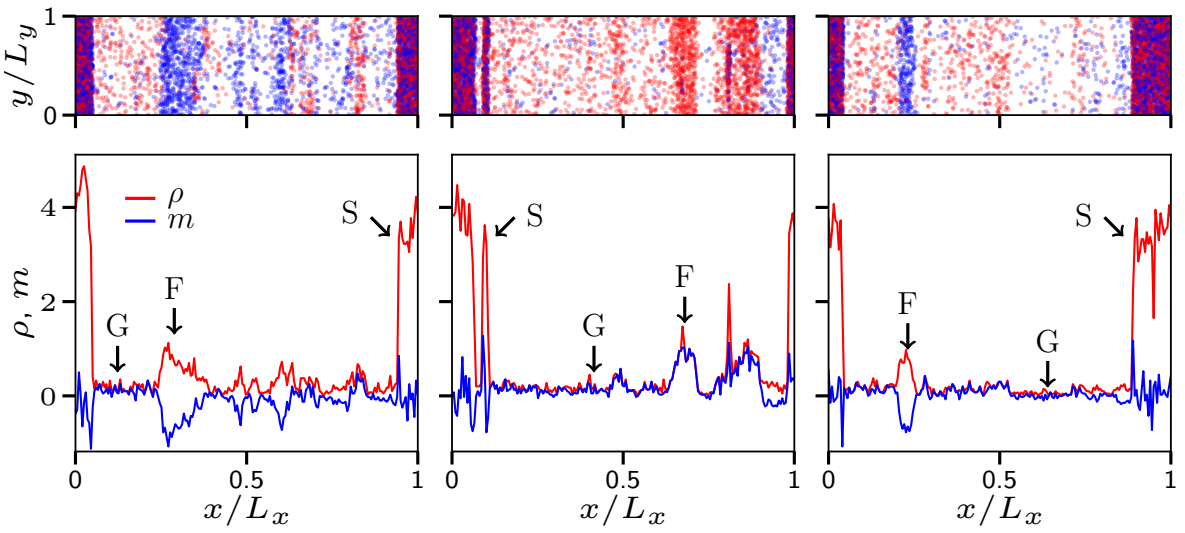

Figure 4.15 – **Top.** Successive snapshots of lattice gas dynamics (4.39)-(4.40) with (4.41) at increasing simulation time $t = (1300, 2330, 4340)$ from left to right. Spins + (−) are indicated by red (blue) dots respectively. **Bottom.** Corresponding profiles of ρ and m averaged over the y direction. Gaseous phase, flocking, and solid phases are indicated by G, F, and S respectively. **Parameters:** $L_x = 400$, $L_y = 10$, $\rho_0 = 1.9$, $D = 0.04$, $v_0 = 0.5$, $N_s = N_a = 10$, $\gamma = 0.5$, $\beta = 3$, $dt = 0.05$.

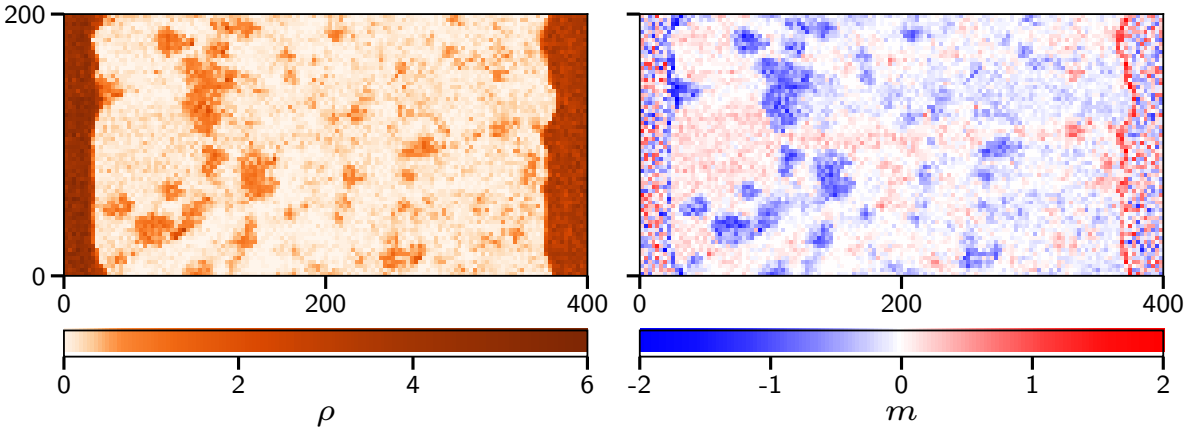

Figure 4.16 – Snapshot resulting from simulations of lattice gas dynamics (4.39)-(4.40) with (4.41) at time $t = 1260$. **Left.** Colormap of the density. **Right.** Colormap of the magnetization. **Parameters:** Same as in Fig. 4.15 but with $L_y = 200$.

However, note that the real aspect ratio of the snapshots in Fig. 4.15 is of order 0.025; this is because for larger values of L_y/L_x the tavelling bands are not necessarily well defined. They can be replaced by polarized moving clusters of + and − spins. In Fig. 4.16, we report a snapshot of our lattice gas in a domain with aspect ratio $L_y/L_x = 0.5$ where we can observe these polarized clusters colliding into a band of solid jam.

4.6 Conclusion

In this chapter, we unveiled a new phase transition occuring at high densities in assemblies of Quincke roller, which we dubbed active solidification. After characterizing it experimentally as a first order transition, we showed that it is well described by an extended MIPS scenario between a polar liquid and a solid jam. We then proved that our phenomelogical analysis is grounded in microscopic models whose coarse-grained properties can be derived exactly.

Our results show that active solidification is a generic feature observed in ensemble of motile particles which both slow down and cease to align at high densities. Finally, our analysis reveals that the flocking transition and the active solidification can interplay together when their spinodals are brought within the same density range. Such an interplay can produce a new exotic steady state with triple coexistence between a gaseous phase, polar bands, and jammed phases which has not been observed experimentally so far. It would be interesting to try and look for it in the setup of section 4.1 by varying the different controlled parameters: the electric field, the diameter of the colloidal beads, the width of the racetrack, etc.

5. Scale-free correlations in anisotropic systems

This chapter stands alone in this manuscript as it tackles both questions and systems differing from the active-matter physics considered so far. More precisely, it is devoted to the study of a minimal nonequilibrium model which exhibits long-ranged correlations. The work presented here is rather recent, yet unpublished, and was performed in collaboration with Mehran Kardar and Yariv Kafri.

In statistical physics, the two-point function $\langle\phi(\mathbf{x})\phi(0)\rangle$ of a spatially-dependent field $\phi(\mathbf{x})$ is said to be long-ranged, or scale-free, whenever $\langle\phi(\mathbf{x})\phi(0)\rangle \underset{|\mathbf{x}|\to\infty}{\sim} |\mathbf{x}|^{-\alpha}$, with α a positive coefficient measuring the algebraic decay. Historically, long-ranged correlations were first discovered in equilibrium systems near the critical point where the correlation length diverges [81–85]. More recently, there has been a large interest in the long-ranged correlations observed in the steady state of nonequilibrium systems [86–94]. In active matter, scale-free correlations were first spotted numerically and analytically within the polar liquid phase of the Vicsek model [158] and of the Toner-Tu equations [115], respectively. Since this first surge of interest, however, there has been few discussions on their role in active-matter systems [95, 97, 98]. This is surprising as long-ranged correlations are expected to be quite generic out of equilibrium. For instance, in the nineties, Grinstein, Lee and Sachdev (GLS) [99] predicted that anisotropic nonequilibrium fluctuations should be sufficient to induce scale-free correlations. Their approach, however, is based on a phenomenological field theory for which, to the best of our knowledge, no corresponding microscopic model has been reported so far. This last chapter is devoted to the presentation of such a microscopic dynamics, which indeed exhibits the scale-free correlations predicted by GLS, but differs from standard active-matter models.

In section 5.1, I start by presenting the seemingly boring case of free diffusion, which allows me to fix notations and tackle, in the simplest of cases, the question of finite-size effects. In section 5.2, I review the established results of Grinstein, Lee and Sachdev [99]. In particular, I highlight an exotic feature which has not been described so far: the GLS model breaks the Stokes-Einstein relation but remains time-reversible. In section 5.3, I present our microscopic model as well as its numerical implementation. Interestingly, while individual particles only experience short-ranged interactions, I show that long-ranged correlations of the density field emerge at the macroscopic level. Finally, in section 5.4, I look for physical signatures induced by the scale-free decay of the two-point function. I show that, upon confining our particles, the correlation of the pressures exerted on two opposite facing plates separated by a distance L exhibits an algebraic, Casimir-like decay as L^{-2}. I verify this last result by performing numerical simulations.

Throughout this chapter, we will take the following convention for continuous Fourier transforms

$$f_{w,\mathbf{k}} = \int e^{iwt - i\mathbf{k}\cdot\mathbf{x}} f(\mathbf{x},t) d\mathbf{x}dt \qquad f(\mathbf{x},t) = \int \frac{dwd\mathbf{k}}{(2\pi)^{1+\mathrm{d}}} e^{-iwt+i\mathbf{k}\cdot\mathbf{x}} f_{w,\mathbf{k}} \,, \tag{5.1}$$

as well as the following convention for Fourier series of L-periodic functions

$$f_{q_n} = \frac{1}{L}\int_0^L e^{-iq_n x} f(x,t) dx \,, \qquad f(x) = \sum_n f_{q_n} e^{iq_n x} \,, \tag{5.2}$$

where $q_n = 2\pi n/L$ and $n \in \mathbb{Z}$.

5.1 The ideal gas

In this section, for simplicity, we consider N particles evolving in a one-dimensional domain of size L endowed with periodic boundary conditions. At the end of our computation, we generalize our results to a domain of volume V in any dimension d. The position x_i of the particles evolve according to the Langevin equation $\dot{x}_i = \sqrt{2D}\eta_i$, where η_i is a Gaussian white noise of unit variance, and D is the diffusion coefficient. Therefore, the stochastic evolution of the density $\rho = \sum_{i=1}^{N} \delta(x - x_i)$ is given by the paradigmatic field equation [159]

$$\partial_t \rho = D\partial_{xx}\rho + \partial_x \left[\sqrt{2D\rho}\, \eta(x,t)\right] , \tag{5.3}$$

where $\eta(x,t)$ is a Gaussian white noise of variance $\langle \eta(x,t)\eta(x',t')\rangle = \delta(t-t')\delta(x-x')$. The fluctuation of the density field is defined as $\delta\rho = \rho - \rho_0$, where $\rho_0 = N/L$ is the homogeneous bulk density. Linearizing (5.3) to first order in $\delta\rho$ then gives

$$\partial_t \delta\rho = D\partial_{xx}\delta\rho + \partial_x \left[\sqrt{2D\rho_0}\, \eta(x,t)\right] . \tag{5.4}$$

Using convention (5.2) for periodic functions, the above evolution becomes linear for the Fourier modes $\delta\rho_{q_n}$ as

$$\partial_t \delta\rho_{q_n} = -Dq_n^2 \delta\rho_{q_n} + iq_n\sqrt{2D\rho_0}\, \eta_{q_n}(t) . \tag{5.5}$$

Solving (5.5) yields $\delta\rho_{q_n}$ as

$$\delta\rho_{q_n}(t) = \delta\rho_{q_n}(0)e^{-Dq_n^2 t} + iq_n \int_0^t e^{-Dq_n^2(t-s)}\sqrt{2D\rho_0}\, \eta_{q_n}(s)ds . \tag{5.6}$$

The first term on the right-hand side of (5.6) can be neglected in the limit $t \to \infty$ for $q_n \neq 0$. For $q_n = 0$, mass conservation imposes $\delta\rho_0(0) = 0$ and thus, for every q_n, we obtain the long-time limit of $\delta\rho_{q_n}$ as

$$\delta\rho_{q_n}(t) = iq_n \int_0^t e^{-Dq_n^2(t-s)}\sqrt{2D\rho_0}\, \eta_{q_n}(s)ds . \tag{5.7}$$

We now express the correlations of the density field in terms of the Fourier modes $\delta\rho_{q_n}$:

$$\langle \delta\rho(x,t)\delta\rho(0,t)\rangle = \sum_{n,n'} e^{iq_n x}\langle \delta\rho_{q_n}(t)\delta\rho_{q_{n'}}(t)\rangle . \tag{5.8}$$

Inserting (5.7) into (5.8), we obtain

$$\langle \delta\rho(x,t)\delta\rho(0,t)\rangle = -2D\rho_0 \sum_{n,n'} q_n q_{n'} e^{iq_n x}\int_0^t ds \int_0^t ds' e^{-Dq_n^2(t-s)}e^{-Dq_{n'}^2(t-s')}\langle \eta_{q_n}(s)\eta_{q_{n'}}(s')\rangle . \tag{5.9}$$

Equation (5.9) shows that, in order to compute the density fluctuations, we need to derive $\langle \eta_{q_n}(s)\eta_{q_{n'}}(s')\rangle$. Using our convention (5.2), it is given by

$$\langle \eta_{q_n}(s)\eta_{q_{n'}}(s')\rangle = \frac{1}{L^2}\int_0^L dx \int_0^L dx' e^{-iq_n x - iq_{n'}x'}\langle \eta(x,s)\eta(x',s')\rangle \tag{5.10}$$

$$\langle \eta_{q_n}(s)\eta_{q_{n'}}(s')\rangle = \frac{1}{L}\delta_{q_n+q_{n'},0}\, \delta(s-s') , \tag{5.11}$$

where, to go from (5.10) to (5.11), we have used that $\langle \eta(x,s)\eta(x',s')\rangle = \delta(s-s')\delta(x-x')$. Injecting (5.11) into (5.9), after a few lines of algebra, we obtain

$$\langle \delta\rho(x,t)\delta\rho(0,t)\rangle = \frac{2D\rho_0}{L}\sum_{n,n'} q_n^2\, e^{iq_n x}\delta_{q_n+q_{n'},0}\, e^{-2tDq_n^2}\int_0^t e^{2sDq_n^2}ds\ . \tag{5.12}$$

Performing the integral over s then yields

$$\langle \delta\rho(x,t)\delta\rho(0,t)\rangle = \frac{\rho_0}{L}\sum_n e^{iq_n x}\left(1-e^{-2tDq_n^2}\right)(1-\delta_{q_n,0})\ . \tag{5.13}$$

In steady state, we can neglect the term decaying exponentially in the above expression. We thus obtain the final form of the density fluctuations as

$$\langle \delta\rho(x,t)\delta\rho(0,t)\rangle = \frac{\rho_0}{L}\left(\sum_n e^{iq_n x}-1\right) = \rho_0\delta(x)-\frac{\rho_0}{L}\ . \tag{5.14}$$

We can readily extend our result (5.14) to a domain of volume V in arbitrary dimension d:

$$\langle \delta\rho(\mathbf{x},t)\delta\rho(0,t)\rangle = \rho_0\delta(\mathbf{x})-\frac{\rho_0}{V}\ . \tag{5.15}$$

Note that, for an infinite domain, (5.15) reduces to the usual two-point function for the ideal gas, *ie* $\langle \delta\rho(\mathbf{x},t)\delta\rho(0,t)\rangle = \rho_0\delta(\mathbf{x})$. However, for a finite-size system, (5.15) shows that there is a volume-dependent correction of the density correlations due to mass conservation. It turns out that such a correction is generic and also appears in the anisotropic model that we present hereafter in sections 5.3 to 5.4. Since we will be interested in the algebraic decay of the density fluctuations, $\langle \delta\rho(\mathbf{x})\delta\rho(0)\rangle \propto |\mathbf{x}|^{-\alpha}$, we will need to subtract this correction from the results of our numerical simulations before comparing them to the theoretical predictions obtained in infinite domain.

5.2 How anisotropic noise induces long-ranged correlations: the GLS model

In their contribution [99], Grinstein, Lee, and Sachdev described how an anisotropy in the stochastic evolution of a scalar field $\phi(\mathbf{x},t)$ could generate long-ranged correlations. This section is a brief review of their results and the interested reader might refer to [99] for a detailed analysis. The dynamics considered by Grinstein, Lee, and Sachdev is given by

$$\partial_t\phi(\mathbf{x},t) = D\boldsymbol{\nabla}^2\phi(\mathbf{x},t)+\eta(\mathbf{x},t)\ , \tag{5.16}$$

with D the diffusion coefficient and $\eta(\mathbf{x},t)$ a Gaussian white noise with variance such that

$$\langle \eta(\mathbf{x},t)\eta(\mathbf{x}',t')\rangle = 2\left(D_\perp\boldsymbol{\nabla}_\perp^2+D_\parallel\boldsymbol{\nabla}_\parallel^2\right)\delta(\mathbf{x}-\mathbf{x}')\delta(t-t')\ . \tag{5.17}$$

Eq (5.17) allows the presence of anisotropy by having two different constants, $D_\perp$ and $D_\parallel$, which describe the magnitudes of the noise in two orthogonal sub-spaces denoted $\perp$ and $\parallel$, respectively. For clarity, we assume that each of these subspaces is of dimension 1,

which amounts to looking at a system of dimension 2. The general case in an arbitrary dimension is treated in section 5.3.1 but leaves the physics unchanged. Note that if $D_\perp = D_\parallel$, dynamics (5.16) falls back to the one of the ideal gas (5.3) presented in section 5.1. On the contrary, whenever $D_\perp \neq D_\parallel$, dynamics (5.16) violates the Stokes-Einstein relation. Using our convention (5.1), we obtain $\phi_{w,\mathbf{k}}$ by performing a Fourier transform of the time evolution (5.16):

$$\phi_{w,\mathbf{k}} = \frac{\eta_{w,\mathbf{k}}}{D\mathbf{k}^2 - iw} \,, \tag{5.18}$$

where $\eta_{w,\mathbf{k}}$ is the fourier transform of the Gaussian white noise. Its variance is given by

$$\langle \eta_{w,\mathbf{k}} \eta_{w',\mathbf{k}'} \rangle = -2 \left(D_\perp k_\perp^2 + D_\parallel k_\parallel^2 \right) \delta(\mathbf{k} + \mathbf{k}') \delta(w + w') (2\pi)^3 \,. \tag{5.19}$$

Using the inverse Fourier transform (5.1), the density fluctuations can be expressed as

$$\langle \phi(\mathbf{x}, t) \phi(0, t) \rangle = \int \frac{d\mathbf{k} d\mathbf{k}'}{(2\pi)^4} \frac{dw dw'}{(2\pi)^2} e^{-i(w+w')t + i\mathbf{k}\cdot\mathbf{x}} \langle \phi_{w,\mathbf{k}} \phi_{w',\mathbf{k}'} \rangle \,. \tag{5.20}$$

Inserting (5.18) into (5.20) yields

$$\langle \phi(\mathbf{x}, t) \phi(0, t) \rangle = \int \frac{d\mathbf{k} d\mathbf{k}'}{(2\pi)^4} \frac{dw dw'}{(2\pi)^2} \frac{e^{-i(w+w')t + i\mathbf{k}\cdot\mathbf{x}}}{\left(D\mathbf{k}^2 - iw \right) \left(D\mathbf{k}'^2 - iw' \right)} \langle \eta_{w,\mathbf{k}} \eta_{w',\mathbf{k}'} \rangle \,. \tag{5.21}$$

Finally, injecting (5.19) in (5.21), and performing the integrals over the frequencies gives

$$\langle \phi(\mathbf{x}, t) \phi(0, t) \rangle = \int \frac{d\mathbf{k}}{(2\pi)^2} \frac{(D_\perp k_\perp^2 + D_\parallel k_\parallel^2)}{D\mathbf{k}^2} e^{i\mathbf{k}\cdot\mathbf{x}} \,. \tag{5.22}$$

Grinstein and co-authors remarked from (5.22) that the two-point function $\langle \phi(\mathbf{x}, t) \phi(0, t) \rangle$ is then given by

$$\langle \phi(\mathbf{x}, t) \phi(0, t) \rangle = \begin{cases} \dfrac{D_\parallel - D_\perp}{2\pi} \dfrac{x_\perp^2 - x_\parallel^2}{\mathbf{x}^4} & \text{if} \quad D_\perp \neq D_\parallel \\ \dfrac{D_\perp}{D} \, \delta(\mathbf{x}) & \text{if} \quad D_\perp = D_\parallel \end{cases} \,, \tag{5.23}$$

where $x_\perp$ and $x_\parallel$ are the coordinates in the $\perp$ and $\parallel$ directions, respectively. In particular, from (5.23), we note that, whenever $D_\perp \neq D_\parallel$, $\langle \phi(\mathbf{x}, t) \phi(0, t) \rangle \propto |\mathbf{x}|^{-2}$ in the limit $|\mathbf{x}| \to \infty$: anisotropy induces long-ranged correlations out of equilibrium.

The GLS model thus possesses two landmark features of nonequilibrium: the emergence of scale-free fluctuations and the violation of the Stokes-Einstein relation. However, is the anisotropic dynamics (5.16) truly out-of-equilibrium ? To answer this question, let us now assess time-reversal symmetry for the field $\phi(\mathbf{x}, t)$. The probability $\mathcal{P}(\{\phi_\mathbf{k}\})$ to observe a given trajectory of the Fourier modes $\phi_\mathbf{k}(t)$, for $t \in [0, t_f]$, reads

$$\mathcal{P}(\{\phi_\mathbf{k}\}) \propto \exp \left(\int_0^{t_f} dt \int d\mathbf{k} \frac{|\dot{\phi}_\mathbf{k} + \mathbf{k}^2 \phi_\mathbf{k}|^2}{D_\perp k_\perp^2 + D_\parallel k_\parallel^2} \right) \,. \tag{5.24}$$

The field-theoretic entropy production rate is defined as

$$\sigma = \lim_{t_f \to \infty} \frac{1}{t_f} \ln \left(\frac{\mathcal{P}(\{\phi_\mathbf{k}\})}{\mathcal{P}(\{\phi_\mathbf{k}^R\})} \right) \,, \tag{5.25}$$

where $\{\phi^R_{\mathbf{k}}\}$ is the reversed trajectory of the Fourier modes, *ie* $\phi^R_{\mathbf{k}}(t) = \phi^R_{\mathbf{k}}(t_f - t)$ for arbitrary $\mathbf{k}$. Inserting (5.24) into (5.25), we obtain the entropy production rate as

$$\sigma = \lim_{t_f\to\infty} \frac{1}{t_f}\left[\int d\mathbf{k} \frac{\mathbf{k}^2|\phi_{\mathbf{k}}|^2}{D_\perp k_\perp^2 + D_\parallel k_\parallel^2}\right]_0^{t_f} = 0\ . \tag{5.26}$$

Interestingly, Eq (5.26) shows that the GLS dynamics (5.16)-(5.17) is time-reversal symmetric. It is thus an exotic system reminescent of the ABC model [87], for which long-ranged correlations are observed, but detailed balance is recovered for special choices of the parameters. Note, however, that if ϕ represents a density field, the microscopic dynamics corresponding to the GLS time evolution (5.16)-(5.17) does not contain any interactions between the particles. As non-interacting systems of particles have a factorized stationary distribution, they cannot exhibit long-ranged density correlations. Therefore, the GLS model (5.16)-(5.17) cannot physically describe the evolution of a density field as it stands. The remainder of this chapter is devoted to the construction of a microscopic system composed of particles interacting anisotropically for which density correlations are scale-free.

5.3 An anisotropic particle-based model

We consider N particles that are submitted to anisotropic Gaussian white noises and evolve according to

$$\dot{\mathbf{r}}_i(t) = \boldsymbol{\eta}_i(t)\ , \quad \text{with} \quad \begin{cases} \langle \eta_i^\alpha(t)\eta_i^\beta(t')\rangle = & D\delta_{\alpha\beta}\delta(t-t') \\ \langle \eta_i^\alpha(t)\eta_j^\beta(t')\rangle = & h^{\alpha\beta}(\mathbf{r}_i - \mathbf{r}_j)\delta(t-t') \quad \text{for} \quad i\neq j\ . \end{cases} \tag{5.27}$$

We now derive the equation of motion for the density field defined as

$$\rho(\mathbf{r},t) = \sum_i \delta(\mathbf{r} - \mathbf{r}_i(t))\ . \tag{5.28}$$

Using Itō calculus [160], and following the procedure introduced in [159], we obtain

$$\begin{aligned}\partial_t\rho(\mathbf{r},t) = &\sum_i [\boldsymbol{\nabla}_{\mathbf{r}_i}\delta(\mathbf{r}-\mathbf{r}_i(t))]\cdot\dot{\mathbf{r}}_i + \frac{D}{2}\sum_{i,\alpha}\partial_i^\alpha\partial_i^\alpha\sum_j\delta(\mathbf{r}-\mathbf{r}_j(t)) \\ &+ \frac{1}{2}\sum_{i,j\neq i}\sum_{\alpha,\beta}h^{\alpha\beta}(\mathbf{r}_i-\mathbf{r}_j)\partial_i^\alpha\partial_j^\beta\sum_k\delta(\mathbf{r}-\mathbf{r}_k(t))\ .\end{aligned} \tag{5.29}$$

The last term on the right-hand side of (5.29) vanishes and, using the equation of motion for $\mathbf{r}_i$, we get

$$\partial_t\rho(\mathbf{r},t) = -\boldsymbol{\nabla}_{\mathbf{r}}\cdot\left[\sum_i \boldsymbol{\eta}_i\delta(\mathbf{r}-\mathbf{r}_i(t))\right] + \frac{D}{2}\boldsymbol{\nabla}^2\left[\rho(\mathbf{r},t)\right]\ . \tag{5.30}$$

We rewrite this equation as

$$\partial_t\rho(\mathbf{r},t) = -\boldsymbol{\nabla}\cdot[\boldsymbol{\Lambda}] + \frac{D}{2}\boldsymbol{\nabla}^2\left[\rho(\mathbf{r},t)\right]\ , \tag{5.31}$$

where $\boldsymbol{\Lambda}(\mathbf{r},t)$ is given by

$$\boldsymbol{\Lambda}(\mathbf{r},t) = \sum_i \boldsymbol{\eta}_i\delta(\mathbf{r}-\mathbf{r}_i(t))\ . \tag{5.32}$$

As the noise $\mathbf{\Lambda}(\mathbf{r},t)$ is a sum of Gaussian white noises, it is itself a Gaussian white noise and we compute its correlations as

$$\langle \Lambda^\alpha(\mathbf{r},t)\Lambda^\beta(\mathbf{r}',t')\rangle = \langle \sum_{i,j} \eta_i^\alpha \eta_j^\beta \delta(\mathbf{r}-\mathbf{r}_i(t))\delta(\mathbf{r}'-\mathbf{r}_j(t'))\rangle \ . \tag{5.33}$$

Splitting the contributions from $i=j$ and $i\neq j$, we obtain

$$\begin{aligned}\langle \Lambda^\alpha(\mathbf{r},t)\Lambda^\beta(\mathbf{r}',t')\rangle = &\sum_{i,j\neq i} h^{\alpha\beta}(\mathbf{r}_i-\mathbf{r}_j)\delta(\mathbf{r}-\mathbf{r}_i(t))\delta(\mathbf{r}'-\mathbf{r}_j(t'))\delta(t-t') \\ &+ \sum_i D\delta_{\alpha\beta}\delta(\mathbf{r}-\mathbf{r}_i(t))\delta(\mathbf{r}'-\mathbf{r}_i(t'))\delta(t-t') \ .\end{aligned} \tag{5.34}$$

Further setting $h^{\alpha\beta}(0)=0$ [159], which only affects the zero-measure event $\mathbf{r}_i=\mathbf{r}_j$, we transform the restricted sum over $i\neq j$ in the above equation into a complete sum over i and j to get

$$\langle \Lambda^\alpha(\mathbf{r},t)\Lambda^\beta(\mathbf{r}',t')\rangle = \left[D\delta_{\alpha\beta}\rho(\mathbf{r},t)\delta(\mathbf{r}-\mathbf{r}') + h^{\alpha\beta}(\mathbf{r}-\mathbf{r}')\rho(\mathbf{r},t)\rho(\mathbf{r}',t)\right]\delta(t-t') \ . \tag{5.35}$$

5.3.1 Generic form of density correlations in infinite systems

We now study the behaviour of the density fluctuations emerging from the dynamics (5.31) together with (5.35). Looking for a solution of the form $\rho=\rho_0+\delta\rho$, we linearize the Dean-Kawasaki equation (5.31) to obtain the dynamics of $\delta\rho$ as

$$\partial_t\delta\rho = -\boldsymbol{\nabla}\cdot\mathbf{\Lambda} + \frac{D}{2}\boldsymbol{\nabla}^2[\delta\rho] \ , \tag{5.36}$$

where the correlation of the noise $\mathbf{\Lambda}(\mathbf{r},t)$ has also been linearized and satisifies

$$\langle \Lambda^\alpha(\mathbf{r},t)\Lambda^\beta(\mathbf{r}',t')\rangle = \left[D\rho_0\delta_{\alpha\beta}\delta(\mathbf{r}-\mathbf{r}') + h^{\alpha\beta}(\mathbf{r}-\mathbf{r}')\rho_0^2\right]\delta(t-t') \ . \tag{5.37}$$

Taking the Fourier transform of (5.36) using convention (5.1), we obtain the density fluctuations in Fourier space as

$$\delta\rho_{w,\mathbf{k}} = \frac{ik_\alpha\Lambda^\alpha_{\mathbf{k}}}{iw-\frac{D}{2}\mathbf{k}^2} \ . \tag{5.38}$$

Further assuming $h^{\alpha\beta}(\mathbf{r})$ to be even, which amounts to $h_{\mathbf{k}}=h_{-\mathbf{k}}$ in Fourier space, we compute that

$$\langle \Lambda^\alpha_{w,\mathbf{k}}\Lambda^\beta_{w',\mathbf{k}'}\rangle = \left(D\rho_0\delta_{\alpha\beta}+\rho_0^2 h^{\alpha\beta}(\mathbf{k})\right)\delta(\mathbf{k}+\mathbf{k}')\delta(w+w')(2\pi)^{d+1} \ . \tag{5.39}$$

Using our Fourier convention (5.1), we derive the two-point correlation function of the density fluctuations as

$$\langle \delta\rho(\mathbf{x},t)\delta\rho(\mathbf{x}',t')\rangle = \int dwd\mathbf{k}dw'd\mathbf{k}'\langle\delta\rho_{w,\mathbf{k}}\delta\rho_{w',\mathbf{k}'}\rangle\frac{e^{i\mathbf{k}\cdot\mathbf{x}+i\mathbf{k}'\cdot\mathbf{x}'-itw-it'w'}}{(2\pi)^{2d+2}} \ . \tag{5.40}$$

Inserting (5.38) in (5.40), we obtain

$$\langle \delta\rho(\mathbf{x},t)\delta\rho(\mathbf{x}',t')\rangle = \int dwd\mathbf{k}dw'd\mathbf{k}'\frac{ik_\alpha ik'_\beta\langle\Lambda^\alpha_{\mathbf{k}}\Lambda^\beta_{\mathbf{k}'}\rangle}{\left(iw-\frac{D}{2}\mathbf{k}^2\right)\left(iw'-\frac{D}{2}\mathbf{k}'^2\right)}\frac{e^{i\mathbf{k}\cdot\mathbf{x}+i\mathbf{k}'\cdot\mathbf{x}'-itw-it'w'}}{(2\pi)^{2d+2}} \ . \tag{5.41}$$

Injecting (5.39) in (5.41) and performing the integrations over $\mathbf{k}'$ and w' then yields

$$\langle \delta\rho(\mathbf{x},t)\delta\rho(\mathbf{x}',t')\rangle = \int d\mathbf{k}dw \frac{k_\alpha k_\beta \left(D\rho_0\delta_{\alpha\beta} + \rho_0^2 h^{\alpha\beta}(\mathbf{k})\right)}{\left(iw - \frac{D}{2}\mathbf{k}^2\right)\left(-iw - \frac{D}{2}\mathbf{k}^2\right)} \frac{e^{i\mathbf{k}(\mathbf{x}-\mathbf{x}')-iw(t-t')}}{(2\pi)^{d+1}} . \tag{5.42}$$

As D is a diffusion coefficient, it must be positive, and we can integrate (5.42) over w using the residue theorem for $t = t'$. We obtain

$$\langle \delta\rho(\mathbf{x},t)\delta\rho(0,t)\rangle = \int \frac{d\mathbf{k}}{(2\pi)^d} e^{i\mathbf{k}\cdot\mathbf{x}} \left[\rho_0 + \frac{\rho_0^2 k_\alpha k_\beta\, h^{\alpha\beta}(\mathbf{k})}{D\mathbf{k}^2}\right] . \tag{5.43}$$

The term proportional to ρ_0 on the right-hand side of the above equation corresponds to a Dirac distribution in real space and we get

$$\langle \delta\rho(\mathbf{x},t)\delta\rho(0,t)\rangle = \rho_0\delta(\mathbf{x}) + \rho_0^2 \int \frac{d\mathbf{k}}{(2\pi)^d} \frac{k_\alpha k_\beta h^{\alpha\beta}(\mathbf{k})}{D\mathbf{k}^2} e^{i\mathbf{k}\cdot\mathbf{x}} . \tag{5.44}$$

We now assume that $h^{\alpha\beta}$ is diagonal but has one anisotropic direction $h_\parallel$ and $\mathrm{d}-1$ others equivalent directions $h_\perp$

$$h^{\alpha\beta}(\mathbf{x}) = \begin{pmatrix} h_\parallel(\mathbf{x}) & 0 & \dots & 0 \\ 0 & h_\perp(\mathbf{x}) & \ddots & \vdots \\ \vdots & \ddots & \ddots & 0 \\ 0 & \dots & 0 & h_\perp(\mathbf{x}) \end{pmatrix} . \tag{5.45}$$

We have yet to specify the functions $h_\perp(\mathbf{x})$ and $h_\parallel(\mathbf{x})$. They must be even functions and the integral in (5.44) has to be well-behaved. We thus propose $h_\perp(\mathbf{k}) = h_\perp h_0(\mathbf{k})$ and $h_\parallel(\mathbf{k}) = h_\parallel h_0(\mathbf{k})$ with $h_0(\mathbf{k}) = \sigma^{2+d}e^{-\sigma^2\mathbf{k}^2/2}$. In real space, we obtain

$$h_\perp(\mathbf{x}) = h_\perp h_0(\mathbf{x}) , \quad h_\parallel(\mathbf{x}) = h_\parallel h_0(\mathbf{x}) , \quad \text{with} \quad h_0(\mathbf{x}) = \frac{\sigma^2}{(\sqrt{2\pi})^d} e^{-\frac{\mathbf{x}^2}{2\sigma^2}} . \tag{5.46}$$

Using these expressions for $h_\perp(\mathbf{x})$ and $h_\parallel(\mathbf{x})$, we compute the integral term in the density correlations (5.44). We first express it in terms of the derivatives of an isotropic function

$$\rho_0^2 \int \frac{d\mathbf{k}}{(2\pi)^2} \frac{k_\alpha k_\beta h^{\alpha\beta}(\mathbf{k})}{D\mathbf{k}^2} e^{i\mathbf{k}\cdot\mathbf{x}} = \frac{\rho_0^2}{D}\left(h_\perp \boldsymbol{\nabla}_\perp^2 + h_\parallel \partial_\parallel^2\right) H(\mathbf{x}) , \tag{5.47}$$

with $H(\mathbf{x})$ given by

$$H(\mathbf{x}) = \int \frac{d\mathbf{k}}{(2\pi)^d} \frac{h_0(\mathbf{k})}{\mathbf{k}^2} e^{i\mathbf{k}\cdot\mathbf{x}} . \tag{5.48}$$

By definition, we remark that $H(\mathbf{x})$ is in fact solution of the Poisson equation

$$\boldsymbol{\nabla}^2 H(\mathbf{x}) = h_0(\mathbf{x}) . \tag{5.49}$$

Because H and h_0 are isotropic, this Poisson equation is only radial and reads

$$\frac{1}{r^{\mathrm{d}-1}} \frac{d}{dr}\left(r^{\mathrm{d}-1}\frac{dH}{dr}\right) = \frac{\sigma^2}{(2\pi)^{\frac{\mathrm{d}}{2}}} e^{-\frac{r^2}{2\sigma^2}} . \tag{5.50}$$

It can be integrated to yield dH/dr as a function of the radius r

$$\frac{dH}{dr} = -\frac{\sigma^{\mathrm{d}+2}}{2\pi^{\frac{\mathrm{d}}{2}} r^{\mathrm{d}-1}} \Psi\left(\frac{\mathrm{d}}{2}, \frac{r^2}{2\sigma^2}\right) + \frac{b}{r^{\mathrm{d}-1}} \,, \tag{5.51}$$

where Ψ is the incomplete Gamma function $\Psi(u,v) = \int_v^\infty s^{u-1} e^{-s} ds$ and b is an integration constant that we now set up to determine. To this aim, let us integrate $\boldsymbol{\nabla}^2 H$ over a hypersphere of radius R containing the origin. Using the Poisson equation (5.49), we have that

$$\int_{V_R} \boldsymbol{\nabla}^2 H = \frac{\int_0^R r^{\mathrm{d}-1} h_0(r) dr}{\int_0^R r^{\mathrm{d}-1} dr} V_R \,, \tag{5.52}$$

where V_R is the volume of the hypersphere. On the other hand, Green-Ostrogradski theorem tells us that

$$\int_{V_R} \boldsymbol{\nabla}^2 H = \oint_{S_R} \vec{\nabla} H . d\vec{S} = S_R \left.\frac{dH}{dr}\right|_R \,, \tag{5.53}$$

where S_R is the area of the hypersphere of radius R. Equating both quantities gives

$$\left.\frac{dH}{dr}\right|_R = \frac{\int_0^R r^{\mathrm{d}-1} h_0(r) dr}{\int_0^R r^{\mathrm{d}-1} dr} \frac{V_R}{S_R} \,. \tag{5.54}$$

Using the expression of $h_0(r)$ and the tabulated value of the ratio $V_R/S_R = R\Gamma(\mathrm{d}/2)/\Gamma(\mathrm{d}/2+1)/2$ with $\Gamma(u)$ the Gamma function, we obtain

$$\left.\frac{dH}{dr}\right|_R = \frac{\Gamma(\frac{\mathrm{d}}{2})}{\Gamma(\frac{\mathrm{d}}{2}+1)} \frac{\mathrm{d}}{2} \frac{\sigma^{\mathrm{d}+2}}{2\pi^{\frac{\mathrm{d}}{2}} R^{\mathrm{d}-1}} \left[\Gamma\left(\frac{\mathrm{d}}{2}\right) - \Psi\left(\frac{\mathrm{d}}{2}, \frac{R^2}{2\sigma^2}\right)\right] \,. \tag{5.55}$$

Using the property $\Gamma(x)x = \Gamma(x+1)$ of the Gamma function, we get

$$\left.\frac{dH}{dr}\right|_R = \frac{\sigma^{\mathrm{d}+2}}{2\pi^{\frac{\mathrm{d}}{2}} R^{\mathrm{d}-1}} \left[\Gamma\left(\frac{\mathrm{d}}{2}\right) - \Psi\left(\frac{\mathrm{d}}{2}, \frac{R^2}{2\sigma^2}\right)\right] \,. \tag{5.56}$$

Finally replacing dH/dr by its expression in (5.51) gives the value of b as

$$b = \frac{\sigma^{\mathrm{d}+2}}{2\pi^{\frac{\mathrm{d}}{2}}} \Gamma\left(\frac{\mathrm{d}}{2}\right) \,. \tag{5.57}$$

We thus obtain dH/dr as

$$\frac{dH}{dr} = \frac{\sigma^{\mathrm{d}+2}}{2\pi^{\frac{\mathrm{d}}{2}} r^{\mathrm{d}-1}} \left[\Gamma\left(\frac{\mathrm{d}}{2}\right) - \Psi\left(\frac{\mathrm{d}}{2}, \frac{r^2}{2\sigma^2}\right)\right] \,. \tag{5.58}$$

We now have to derive H twice, once with respect to the $\parallel$ directon, and once with respect to one of the $\perp$ directions. We decompose the vector $\mathbf{x}$ according to $\mathbf{x} = x_\parallel \mathbf{e}_\parallel + \mathbf{x}_\perp$ with $\mathbf{x}_\perp = x_\perp^1 \mathbf{e}_\perp^1 + \cdots + x_\perp^{\mathrm{d}-1} \mathbf{e}_\perp^{\mathrm{d}-1}$. Let us start by deriving H with respect to one of the $\perp$ direction $x_\perp^\alpha$

$$\frac{\partial^2 H}{\partial^2 x_\perp^\alpha} = \frac{\sigma^2 (x_\perp^\alpha)^2}{(\sqrt{2\pi})^{\mathrm{d}} r^2} e^{-\frac{r^2}{2\sigma^2}} + \frac{\sigma^{2+\mathrm{d}}}{2\pi^{\frac{\mathrm{d}}{2}} r^{2+\mathrm{d}}} \left[r^2 - \mathrm{d}(x_\perp^\alpha)^2\right] \left[\Gamma\left(\tfrac{d}{2}\right) - \Psi\left(\tfrac{\mathrm{d}}{2}, \tfrac{r^2}{2\sigma^2}\right)\right] \tag{5.59}$$

Making the change $x_\perp^\alpha \leftrightarrow x_\parallel$, we deduce by symmetry that

$$\frac{\partial^2 H}{\partial^2 x_\parallel} = \frac{\sigma^2 x_\parallel^2}{(\sqrt{2\pi})^{\mathrm{d}} r^2} e^{-\frac{r^2}{2\sigma^2}} + \frac{\sigma^{2+\mathrm{d}}}{2\pi^{\frac{\mathrm{d}}{2}} r^{2+\mathrm{d}}} \left[r^2 - \mathrm{d}x_\parallel^2\right] \left[\Gamma\left(\tfrac{\mathrm{d}}{2}\right) - \Psi\left(\tfrac{\mathrm{d}}{2}, \tfrac{r^2}{2\sigma^2}\right)\right] \,. \tag{5.60}$$

Using (5.59) and (5.60), we can compute the anisotropic Laplacian of (5.47) as

$$\left(h_\perp \boldsymbol{\nabla}_\perp^2 + h_\parallel \partial_\parallel^2\right) H(\mathbf{x}) = \frac{\sigma^{2+\mathrm{d}}(h_\parallel - h_\perp)}{2\pi^{\frac{\mathrm{d}}{2}} r^{2+\mathrm{d}}} \left[r^2 - \mathrm{d}x_\parallel^2\right] \left[\Gamma\left(\tfrac{\mathrm{d}}{2}\right) - \Psi\left(\tfrac{\mathrm{d}}{2}, \tfrac{r^2}{2\sigma^2}\right)\right] + \frac{\sigma^2\left(h_\perp \mathbf{x}_\perp^2 + h_\parallel x_\parallel^2\right)}{(\sqrt{2\pi})^{\mathrm{d}} r^2} e^{-\frac{r^2}{2\sigma^2}} . \tag{5.61}$$

Wrapping everything together, we obtain

$$\frac{\rho_0^2}{D}\int \frac{d\mathbf{k}}{(2\pi)^2} \frac{k_\alpha k_\beta h^{\alpha\beta}(\mathbf{k})}{\mathbf{k}^2} e^{i\mathbf{k}\cdot\mathbf{x}} = \frac{\rho_0^2\sigma^2}{\pi^{\frac{\mathrm{d}}{2}} D r^2}\left(\frac{\sigma^{\mathrm{d}}(h_\parallel - h_\perp)}{2r^{\mathrm{d}}} \left[r^2 - \mathrm{d}x_\parallel^2\right] \left[\Gamma\left(\tfrac{\mathrm{d}}{2}\right) - \Psi\left(\tfrac{\mathrm{d}}{2}, \tfrac{r^2}{2\sigma^2}\right)\right] + \frac{h_\perp \mathbf{x}_\perp^2 + h_\parallel x_\parallel^2}{2^{\frac{\mathrm{d}}{2}}} e^{-\frac{r^2}{2\sigma^2}}\right) . \tag{5.62}$$

Inserting the above expression into (5.44), we derive the correlation of the density fluctuations in real space as

$$\langle \delta\rho(\mathbf{x},t)\delta\rho(0,t)\rangle = \frac{\rho_0^2\sigma^2}{\pi^{\frac{\mathrm{d}}{2}} D}\left(\frac{\sigma^{\mathrm{d}}(h_\parallel - h_\perp)}{2r^{\mathrm{d}}} \left[1 - \frac{\mathrm{d}x_\parallel^2}{r^2}\right] \left[\Gamma\left(\tfrac{\mathrm{d}}{2}\right) - \Psi\left(\tfrac{\mathrm{d}}{2}, \tfrac{r^2}{2\sigma^2}\right)\right] + \frac{h_\perp \mathbf{x}_\perp^2 + h_\parallel x_\parallel^2}{2^{\frac{\mathrm{d}}{2}} r^2} e^{-\frac{r^2}{2\sigma^2}}\right) + \rho_0\delta(\mathbf{x}) . \tag{5.63}$$

When $|\mathbf{x}| = r \to \infty$, $\Psi\left(\frac{\mathrm{d}}{2}, \frac{r^2}{2\sigma^2}\right) \propto e^{-\frac{r^2}{2\sigma^2}}$, and the two-point function exhibits a long-ranged, algebraic decay $\propto r^{-\mathrm{d}}$

$$\langle \delta\rho(\mathbf{x},t)\delta\rho(0,t)\rangle = \frac{\rho_0^2\sigma^{2+\mathrm{d}}}{2\pi^{\frac{\mathrm{d}}{2}} D r^{\mathrm{d}}}\left(1 - \mathrm{d}\frac{x_\parallel^2}{r^2}\right)\left(h_\parallel - h_\perp\right)\Gamma(\tfrac{\mathrm{d}}{2}) + \mathcal{O}\left(r^{-\mathrm{d}}\right) \tag{5.64}$$

Having detailed how the specific dynamics (5.27) leads to the algebraically decaying density fluctuations of (5.63), we now verify our predictions by performing numerical simulations.

5.3.2 Numerical simulations in finite-size systems

In this section, we describe how to simulate a system of N particles evolving according to (5.27) with isotropic auto-correlation $\sigma^{\alpha\beta} = D\delta_{\alpha\beta}$ and anisotropic pair-correlation $h^{\alpha\beta}(\mathbf{r}) = h^\alpha(\mathbf{r})\delta_{\alpha\beta}$. To this aim, we consider the noise η_i^α acting on the α coordinate of the i-th particle to be a sum of N Gaussian white noises, each of them corresponding to a pairing of particles

$$\eta_i^\alpha = \sqrt{h^\alpha(\mathbf{r}_i - \mathbf{r}_1)}\eta_{i,1}^\alpha + \sqrt{h^\alpha(\mathbf{r}_i - \mathbf{r}_2)}\eta_{i,2}^\alpha + \ldots + \sqrt{\gamma^\alpha}\,\eta_{i,i}^\alpha + \ldots + \sqrt{h^\alpha(\mathbf{r}_i - \mathbf{r}_N)}\eta_{i,N}^\alpha . \tag{5.65}$$

We further enforce pairing symmetry $h^\alpha(\mathbf{r}_i - \mathbf{r}_j) = h^\alpha(\mathbf{r}_j - \mathbf{r}_i)$ and $\eta_{i,j}^\alpha = \eta_{j,i}^\alpha$ such that $\langle \eta_{i,j}^\alpha \eta_{k,l}^\beta\rangle = \delta_{\alpha\beta}(\delta_{ik}\delta_{jl} + \delta_{il}\delta_{jk})\delta(t-t')$. We now compute the noise correlation between two different particles $i \neq j$ as

$$\langle \eta_i^\alpha \eta_j^\beta\rangle = \sum_{k,l}\langle \eta_{i,k}^\alpha \eta_{j,l}^\beta\rangle \sqrt{h^\alpha(\mathbf{r}_i - \mathbf{r}_k)}\sqrt{h^\beta(\mathbf{r}_j - \mathbf{r}_l)} \tag{5.66}$$

$$= \sum_{k,l}\delta_{\alpha\beta}\left(\delta_{ij}\delta_{kl} + \delta_{il}\delta_{jk}\right)\delta(t-t')\sqrt{h^\alpha(\mathbf{r}_i - \mathbf{r}_k)}\sqrt{h^\beta(\mathbf{r}_j - \mathbf{r}_l)} . \tag{5.67}$$

Since $i \neq j$, we find

$$\langle \eta_i^\alpha \eta_j^\beta \rangle = h^\alpha(\mathbf{r}_i - \mathbf{r}_j)\delta_{\alpha\beta}\delta(t - t') \; . \tag{5.68}$$

Furthermore, the noise auto-correlation on particle i reads

$$\langle \eta_i^\alpha \eta_i^\beta \rangle = \delta_{\alpha\beta} \left(\sum_{j \neq i} h^\alpha(\mathbf{r}_i - \mathbf{r}_j) + \gamma^\alpha \right) \; . \tag{5.69}$$

Thus, if we impose $\gamma^\alpha = D - \sum_{j\neq i} h^\alpha(\mathbf{r}_i - \mathbf{r}_j)$ we recover

$$\langle \eta_i^\alpha \eta_i^\beta \rangle = D\delta_{\alpha\beta} \; . \tag{5.70}$$

By introducing $\mathrm{d}N(N+1)/2$ Gaussian white noises, we are thus able to simulate the noise in dynamics (5.27). However, D is not independent of the other parameters since it must be sufficiently large such that $D - \sum_j h^\alpha(\mathbf{r}_i - \mathbf{r}_j)$ remains positive. Otherwise the noise η_i^α would have a negative variance in our dynamics: this would be unphysical. In practice, to chose D in the simulations, we compute the average number of particles within a circle of radius 5σ and we multiply it by the maximum between $h_\parallel(\mathbf{x} = 0)$ and $h_\perp(\mathbf{x} = 0)$. This sets an upper bound for the sum $\sum_j h^\alpha(\mathbf{r}_i - \mathbf{r}_j)$. Equating D with this upper bound then yields

$$D \sim 9\rho_0(5\sigma)^2 \max(h_\perp, h_\parallel)\frac{\sigma^2}{2\pi} \tag{5.71}$$

In practice, (5.71) proved itself to be a sufficient choice in the simulations.

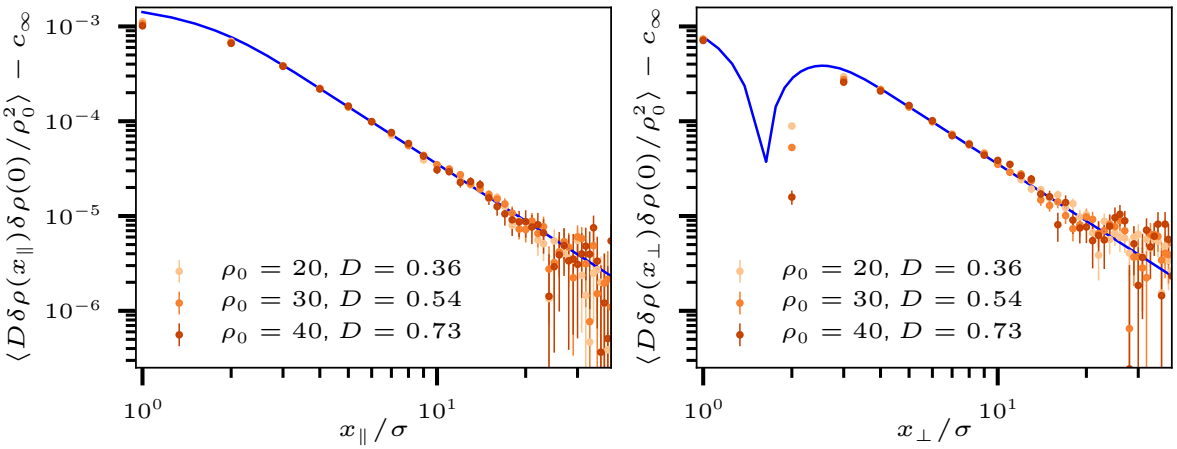

Figure 5.1 – Correlation of the density fluctuations in the $\parallel$ and $\perp$ direction for different values of $\rho_0 = N/(L_\perp L_\parallel)$ and diffusion D. The blue line is the prediction of (5.72) for $\mathrm{d} = 2$ and $V = L_\parallel \times L_\perp$. Note that we have subtracted the finite-size correction ρ_0/V. The orange dots are obtained via numerical simulations of the Langevin system described by (5.27) as explained in section 5.3.2. The error bars correspond to the standard deviation. Parameters: $L_\parallel = 20$, $L_\perp = 20$, $dt = 0.01$, $\sigma = 0.15$.

Note that, in simulations, we have only access to finite-size systems of volume V. In this case, as shown in (5.15) of section 5.1, a finite-size correction $c_\infty = -\rho_0/V$ must be

subtracted from the density fluctuations of Eq (5.63) to enforce mass conservation. The two-point function measured in finite-size simulations thus satisfies

$$\langle \delta\rho(\mathbf{x},t)\delta\rho(0,t)\rangle - c_\infty = \frac{\rho_0^2\sigma^2}{\pi^{\frac{\mathrm{d}}{2}}D}\left(\frac{\sigma^{\mathrm{d}}(h_\parallel - h_\perp)}{2r^{\mathrm{d}}}\left[1-\frac{\mathrm{d}x_\parallel^2}{r^2}\right]\left[\Gamma\left(\tfrac{\mathrm{d}}{2}\right)-\Psi\left(\tfrac{\mathrm{d}}{2},\tfrac{r^2}{2\sigma^2}\right)\right] + \frac{h_\perp \mathbf{x}_\perp^2 + h_\parallel x_\parallel^2}{2^{\frac{\mathrm{d}}{2}}r^2}e^{-\frac{r^2}{2\sigma^2}}\right) + \rho_0\delta(\mathbf{x})\ . \tag{5.72}$$

In Fig. 5.1, we compare our expression (5.72) for the correlator $\langle \delta\rho(\mathbf{x},t)\delta\rho(0,t)\rangle$ with the results of numerical simulations performed in a 2D periodic system of size $L_\perp \times L_\parallel$. Without any fitting parameters, the theory accurately follows the data over one decade and a half, confirming the emergence of algebraic decay at the macroscopic level. We conclude that an anisotropic noise can efficiently induce long-ranged correlations through a GLS mechanism. As our microscopic dynamics (5.27) effectively corresponds to a system of N particles evolving in a Gaussian field $\boldsymbol{\psi}(\mathbf{x},t)$ of variance $\langle \psi^\alpha(\mathbf{x},t)\psi^\beta(\mathbf{x}',t')\rangle = h^{\alpha\beta}(\mathbf{x}-\mathbf{x}')\delta(t-t')$, it would be interesting to find a corresponding experimental realization. For example, one could use a laser with an elliptic beam, whose principal and secondary axis corresponds to the $\parallel$ and $\perp$ directions, respectively. Heating self-phoretic particles with such an anisotropic light source could then yield dynamics (5.27).

Having established the existence of long-ranged density fluctuations in anisotropic systems, we now study the physical implications of such an atypical behaviour. Indeed, previous works [86,88–90,95,161] have exhibited a clear relationship between algebraically decaying density correlations and the existence of Casimir forces for a system confined between two plates separated by a distance L.

5.4 Casimir forces: a generic feature of long-ranged density fluctuations ?

In this section, we study how the dynamics (5.27) behaves under confinement and determine the corresponding pressure induced by the particles on the walls. To simplify our study, we consider the case of a 2-dimensional system of size $L_\parallel \times L_\perp$ with periodic boundary conditions in the $\parallel$ direction. Confinement takes place in the $\perp$ direction: we assume that two walls are located at positions $x_\perp = 0$ and $x_\perp = L_\perp$. We model them by a smooth potential such that $\boldsymbol{\nabla}\phi = \partial_\perp\phi(x_\perp)\mathbf{e}_\perp$, where $\phi(0 < x_\perp < L_\perp) = 0$ in the bulk, whereas ϕ sharply increases for $x_\perp < 0$ and $x_\perp > L_\perp$. In Fig. 5.2, we represent $\phi(x_\perp)$ as a function of $x_\perp$ in the case of quadratic walls of stiffness κ.

We first show that the global pressure measured by an observer on the walls does not exhibit the Casimir-like dependence that we could have expected based on previous observations made for specific nonequilibrium systems [89]. However, as we then show, the equal time fluctuations of the local pressure $\langle p(0,x_\parallel)p(L_\perp,x_\parallel)\rangle - \langle p(0,x_\parallel)\rangle\langle p(L_\perp,x_\parallel)\rangle$ exerted on the two facing sides of the plates does show a Casimir behaviour with an algebraic decay $\propto L_\perp^{-2}$.

The confinement modifies the dynamics (5.27) of the particles according to

$$\dot{\mathbf{r}}_i(t) = -\boldsymbol{\nabla}\phi + \boldsymbol{\eta}_i(t)\ , \quad \text{with} \quad \begin{cases} \langle \eta_i^\alpha(t)\eta_i^\beta(t')\rangle = & D\delta_{\alpha\beta}\delta(t-t') \\ \langle \eta_i^\alpha(t)\eta_j^\beta(t')\rangle = & h^{\alpha\beta}(\mathbf{r}_i-\mathbf{r}_j)\delta(t-t') \quad \text{for} \quad i\neq j\ . \end{cases} \tag{5.73}$$

The time-evolution of the density field $\rho(\mathbf{x},t)$ is thus modified accordingly into

$$\partial_t \rho(\mathbf{r},t) = \boldsymbol{\nabla}\cdot\left[\rho(\mathbf{r},t)\boldsymbol{\nabla}\phi - \boldsymbol{\Lambda}\right] + \frac{D}{2}\boldsymbol{\nabla}^2\left[\rho(\mathbf{r},t)\right] \ , \tag{5.74}$$

where the correlations of the Gaussian noise $\boldsymbol{\Lambda}(\mathbf{r},t)$ are still given by (5.35). Averaging (5.74) over the noise's realizations, the mean steady-state density profile is simply given by the Boltzmann weight:

$$\langle\rho(\mathbf{r})\rangle = \rho_b \exp\left(-2\frac{\phi(x_\perp)}{D}\right) \ , \tag{5.75}$$

where ρ_b is the density in the bulk for $0 < x_\perp < L$. The pressure P_ℓ exerted on the wall located at $x_\perp = 0$ is obtained as the total force exerted by the particles on this wall divided by its length $L_\parallel$. Introducing the rectangle $V_\ell = [0, L_\parallel] \times [-\infty, x_\perp^b]$, where the coordinate $x_\perp^b$ must lie inside the bulk, *ie* $0 < x_\perp^b < L_\perp$, we express P_ℓ as

$$P_\ell(t) = -\frac{1}{L_\parallel}\int_{V_\ell} d\mathbf{r}\rho(\mathbf{r},t)\partial_\perp\phi(\mathbf{r}) \ . \tag{5.76}$$

Note that the pressure defined in (5.76) is a stochastic quantity because ρ is itself a stochastic field. Its first moment in the steady state satisifies

$$\langle P_\ell\rangle = -\frac{1}{L_\parallel}\int_{V_\ell} d\mathbf{r}\langle\rho(\mathbf{r})\rangle\partial_\perp\phi(\mathbf{r}) = -\int_{-\infty}^{x_\perp^b} dx_\perp \exp\left(-2\frac{\phi(x_\perp)}{D}\right)\partial_\perp\phi(x_\perp) = \frac{D}{2}\rho_b \ . \tag{5.77}$$

Equation (5.77) is similar to the case of an ideal gas: the confined system does not exhibit a Casimir-like pressure and, in fact, displays a behaviour similar to a non-interacting equilibrium system. In Fig. 5.2, we test our prediction (5.77) against simulations: the agreement is very good. As $\langle P_\ell\rangle$ only depends on the one point average $\langle\rho(\mathbf{r})\rangle$, the algebraic decay of the two-point function $\langle\rho(\mathbf{r})\rho(0)\rangle$ cannot affect it; the first moment of the pressure does not exhibit a Casimir-like behaviour. However, we note that the second moment of P_ℓ will feature the two-point density correlations as

$$\langle P_\ell^2(t)\rangle = \frac{1}{L_\parallel^2}\int_{V_\ell} d\mathbf{r}\int_{V_\ell} d\mathbf{r}'\langle\rho(\mathbf{r},t)\rho(\mathbf{r}',t)\rangle\partial_\perp\phi(\mathbf{r})\partial_\perp\phi(\mathbf{r}') \ . \tag{5.78}$$

Intuitively, the measurement of $\langle P_\ell^2(t)\rangle$ might thus provide a quantitative assessment of the long-ranged nature of the correlations.

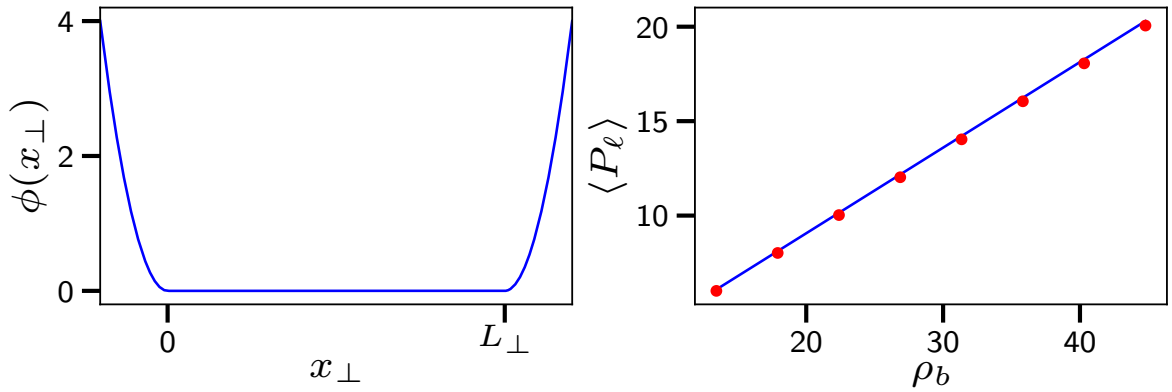

Figure 5.2 – **Left:** Potential ϕ modelling quadratic walls of stiffness $\kappa = 2$ starting at $x_\perp = 0$ and $x_\perp = L_\perp$. **Right:** Averaged pressure on the left wall measured in the simulations (red points) and theoretical prediction given by (5.77) (blue line). Parameters: $L_\parallel = 20$, $L_\perp = 20$, $h_\parallel = 0.01$,$h_\perp = 1$, $\sigma = 0.15$, $\kappa = 2$, $D = 0.9064$, $dt = 0.01$.

5.4.1 Variance of the pressure on a wall

In this part, we compute the variance of the pressure $\langle P_\ell^2\rangle - \langle P_\ell\rangle^2$ in the case of hard walls and show that its dominant contribution is an equilibrium one, already present in the ideal gas. Thus the second moment of the pressure will not bear the footprint of long-ranged correlations and cannot reveal a nonequilibrium Casimir-like decay. Let us define the density fluctuation $\delta\rho$ as the variation around the steady-state profile $\langle\rho\rangle$, *ie* $\delta\rho(\mathbf{r},t) = \rho(\mathbf{r},t) - \langle\rho(\mathbf{r})\rangle$. Linearizing (5.74) around $\langle\rho\rangle$ defined in (5.75), the time-evolution of $\delta\rho$ is different in the bulk and within the walls. In the bulk, the potential is zero and $\langle\rho\rangle = \rho_b$, so the dynamics of $\delta\rho$ simply reads

$$\partial_t\delta\rho = \boldsymbol{\nabla}\cdot[\boldsymbol{\Lambda}] + \frac{D}{2}\boldsymbol{\nabla}^2\delta\rho\ , \tag{5.79}$$

where $\boldsymbol{\Lambda}$ is a Gaussian white noise with correlations

$$\langle\Lambda^\alpha(\mathbf{r},t)\Lambda^\beta(\mathbf{r}',t')\rangle = \left[D\delta^{\alpha\beta}\rho_b\delta(\mathbf{r}-\mathbf{r}') + h_\alpha h_0(\mathbf{r}-\mathbf{r}')\delta^{\alpha\beta}\rho_b^2\right]\delta(t-t')\ . \tag{5.80}$$

Within the wall, the potential is sharp, $\boldsymbol{\nabla}\phi \neq 0$, and $\langle\rho\rangle = \exp(-2\phi/D)$. After linearization, we obtain the following dynamics for the density fluctuation

$$\partial_t\delta\rho = \boldsymbol{\nabla}\cdot[\boldsymbol{\Lambda} + \delta\rho(\mathbf{r},t)\boldsymbol{\nabla}\phi] + \frac{D}{2}\boldsymbol{\nabla}^2\delta\rho\ , \tag{5.81}$$

where the correlation of the Gaussian white noise $\boldsymbol{\Lambda}$ now reads

$$\langle\Lambda^\alpha(\mathbf{r},t)\Lambda^\beta(\mathbf{r}',t')\rangle = \left[D\delta^{\alpha\beta}\rho_b e^{-\frac{2\phi(\mathbf{r})}{D}}\delta(\mathbf{r}-\mathbf{r}') + h_\alpha h_0(\mathbf{r}-\mathbf{r}')\delta^{\alpha\beta}\rho_b^2 e^{-\frac{2\phi(\mathbf{r})}{D}-\frac{2\phi(\mathbf{r}')}{D}}\right]\delta(t-t')\ . \tag{5.82}$$

In the limit of hard wall, the noise $\boldsymbol{\Lambda}$ defined in (5.82) vanishes, and, because $\boldsymbol{\nabla}\phi$ becomes very large, $\delta\rho$ in the wall relaxes on faster time-scale than $\delta\rho$ in the bulk. Taking into account these two simplifications, the density fluctuation inside the wall becomes directly enslaved to the density fluctuations at $x_\perp = 0$

$$\delta\rho(\mathbf{x},t) = \delta\rho(0,x_\parallel,t)e^{-\frac{2\phi(x_\perp)}{D}}\ . \tag{5.83}$$

Note that (5.83) is valid for the wall on the left, namely for $x_\perp < 0$. The corresponding expression for $\delta\rho$ in the wall on the right is given by

$$\delta\rho(\mathbf{x},t) = \delta\rho(L_\perp,x_\parallel,t)e^{-\frac{2\phi(x_\perp)}{D}}\ . \tag{5.84}$$

Note that the variation $\delta\rho(\mathbf{x},t)$ inside both walls (5.83)-(5.84) are stochastic quantities through their dependencies on the field $\delta\rho(0,x_\parallel,t)$ and $\delta\rho(L_\perp,x_\parallel,t)$, respectively. We now express the variance of P_ℓ in terms of $\delta\rho$ as

$$\begin{aligned}\langle P_\ell^2\rangle - \langle P_\ell\rangle^2 =& \frac{1}{L_\parallel^2}\left[\int_{V_\ell}d\mathbf{r}\int_{V_\ell}d\mathbf{r}'\langle\rho(\mathbf{r},t)\rho(\mathbf{r}',t)\rangle\partial_\perp\phi(\mathbf{r})\partial_\perp\phi(\mathbf{r}') - \left(\int_{V_\ell}d\mathbf{r}\langle\rho(\mathbf{r},t)\rangle\partial_\perp\phi(\mathbf{r})\right)^2\right]\\ =& \frac{1}{L_\parallel^2}\int_{V_\ell}d\mathbf{r}\int_{V_\ell}d\mathbf{r}'\langle\delta\rho(\mathbf{r},t)\delta\rho(\mathbf{r}',t)\rangle\partial_\perp\phi(\mathbf{r})\partial_\perp\phi(\mathbf{r}')\ .\end{aligned} \tag{5.85}$$

Using (5.83), we remark that performing the above integrals in the $\perp$ direction amounts to integrating $e^{-\frac{2\phi(x_\perp)}{D}}\partial_\perp\phi$ and we obtain

$$\langle P_\ell^2\rangle - \langle P_\ell\rangle^2 = \frac{D^2}{4L_\parallel^2}\int_0^{L_\parallel} dx_\parallel \int_0^{L_\parallel} dx'_\parallel \langle \delta\rho(0,x_\parallel,t)\delta\rho(0,x'_\parallel,t)\rangle \ . \tag{5.86}$$

Finally making use of the periodicity in the $\parallel$ direction, we get

$$\langle P_\ell^2\rangle - \langle P_\ell\rangle^2 = \frac{D^2}{4L_\parallel}\int_0^{L_\parallel} dx_\parallel \langle \delta\rho(0,x_\parallel,t)\delta\rho(0,0,t)\rangle \ . \tag{5.87}$$

The last step to derive the second moment of P_ℓ is to evaluate the two-point function $\langle\delta\rho(0,x_\parallel,t)\delta\rho(0,0,t)\rangle$. In appendix D.1, we do it by using the time-evolution of $\delta\rho$ in the bulk (5.79)-(5.80) with no-flux boundary conditions. Note that this no-flux boundary condition is necessary to model the hard wall limit considered here. We obtain

$$\langle \delta\rho(0,x_\parallel,t)\delta\rho(0,0,t)\rangle = \int \frac{dk}{2\pi}\frac{e^{ikx_\parallel}}{L_\perp}\sum_{n=0}^{\infty}\mathcal{N}_n\left[\rho_b + \frac{\rho_b^2}{D}\frac{(h_\parallel k^2 + h_\perp q_n^2)h_0(k,q_n)}{k^2+q_n^2}\right] - \frac{\rho_b}{2L_\perp L_\parallel} \ , \tag{5.88}$$

where $q_n = n\pi/L_\perp$, $\mathcal{N} = 1-\delta_{n,0}/2$ and $h_0(k,q) = \sigma^4 e^{-\frac{(k^2+q^2)\sigma^2}{2}}$. Integrating (5.88) with respect to $x_\parallel$ selects the $k=0$ mode and gives the variance of P_ℓ using (5.87):

$$\langle P_\ell^2\rangle - \langle P_\ell\rangle^2 = \frac{D^2}{4L_\parallel L_\perp}\left[\sum_{n=1}^{\infty}\rho_b + \sum_{n=0}^{\infty}\mathcal{N}_n\frac{\rho_b^2 h_\perp}{D}h_0(0,q_n) - \frac{\rho_b}{2}\right] \ . \tag{5.89}$$

Following [162], the first term on the right-hand side of (5.89) can be regularized through zeta function regularization, which states that $\sum_{n=1}^{\infty}1 = \infty - 1/2$. Neglecting the infinite contribution, we replace $\sum_{n=1}^{\infty}\rho_b$ by $-\rho_b/2$ in the right-hand side of (5.89). We obtain

$$\langle P_\ell^2\rangle - \langle P_\ell\rangle^2 = \frac{D^2}{4L_\parallel L_\perp}\left[\sum_{n=0}^{\infty}\mathcal{N}_n\frac{\rho_b^2 h_\perp}{D}h_0(0,q_n) - \rho_b\right] \ . \tag{5.90}$$

The first term on the right-hand side of (5.90) can be simplified as

$$\sum_{n=0}^{\infty}\mathcal{N}_n\frac{\rho_b^2 h_\perp}{D}h_0(0,q_n) = \frac{\rho_b^2 h_\perp \sigma^4}{D}\Theta_3(0,e^{-\frac{\sigma^2\pi^2}{2L_\perp}}) \ , \tag{5.91}$$

where $\Theta_3(u,v) = 1 + 2\sum_{n>1}v^{n^2}\cos(2nu)$ is the third elliptic theta function. Inserting (5.91) into (5.90) gives

$$\langle P_\ell^2\rangle - \langle P_\ell\rangle^2 = \frac{D^2}{4L_\parallel L_\perp}\left[\frac{\rho_b^2 h_\perp\sigma^4}{D}\Theta_3(0,e^{-\frac{\sigma^2\pi^2}{2L_\perp}}) - \rho_b\right] \ . \tag{5.92}$$

The second moment of P_ℓ is thus inversely proportional to the volume of the system. In particular, it vanishes in the limit $L_\parallel \to \infty$: as such it cannot exhibit a Casimir-like behavior. Interestingly, we note that even in the case of an ideal gas, when $h_\perp = h_\parallel = 0$, $\langle P_\ell^2\rangle - \langle P_\ell\rangle^2$ is nonzero and features a finite-size correction $\propto -D^2\rho_b/(4L_\perp L_\parallel)$. We conclude that the variance of the pressure exerted on a single wall cannot provide a quantitative assessment of the scale-free decay of density correlations: it only exhibits

finite-size corrections. Unraveling our derivation of $\langle P_\ell^2\rangle - \langle P_\ell\rangle^2$, we can identify the key step that killed long-ranged correlations: the integral over $x_\parallel$ in expression (5.87). By performing this integration, we select the mode $k = 0$ of the correlator $\langle\delta\rho(\mathbf{x},t)\delta\rho(0,t)\rangle$. This selection simplifies the anisotropic term $(h_\parallel k^2 + h_\perp q_n^2)/(k^2+q_n^2)$ into $h_\perp$, killing the algebraic decay. Having understood this mechanism, we propose to measure a different physical quantity: the correlation of the pressure exerted at a given point on the two facing walls.

5.4.2 Correlation of the pressure between two facing patches

In this part, we compute the correlations between the pressure exerted on the right wall and the pressure on the left wall at a given coordinate $x_\parallel$. Let us define the local pressure on the left wall $p_\ell(x_\parallel)$ as

$$p_\ell(x_\parallel) = \int_{-\infty}^{0} dx_\perp \rho(x_\parallel, x_\perp)\partial_\perp\phi(x_\perp)\ . \tag{5.93}$$

Using that $\rho(\mathbf{r}) = \langle\rho(\mathbf{r})\rangle + \delta\rho(\mathbf{r}) = \rho_b \exp(-2\phi(\mathbf{r})/D) + \delta\rho(\mathbf{r})$, we cast p_ℓ into

$$p_\ell(x_\parallel) = \frac{D}{2}\rho_b + \int_{-\infty}^{0} dx_\perp \delta\rho(x_\parallel, x_\perp)\partial_\perp\phi(x_\perp)\ . \tag{5.94}$$

Further inserting expression (5.83) for $\delta\rho(x_\parallel, x_\perp)$ within the wall, we get

$$p_\ell(x_\parallel) = \frac{D}{2}\rho_b + \frac{D}{2}\delta\rho(x_\parallel, 0, t)\ . \tag{5.95}$$

Note that $\delta\rho(x_\parallel, 0, t)$ in the above equality is, in fact, a stochastic quantity. It is obtained as the boundary value at $x_\perp = 0$ of the stochastic field $\delta\rho(\mathbf{x})$ in the bulk. Similarly, for the right wall, we obtain $p_r(x_\parallel)$ as

$$p_r(x_\parallel) = \frac{D}{2}\rho_b + \frac{D}{2}\delta\rho(x_\parallel, L_\perp, t)\ , \tag{5.96}$$

where $\delta\rho(x_\parallel, L_\perp, t)$ is the boundary value at $x_\perp = L_\perp$ of the stochastic field $\delta\rho(\mathbf{x})$ in the bulk. We then deduce the correlation between p_ℓ and p_r as

$$\langle p_\ell(x_\parallel)p_r(x_\parallel)\rangle - \langle p_\ell(x_\parallel)\rangle\langle p_r(x_\parallel)\rangle = \frac{D^2}{4}\langle\delta\rho(x_\parallel,0,t)\delta\rho(x_\parallel,L_\perp,t)\rangle\ . \tag{5.97}$$

To close the above formula and compute the correlation of the pressure between the two walls, we use the expression of $\langle\delta\rho(\mathbf{x},t)\delta\rho(0,t)\rangle$ computed in (D.21) within appendix 5.4 in the hard wall limit:

$$\langle\delta\rho(x_\parallel,0,t)\delta\rho(x_\parallel,L_\perp,t)\rangle = \int\frac{dk}{2\pi}\frac{\rho_b^2}{DL_\perp}\sum_{n=0}^{\infty}\mathcal{N}_n(-1)^n\left[\frac{(h_\parallel k^2 + h_\perp q_n^2)h_0(k,q_n)}{k^2+q_n^2}\right] - \frac{\rho_b}{2L_\perp L_\parallel}\ , \tag{5.98}$$

where $q_n = n\pi/L$, $\mathcal{N} = 1-\delta_{n,0}$ and $h_0(k,q) = \sigma^4 e^{-\frac{(k^2+q^2)\sigma^2}{2}}$. The first term on the right-hand side of (5.98) is computed in (D.31) of appendix D.2 by using the Poisson

summation formula. We report the result here as

$$\int \frac{dk}{2\pi} \sum_{n=0}^{\infty} \frac{\mathcal{N}_n}{L_\perp} (-1)^n \left[\frac{(h_\parallel k^2 + h_\perp q_n^2) h_0(k, q_n)}{k^2 + q_n^2} \right] = \frac{\sigma^2 h_\perp}{\pi} \left[\Theta_3(0, e^{-\frac{L_\perp^2}{2\sigma^2}}) - \Theta_3(0, e^{-2\frac{L_\perp^2}{\sigma^2}}) \right] + \frac{(h_\parallel - h_\perp)\sigma^4}{4\pi L_\perp^2} \sum_{n=1}^{\infty} \left[\frac{e^{-2\, n^2 \frac{L_\perp^2}{\sigma^2}} - 4 e^{-n^2 \frac{L_\perp^2}{2\sigma^2}}}{n^2} \right] + \frac{\sigma^4 \pi (h_\parallel - h_\perp)}{8 L_\perp^2} \,. \quad (5.99)$$

In the limit $L_\perp \gg \sigma$, the above expression simplifies as

$$\int \frac{dk}{2\pi} \sum_{n=0}^{\infty} \frac{\mathcal{N}_n}{L_\perp} (-1)^n \left[\frac{(h_\parallel k^2 + h_\perp q_n^2) h_0(k, q_n)}{k^2 + q_n^2} \right] = \frac{\sigma^4 \pi (h_\parallel - h_\perp)}{8 L_\perp^2} + \mathcal{O}(L_\perp^{-3}) \,. \quad (5.100)$$

Inserting (5.100) into (5.98), we obtain

$$\langle \delta\rho(x_\parallel, 0, t) \delta\rho(x_\parallel, L_\perp, t) \rangle = \frac{\rho_b^2 \sigma^4 \pi (h_\parallel - h_\perp)}{8 D L_\perp^2} - \frac{\rho_b}{2 L_\perp L_\parallel} + \mathcal{O}(L_\perp^{-3}) \,. \quad (5.101)$$

Injecting the above expression into (5.97) yields

$$\langle p_\ell(x_\parallel) p_r(x_\parallel) \rangle - \langle p_\ell(x_\parallel) \rangle \langle p_r(x_\parallel) \rangle = \frac{\rho_b^2 D \sigma^4 \pi (h_\parallel - h_\perp)}{32\, L_\perp^2} - \frac{\rho_b D^2}{8 L_\perp L_\parallel} + \mathcal{O}(L_\perp^{-3}) \,. \quad (5.102)$$

The variance of the local pressure $\langle p_\ell p_r \rangle - \langle p_\ell \rangle \langle p_r \rangle$ in (5.102) exihibits a Casimir-like decay $\propto 1/L_\perp^2$. In particular, we note that this algebraic decay is not due to finite-size corrections as it survives in the regime $L_\parallel \to \infty$. Introducing $c_\infty^p = -\rho_b D^2/(8 L_\perp L_\parallel)$, we have

$$\langle p_\ell(x_\parallel) p_r(x_\parallel) \rangle - \langle p_\ell(x_\parallel) \rangle \langle p_r(x_\parallel) \rangle - c_\infty^p = \frac{\rho_b^2 D \sigma^4 \pi (h_\parallel - h_\perp)}{32\, L_\perp^2} + \mathcal{O}(L_\perp^{-3}) \,. \quad (5.103)$$

Thus, $\langle p_\ell p_r \rangle - \langle p_\ell \rangle \langle p_r \rangle - c_\infty^p$ is a good observable to measure in order to probe anisotropy-induced scale-free correlations in the system. In Fig. 5.3, we compare our prediction (5.103) with numerical simulations performed for quadratic walls of stiffness κ. It seems that there is a good agreement between theory and numerics for $L_\perp > 15\sigma$. However, we still have to probe for values of $L_\perp$ larger than 30σ to confirm this trend. The difficulty lies in the simulations performed in Fig. 5.3, which are computationally heavier compared to the ones carried out in Fig. 5.1 as we can only collect data at the walls and not in the bulk. For example, producing enough data to overcome noise at $L_\perp \sim 30\sigma$ takes roughly a month on 80 cores. Note that, despite the amount of hypothesis assumed to obtain expression (5.103) (hard wall limit, regularization, linearization of density fluctuations...), our theory seems to sucessfully predict the good exponent of the decay and the right order of magnitude for its prefactor.

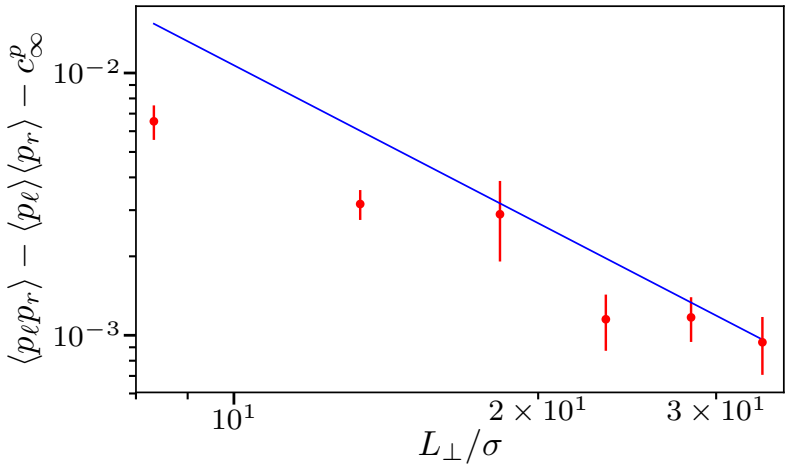

Figure 5.3 – $\langle p_\ell p_r \rangle - \langle p_\ell \rangle \langle p_r \rangle - c^p_\infty$ in the simulations (red dots) and theoretical prediction given by (5.103) (blue line). The errorbars are given by the standard deviation observed in the simulations. Parameters: $L_\parallel = 1200$, $dt = 0.01$, $\sigma = 0.15$, $\rho_b = 30$, $h_\parallel = 0.01$, $h_\perp = 1$, $\kappa = 2$, $D = 0.5439$.

5.5 Conclusion

In this chapter, we studied a system of N particles submitted to anisotropic fluctuations. Their dynamics (5.27) is coupled through spatial interactions: particles within a radius σ feel a similar, correlated noise. In section 5.3.1, we showed that, due to anisotropy, long-ranged density correlations emerged in this system at the macroscopic level. We confirmed our predictions by performing particle-based simulations: we measured a very good agreement with our theory. In section 5.4, we looked for a simple measurable quantity bearing the footprint of the underlying scale-free decay of density correlations. We showed that, contrary to other nonequilibrium systems, the averaged pressure exerted by our system on a confining wall does not exhibit a Casimir-like behavior: it is instead similar to an ideal gas. However, we find that the correlation of the pressure between two facing patches separated by a distance L features an algebraic decay $\propto L^{-2}$.

6. Conclusion

I conclude this manuscript by a quick overview of our contributions. In the same time, I highlight future directions of research that could be undertaken following our works.

In chapter 2, I developed a recursive scheme to determine the exact steady-state distribution of AOUPs in the limit of small persistence time. Building on it, I derived exact formulas for signatures of nonequilibrium such as the ratchet current and the entropy production rate. I note that our perturbative approach can be generalized to more complex dynamics than the Brownian case. Let us illustrate this point by considering a stochastic dynamics $\mathcal{S}$ whose corresponding Fokker-Planck operator is $\mathcal{L}_{\mathcal{S}}$. Adding an Ornstein-Uhlenbeck noise of amplitude D to $\mathcal{S}$ amounts to adding the operators $L_1 + L_2$ defined in (2.15) to $L_{\mathcal{S}}$. The starting point for our perturbative expansion, A_0^0, is defined by the equation $(\mathcal{L}_{\mathcal{S}} + D\partial_{xx})A_0^0 = 0$. As long as A_0^0 defined this way is known analytically, the recursion can be carried out and the effect of the Ornstein-Uhlenbeck noise can be taken into account perturbatively in τ. For example, using our method, we could try to assess the effect of a colored noise on an underdamped Langevin dynamics and compare the result with the overdamped scenario.

In chapter 3, I revisited the classification of the transition in models of collective motion by highlighting the mechanism of fluctuation-induced first-order transition. I showed that the microscopic noise generically renormalizes the mean-field critical temperature to make it density dependent. This dependency on the density turns a deceptive continuous emergence of flocking at mean-field level into a first order scenario. At odds with the existing literature, I showed that topological alignment gives no protection against the microscopic noise. The same mechanism applies and the emergence of collective motion is also discontinuous in "metric-free" models. Interestingly, the dynamics that we introduced in (3.83)-(3.84) could be extended into a minimalist version of anisotropic flocking model in future directions of research. The idea would be to introduce a bias modelling the visual cones of birds. As birds only see their closest relatives in front of them in the flocks, we would like aligning interactions taking into account the direction of motion of the flying spins. To this aim, we could introduce the two sets $\mathcal{N}_i^+$ and $\mathcal{N}_i^-$ corresponding respectively to the k-nearest neighbours located at the right or at the left of the i-th particle. Alignment would then occur according to the direction of the i-th particle: a right-moving plus spin aligns with the set $\mathcal{N}_i^+$ while a left-moving minus spin aligns with $\mathcal{N}_i^+$. It would be interesting to study the emergence of flocking in this anisotropic, physically-relevant model. More generically, we note that we did not obtain necessary and sufficient conditions on the aligning field $\bar{m}$ to observe phase separation at the onset of order. In futur works, it would be interesting to look for such conditions in order to understand the minimal ingredients needed for a fluctuation-induced first-order transition.

In chapter 4, we unveiled a new phase transition occurring at high density in roller flocks: we dubbed it active solidification. We showed that it is well described by an extended MIPS phase transition between a polar flock and an active solid. Thus, we expect active solidification to be a general feature caused by speed reduction in dense flocks of active polar units. The agreement between our phenomenological hydrodynamics and the experiments goes beyond the mere phase diagram: both predict a first order transition, the presence of hysteresis loops and the existence of a coarsening dynamics. In section 4.5.3, we predicted the existence of a phase transition between flocking bands

and an active solid: it would be interesting to confirm this coexistence domain in the experiments. As a future direction of research, we could relax the hypothesis of a loss of order at high density and assume that particles conserve their orientation even in the jammed phase. While there has been some previous works in this direction [75, 76], a complete picture of the different phases that can emerge is still lacking.

Finally, in chapter 5, we described how long-range density correlations may emerge from an anisotropic microscopic dynamics. In 5.4, we discussed the impact of the scale-free decay of the two-point function on the pressure exerted by the system, showing that the forces applied on the confining walls can exhibit a Casimir-like behaviour. Interestingly, our model could be used to assess the effect of long-range fluctuations on different physical quantities not discussed in this manuscript. For example, one could add a tracer on top of the dynamics of the bath (5.27) and derive the effect of the anisotropic noise on its diffusion constant following the method developed in [163, 164].

A. Nonequilibrium signatures of Active Ornstein Uhlenbeck Particles

A.1 A single particle in 1D in the presence of a thermal noise

A.1.1 Recursion for the A_n's

In this appendix, we show how the A_n's entering the ansatz (2.19) for $\mathcal{P}_s(x,v)$ can be obtained recursively as a series in $\tau^{1/2}$. For conciseness, we perform this derivation for an AOUP experiencing an additional thermal noise as in (2.50)-(2.51). The results are readily extended to the athermal case (2.9)-(2.10) of section 2.1 by taking $T=0$ in all the formulas.

Inserting $\mathcal{P}_s(x,v)=\sum_n P_n(v)A_n(x)$ into the stationary Fokker-Planck $\tilde{\mathcal{L}}_T\mathcal{P}_s(x,v)=0$ with $\tilde{\mathcal{L}}_T$ defined in (2.53), further using (2.17), we find that A_n is a solution of

$$\sum_n P_n(v)\partial_x\left(\partial_x\phi A_n\right)+\sum_n P_n(v)T\partial_{xx}A_n-\sum_n\frac{nP_n(v)}{\tau}A_n-\sum_n\frac{vP_n(v)}{\sqrt{\tau}}\partial_x A_n=0\ . \quad \text{(A.1)}$$

Using the recurrence property of Hermite polynomials, $H_{n+1}(v)=2vH_n(v)-2nH_{n-1}(v)$, we decompose vP_n into a sum of P_{n+1} and P_{n-1}

$$vP_n=\sqrt{(n+1)D}P_{n+1}+\sqrt{nD}P_{n-1}\ . \quad \text{(A.2)}$$

Plugging (A.2) into (A.1), we are now in position to project (A.1) onto H_k and to use the orthogonality relation (2.18). This leads us to the following recursion relation for the A_n's

$$0=-nA_n-\sqrt{\tau}\sqrt{(n+1)D}\partial_x A_{n+1}-\sqrt{\tau}\sqrt{nD}\ \partial_x A_{n-1}+\tau\partial_x\left(\partial_x\phi A_n\right)+\tau T\partial_{xx}A_n\ . \quad \text{(A.3)}$$

We now look for the A_n's as series in powers of $\tau^{1/2}$. Because $\tilde{\mathcal{L}}_T$ is formally invariant upon the reversal $\{\tilde{v},\sqrt{\tau}\}\to-\{\tilde{v},\sqrt{\tau}\}$, so is the stationary distribution $\mathcal{P}_s$. Consequently, A_{2k} contains only integer powers of τ while A_{2k+1} contains only half-integer powers of τ. We shall further assume that the first nonzero contribution to A_k is of order $\tau^{k/2}$. This hierarchical ansatz is necessary to disentangle and solve, starting from A_0 and order by order in powers of $\tau^{1/2}$, the recurrence equation (A.3). Its validity is a posteriori confirmed by inserting our final result for $\mathcal{P}_s$ into the Fokker-Planck equation and checking that $\tilde{\mathcal{L}}_T\mathcal{P}_s$ vanishes order by order in τ. Our scaling ansatz is thus

$$A_0=A_0^0(x)+\tau A_0^2(x)+\tau^2A_0^4(x)+... \quad \text{(A.4)}$$
$$A_1=\tau^{1/2}A_1^1(x)+\tau^{3/2}A_1^3(x)+\tau^{5/2}A_1^5(x)+... \quad \text{(A.5)}$$
$$A_2=\tau A_2^2(x)+\tau^2A_2^4(x)+\tau^3A_2^6(x)+... \quad \text{(A.6)}$$
$$\vdots$$

Let us now show that the A_i^j can be computed recursively. Looking at (A.3) for $n=0$, we get

$$\partial_x A_1=\sqrt{\frac{\tau}{D}}\left[\partial_x\left(\partial_x\phi A_0\right)+T\partial_{xx}A_0\right]\ . \quad \text{(A.7)}$$

Expanding A_0 and A_1 according to (A.4) and (A.5), equating coefficients of order $\tau^{k/2}$ on both sides of (A.7), and integrating over x leads to

$$A_1^k = \frac{1}{\sqrt{D}}\left[\partial_x\phi A_0^{k-1} + T\partial_x A_0^{k-1}\right] + b_k \ , \tag{A.8}$$

where b_k is an integration constant. Expanding A_n, A_{n+1} and A_{n-1} according to our scaling ansatz (A.6) in (A.3), equating coefficients of order $\tau^{k/2}$ on both sides, we obtain:

$$A_n^k = -\frac{\sqrt{(n+1)D}}{n}\partial_x A_{n+1}^{k-1} - \sqrt{\frac{D}{n}}\partial_x A_{n-1}^{k-1} + \frac{\partial_x\left(\partial_x\phi A_n^{k-2}\right)}{n} + \frac{T}{n}\partial_{xx}A_n^{k-2} \ . \tag{A.9}$$

Taking $k = n$ in (A.9) and using that $A_n^j = 0$ for $j \leq n$ yields the expression of A_n^n as a function of A_0^0:

$$A_n^n = -\sqrt{\frac{D}{n}}\partial_x A_{n-1}^{n-1} = (-1)^n\frac{D^{n/2}}{\sqrt{n!}}\partial_x^n A_0^0 \ . \tag{A.10}$$

Using expression (A.8) for $k = 1$ and expression (A.10) for $n = 1$, we obtain a closed equation on A_0^0:

$$\partial_x\phi\ A_0^0 + (T+D)\partial_x A_0^0 = -b_1\sqrt{D} \ . \tag{A.11}$$

Since $A_0^0(x)$ corresponds to the Boltzmann weight when $\tau = 0$ we must have

$$\int_{-\infty}^{+\infty}\mathcal{P}_s(x,v)|_{\tau=0}\ dv = A_0^0 = c_0\ e^{-\frac{\phi}{T+D}} \ , \tag{A.12}$$

with c_0 fixed by normalization according to (2.58). The constant b_1 is self-consistently fixed to zero such that (A.12) is a solution of (A.11). We now set out to compute the next order correction A_0^2. Applying (A.9) for $n = 1$ and $k = 3$ gives:

$$A_1^3 = -\sqrt{2D}\partial_x A_2^2 - \sqrt{D}\partial_x A_0^2 + \partial_x\left(\partial_x\phi A_1^1\right) + T\partial_{xx}A_1^1 \ . \tag{A.13}$$

In (A.13), we can use (A.10) to express A_1^1 and A_2^2 as a function of A_0^0 and (A.8) to express A_1^3 as a function of A_0^2. We thus obtain a differential equation for A_0^2:

$$\frac{\partial_x\phi}{T+D}A_0^2 + \partial_x A_0^2 = -\frac{D^2\partial_x^3 A_0^0}{T+D} + \frac{D\partial_x\left(\partial_x\phi\partial_x A_0^0\right)}{T+D} + \frac{TD\partial_x^3 A_0^0}{T+D} - \frac{b_3\sqrt{D}}{T+D} \ . \tag{A.14}$$

Using (A.12), we can integrate (A.14) and finally determine the expression (2.57) of A_0^2 in main text

$$A_0^2 = \ c_0\ e^{-\frac{\phi}{T+D}}\left(\frac{D\partial_{xx}\phi}{T+D} - \frac{D\left(\partial_x\phi\right)^2}{2(T+D)^2}\right) + c_2\ e^{-\frac{\phi}{T+D}} - \frac{b_3\sqrt{D}}{T+D}e^{-\frac{\phi}{T+D}}\int_0^x e^{\frac{\phi}{T+D}}dx \ . \tag{A.15}$$

The A_i^k for $i \geq 0$ and $k \geq i$ can be systematically derived from (A.9) to yield $\mathcal{P}_s(x,v)$ to arbitrary order in τ. However, their expression does not seem to lead to a simple recognizable pattern and their computation is more easily solved in a formal calculation software such as Mathematica [102].

A.1.2 Full steady-state distribution

In this appendix, we report the steady-state probability density $\mathcal{P}_s(x,v)$ to order τ^2 obtained via our recurrence scheme described in Appendix A.1.1. For conciseness, we report $\mathcal{P}_s(x,v)$ for an AOUP experiencing an additional thermal noise as in (2.50)-(2.51), but our results readily extend to the athermal case (2.9)-(2.10) of section 2.1 by taking $T=0$.

$$
\begin{aligned}
e^{\frac{\phi}{T+D}}\mathcal{P}_s(x,v) = c_0 &+ \sqrt{\tau}P_1(v)\frac{c_0\sqrt{D}\phi^{(1)}(x)}{T+D} + \tau P_0(v)\Bigg[-\frac{c_0 D\phi^{(1)2}}{2(T+D)^2} + c_2 + \frac{Dc_0\phi^{(2)}}{T+D} \\
&- \frac{\sqrt{D}b_3}{T+D}\int_0^x e^{\frac{\phi(z)}{T+D}}dz\Bigg] + \tau^{\frac{3}{2}}\Bigg[\frac{P_3(v)c_0 D^{\frac{3}{2}}}{\sqrt{6}}\left(\frac{\phi^{(1)3}}{(T+D)^3} - \frac{3\phi^{(1)}\phi^{(2)}}{(T+D)^2} + \frac{\phi^{(3)}}{T+D}\right) \\
&+ P_1(v)\left(\frac{b_3 D e^{\frac{\phi}{T+D}}}{T+D} - \frac{\phi^{(1)}b_3 D}{(T+D)^2}\int_0^x e^{\frac{\phi(z)}{T+D}}dz + \frac{\sqrt{D}c_2\phi^{(1)}}{T+D} - \frac{c_0 D^{\frac{3}{2}}\phi^{(1)3}}{2(T+D)^3}\right. \\
&\left.+ \frac{c_0\sqrt{D}(D^2-T^2)\phi^{(1)}\phi^{(2)}}{(T+D)^3} + \frac{c_0\sqrt{D}T\phi^{(3)}}{T+D}\right)\Bigg] + \tau^2 P_0(v)\Bigg[\frac{c_2 D\phi^{(2)}}{T+D} - \frac{c_2 D\phi^{(1)2}}{2(T+D)^2} \\
&- \frac{D^{\frac{3}{2}}b_3}{(T+D)^2}\int_0^x e^{\frac{\phi(z)}{T+D}}\phi^{(2)}(z)dz + \frac{c_0 D^2}{8(T+D)^4}\phi^{(1)4} - \frac{c_0 D(D-T)\phi^{(1)2}\phi^{(2)}}{2(T+D)^3} \\
&+ \frac{b_3 D^{\frac{3}{2}}}{(T+D)^3}\int_0^x\left(\int_0^s e^{\frac{\phi(z)}{T+D}}dz\right)\left(\phi^{(1)}(s)\phi^{(2)}(s) - (T+D)\phi^{(3)}(s)\right)ds + c_4 \\
&+ \frac{Dc_0}{2(T+D)}\int_0^x \phi^{(1)2}(z)\phi^{(3)}(z)dz - \frac{Dc_0(D+2T)}{(T+D)^2}\phi^{(3)}\phi^{(1)} - \frac{\sqrt{D}b_5}{T+D}\int_0^x e^{\frac{\phi(z)}{T+D}}dz \\
&+ \frac{Dc_0(D-2T)\phi^{(2)2}}{4(T+D)^2} + \frac{Dc_0(D+2T)\phi^{(4)}}{2(T+D)}\Bigg]\,. \qquad \text{(A.16)}
\end{aligned}
$$

In (A.16), c_0 is given by (2.58) while c_2, c_4, b_3 and b_5 are integration constants whose expressions must be adapted to the boundary conditions. For a confining potential, $\mathcal{P}_s(x,v)$ must vanish for $x\to\pm\infty$ which leads to $b_3=b_5=0$. All in all, one finds the following spatial distribution to order τ^2:

$$
\begin{aligned}
e^{\frac{\phi}{T+D}}\mathcal{P}_s(x) = c_0 &+ \tau\left[-\frac{c_0 D\phi^{(1)2}}{2(T+D)^2} + c_2 + \frac{Dc_0\phi^{(2)}}{T+D}\right] + \tau^2\left[\frac{c_2 D\phi^{(2)}}{T+D} - \frac{c_2 D\phi^{(1)2}}{2(T+D)^2} + c_4\right. \\
&+ \frac{c_0 D^2}{8(T+D)^4}\phi^{(1)4} - \frac{c_0 D(D-T)\phi^{(1)2}\phi^{(2)}}{2(T+D)^3} + \frac{Dc_0}{2(T+D)}\int_0^x \phi^{(1)2}(z)\phi^{(3)}(z)dz \\
&\left.- \frac{Dc_0(D+2T)}{(T+D)^2}\phi^{(3)}\phi^{(1)} + \frac{Dc_0(D-2T)\phi^{(2)2}}{4(T+D)^2} + \frac{Dc_0(D+2T)\phi^{(4)}}{2(T+D)}\right]\,. \qquad \text{(A.17)}
\end{aligned}
$$

The integration constants c_2 and c_4 are finally found by normalization, *ie* by requiring $\int_{-\infty}^{+\infty}\mathcal{P}_s(x)dx=1$ at every order in τ.

For a periodic potential of period L, the spatial distribution must respect $\mathcal{P}_s(x+L)=\mathcal{P}_s(x)$. This condition implies $b_3=0$, but leads to a nonzero b_5 which is given by

$$
b_5 = \frac{D}{2(T+D)}\frac{\int_0^L \phi^{(1)2}\phi^{(3)}dx}{\int_0^L e^{\frac{\phi}{T+D}}dx\int_0^L e^{-\frac{\phi}{T+D}}dx}\,. \qquad \text{(A.18)}
$$

All in all, $\mathcal{P}_s$ in the case of a periodic potential reads:

$$
\begin{aligned}
e^{\frac{\phi}{T+D}}\mathcal{P}_s(x) = c_0 + \tau\Bigg[&- \frac{c_0 D\phi^{(1)2}}{2(T+D)^2} + c_2 + \frac{Dc_0\phi^{(2)}}{T+D}\Bigg] + \tau^2\Bigg[\frac{c_2 D\phi^{(2)}}{T+D} - \frac{c_2 D\phi^{(1)2}}{2(T+D)^2} + c_4 \\
&+ \frac{c_0 D^2}{8(T+D)^4}\phi^{(1)4} - \frac{c_0 D(D-T)\phi^{(1)2}\phi^{(2)}}{2(T+D)^3} + \frac{Dc_0}{2(T+D)}\int_0^x \phi^{(1)2}(z)\phi^{(3)}(z)dz \\
&- \frac{Dc_0(D+2T)}{(T+D)^2}\phi^{(3)}\phi^{(1)} + \frac{Dc_0(D-2T)\phi^{(2)2}}{4(T+D)^2} + \frac{Dc_0(D+2T)\phi^{(4)}}{2(T+D)} \\
&- \frac{\sqrt{D}b_5}{T+D}\int_0^x e^{\frac{\phi(z)}{T+D}}dz\Bigg] ,
\end{aligned}
\tag{A.19}
$$

Once again, c_2 and c_4 are then found by normalization. Note that in expression (A.16), v corresponds to the rescaled variable $\tilde{v}$. To get the exact steady-state distribution, one thus has to make the change of variable $v \to \sqrt{\tau}v$.

A.1.3 Derivation of the entropy production rate

This appendix is devoted to the perturbative derivation of the entropy production as a series in $\tau^{1/2}$ for an AOUP experiencing an additional thermal noise. As shown in (2.72), the entropy production rate of dynamics (2.50)-(2.51) can be expressed as

$$
\sigma = \frac{2}{\tau}\left\langle \int_{-\infty}^{+\infty} dt\, G(t)\, \dot{x}(0)\, \phi'(x(t)) \right\rangle . \tag{A.20}
$$

The series in $\tau^{1/2}$ of (A.20) is obtained by expanding $\phi'(x(t))$ in powers of the particle displacement. In order to make such an expansion more explicit, we rescale time as $s = t/\tau$ and the self-propulsion v as $\tilde{v} = v\sqrt{\tau}$. The entropy production rate then reads

$$
\sigma = \frac{2}{\tau}\left\langle \int_{-\infty}^{+\infty} ds\, \tilde{G}(s)\, \frac{dx}{ds}(0)\, \phi'(x(s)) \right\rangle , \tag{A.21}
$$

where $\tilde{G}(s)$ is given by

$$
\tilde{G}(s) = \frac{D}{4T^2}\sqrt{\frac{T}{D+T}}\exp\left(-\sqrt{\frac{D+T}{T}}|s|\right) , \tag{A.22}
$$

and the ensemble measure $\langle\cdot\rangle$ now corresponds to the stochastic process

$$
\frac{dx}{ds} = -\tau\phi'(x(s)) + \sqrt{\tau}\left(\tilde{v}(s) + \sqrt{2T}\,\tilde{\eta}_1(s)\right) \tag{A.23}
$$

$$
\frac{d\tilde{v}}{ds} = -\tilde{v} + \sqrt{2D}\,\tilde{\eta}_2(s) , \tag{A.24}
$$

with $\tilde{\eta}_1(s)$ and $\tilde{\eta}_2(s)$ being two independent Gaussian white noises. To lighten the notations, we omit the tilde in the remainder of this appendix. We introduce the particle displacement during time s as

$$
\Delta(s) = x(s) - x(0) . \tag{A.25}
$$

Hence, we have

$$\sigma = \frac{2}{\tau}\int_{-\infty}^{\infty} ds\, G(s) \sum_{n=0}^{+\infty} \frac{1}{n!} \left\langle \dot{x}(0)\phi^{(n+1)}(x(0))\Delta(s)^n \right\rangle \ . \tag{A.26}$$

The first term of the series (A.26) involves the Stratonovich average $\langle \dot{x}(0)\phi'(x(0))\rangle = \lim_{t\to\infty}\int_0^t d\phi/dt dt$ and vanishes. We now focus on the second one that we denote by σ_1. We have

$$\begin{aligned}\sigma_1 &= \frac{2}{\tau}\int_{-\infty}^{+\infty} ds\, G(s) \left\langle \dot{x}(0)\phi^{(2)}(x(0))\Delta(s) \right\rangle \\ &= \frac{2}{\tau}\int_{0}^{+\infty} ds\, G(s) \left\langle \dot{x}(0)\phi^{(2)}(x(0)) \left(\Delta(s)+\Delta(-s)\right) \right\rangle\end{aligned}$$

Replacing $\Delta(s)$ by its integral form $\Delta(s) = \int_0^s \dot{x}(s')ds'$, we get

$$\sigma_1 = \frac{2}{\tau}\int_{0}^{+\infty} ds\, G(s) \int_0^s ds' \left\langle \dot{x}(0)\phi^{(2)}(x(0)) \left(\dot{x}(s') - \dot{x}(-s')\right) \right\rangle \ . \tag{A.27}$$

Using time-translation invariance in the steady state, we replace $\int_0^s \langle \dot{x}(0)\phi^{(2)}(x(0))\dot{x}(-s')\rangle ds'$ by $\int_0^s \langle \dot{x}(0)\phi^{(2)}(x(s'))\dot{x}(s')\rangle ds'$ and we obtain

$$\sigma_1 = \frac{2}{\tau}\int_{0}^{+\infty} ds\, G(s) \int_0^s ds' \left\langle \dot{x}(0)\dot{x}(s') \left(\phi^{(2)}(x(0)) - \phi^{(2)}(x(s'))\right) \right\rangle \ . \tag{A.28}$$

We now expand again (A.28) in powers of the displacement, which gives

$$\sigma_1 = -\frac{2}{\tau}\int_{0}^{+\infty} ds\, G(s) \int_0^s ds' \sum_{n=1}^{+\infty} \frac{1}{n!} \left\langle \dot{x}(0)\phi^{(n+2)}(x(0))\dot{x}(s')\Delta(s')^n \right\rangle \ . \tag{A.29}$$

In the Stratonovitch convention, we recognize a total derivative as $\dot{x}(s')\Delta(s')^n = (n+1)^{-1}d\Delta(s')^{n+1}/ds'$. We can thus perform the integral over s' in (A.29) and replace $\int_0^s \dot{x}(s')\Delta(s')^n ds'$ by $(n+1)^{-1}\Delta(s)^{n+1}$:

$$\sigma_1 = -\frac{2}{\tau}\int_{0}^{+\infty} ds G(s) \sum_{n=1}^{+\infty} \frac{1}{(n+1)!} \left\langle \dot{x}(0)\phi^{(n+2)}(x(0))\Delta(s)^{n+1} \right\rangle \ . \tag{A.30}$$

Plugging back this final expression for σ_1 in (A.26), we remark that it cancels the integral between 0 and ∞ of all the terms of the series. Making the change of variable $s \to -s$ for the remaining integral between $-\infty$ and 0, we obtain

$$\sigma = \frac{2}{\tau}\sum_{n=2}^{+\infty} \frac{1}{n!} \int_{0}^{+\infty} ds\, G(s) \left\langle \dot{x}(0)\phi^{(n+1)}(x(0))\Delta(-s)^n \right\rangle \ . \tag{A.31}$$

This first result shows that any additive Gaussian process in a harmonic potential has a vanishing entropy production rate. We can replace $\dot{x}(0)$ by its expression $-\tau\phi'(x(0)) + \sqrt{\tau}v(0) + \sqrt{2T\tau}\eta_1(0)$ in (A.31) to obtain

$$\sigma = \frac{2}{\tau}\sum_{n=2}^{+\infty} \frac{1}{n!} \int_{0}^{+\infty} ds\, G(s) \left\langle \left(-\tau\phi'(x(0)) + \sqrt{\tau}v(0) + \sqrt{2T\tau}\eta_1(0)\right) \phi^{(n+1)}(x(0))\Delta(-s)^n \right\rangle \ . \tag{A.32}$$

We are now in position to integrate out the thermal noise $\eta_1(0)$ in the above expression. To this aim, we use the Stratonovitch average $\langle \sqrt{2T\tau}\eta_1(0) f(x(0))\rangle = T\tau f'(x(0))$, which is

valid for any arbitrary funtion f depending on $x(0)$. Applying this formula for $f(x(0)) = \phi^{(n+1)}(x(0))\Delta(-s)^n$ yields

$$\left\langle \sqrt{2T\tau}\,\eta(0)\phi^{(n+1)}(x(0))\Delta(-s)^n \right\rangle = T\tau \left\langle \phi^{(n+2)}(x(0))\Delta(-s)^n - n\phi^{(n+1)}(x(0))\Delta(-s)^{n-1} \right\rangle , \tag{A.33}$$

where the second term on the right hand side stems from the dependence of $\Delta(-s)$ on $x(0)$ through the relation $\Delta(-s) = x(-s) - x(0)$. Inserting expression (A.33) into (A.32), we obtain σ in terms of the position x and self-propulsion v:

$$\begin{aligned}\sigma = &\frac{2}{\tau}\sum_{n=2}^{+\infty}\frac{1}{n!}\int_0^{+\infty} ds\, G(s) T\tau \left\langle \phi^{(n+2)}(x(0))\Delta(-s)^n - n\phi^{(n+1)}(x(0))\Delta(-s)^{n-1} \right\rangle \\ &+ \frac{2}{\tau}\sum_{n=2}^{+\infty}\frac{1}{n!}\int_0^{+\infty} ds\, G(s) \left\langle \left(-\tau\phi'(x(0)) + \sqrt{\tau}v(0)\right)\phi^{(n+1)}(x(0))\Delta(-s)^n \right\rangle . \end{aligned} \tag{A.34}$$

The first term on the right hand side of (A.34) is a telescopic sum as

$$\sum_{n=2}^{+\infty}\frac{1}{n!}\left\langle \phi^{(n+2)}(x(0))\Delta(-s)^n - n\phi^{(n+1)}(x(0))\Delta(-s)^{n-1} \right\rangle = -\langle \phi^{(3)}(x(0))\Delta(-s)\rangle , \tag{A.35}$$

and we can thus simplify σ as

$$\begin{aligned}\sigma = &\frac{2}{\tau}\sum_{n=2}^{+\infty}\frac{1}{n!}\int_0^{+\infty} ds\, G(s) \left\langle \left(-\tau\phi'(x(0)) + \sqrt{\tau}v(0)\right)\phi^{(n+1)}(x(0))\Delta(-s)^n \right\rangle \\ &- 2T\int_0^{\infty} ds\, G(s)\langle \phi^{(3)}(x(0))\Delta(-s)\rangle . \end{aligned} \tag{A.36}$$

Using time translation invariance and the definition $\Delta(-s) = x(-s) - x(0)$, we have

$$\begin{aligned}\langle f\left[x(0), v(0)\right]\Delta(-s)^n\rangle &= \langle f\left[x(0), v(0)\right](x(-s) - x(0))^n\rangle \\ &= \langle f\left[x(s), v(s)\right](x(0) - x(s))^n\rangle \\ &= (-1)^n \langle f\left[x(s), v(s)\right]\Delta(s)^n\rangle , \end{aligned} \tag{A.37}$$

where f is an arbitrary function depending on $x(0)$ and $v(0)$. Applying (A.37) for $f = (-\tau\phi'(x(0)) + \sqrt{\tau}v(0))\,\phi^{(n+1)}(x(0))$ and $f = \phi^{(3)}(x(0))$ in (A.36), we obtain the entropy production rate as

$$\begin{aligned}\sigma = &\frac{2}{\tau}\left\langle \int_0^{+\infty} ds\, G(s) \left[\sum_{n=2}^{+\infty}\frac{(-1)^n}{n!}\left(-\tau\phi'(x(s)) + \sqrt{\tau}v(s)\right)\phi^{(n+1)}(x(s))\Delta(s)^n\right]\right\rangle \\ &+ \frac{2}{\tau}\left\langle \int_0^{+\infty} ds\, G(s) T\tau\phi^{(3)}(x(s))\Delta(s)\right\rangle . \end{aligned} \tag{A.38}$$

Since $\Delta(s) = x(s) - x(0)$, the above exact expression still involves two-time averages. In order to reduce the result to the evaluation of stationary-state averages, we will have to expand again (A.38) in powers of $\Delta(s)$. As readily observed in (A.38), the entropy production rate is the sum of two contributions

$$\sigma = \sigma_b + \sigma_a , \tag{A.39}$$

with the first one given by

$$\begin{aligned}\sigma_a &= 2T\int_0^{+\infty} ds\, G(s)\left\langle \phi^{(3)}(x(s))\Delta(s)\right\rangle \\ &= 2T\sum_{n=0}^{+\infty}\int_0^{+\infty} ds\, G(s)\frac{\tau^{\frac{n+1}{2}}}{n!}\left\langle \phi^{(n+3)}(x(0))\left(\frac{\Delta(s)}{\sqrt{\tau}}\right)^{n+1}\right\rangle , \end{aligned} \tag{A.40}$$

and the second one by

$$\sigma_b = \int_0^{+\infty} ds\, G(s) \sum_{n=2}^{+\infty} \frac{2(-1)^n}{\tau n!} \left\langle \left(-\tau\phi'(x(s)) + \sqrt{\tau} v(s)\right) \phi^{(n+1)}(x(s)) \Delta(s)^n \right\rangle \ . \tag{A.41}$$

Taylor expanding (A.41) around $x(0)$, we further express σ_b as

$$\begin{aligned}\sigma_b = &\sum_{n=2}^{+\infty}\sum_{p=0}^{+\infty} \frac{2(-1)^n}{p!\, n!} \tau^{\frac{n+p}{2}} \int_0^{+\infty} ds G(s) \left\langle \partial_x^p \left[-\phi'(x)\phi^{(n+1)}(x)\right]\Big|_{x(0)} \left(\frac{\Delta(s)}{\sqrt{\tau}}\right)^{n+p} \right\rangle \\ &+ \sum_{n=2}^{+\infty}\sum_{p=0}^{+\infty} \frac{2(-1)^n}{p!\, n!} \tau^{\frac{n+p-1}{2}} \int_0^{+\infty} ds G(s) \left\langle \left[v(s)\phi^{(n+1+p)}\right]\Big|_{x(0)} \left(\frac{\Delta(s)}{\sqrt{\tau}}\right)^{n+p} \right\rangle \ . \end{aligned} \tag{A.42}$$

Note that in (A.42), the velocity is still evaluated at time s. However, this raises no difficulty since the equation of motion on v can be integrated exactly as

$$v(s) = v(0)e^{-s} + \sqrt{2D} e^{-s} \int_0^s ds'\, e^{s'} \eta_2(s') \ . \tag{A.43}$$

Finally, in order use only stationary-state averages when computing the entropy production rate, one needs to express $\Delta(s)$ as a function of $x(0)$. This is done by integrating the equation of motion recursively in powers of τ,

$$\frac{\Delta(s)}{\sqrt{\tau}} = -\sqrt{\tau} \int_0^s ds'\, \phi'(x(s')) + \int_0^s ds' \left(v(s') + \sqrt{2T}\eta_1(s')\right) \ . \tag{A.44}$$

Applying (A.44) recursively in powers of τ allows us to compute $\Delta(s)$ up to order $\tau^{\frac{3}{2}}$

$$\begin{aligned}\frac{\Delta(s)}{\sqrt{\tau}} =& -\sqrt{\tau} s\phi'(x(0)) - \tau \int_0^s ds' \frac{\phi'(x(s')) - \phi'(x(0))}{\sqrt{\tau}} + \int_0^s ds' \left(v(s') + \sqrt{2T}\eta_1(s')\right) \\ =& \int_0^s ds' \left(v(s') + \sqrt{2T}\eta_1(s')\right) - \sqrt{\tau} s\phi'(x(0)) - \tau\phi^{(2)}(x(0)) \int_0^s ds' \int_0^{s'} ds'' v(s'') \\ &- \tau\phi^{(2)}(x(0)) \int_0^s ds' \int_0^{s'} ds'' \sqrt{2T}\eta_1(s'') + O(\tau^{3/2}) \end{aligned} \tag{A.45}$$

where the above order in the expansion is enough to collect all terms of order τ^2 in the entropy production rate. Equation (A.45) can then be plugged into (A.40) and (A.42). After averaging over the white noises $\eta_1(s)$ and $\eta_2(s)$, this allows us to obtain the entropy production rate, to order τ^2, solely expressed in terms of stationary-state averages over both x and v. Using (A.16), we directly obtain (2.74) of the main text:

$$\sigma = D\tau^2 H\left(\frac{T}{D}\right) \frac{\int_{-\infty}^{+\infty} \phi^{(3)2}\ e^{-\frac{\phi}{T+D}} dx}{\int_{-\infty}^{+\infty} e^{-\frac{\phi}{T+D}} dx} + O(\tau^{\frac{5}{2}}) \ , \tag{A.46}$$

where the function H is given by

$$H(x) = \frac{4\sqrt{\frac{x}{x+1}} + x\left(4\sqrt{\frac{x}{x+1}} + 2\right) + 1}{8\sqrt{x(x+1)} + 2x\left(6x + 6\sqrt{x(x+1)} + 7\right) + 2} \ . \tag{A.47}$$

A.2 Steady-state distribution of N interacting active particles

This appendix is devoted to the analytical characterization of the stationary distribution of N-interacting AOUPs following the dynamics (2.78)-(2.79) in the limit of small τ. Let us start by introducing the particle velocities $\mathbf{p}_i = \dot{\mathbf{r}}_i$ to recast the dynamics (2.78)-(2.79) into:

$$\tau \dot{\mathbf{p}}_i = -\mathbf{p}_i - (1 + \tau \mathbf{p}_j \cdot \boldsymbol{\nabla}_j)\boldsymbol{\nabla}_i \Phi + (2D)^{1/2}\boldsymbol{\eta}_i \,. \tag{A.48}$$

Note that, by setting $\tau = 0$ in both sides of Eq. (A.48), we indeed recover the standard overdamped equilibrium dynamics:

$$\mathbf{p}_i = -\boldsymbol{\nabla}_i \Phi + (2D)^{1/2}\boldsymbol{\eta}_i. \tag{A.49}$$

We now discuss how a small τ expansion of (A.48) can be systematically derived. In the spirit of [56, 165, 166], we first introduce the scaled variables $\bar{t} \equiv \tau^{-1/2} t$ and $\bar{\mathbf{p}}_i \equiv \mathbf{p}_i \tau^{1/2}$. As a result, the stationary distribution satisfies $\mathcal{L} P_s(\{\mathbf{r}_i, \bar{\mathbf{p}}_i\}) = 0$, where the operator $\mathcal{L}$ reads

$$\mathcal{L} = -\,\bar{\mathbf{p}}_i \cdot \boldsymbol{\nabla}_i + \tau^{-1/2} \frac{\partial}{\partial \bar{p}_{i\alpha}} \left(\bar{p}_{i\alpha} + \tau \bar{p}_{j\beta} \frac{\partial^2 \Phi}{\partial r_{i\alpha} r_{j\beta}} \right) + \frac{\partial}{\partial \bar{p}_{i\alpha}} \frac{\partial \Phi}{\partial r_{i\alpha}} + D\tau^{-1/2} \frac{\partial^2}{\partial \bar{p}_{i\alpha}^2} \,. \tag{A.50}$$

Here, and throughout this appendix, summations over repeated indices are implicit including for terms like $\bar{\mathbf{p}}_i^2$ or $\frac{\partial^2}{\partial \bar{p}_{i\alpha}^2}$. To compute the stationary distribution, we propose the following ansatz:

$$P_s(\mathbf{r}, \bar{\mathbf{p}}) \sim e^{-\frac{\Phi}{D} - \frac{\bar{\mathbf{p}}_i^2}{2D}} \left(1 + \sum_{n=2}^{\infty} \tau^{\frac{n}{2}} A_n \left(\mathbf{r}, \bar{\mathbf{p}} \right) \right) \tag{A.51}$$

where, for convenience, we define $A_0 \equiv 1$ and $A_1 \equiv 0$, and we introduce the notation $\mathbf{r} = \{\mathbf{r}_i\}, \bar{\mathbf{p}} = \{\bar{\mathbf{p}}_i\}$, which lightens the notations in the many-particle case. Note that, for normalization purposes, $\int e^{-\frac{\Phi}{D} - \frac{\bar{\mathbf{p}}_i^2}{2D}} A_n$ has to vanish. Inserting (A.51) into (A.50), we obtain a set of recursive equations for the A_n by equating every order in $\tau^{1/2}$

$$\left(\bar{p}_{i\alpha} \frac{\partial}{\partial \bar{p}_{i\alpha}} - D \frac{\partial^2}{\partial \bar{p}_{i\alpha}^2} \right) A_n = f_n \left(\mathbf{r}, \bar{\mathbf{p}} \right) \tag{A.52}$$

where

$$\begin{aligned} f_n \left(\mathbf{r}, \bar{\mathbf{p}} \right) = &- \bar{p}_{i\alpha} \frac{\partial A_{n-1}}{\partial r_{i\alpha}} + \frac{\partial \Phi}{\partial r_{i\alpha}} \frac{\partial A_{n-1}}{\partial \bar{p}_{i\alpha}} + \frac{\partial^2 \Phi}{\partial r_{i\alpha}^2} A_{n-2} - \frac{\bar{p}_{i\alpha} \bar{p}_{j\beta}}{D} \frac{\partial \Phi}{\partial r_{i\alpha} \partial r_{j\beta}} A_{n-2} \\ &+ \bar{p}_{i\alpha} \frac{\partial^2 \Phi}{\partial r_{i\alpha} \partial r_{j\beta}} \frac{\partial A_{n-2}}{\partial \bar{p}_{j\beta}} \,. \end{aligned} \tag{A.53}$$

Inspection of (A.52)-(A.53) suggests an ansatz for the A_n in the form of degree-n polynomials in the momenta. Indeed, if A_k with $k \leq n$ are assumed to be polynomials of degree-k, then A_{n+1} is also a polynomial of degree $n+1$. We can further show that A_{2n} contains only even terms in the momenta $\bar{\mathbf{p}}$ while A_{2n+1} only contains odd ones. This results from the symmetry of the equation $\mathcal{L} P_s = 0$ under the transformation $\left\{\tau^{1/2}, \bar{\mathbf{p}}\right\} \to -\left\{\tau^{1/2}, \bar{\mathbf{p}}\right\}$. We will use the following tensorial notation for the A_n's

$$A_n = \bar{p}_{i_1,\alpha_1} \ldots \bar{p}_{i_n,\alpha_n} \frac{a^{(n,n)}_{i_1,\ldots,i_n,\alpha_1,\ldots,\alpha_n}}{n!} + \bar{p}_{i_1,\alpha_1} \ldots \bar{p}_{i_{n-2},\alpha_{n-2}} \frac{a^{(n,n-2)}_{i_1,\ldots,i_{n-2},\alpha_1,\ldots,\alpha_{n-2}}}{(n-2)!} + \ldots \tag{A.54}$$

where the $a^{(m,n)}$'s depend on the particles' positions. Note that A_n contains a $\bar{\mathbf{p}}$-independent term $a^{(n,0)}$ only if n is even. Note also that (A.54) is a local function of the momenta, which could be restrictive, but still allow for non-local dependence on the particle positions.

Plugging the expression (A.54) for A_n in (A.52), and equating order by order in $\bar{\mathbf{p}}$, yields the explicit expressions of all tensors $a^{(n,m)}$ for $0 < m \leq n$. For even n, this leaves $a^{(n,0)}$ unconstrained (whereas $a^{(2k+1,0)} = 0$ by definition) but constrains $a^{(n-2,0)}$. For instance, we get for $n = 2, 3, 4$:

$$A_2 = -\frac{(\bar{\mathbf{p}}_i \cdot \boldsymbol{\nabla}_i)^2 \Phi}{2D} + a^{(2,0)}(\mathbf{r}) \tag{A.55}$$

$$A_3 = \frac{(\bar{\mathbf{p}}_i \cdot \boldsymbol{\nabla}_i)^3 \Phi}{6D} + (\bar{\mathbf{p}}_i \cdot \boldsymbol{\nabla}_i)\boldsymbol{\nabla}_j^2 \Phi - \frac{1}{2D}(\bar{\mathbf{p}}_i \cdot \boldsymbol{\nabla}_i)(\boldsymbol{\nabla}_j \Phi)^2 - (\bar{\mathbf{p}}_i \cdot \boldsymbol{\nabla}_i) a^{(2,0)} \tag{A.56}$$

$$\begin{aligned} A_4 =& \frac{1}{8D^2}\left[(\bar{\mathbf{p}}_i \cdot \boldsymbol{\nabla}_i)^2 \Phi\right]\left[(\bar{\mathbf{p}}_j \cdot \boldsymbol{\nabla}_j)^2 \Phi\right] - \frac{(\bar{\mathbf{p}}_i \cdot \boldsymbol{\nabla}_i)^4 \Phi}{24D} + \frac{(\bar{\mathbf{p}}_i \cdot \boldsymbol{\nabla}_i)^2 \left[a^{(2,0)} - \boldsymbol{\nabla}_j^2 \Phi\right]}{2} \\ &+ \frac{3}{4D}\frac{\partial \Phi}{\partial r_{j,\alpha}}\frac{\partial}{\partial r_{j,\alpha}}(\bar{\mathbf{p}}_i \cdot \boldsymbol{\nabla}_i)^2 \Phi + \frac{1}{2D}\frac{\partial\left[(\bar{\mathbf{p}}_j \cdot \boldsymbol{\nabla}_j)\Phi\right]}{\partial r_{i,\alpha}}\frac{\partial\left[(\bar{\mathbf{p}}_k \cdot \boldsymbol{\nabla}_k)\Phi\right]}{\partial r_{i,\alpha}} + a^{(4,0)}(\mathbf{r}) \end{aligned} \tag{A.57}$$

Projected on the lowest order in $\bar{\mathbf{p}}$, equation (A.52) for A_n of the form (A.54) further yields the integrability condition for $a^{(n-2,0)}$

$$\left(D\frac{\partial^2}{\partial r_{i\alpha}^2} - \frac{\partial \Phi}{\partial r_{i\alpha}}\frac{\partial}{\partial r_{i\alpha}}\right) a^{(n-2,0)} = g_n(\mathbf{r}) \tag{A.58}$$

where $g_n(\mathbf{r})$ are functions of the particle positions only that can be computed explicitly. We note that the left hand side of the solvability equation (A.58) is nothing else than the backward Fokker-Planck operator for the equilibrium dynamics (A.49) applied to $a^{(n-2,0)}$, while its right hand side is a source term g_n. Finding a solution to (A.58) would thus provide a closed expression for the perturbative expansion of $\mathcal{P}_s(\mathbf{r}, \bar{\mathbf{p}})$ up to order $n-2$.

From the Fredholm alternative theorem, the condition under which such a solution exists, and the expansion can be carried out, is that g_n should be orthogonal to $e^{-\Phi/D}$ [167]. This is always possible in the small D limit, following [168], but the existence of a solution to arbitrary order remains, in the general case, an open problem. Here we show that it can be carried out explicitly up to order $\tau^{3/2}$. g_4 indeed reads

$$g_4 = \frac{1}{D}\frac{\partial^2 \Phi}{\partial r_{i\alpha}\partial r_{j\beta}}\frac{\partial \Phi}{\partial r_{i\alpha}}\frac{\partial \Phi}{\partial r_{j\beta}} - \frac{5}{2}\frac{\partial^3 \Phi}{\partial^2 r_{i\alpha}\partial r_{j\beta}}\frac{\partial \Phi}{\partial r_{j\beta}} - \frac{\partial^2 \Phi}{\partial r_{i\alpha}\partial r_{j\beta}}\frac{\partial^2 \Phi}{\partial r_{i\alpha}\partial r_{j\beta}} + \frac{3D}{2}\frac{\partial^4 \Phi}{\partial^2 r_{i\alpha}\partial^2 r_{j\beta}}\,. \tag{A.59}$$

and the integrability condition (A.58) is solved, for $n = 2$, by

$$a^{(2,0)}(\mathbf{r}) = -\frac{1}{2D}\left(\boldsymbol{\nabla}_i \Phi\right)^2 + \frac{3}{2}\boldsymbol{\nabla}_i^2 \Phi\,, \tag{A.60}$$

where the sum over the index i is implicit. This yields the following expression for the stationary measure of N interacting AOUPs, valid up to order $\tau^{3/2}$,

$$\begin{aligned} P_s(\mathbf{r}, \bar{\mathbf{p}}) \sim e^{-\frac{\Phi + \bar{\mathbf{p}}_i^2/2}{D}} \Big\{ 1 - \frac{\tau}{2D}\left[\left(\boldsymbol{\nabla}_i \Phi\right)^2 + \left(\bar{\mathbf{p}}_i \cdot \boldsymbol{\nabla}_i\right)^2 \Phi - 3D\boldsymbol{\nabla}_i^2 \Phi\right] \\ + \frac{\tau^{3/2}}{6D}(\bar{\mathbf{p}}_i \cdot \boldsymbol{\nabla}_i)\left[\left(\bar{\mathbf{p}}_j \cdot \boldsymbol{\nabla}_j\right)^2 - 3D\boldsymbol{\nabla}_j^2\right]\Phi + \mathcal{O}\left(\tau^2\right)\Big\}. \end{aligned} \tag{A.61}$$

Integrating over momentums $\bar{\mathbf{p}}$, we obtain the many-body marginal distribution, in position space, $P_s(\mathbf{r})$:

$$P_s(\mathbf{r}) \sim \exp\left[-\frac{\Phi}{D} - \frac{\tau}{2D}(\boldsymbol{\nabla}_i\Phi)^2 + \tau\boldsymbol{\nabla}_i^2\Phi + \mathcal{O}\left(\tau^2\right)\right]. \tag{A.62}$$

It is interesting to note that similar functional forms to (A.61) and (A.62) are encountered in many contexts, from the semi-classical expansion of the Boltzmann distribution in powers of $\hbar$ [169] to the Hermitian form of the Fokker-Planck operator [170]. It would be interesting to know whether this is just a coincidence or reflects the presence of a deeper connection.

A.3 Numerical methods

To simulate dynamics (2.50), we used a discretized Heun scheme while dynamics (2.51) was integrated exactly using Gillespie's method [171]. The obtained algorithm iterates as follows:

1 μ = exp(−dt/τ);
2 σ_x = $\sqrt{D(1-\mu^2)/\tau}$;
3 Y_1 = $\sqrt{2D\tau\,(\mathrm{dt}/\tau - 2(1-\mu) + 0.5(1-\mu^2)) - \tau D(1-\mu)^4/(1-\mu^2)}$;
4 Y_2 = $\sqrt{\tau D}(1-\mu)^2/\sqrt{1-\mu^2}$;
5 T_1 = $\sqrt{2T\mathrm{dt}}$;
6 Y = x = 0;
7 v = $\sqrt{D/\tau}$*normal_distribution(0,1);
8
9 **while**(t < totaltime){
10 η_1 = normal_distribution(0,1);
11 η_2 = normal_distribution(0,1);
12 η_3 = normal_distribution(0,1);
13 Y = τ*v*(1−μ) + Y_1*η_2 + Y_2*η_1;
14 v = v*μ + σ_x*η_1;
15 x_1 = x − dt*$\partial_x\phi(x)$ + Y + T_1*η_3;
16 x += Y + T_1*η_3 −0.5*dt*($\partial_x\phi(x)$ + $\partial_x\phi(x_1)$);
17 t += dt;}

At step (17), x(t) is stored in the variable x. The steady-state marginal in space of the distribution $\mathcal{P}_s(x)$ was then obtained by recording the particle's position recurrently into an histogram. The current J was computed using the distance travelled by the particle divided by the duration of the simulation: the error bar on J corresponds to the standard deviation of this quantity. Such a definition for the current was heuristically found to converge faster than computing $J = \langle -\partial_x\phi + v/\sqrt{\tau}\rangle$ with recurrent recordings.

B. Fluctuation-induced first-order transition to collective motion

B.1 The Boltzmann approach to the Vicsek model

This appendix is devoted to the derivation of the evolution equation for $\mathbf{W}$ following the method established in [114, 120]. Using the periodicity of f with respect to θ, we introduce the Fourier series of $\mathbf{W}$ as

$$\hat{f}_k(\mathbf{r},t) = \int_{-\pi}^{\pi} d\theta\, f(\mathbf{r},\theta,t)\, e^{ik\theta}. \tag{B.1}$$

The one-particle probability distribution f can then be retrieved from its Fourier modes through the relation

$$f(\mathbf{r},\theta,t) = \frac{1}{2\pi}\sum_{k\in\mathbb{Z}} \hat{f}_k(\mathbf{r},t)\, e^{-ik\theta}. \tag{B.2}$$

The hydrodynamic fields (3.6) can be related to the zero-th and first Fourier modes defined in (B.1). Indeed, we note that $\rho(\mathbf{r},t) = \hat{f}_0(\mathbf{r},t)$ while the vector associated to $\mathbf{W}(\mathbf{r},t)$ in the complex plane is $v\hat{f}_1$:

$$W_x(\mathbf{r},t) = v\Re(\hat{f}_1(\mathbf{r},t))\ , \quad \text{and} \quad W_y(\mathbf{r},t) = v\Im(\hat{f}_1(\mathbf{r},t))\ . \tag{B.3}$$

We will make use of this correspondence with the complex plane by first deriving the time-evolution of $\hat{f}_1$ before casting it into an evolution equation for $\mathbf{W}$. Let us now construct the evolution equation for $\hat{f}_k$ by multiplying (3.3) by $e^{ik\theta}$ and integrating over θ. We obtain

$$\frac{\partial}{\partial t}\hat{f}_k + \boldsymbol{\nabla}\cdot\left[v\int_{-\pi}^{\pi} d\theta\, e^{ik\theta}\mathbf{e}(\theta) f(\mathbf{r},\theta,t)\right] = \int_{-\pi}^{\pi} d\theta\, e^{ik\theta}\left(I_{\text{dif}}[f] + I_{\text{col}}[f,f]\right). \tag{B.4}$$

The gradient term on the left hand side of (B.4) is the k-th Fourier mode of the velocity field $\hat{\mathbf{W}}^{(k)}(\mathbf{r},t)$

$$\hat{\mathbf{W}}^{(k)}(\mathbf{r},t) = v\int_{-\pi}^{\pi} d\theta\, e^{ik\theta}\mathbf{e}(\theta) f(\mathbf{r},\theta,t) \tag{B.5}$$

which can be related to $\hat{f}_k(\mathbf{r},t)$ through

$$\hat{W}_x^{(k)}(\mathbf{r},t) = \frac{v}{2}[\hat{f}_{k+1}(\mathbf{r},t) + \hat{f}_{k-1}(\mathbf{r},t)]\ , \qquad \hat{W}_y^{(k)}(\mathbf{r},t) = \frac{v}{2i}[\hat{f}_{k+1}(\mathbf{r},t) - \hat{f}_{k-1}(\mathbf{r},t)]. \tag{B.6}$$

Injecting (B.6) into (B.4), we get

$$\frac{\partial}{\partial t}\hat{f}_k + \frac{v}{2}\frac{\partial}{\partial x}\left[\hat{f}_{k+1} + \hat{f}_{k-1}\right] + \frac{v}{2i}\frac{\partial}{\partial y}\left[\hat{f}_{k+1} - \hat{f}_{k-1}\right] = \int_{-\pi}^{\pi} d\theta\, e^{ik\theta}\left(I_{\text{dif}}[f] + I_{\text{col}}[f,f]\right). \tag{B.7}$$

The right-hand side of (B.7) can be evaluated by inserting (B.2) in (3.5):

$$\int_{-\pi}^{\pi} e^{ik\theta} I_{\text{dif}}[f] d\theta = -\,D\left[1 - \text{sinc}\left(\sigma\pi k\right)\right]\hat{f}_k \tag{B.8}$$

$$\int_{-\pi}^{\pi} e^{ik\theta} I_{\text{col}}[f] d\theta = -\,\frac{2r_0 v}{\pi}\sum_{q\in\mathbb{Z}}\left[I_q - \text{sinc}\left(\sigma\pi k\right) I_{q-k/2}\right]\hat{f}_q\hat{f}_{k-q}\,, \tag{B.9}$$

where I_q is given by the integral

$$I_q = \int_{-\pi}^{\pi} d\theta \left|\sin\frac{\theta}{2}\right| \cos q\theta. \tag{B.10}$$

For an integer q we thus obtain

$$I_q = \frac{4}{1-4q^2}\,, \tag{B.11}$$

while for a half integer $q = m + \frac{1}{2}$ we have

$$I_{\frac{1}{2}} = I_{-\frac{1}{2}} = 2, \tag{B.12}$$

$$I_{m+\frac{1}{2}} = \frac{1}{m(m+1)}\left[(-1)^m(2m+1)-1\right], \qquad m \neq -1, 0. \tag{B.13}$$

Inserting (B.8)-(B.9) into (B.7), we obtain the final form of the time-evolution of $\hat{f}_k$ as

$$\begin{aligned}\frac{\partial}{\partial t}\hat{f}_k =& -\frac{v}{2}\frac{\partial}{\partial x}\left[\hat{f}_{k+1}+\hat{f}_{k-1}\right] - \frac{v}{2i}\frac{\partial}{\partial y}\left[\hat{f}_{k+1}-\hat{f}_{k-1}\right] - D\left[1-\mathrm{sinc}\left(\sigma\pi k\right)\right]\hat{f}_k \\ & - \frac{2r_0 v}{\pi}\sum_{q\in\mathbb{Z}}\left[I_q - \mathrm{sinc}\left(\sigma\pi k\right) I_{q-k/2}\right]\hat{f}_q\hat{f}_{k-q}\,.\end{aligned} \tag{B.14}$$

To get the evolution of $\hat{f}_1$, we need to close (B.14) for $k = 1$ in terms of the modes $\hat{f}_0$ and $\hat{f}_1$. To perform such a closure, we assume that f is weakly anisotropic and consider that we can neglect f_k for $|k| > 2$. Within this approximation, (B.14) reads for $k = 1$

$$\begin{aligned}\frac{\partial\hat{f}_1}{\partial t} + \frac{v}{2}\frac{\partial}{\partial x_1}(\hat{f}_2+\hat{f}_0) + \frac{v}{2i}\frac{\partial}{\partial x_2}(\hat{f}_2-\hat{f}_0) =& -\frac{8}{\pi}r_0 v\left(\mathrm{sinc}(\sigma\pi)-\frac{2}{5}\right)\hat{f}_1^*\hat{f}_2 \\ & - \left[D\left(1-\mathrm{sinc}(\sigma\pi)\right) + \frac{8}{\pi}d_0 v_0\left(\frac{2}{3}-\mathrm{sinc}(\sigma\pi)\right)\hat{f}_0\right]\hat{f}_1\,,\end{aligned} \tag{B.15}$$

while (B.14), taken at $k = 2$, yields

$$\begin{aligned}\frac{\partial\hat{f}_2}{\partial t} =& -\frac{v}{2}\frac{\partial\hat{f}_1}{\partial x} + \frac{v}{2i}\frac{\partial\hat{f}_1}{\partial y} - \left[D\left(1-\mathrm{sinc}(2\sigma\pi)\right) + \frac{16}{3\pi}r_0 v\left(\frac{7}{5}+\mathrm{sinc}(2\sigma\pi)\right)\hat{f}_0\right]\hat{f}_2 \\ & + \frac{8}{\pi}r_0 v\left(\frac{1}{3}+\mathrm{sinc}(2\sigma\pi)\right)\hat{f}_1^2.\end{aligned} \tag{B.16}$$

Note that to obtain (B.15) and (B.16), we made use of the values of I_q computed in (B.11) to (B.13). Because $\hat{f}_2$ is not an hydrodynamic field, it has to be a fast mode such that $\partial\hat{f}_2/\partial t = 0$. From (B.16), we thus deduce that it is enslaved to $\hat{f}_0$ and $\hat{f}_1$ through

$$\hat{f}_2 = \frac{-\frac{v}{2}\frac{\partial\hat{f}_1}{\partial x} + \frac{v}{2i}\frac{\partial\hat{f}_1}{\partial y} + \frac{8}{\pi}r_0 v\left(\frac{1}{3}+\mathrm{sinc}(2\sigma\pi)\right)\hat{f}_1^2}{D\left(1-\mathrm{sinc}(2\sigma\pi)\right) + \frac{16}{3\pi}r_0 v\left(\frac{7}{5}+\mathrm{sinc}(2\sigma\pi)\right)\hat{f}_0}\,. \tag{B.17}$$

Plugging (B.17) into (B.15), mapping back $\hat{f}_1$ and $\hat{f}_0$ to $\mathbf{W}/v$ and ρ respectively, we obtain the hydrodynamic equation (3.8) of the main text

$$\begin{aligned}\frac{\partial\mathbf{W}}{\partial t} + \gamma(\mathbf{W}\cdot\nabla)\mathbf{W} =& -\frac{v^2}{2}\nabla\rho + \frac{\kappa}{2}\nabla\mathbf{W}^2 + (\alpha-\xi\mathbf{W}^2)\mathbf{W} + \nu\nabla^2\mathbf{W} \\ & - \kappa(\nabla\cdot\mathbf{W})\mathbf{W} + 2\nu'\nabla\rho\cdot\mathbf{M} - \nu'(\nabla\cdot\mathbf{W})\nabla\rho,\end{aligned} \tag{B.18}$$

where $\nu' = \partial\nu/\partial\rho$, $\mathbf{M} = \frac{1}{2}(\nabla\mathbf{W} + \nabla\mathbf{W}^{\mathbf{T}})$ is the symmetric part of the momentum gradient tensor and the different coefficients are given by

$$\nu = \frac{v^2}{4}\left[D\left(1-\mathrm{sinc}(2\sigma\pi)\right) + \frac{16}{3\pi}r_0 v\rho\left(\frac{7}{5}+\mathrm{sinc}(2\sigma\pi)\right)\right]^{-1}, \tag{B.19}$$

$$\gamma = \frac{16\nu r_0}{\pi v}\left(\frac{16}{15}+2\,\mathrm{sinc}(2\sigma\pi)-\mathrm{sinc}(\sigma\pi)\right), \tag{B.20}$$

$$\kappa = \frac{16\nu r_0}{\pi v}\left(\frac{4}{15}+2\,\mathrm{sinc}(2\sigma\pi)+\mathrm{sinc}(\sigma\pi)\right), \tag{B.21}$$

$$\alpha = \frac{8}{\pi}r_0 v\rho\left(\mathrm{sinc}(\sigma\pi)-\frac{2}{3}\right) - D\left(1-\mathrm{sinc}(\sigma\pi)\right), \tag{B.22}$$

$$\xi = \frac{256\nu r_0^2}{\pi^2 v^2}\left(\mathrm{sinc}(\sigma\pi)-\frac{2}{5}\right)\left(\frac{1}{3}+\mathrm{sinc}(2\sigma\pi)\right). \tag{B.23}$$

B.2 The Active Ising Model

Throughout this appendix, we use Fourier series for L-periodic functions f with the convention

$$f^q = \frac{1}{L}\int_0^L f(x)e^{-iqx}\,, \qquad f(x) = \sum_{n\in\mathbb{Z}} f^q e^{iqx}\,, \tag{B.24}$$

where $q = 2\pi n/L$. We note that for an arbitrary stochastic function $f(x)$ verifying $\langle f^q f^{q'}\rangle \propto \langle f^q f^{-q}\rangle L^{-1}\delta_{q+q',0}$, $\langle f^2(x)\rangle$ is given in the large-system-size limit $L\to\infty$ as

$$\lim_{L\to\infty}\langle f^2(x)\rangle = \lim_{L\to\infty}\sum_{q,q'}\langle f^q f^{q'}\rangle e^{iqx+iq'x} = \lim_{L\to\infty}\sum_q \frac{1}{L}\langle f^q f^{-q}\rangle = \int_{-\infty}^{+\infty}\frac{dq}{2\pi}\langle f^q f^{-q}\rangle\,. \tag{B.25}$$

B.2.1 Derivation of the correlators in the high temperature phase

This appendix is devoted to the computation of the correlators $\langle\delta\rho_1^2\rangle$, $\langle\delta m_1^2\rangle$ and $\langle\delta m_1\delta\rho_1\rangle$ which are needed to close the renormalized hydrodynamics (3.66) of the AIM. Using assumption AI, we start by casting the stochastic evolution (3.55)-(3.56) of $\delta\rho_1$ and δm_1 into Fourier space with the Fourier convention defined in (B.24). We obtain

$$\partial_t\begin{pmatrix}\delta\rho_1^q\\ \delta m_1^q\end{pmatrix} = \begin{pmatrix}M_{11}^q & M_{12}^q\\ M_{21}^q & M_{22}^q\end{pmatrix}\begin{pmatrix}\delta\rho_1^q\\ \delta m_1^q\end{pmatrix} + \begin{pmatrix}0\\ \sqrt{2\rho_0}\,\eta^q\end{pmatrix}\,, \tag{B.26}$$

where η^q is the q-th Fourier mode of the Gaussian white noise with correlations $\langle\eta^q(t)\eta^{q'}(t')\rangle = L^{-1}\delta_{q+q',0}\delta(t-t')$ and the matrix coefficients M_{11}^q, M_{12}^q, M_{21}^q, M_{22}^q are given by

$$M_{11}^q = -Dq^2\,,\quad M_{12}^q = -ivq\,,\quad M_{21}^q = -iqv + 2\gamma\frac{m_0^3}{\rho_0^3}\,,\quad M_{22}^q = -Dq^2-\alpha-3\gamma\frac{m_0^2}{\rho_0^2}\,. \tag{B.27}$$

To compute the equal-time two-point correlation functions in the steady-state, we use Itō calculus on the stochastic system (B.26) to get the following closed system of equations

$$\frac{d}{dt}\langle\delta\rho_1^q\delta\rho_1^{q'}\rangle = (M_{11}^q + M_{11}^{q'})\langle\delta\rho_1^q\delta\rho_1^{q'}\rangle + M_{12}^q\langle\delta m_1^q\delta\rho_1^{q'}\rangle + M_{12}^{q'}\langle\delta\rho_1^q\delta m_1^{q'}\rangle \tag{B.28}$$

$$\frac{d}{dt}\langle\delta m_1^q\delta\rho_1^{q'}\rangle = (M_{22}^q + M_{11}^{q'})\langle\delta m_1^q\delta\rho_1^{q'}\rangle + M_{21}^q\langle\delta\rho_1^q\delta\rho_1^{q'}\rangle + M_{12}^{q'}\langle\delta m_1^q\delta m_1^{q'}\rangle \tag{B.29}$$

$$\frac{d}{dt}\langle\delta m_1^q\delta m_1^{q'}\rangle = (M_{22}^q + M_{22}^{q'})\langle\delta m_1^q\delta m_1^{q'}\rangle + M_{21}^q\langle\delta\rho_1^q\delta m_1^{q'}\rangle + M_{21}^{q'}\langle\delta m_1^q\delta\rho_1^{q'}\rangle + \frac{2\rho_0}{L}\delta_{q+q',0}\ , \tag{B.30}$$

In the steady state, this leads to the system

$$0 = (M_{11}^q + M_{11}^{q'})\langle\delta\rho_1^q\delta\rho_1^{q'}\rangle + M_{12}^q\langle\delta m_1^q\delta\rho_1^{q'}\rangle + M_{12}^{q'}\langle\delta\rho_1^q\delta m_1^{q'}\rangle \tag{B.31}$$

$$0 = (M_{22}^q + M_{11}^{q'})\langle\delta m_1^q\delta\rho_1^{q'}\rangle + M_{21}^q\langle\delta\rho_1^q\delta\rho_1^{q'}\rangle + M_{12}^{q'}\langle\delta m_1^q\delta m_1^{q'}\rangle \tag{B.32}$$

$$-\frac{2\rho_0}{L}\delta_{q+q',0} = (M_{22}^q + M_{22}^{q'})\langle\delta m_1^q\delta m_1^{q'}\rangle + M_{21}^q\langle\delta\rho_1^q\delta m_1^{q'}\rangle + M_{21}^{q'}\langle\delta m_1^q\delta\rho_1^{q'}\rangle\ , \tag{B.33}$$

Solving this linear system yields

$$\langle\delta m_1^q\delta m_1^{q'}\rangle = \rho_0\Bigg[-\frac{3\gamma\left(2D^2q^2+\alpha D+vDq+v^2\right)\left(2D^2q^2+D(\alpha-qv)+v^2\right)}{\left(\alpha+2Dq^2\right)\left(D^2q^2+\alpha D+v^2\right)^2}\frac{m_0^2}{\rho_0^2} + \frac{2D^2q^2+\alpha D+v^2}{\left(2Dq^2+\alpha\right)\left(D^2q^2+\alpha D+v^2\right)}\Bigg]\frac{\delta_{q+q',0}}{L} + \mathcal{O}\left(m_0^3\right) \tag{B.34}$$

$$\langle\delta\rho_1^q\delta\rho_1^{q'}\rangle = \frac{\rho_0 v^2}{\left(2Dq^2+\alpha\right)\left(D^2q^2+\alpha D+v^2\right)}\frac{\delta_{q+q',0}}{L} + \mathcal{O}\left(m_0^2\right) \tag{B.35}$$

$$\langle\delta m_1^q\delta\rho_1^{q'}\rangle = \frac{i\rho_0 vDq}{\left(2Dq^2+\alpha\right)\left(D^2q^2+\alpha D+v^2\right)}\frac{\delta_{q+q',0}}{L} + \mathcal{O}\left(m_0^2\right)\ . \tag{B.36}$$

Applying formula (B.25) for $\langle\delta m_1^2\rangle$, $\langle\delta\rho_1^2\rangle$ and $\langle\delta\rho_1\delta m_1\rangle$, we note that assumption AII ensures the convergence of the integral over q. Performing this integration analytically then gives (3.67)-(3.68) of the main text

$$\langle\delta m_1^2\rangle = \rho_0\frac{v^2\sqrt{\frac{2\alpha}{D}}+\alpha\sqrt{v^2+\alpha D}}{4\alpha v^2+2\alpha^2 D} - \rho_0\frac{3\gamma D\left(\frac{\alpha D}{\sqrt{v^2+\alpha D}}+\frac{\sqrt{2}v^2\left(2v^2+3\alpha D\right)}{(\alpha D)^{3/2}}\right)}{4\left(\alpha D+2v^2\right)^2}\frac{m_0^2}{\rho_0^2} + \mathcal{O}(m_0^3) \tag{B.37}$$

$$\langle\delta\rho_1^2\rangle = \rho_0\frac{v^2\left(\sqrt{\frac{2\alpha}{D}}-\frac{\alpha}{\sqrt{v^2+\alpha D}}\right)}{2\alpha\left(\alpha D+2v^2\right)} + \mathcal{O}(m_0^2)\,, \qquad \langle\delta\rho_1\delta m_1\rangle = 0 + \mathcal{O}(m_0^2)\ . \tag{B.38}$$

B.2.2 Renormalization in the low temperature phase

In this appendix, we detail the quasi-linear renormalization approach in the low temperature phase, where $\alpha < 0$. As seen in assumption AII, the main obstacle in this regime is the absence of mass for the fluctuations δm_1 and $\delta\rho_1$. To circumvent this issue, we change variables for the field w defined as

$$w = m - \sqrt{\frac{|\alpha|}{\gamma}}\rho \tag{B.39}$$

In term of this new field, the time-evolution (3.40)-(3.41) reads

$$\partial_t \rho = D\partial_{xx}\rho - v\partial_x w - v\sqrt{\frac{|\alpha|}{\gamma}}\partial_x \rho \tag{B.40}$$

$$\partial_t w = D\partial_{xx} w + v\sqrt{\frac{|\alpha|}{\gamma}}\partial_x w - v\left(1-\frac{|\alpha|}{\gamma}\right)\partial_x \rho - 2|\alpha| w - 3\sqrt{\gamma|\alpha|}\frac{w^2}{\rho} - \gamma w^3/\rho^2 \ . \tag{B.41}$$

Note that now there is a clear mass $-2|\alpha|w$ in (B.41). Introducing $v_1 = v\sqrt{|\alpha|/\gamma}$, $v_2 = v(1-|\alpha|/\gamma)$, $a_1 = 2|\alpha|$, $a_2 = 3\sqrt{\gamma|\alpha|}$ and $\mathcal{F}_\ell(w,\rho) = a_1 w + a_2 w^2/\rho + \gamma w^3/\rho^2$, we cast the above evolution into

$$\partial_t \rho = D\partial_{xx}\rho - v\partial_x w - v_1\partial_x \rho \tag{B.42}$$

$$\partial_t w = D\partial_{xx} w + v_1\partial_x w - v_2\partial_x \rho - \mathcal{F}_\ell(w,\rho) \ . \tag{B.43}$$

We now switch on the fluctuations to assess how they renormalize (B.42)-(B.43). The change of variable (B.39) being linear, the noise acting on w is the same as the noise acting on m in (3.53) and we obtain the following fluctuating hydrodynamics

$$\partial_t \rho = D\partial_{xx}\rho - v\partial_x w - v_1\partial_x \rho \tag{B.44}$$

$$\partial_t w = D\partial_{xx} w + v_1\partial_x w - v_2\partial_x \rho - \mathcal{F}_\ell(w,\rho) + \sqrt{2\sigma\rho}\,\eta \ , \tag{B.45}$$

where η is a Gaussian white noise with correlations $\langle \eta(x,t)\eta(x',t')\rangle = \delta(t-t')\delta(x-x')$. Using the expansions $\rho = \rho_0 + \sqrt{\sigma}\delta\rho_1 + ..$ and $w = w_0 + \sqrt{\sigma}\delta w_1 + ..$, we repeat the computations detailed in section 3.4 to obtain the renormalized hydrodynamic for $\tilde{\rho} = \langle \rho \rangle$ and $\tilde{w} = \langle w \rangle$ to order σ as

$$\partial_t \tilde{\rho} = D\partial_{xx}\tilde{\rho} - v\partial_x \tilde{w} - v_1\partial_x \tilde{\rho} \tag{B.46}$$

$$\begin{aligned}\partial_t \tilde{w} =& D\partial_{xx}\tilde{w} + v_1\partial_x \tilde{w} - v_2\partial_x\tilde{\rho} - \mathcal{F}_l(\tilde{\rho},\tilde{w}) - \sigma\frac{\partial^2 \mathcal{F}_\ell}{\partial w^2}\left(\frac{\langle \delta w_1^2\rangle - \langle \delta w_1\rangle^2}{2}\right) \\ & - \sigma\frac{\partial^2 \mathcal{F}_\ell}{\partial \rho^2}\left(\frac{\langle \delta \rho_1^2\rangle - \langle \delta \rho_1\rangle^2}{2}\right) - \sigma\frac{\partial^2 \mathcal{F}_\ell}{\partial w \partial \rho}\left(\langle \delta w_1 \delta\rho_1\rangle - \langle \delta w_1\rangle\langle \delta\rho_1\rangle\right) \ .\end{aligned} \tag{B.47}$$

To close the above time evolution, we have to compute the correlators involving δw_1 and $\delta\rho_1$ by using their linearized stochastic evolution which reads

$$\partial_t \delta\rho_1 = D\partial_{xx}\delta\rho_1 - v\partial_x \delta w_1 - v_1\partial_x\delta\rho \tag{B.48}$$

$$\partial_t \delta w_1 = D\partial_{xx}\delta w_1 + v_1\partial_x\delta w_1 - v_2\partial_x\delta\rho_1 - \frac{\partial \mathcal{F}_\ell}{\partial\rho}\delta\rho_1 - \frac{\partial \mathcal{F}_\ell}{\partial w}\delta w_1 + \sqrt{2\rho_0}\,\eta \ . \tag{B.49}$$

In Fourier space, using the Fourier convention (B.24), we obtain

$$\partial_t \begin{pmatrix} \delta\rho_1^q \\ \delta w_1^q \end{pmatrix} = \begin{pmatrix} B_{11}^q & B_{12}^q \\ B_{21}^q & B_{22}^q \end{pmatrix}\begin{pmatrix} \delta\rho_1^q \\ \delta w_1^q \end{pmatrix} + \begin{pmatrix} 0 \\ \sqrt{2\rho_0}\,\eta^q \end{pmatrix} \ , \tag{B.50}$$

where η^q is the q-th Fourier mode of the Gaussian white noise with correlations $\langle \eta^q(t)\eta^{q'}(t')\rangle = L^{-1}\delta_{q+q',0}\delta(t-t')$ and the matrix coefficients B_{11}^q, B_{12}^q, B_{21}^q, B_{22}^q are given by

$$B_{11}^q = -Dq^2 - iv_1 q \ , \qquad B_{12}^q = -ivq \ , \tag{B.51}$$

$$B_{21}^q = -iqv_2 + a_2\frac{w_0^2}{\rho_0^2} + 2\gamma\frac{w_0^3}{\rho_0^3} \ , \quad B_{22}^q = -Dq^2 + v_1 iq - a_1 - 2a_2\frac{w_0}{\rho_0} - 3\gamma\frac{w_0^2}{\rho_0^2} \ . \tag{B.52}$$

Using Itō calculus on (B.50), we obtain the same closed system of equations as in (B.31) to (B.33) but with the matrix M^q replaced by the matrix B^q and δm_1 replaced by δw_1. Solving this system yields the correlators in Fourier space as

$$\begin{aligned}\langle \delta w_1^q \delta w_1^{q'} \rangle =& \langle \delta w_1^q \delta w_1^{-q} \rangle \frac{\delta_{q+q',0}}{L} + \mathcal{O}(w_0) \ , \quad \langle \delta \rho_1^q \delta \rho_1^{q'} \rangle = \langle \delta \rho_1^q \delta \rho_1^{-q} \rangle \frac{\delta_{q+q',0}}{L} + \mathcal{O}(w_0) \\ \langle \delta w_1^q \delta \rho_1^{q'} \rangle =& \langle \delta w_1^q \delta \rho_1^{-q} \rangle \frac{\delta_{q+q',0}}{L} + \mathcal{O}(w_0) \ ,\end{aligned} \tag{B.53}$$

where $\langle \delta w_1^q \delta w_1^{-q} \rangle$, $\langle \delta \rho_1^q \delta \rho_1^{-q} \rangle$ and $\langle \delta w_1^q \delta \rho_1^{-q} \rangle$ are given by

$$\langle \delta w_1^q \delta w_1^{q'} \rangle = \frac{\rho_0 v^2 \left(a_1 + 2Dq^2\right)}{v v_2 \left(a_1 + 2Dq^2\right)^2 + D\left(a_1 + Dq^2\right)\left(\left(a_1 + 2Dq^2\right)^2 + 4q^2 v_1^2\right)} \tag{B.54}$$

$$\langle \delta \rho_1^q \delta \rho_1^{q'} \rangle = \frac{\rho_0 \left(v v_2 \left(a_1 + 2Dq^2\right) + D\left(\left(a_1 + 2Dq^2\right)^2 + 4q^2 v_1^2\right)\right)}{v v_2 \left(a_1 + 2Dq^2\right)^2 + D\left(a_1 + Dq^2\right)\left(\left(a_1 + 2Dq^2\right)^2 + 4q^2 v_1^2\right)} \tag{B.55}$$

$$\langle \delta w_1^q \delta \rho_1^{q'} \rangle = \frac{iDq\rho_0 v \left(a_1 + 2q(Dq + iv_1)\right)}{v v_2 \left(a_1 + 2Dq^2\right)^2 + D\left(a_1 + Dq^2\right)\left(\left(a_1 + 2Dq^2\right)^2 + 4q^2 v_1^2\right)} \ . \tag{B.56}$$

Because v, v_1, v_2, a_1, a_2 and γ are positive, the denominators in the above expressions remains positive as well. This allows us to integrate over q, and, using (B.25), we obtain the correlators in real space as

$$\langle \delta w_1^2 \rangle = \frac{\rho_0 v}{v_2 a_1} f_w \left(\frac{v}{\sqrt{Da_1}}, \frac{v_1}{\sqrt{Da_1}}, \frac{v_2}{\sqrt{Da_1}} \right) + \mathcal{O}(w_0) \ , \tag{B.57}$$

$$\langle \delta \rho_1^2 \rangle = \frac{\rho_0}{a_1} f_\rho \left(\frac{v}{\sqrt{Da_1}}, \frac{v_1}{\sqrt{Da_1}}, \frac{v_2}{\sqrt{Da_1}} \right) + \mathcal{O}(w_0) \ , \qquad \langle \delta \rho_1 \delta w_1 \rangle = 0 + \mathcal{O}(w_0) \ , \tag{B.58}$$

where $f_w(s,u,z)$ and $f_\rho(s,u,z)$ are given by

$$f_w(s,u,z) = \int_{-\infty}^{+\infty} \frac{d\tilde{q}}{2\pi} \frac{sz\left(1 + 2\tilde{q}^2 s^2\right)}{sz\left(1 + 2\tilde{q}^2 s^2\right)^2 + \left(1 + \tilde{q}^2 s^2\right)\left(\left(1 + 2\tilde{q}^2 s^2\right)^2 + 4\tilde{q}^2 s^2 u^2\right)} \tag{B.59}$$

$$f_\rho(s,u,z) = \int_{-\infty}^{+\infty} \frac{d\tilde{q}}{2\pi} \frac{sz\left(1 + 2\tilde{q}^2 s^2\right) + \left(1 + 2\tilde{q}^2 s^2\right)^2 + 4\tilde{q}^2 s^2 u^2}{sz\left(1 + 2\tilde{q}^2 s^2\right)^2 + \left(1 + \tilde{q}^2 s^2\right)\left(\left(1 + 2\tilde{q}^2 s^2\right)^2 + 4\tilde{q}^2 s^2 u^2\right)} \ . \tag{B.60}$$

Inserting (B.57)-(B.58) into (B.47), truncating terms beyond order σ, $\tilde{w}$ and $\sigma\tilde{w}$, we obtain

$$\partial_t \tilde{w} = D\partial_{xx}\tilde{w} + v_1 \partial_x \tilde{w} - v_2 \partial_x \tilde{\rho} - a_1 \tilde{w} - \frac{a_2 v}{v_2 a_1} \sigma f_w + \mathcal{O}(\sigma^{\frac{3}{2}}) + \mathcal{O}(\sigma\tilde{w}) \tag{B.61}$$

We note that $\tilde{w} = -\sigma a_2 v f_w / (v_2 a_1^2)$ and $\tilde{\rho} = \rho_0$ are homogeneous solutions of the above renormalized evolution (B.61)-(B.46). Such a solution, which is only valid up to order σ, is consistent with the terms discarded in (B.61) which are all of order σ^2 at least. Note also that, due to mass conservation, fluctuations cannot generate any correction to an homogeneous solution for $\tilde{\rho}$. Looking back at the definition of w (B.39), we have shown that, to first order in σ, fluctuations lower the homogeneous magnetization in the ordered phase according to

$$\tilde{m} = \sqrt{\frac{|\alpha|}{\gamma}} \rho_0 - \sigma \frac{a_2 v}{v_2 a_1^2} f_w \left(\frac{v}{\sqrt{Da_1}}, \frac{v_1}{\sqrt{Da_1}}, \frac{v_2}{\sqrt{Da_1}} \right) \ . \tag{B.62}$$

Finally inserting the expression of v_1, v_2, a_2 and a_1 in terms of $|\alpha|$ and γ, we get

$$\tilde{m} = \sqrt{\frac{|\alpha|}{\gamma}}\rho_0 - \sigma \frac{3\gamma\sqrt{\gamma|\alpha|}}{4(\gamma-|\alpha|)\alpha^2} f_w\left(\frac{v}{\sqrt{2D|\alpha|}}, \frac{v}{\sqrt{2D\gamma}}, \frac{v(\gamma-|\alpha|)}{\gamma\sqrt{2D|\alpha|}}\right) . \tag{B.63}$$

This lowering of the magnetization in the ordered phase can be absorbed in a renormalization of the coefficient $|\alpha|$ according to $\tilde{m} = \sqrt{|\hat{\alpha}|/\gamma}\,\rho_0$, with $|\hat{\alpha}|$ defined as

$$|\hat{\alpha}| = |\alpha| - \frac{\sigma}{\rho_0}\frac{3\gamma^2|\alpha|}{2(\gamma-|\alpha|)\alpha^2} f_w\left(\frac{v}{\sqrt{2D|\alpha|}}, \frac{v}{\sqrt{2D\gamma}}, \frac{v(\gamma-|\alpha|)}{\gamma\sqrt{2D|\alpha|}}\right) . \tag{B.64}$$

Note that, consistently with our result (3.71) obtained in the high temperature phase, the fluctuation-induced correction of α also scales as ρ_0^{-1} in the low temperature phase.

B.3 The Topological Active Ising Model

We recall below the definition of the topological hydrodynamics studied in section 3.5.1 of the main text

$$\partial_t \rho = D\nabla^2\rho - v\nabla m \tag{B.65}$$

$$\partial_t m = D\nabla^2 m - v\nabla\rho + 2\Gamma\rho\beta\bar{m}\left(1+\frac{\beta^2\bar{m}^2}{6}\right) - 2\Gamma m\left(1+\frac{\beta^2}{2}\bar{m}^2\right) \tag{B.66}$$

where $\bar{m} = \frac{1}{k}\int_{x-y(x)}^{x+y(x)} m(x)dx$ and $y(x)$ is defined implicitly through $k = \int_{x-y(x)}^{x+y(x)} \rho(x)dx$. Throughout this appendix, we will use Fourier series for L-periodic functions f with the same Fourier convention as defined in (B.24). Ultimately, we will take the limit $L \to \infty$ to recover the usual Fourier tranform.

B.3.1 Linear stability analysis of the homogeneous solutions

In this Appendix, we study the linear stability of homogeneous solutions $\rho = \rho_0$, $m = m_0$, $y = y_0$ and $\bar{m} = \bar{m}_0$ of Eqs. (B.65) and (B.66). Because $y(x)$ and $\bar{m}(x)$ are enslaved to $\rho(x)$ and $m(x)$ through (3.74)-(3.75), $\delta\rho$ and δm are the only two independent perturbations in the system and we further have that $y_0 = k/(2\rho_0)$ and that $\bar{m}_0 = m_0/\rho_0$. We first relate $\delta\bar{m}$ to $\delta\rho$ and δm. To first order,

$$\begin{aligned}\delta\bar{m} =& \frac{\int_{x-y_0-\delta y}^{x+y_0+\delta y}(m_0+\delta m(z))dz}{k} - \frac{m_0}{\rho_0} \\ =& \int_{x-y_0}^{x+y_0}\frac{\delta m(z)dz}{k} + 2\delta y\frac{m_0}{k} + \mathcal{O}(\delta m^2) + \mathcal{O}(\delta y^2) .\end{aligned} \tag{B.67}$$

We then express δy as a function of $\delta\rho$ using the implicit equation $k = \int_{x-y(x)}^{x+y(x)}\rho(x)dx$:

$$\delta y = -\frac{1}{2\rho_0}\int_{x-y_0}^{x+y_0}\delta\rho(z)dz + \mathcal{O}(\delta\rho^2) . \tag{B.68}$$

Interestingly, the fluctuations of ρ impact $\bar{m}$ through δy, despite the topological nature of the alignment. To study the linear stability of (B.65)-(B.66) in Fourier space, we express

δy^q and $\delta\bar{m}^q$ in terms of $\delta\rho^q$ and δm^q. To this aim, we compute the Fourier transform of (B.67) and (B.68). We start by determining δy^q as

$$\delta y^q = -\frac{y_0}{\rho_0}\,\mathrm{sinc}(qy_0)\delta\rho^q\ . \tag{B.69}$$

We then get δm_q as

$$\delta\bar{m}^q = \frac{y_0}{k}2\,\mathrm{sinc}(qy_0)\delta m^q + 2\frac{m_0}{k}\delta y^q\ . \tag{B.70}$$

Reinserting (B.69) in (B.70) and further using $k = 2y_0\rho_0$ we obtain

$$\delta\bar{m}^q = \frac{1}{\rho_0}\,\mathrm{sinc}(qy_0)\delta m^q - \frac{m_0}{\rho_0^2}\,\mathrm{sinc}(qy_0)\delta\rho^q\ . \tag{B.71}$$

Linearizing (B.65)-(B.66) to first order in δm, $\delta\rho$, $\delta\bar{m}$, multiplying both sides by e^{-iqx}, and integrating over q yields the dynamics for the q-th Fourier modes δm^q, $\delta\rho^q$ and $\delta\bar{m}^q$. Further using (B.71), we obtain the following dynamics for δm^q and $\delta\rho^q$

$$\partial_t\begin{pmatrix}\delta\rho^q\\ \delta m^q\end{pmatrix} = \begin{pmatrix}M_{11}^q & M_{12}^q\\ M_{21}^q & M_{22}^q\end{pmatrix}\begin{pmatrix}\delta\rho^q\\ \delta m^q\end{pmatrix}\ , \tag{B.72}$$

where the matrix coefficients M_{11}^q, M_{12}^q, M_{21}^q and M_{22}^q are given by:

$$M_{11}^q = -Dq^2\ , \qquad M_{12}^q = -ivq \tag{B.73}$$

$$M_{21}^q = \frac{\Gamma}{3}\left(\frac{\beta m_0}{\rho_0}\right)^3 + 2\Gamma\beta\frac{m_0}{\rho_0} - iqv + \Gamma\,\mathrm{sinc}(qy_0)\frac{m_0}{\rho_0}\left(\left(\frac{\beta m_0}{\rho_0}\right)^2(-\beta+2) - 2\beta\right) \tag{B.74}$$

$$M_{22}^q = -2\Gamma - \Gamma\left(\frac{\beta m_0}{\rho_0}\right)^2 + \Gamma\,\mathrm{sinc}(qy_0)\left(\left(\frac{\beta m_0}{\rho_0}\right)^2(\beta-2) + 2\beta\right) - Dq^2\ . \tag{B.75}$$

We are interested in the onset of the transition where m_0 is small and $\beta = 1 + \mathcal{O}(m_0)$. To leading order in m_0, the matrix coefficients simplify into

$$M_{11}^q = -Dq^2 + \mathcal{O}(m_0) \qquad M_{12}^q = -iqv + \mathcal{O}(m_0) \tag{B.76}$$

$$M_{21}^q = -iqv + \mathcal{O}(m_0) \qquad M_{22}^q = 2\Gamma\left(\mathrm{sinc}(qy_0) - 1\right) - Dq^2 + \mathcal{O}(m_0)\ . \tag{B.77}$$

Within this regime, the eigenvalues of the linearized dynamic (B.72) are given by

$$\lambda_\pm = \frac{-\left(2Dq^2 + 2\Gamma\left(1 - \mathrm{sinc}(qy_0)\right)\right) \pm \sqrt{\Delta}}{2}\ , \tag{B.78}$$

with the discriminant Δ reading

$$\Delta = \left(2Dq^2 + 2\Gamma\left(1 - \mathrm{sinc}(qy_0)\right)\right)^2 - 4v^2q^2 - 4Dq^2\left(Dq^2 + 2\Gamma\left(1 - \mathrm{sinc}(qy_0)\right)\right)\ . \tag{B.79}$$

An instability emerges when at least one of the eigenvalues $\lambda_\pm$ has a positive real part, which translates into

$$2\Re(\sqrt{\Delta})^2 - 2\Re\left(2Dq^2 + 2\Gamma\left(1 - \mathrm{sinc}(qy_0)\right)\right)^2 > 0\ . \tag{B.80}$$

This condition can be simplified by noticing that

$$2\Re(\sqrt{\Delta})^2 - 2\Re\left(2Dq^2 + 2\Gamma\left(1-\mathrm{sinc}(qy_0)\right)\right)^2 = -a + \sqrt{a^2+b(q)} > 0\ , \tag{B.81}$$

where a and b reads:

$$a(q) = \left[2Dq^2 + 2\Gamma(1-\mathrm{sinc}(qy_0))\right]^2 + 4v^2q^2 + 4Dq^2\left[Dq^2 + 2\Gamma(1-\mathrm{sinc}(qy_0))\right] \tag{B.82}$$

$$\begin{aligned}\frac{b(q)}{64q^2} =& -\Gamma^2\left(\mathrm{sinc}(qy_0)-1\right)^2\left[v^2 + 2D\Gamma\left(1-\mathrm{sinc}(qy_0)\right)\right] - D^2q^4\left[4D\Gamma\left(1-\mathrm{sinc}(qy_0)\right)+v^2\right]\\ &- q^2D\Gamma\left(1-\mathrm{sinc}(qy_0)\right)\left[5D\Gamma\left(1-\mathrm{sinc}(qy_0)\right)+2v^2\right] - D^4q^6\end{aligned} \tag{B.83}$$

We remark that $a(q)$ is a positive term and thus that the stability is determined by the sign of $b(q)$. All the terms in its expression (B.83) are negative; the homogeneous ordered solution is thus always stable at onset. Our topological field theory (B.65)-(B.66) thus predicts a continuous transition to collective motion without phase separation.

B.3.2 Renormalization of the hydrodynamics

In this appendix, we compute how $\mathcal{F}_{\mathrm{topo}}$ given in (3.76) is renormalized due to the addition of the noise term in (3.78)-(3.79). To remain as general as possible, we first compute this renormalization for a generic unconstrained $\bar{m}$, which we take to be a functional of ρ and m: $\bar{m} = \mathcal{G}(x,\{\rho,m\})$. At the end of this appendix, we apply our results for the specific case of $\bar{m}$ defined by (3.75)-(3.74) and obtain expression (3.82) of main text. The crucial assumptions that we will need are summed up in AI-AII-AIII. We first recall the stochastic evolution of the fields

$$\partial_t\rho = D\nabla^2\rho - v\nabla m\ , \qquad \partial_t m = D\nabla^2 m - v\nabla\rho - \mathcal{F}_{\mathrm{topo}}(\bar{m},m,\rho) + \sqrt{2\sigma\rho}\,\eta\ . \tag{B.84}$$

Following section 3.4, we perform a perturbative expansion of the fields m and ρ as

$$\rho = \rho_0 + \sqrt{\sigma}\delta\rho_1 + \sigma\delta\rho_2 + ..+\ , \qquad m = m_0 + \sqrt{\sigma}\delta m_1 + \sigma\delta m_2 + ..+ \tag{B.85}$$

where ρ_0 and m_0 are solutions of (B.84) with $\sigma = 0$

$$\partial_t\rho_0 = D\nabla^2\rho_0 - v\nabla m_0\ , \tag{B.86}$$

$$\partial_t m_0 = D\nabla^2 m_0 - v\nabla\rho_0 - \mathcal{F}_{\mathrm{topo}}(\bar{m}_0,m_0,\rho_0)\ . \tag{B.87}$$

Noting that $\bar{m}$ is enslaved to ρ and m through $\bar{m} = \mathcal{G}(x,\{\rho,m\})$, it can be expanded in powers of $\sigma^{1/2}$ as

$$\begin{aligned}\bar{m} =& \bar{m}_0 + \sqrt{\sigma}\left[\int\frac{\delta\bar{m}(x)}{\delta m(z)}\delta m_1(z)dz + \int\frac{\delta\bar{m}(x)}{\delta\rho(z)}\delta\rho_1(z)dz\right]\\ &+\sigma\left[\int\left(\frac{1}{2}\frac{\delta^2\bar{m}(x)}{\delta m(s)\delta m(z)}\delta m_1(s)\delta m_1(z) + \frac{1}{2}\frac{\delta^2\bar{m}(x)}{\delta\rho(s)\delta\rho(z)}\delta\rho_1(s)\delta\rho_1(z)\right)dsdz\right.\\ &\left.+\int\frac{\delta^2\bar{m}(x)}{\delta\rho(s)\delta m(z)}\delta\rho_1(s)\delta m_1(z)dsdz + \int\frac{\delta\bar{m}(x)}{\delta m(z)}\delta m_2(z)dz + \int\frac{\delta\bar{m}(x)}{\delta\rho(z)}\delta\rho_2(z)dz\right] + ..+\ .\end{aligned} \tag{B.88}$$

Inserting (B.85) and (B.88) into (B.84) and projecting on $\sigma^{n/2}$ gives the evolution equation for $\delta\rho_n$ and δm_n. For $n = 1$, it yields

$$\partial_t \delta\rho_1 = D\nabla^2\delta\rho_1 - v\nabla\delta m_1 \tag{B.89}$$

$$\begin{aligned}\partial_t \delta m_1 = {} & D\nabla^2\delta m_1 - v\nabla\delta\rho_1 - \frac{\partial\mathcal{F}_{\text{topo}}}{\partial m}\delta m_1 - \frac{\partial\mathcal{F}_{\text{topo}}}{\partial\rho}\delta\rho_1 \\ & - \frac{\partial\mathcal{F}_{\text{topo}}}{\partial\bar{m}}\left[\int\frac{\delta\bar{m}(x)}{\delta m(z)}\delta m_1(z)dz + \int\frac{\delta\bar{m}(x)}{\delta\rho(z)}\delta\rho_1(z)dz\right] + \sqrt{2\rho_0}\,\eta\ .\end{aligned} \tag{B.90}$$

Noting that $\partial_{\rho\rho}\mathcal{F}_{\text{topo}} = \partial_{mm}\mathcal{F}_{\text{topo}} = \partial_{m\rho}\mathcal{F}_{\text{topo}} = 0$, we obtain for $n = 2$

$$\partial_t \delta\rho_2 = D\nabla^2\delta\rho_2 - v\nabla\delta m_2 \tag{B.91}$$

$$\begin{aligned}\partial_t \delta m_2 = {} & D\nabla^2\delta m_2 - v\nabla\delta\rho_2 - \frac{\partial\mathcal{F}_{\text{topo}}}{\partial m}\delta m_2 - \frac{\partial\mathcal{F}_{\text{topo}}}{\partial\rho}\delta\rho_2 - \frac{\partial\mathcal{F}_{\text{topo}}}{\partial\bar{m}}\delta\bar{m}_2 \\ & - \frac{1}{2}\frac{\partial^2\mathcal{F}_{\text{topo}}}{\partial\bar{m}^2}\left[\int\frac{\delta\bar{m}(x)}{\delta m(z)}\delta m_1(z)dz + \int\frac{\delta\bar{m}(x)}{\delta\rho(z)}\delta\rho_1(z)dz\right]^2 \\ & - \frac{\partial^2\mathcal{F}_{\text{topo}}}{\partial\bar{m}\partial m}\delta m_1\left[\int\frac{\delta\bar{m}(x)}{\delta m(z)}\delta m_1(z)dz + \int\frac{\delta\bar{m}(x)}{\delta\rho(z)}\delta\rho_1(z)dz\right] \\ & - \frac{\partial^2\mathcal{F}_{\text{topo}}}{\partial\bar{m}\partial\rho}\delta\rho_1\left[\int\frac{\delta\bar{m}(x)}{\delta m(z)}\delta m_1(z)dz + \int\frac{\delta\bar{m}(x)}{\delta\rho(z)}\delta\rho_1(z)dz\right] \\ & - \frac{\partial\mathcal{F}_{\text{topo}}}{\partial\bar{m}}\left[\int\frac{\delta\bar{m}(x)}{\delta m(z)}\delta m_2(z)dz + \int\frac{\delta\bar{m}(x)}{\delta\rho(z)}\delta\rho_2(z)dz\right] \\ & - \frac{\partial\mathcal{F}_{\text{topo}}}{\partial\bar{m}}\int\left(\frac{1}{2}\frac{\delta^2\bar{m}(x)}{\delta m(s)\delta m(z)}\delta m_1(s)\delta m_1(z) + \frac{1}{2}\frac{\delta^2\bar{m}(x)}{\delta\rho(s)\delta\rho(z)}\delta\rho_1(s)\delta\rho_1(z)\right)dsdz \\ & - \frac{\partial\mathcal{F}_{\text{topo}}}{\partial\bar{m}}\int\frac{\delta^2\bar{m}(x)}{\delta\rho(s)\delta m(z)}\delta\rho_1(s)\delta m_1(z)dsdz + \frac{\delta\rho_1}{\sqrt{2\rho_0}}\,\eta\ .\end{aligned} \tag{B.92}$$

Summing together (B.86), (B.89) multiplied by $\sqrt{\sigma}$, and (B.91) multiplied by σ gives the stochastic evolution of ρ up to order σ. Averaging the result over the noise using Itō prescription, we obtain the time evolution of $\tilde{\rho} = \langle\rho\rangle$ to order σ as

$$\partial_t\tilde{\rho} = D\nabla^2\tilde{\rho} - v\nabla\tilde{m}\ . \tag{B.93}$$

Likewise, summing (B.87), (B.90) multiplied by $\sqrt{\sigma}$, and (B.92) multiplied by σ gives the stochastic evolution of m to order σ. Averaging the result over the noise using Itō prescription, we obtain the time evolution of $\tilde{m} = \langle m\rangle$ to order σ as

$$\partial_t\tilde{m} = D\nabla^2\tilde{m} - v\nabla\delta\tilde{\rho} - \mathcal{F}_{\text{topo}}(\tilde{m},\tilde{\rho},\tilde{\bar{m}}) - \sigma\Delta\mathcal{F}_{\text{topo}}\ . \tag{B.94}$$

In (B.94), $\tilde{\bar{m}}$ is the topological field constructed with $\tilde{\rho}$ and $\tilde{m}$, *ie* $\tilde{\bar{m}} = \mathcal{G}(x,\{\tilde{m},\tilde{\rho}\})$, and $\Delta\mathcal{F}_{\text{topo}}$ is given by

$$\Delta\mathcal{F}_{\text{topo}} = \frac{1}{2}\frac{\partial^2\mathcal{F}_{\text{topo}}}{\partial\bar{m}^2}C_1 + \frac{\partial^2\mathcal{F}_{\text{topo}}}{\partial\bar{m}\partial m}C_2 + \frac{\partial^2\mathcal{F}_{\text{topo}}}{\partial\bar{m}\partial\rho}C_3 + \frac{\partial\mathcal{F}_{\text{topo}}}{\partial\bar{m}}C_4\ , \tag{B.95}$$

where the C_i's are correlators given by

$$\begin{aligned}
C_1 =& \int \frac{\delta\bar{m}(x)}{\delta m(s)}\frac{\delta\bar{m}(x)}{\delta m(z)}\Big[\langle\delta m_1(s)\delta m_1(z)\rangle - \langle\delta m_1(s)\rangle\langle\delta m_1(z)\rangle\Big]dsdz \\
&+ \int \frac{\delta\bar{m}(x)}{\delta\rho(s)}\frac{\delta\bar{m}(x)}{\delta\rho(z)}\Big[\langle\delta\rho_1(s)\delta\rho_1(z)\rangle - \langle\delta\rho_1(s)\rangle\langle\delta\rho_1(z)\rangle\Big]dsdz \\
&+ 2\int \frac{\delta\bar{m}(x)}{\delta\rho(s)}\frac{\delta\bar{m}(x)}{\delta m(z)}\Big[\langle\delta\rho_1(s)\delta m_1(z)\rangle - \langle\delta\rho_1(s)\rangle\langle\delta m_1(z)\rangle\Big]dsdz \qquad \text{(B.96)} \\
C_2 =& \int \frac{\delta\bar{m}(x)}{\delta m(z)}\Big[\langle\delta m_1(z)\delta m_1(x)\rangle - \langle\delta m_1(z)\rangle\langle\delta m_1(x)\rangle\Big]dz \\
&+ \int \frac{\delta\bar{m}(x)}{\delta\rho(z)}\Big[\langle\delta\rho_1(z)\delta m_1(x)\rangle - \langle\delta\rho_1(z)\rangle\langle\delta m_1(x)\rangle\Big]dz \qquad \text{(B.97)} \\
C_3 =& \int \frac{\delta\bar{m}(x)}{\delta m(z)}\Big[\langle\delta m_1(z)\delta\rho_1(x)\rangle - \langle\delta m_1(z)\rangle\langle\delta m_1(x)\rangle\Big]dz \\
&+ \int \frac{\delta\bar{m}(x)}{\delta\rho(z)}\Big[\langle\delta\rho_1(z)\delta\rho_1(x)\rangle - \langle\delta\rho_1(z)\rangle\langle\delta\rho_1(x)\rangle\Big]dz \qquad \text{(B.98)} \\
C_4 =& \int \frac{1}{2}\frac{\delta^2\bar{m}(x)}{\delta m(s)\delta m(z)}\Big[\langle\delta m_1(s)\delta m_1(z)\rangle - \langle\delta m_1(s)\rangle\langle\delta m_1(z)\rangle\Big]dsdz \\
&+ \int \frac{1}{2}\frac{\delta^2\bar{m}(x)}{\delta\rho(s)\delta\rho(z)}\Big[\langle\delta\rho_1(s)\delta\rho_1(z)\rangle - \langle\delta\rho_1(s)\rangle\langle\delta\rho_1(z)\rangle\Big]dsdz \\
&+ \int \frac{\delta^2\bar{m}(x)}{\delta\rho(s)\delta m(z)}\Big[\langle\delta\rho_1(s)\delta m_1(z)\rangle - \langle\delta\rho_1(s)\rangle\langle\delta m_1(z)\rangle\Big]dsdz \qquad \text{(B.99)}
\end{aligned}$$

To simplify (B.96) to (B.99), we need to derive the correlators involving $\delta\rho_1$ and δm_1 by using their stochastic evolution (B.89)-(B.90). We readily find that $\langle\delta m_1\rangle = \langle\delta\rho_1\rangle = 0$. We now use the assumption that ρ_0, m_0 and $\bar{m}_0 = \mathcal{G}(x, \{\rho_0, m_0\})$ can be considered homogeneous in the dynamics of $\delta\rho_1$ and δm_1 (see AI, AIII). Under such an assumption, (B.89)-(B.90) becomes a linear system and its dynamic in Fourier space reads

$$\partial_t \begin{pmatrix} \delta\rho_1^q \\ \delta m_1^q \end{pmatrix} = \begin{pmatrix} A_{11}^q & A_{12}^q \\ A_{21}^q & A_{22}^q \end{pmatrix} \begin{pmatrix} \delta\rho_1^q \\ \delta m_1^q \end{pmatrix} + \begin{pmatrix} 0 \\ \sqrt{2\rho_0}\,\eta^q \end{pmatrix} , \qquad \text{(B.100)}$$

where η^q is the q-th Fourier mode of the Gaussian white noise, with correlations $\langle\eta^q(t)\eta^{q'}(t')\rangle = L^{-1}\delta_{q+q',0}\delta(t-t')$. To pursue our derivation, we won't need the exact expression of the A_{ij}^q's, so we just remark that they generically depend on the homogeneous fields ρ_0, m_0, $\bar{m}_0$ as well as on the Fourier transform of the functional derivatives $\delta\bar{m}(x)/\delta\rho(y)$ and $\delta\bar{m}(x)/\delta m(y)$. The steady-state correlators of (B.100) are obtained by using Itō calculus. They satisfy

$$\begin{aligned}
0 =& (A_{11}^q + A_{11}^{q'})\langle\delta\rho_1^q\delta\rho_1^{q'}\rangle + A_{12}^q\langle\delta m_1^q\delta\rho_1^{q'}\rangle + A_{12}^{q'}\langle\delta\rho_1^q\delta m_1^{q'}\rangle \qquad \text{(B.101)} \\
0 =& (A_{22}^q + A_{11}^{q'})\langle\delta m_1^q\delta\rho_1^{q'}\rangle + A_{21}^q\langle\delta\rho_1^q\delta\rho_1^{q'}\rangle + A_{12}^{q'}\langle\delta m_1^q\delta m_1^{q'}\rangle \qquad \text{(B.102)} \\
0 =& (A_{22}^q + A_{22}^{q'})\langle\delta m_1^q\delta m_1^{q'}\rangle + A_{21}^q\langle\delta\rho_1^q\delta m_1^{q'}\rangle + A_{21}^{q'}\langle\delta m_1^q\delta\rho_1^{q'}\rangle + \frac{2\rho_0}{L}\delta_{q+q',0} , \qquad \text{(B.103)}
\end{aligned}$$

which can be solved as

$$\langle \delta m_1^q \delta m_1^{q'} \rangle = \langle \delta m_1^q \delta m_1^{-q} \rangle \frac{\delta_{q+q',0}}{L} \tag{B.104}$$

$$\langle \delta \rho_1^q \delta \rho_1^{q'} \rangle = \langle \delta \rho_1^q \delta \rho_1^{-q} \rangle \frac{\delta_{q+q',0}}{L} \tag{B.105}$$

$$\langle \delta m_1^q \delta \rho_1^{q'} \rangle = \langle \delta m_1^q \delta \rho_1^{-q} \rangle \frac{\delta_{q+q',0}}{L} \ , \tag{B.106}$$

where $\langle \delta m_1^q \delta m_1^{-q} \rangle$, $\langle \delta \rho_1^q \delta \rho_1^{-q} \rangle$ and $\langle \delta m_1^q \delta \rho_1^{-q} \rangle$ are functions depending on the A_{ij}^q whose explicit expression will not be needed. Using our convention (B.24), the Fourier development of δm_1 and $\delta \rho_1$ reads

$$\delta m_1 = \sum_q \delta m_1^q e^{iqx} \qquad \delta \rho_1 = \sum_q \delta \rho_1^q e^{iqx} \ . \tag{B.107}$$

Injecting this development (B.107) into (B.96) to (B.99), and using the scalings (B.104) to (B.106) allow us to compute the expression of the C_i's. For C_1, we obtain

$$C_1 = \frac{1}{L} \sum_q \bar{m}_m^q \bar{m}_m^{-q} \langle \delta m_1^q \delta m_1^{-q} \rangle + \bar{m}_\rho^q \bar{m}_\rho^{-q} \langle \delta \rho_1^q \delta \rho_1^{-q} \rangle + \bar{m}_m^q \bar{m}_\rho^{-q} \langle \delta m_1^q \delta \rho_1^{-q} \rangle \ , \tag{B.108}$$

where $\bar{m}_\rho^q$ and $\bar{m}_m^q$ are the Fourier transforms of the functional derivatives of $\bar{m}$ with respect to ρ and m respectively

$$\bar{m}_\rho^q = \int_0^L e^{-iqz} \frac{\delta \bar{m}}{\delta \rho}(z) \ dz, \qquad \bar{m}_m^q = \int_0^L e^{-iqz} \frac{\delta \bar{m}}{\delta m}(z) \ dz \ . \tag{B.109}$$

For C_2 and C_3, we get

$$C_2 = \frac{1}{L} \sum_q \bar{m}_m^q \langle \delta m_1^q \delta m_1^{-q} \rangle + \bar{m}_\rho^{-q} \langle \delta m_1^q \delta \rho_1^{-q} \rangle \tag{B.110}$$

$$C_3 = \frac{1}{L} \sum_q \bar{m}_\rho^q \langle \delta \rho_1^q \delta \rho_1^{-q} \rangle + \bar{m}_m^q \langle \delta m_1^q \delta \rho_1^{-q} \rangle \ . \tag{B.111}$$

Finally, C_4 reads

$$C_4 = \frac{1}{2L} \sum_q \bar{m}_{m,m}^{q,-q} \langle \delta m_1^q \delta m_1^{-q} \rangle + \bar{m}_{\rho,\rho}^{q,-q} \langle \delta \rho_1^q \delta \rho_1^{-q} \rangle + 2 \bar{m}_{m,\rho}^{q,-q} \langle \delta m_1^q \delta \rho_1^{-q} \rangle \ , \tag{B.112}$$

where $\bar{m}_{m,m}^{q,q'}$, $\bar{m}_{\rho,\rho}^{q,q'}$ and $\bar{m}_{m,\rho}^{q,q'}$ are the Fourier transform of the second functional derivatives of $\bar{m}$ with respect to ρ and m

$$\bar{m}_{m,m}^{q,q'} = \int_0^L \int_0^L e^{-iqs-iq'z} \frac{\delta^2 \bar{m}}{\delta m \delta m}(s,z) \ dsdz \ , \quad \bar{m}_{\rho,\rho}^{q,q'} = \int_0^L \int_0^L e^{-iqs-iq'z} \frac{\delta^2 \bar{m}}{\delta \rho \delta \rho}(s,z) \ dsdz$$
$$\bar{m}_{m,\rho}^{q,q'} = \int_0^L \int_0^L e^{-iqs-iq'z} \frac{\delta^2 \bar{m}}{\delta m \delta \rho}(s,z) \ dsdz \ . \tag{B.113}$$

The last step is to take the large system size limit $L \to \infty$ in (B.108)-(B.110)-(B.111)-(B.112) to obtain the C_i's as integrals over Fourier modes q

$$C_1 = \int \frac{dq}{2\pi} |\bar{m}_m^q|^2 \langle \delta m_1^q \delta m_1^{-q} \rangle + |\bar{m}_\rho^q|^2 \langle \delta \rho_1^q \delta \rho_1^{-q} \rangle + \bar{m}_m^q \bar{m}_\rho^{-q} \langle \delta m_1^q \delta \rho_1^{-q} \rangle \tag{B.114}$$

$$C_2 = \int \frac{dq}{2\pi} \bar{m}_m^q \langle \delta m_1^q \delta m_1^{-q} \rangle + \bar{m}_\rho^{-q} \langle \delta m_1^q \delta \rho_1^{-q} \rangle \tag{B.115}$$

$$C_3 = \int \frac{dq}{2\pi} \bar{m}_\rho^q \langle \delta \rho_1^q \delta \rho_1^{-q} \rangle + \bar{m}_m^q \langle \delta m_1^q \delta \rho_1^{-q} \rangle \tag{B.116}$$

$$C_4 = \int \frac{dq}{4\pi} \bar{m}_{m,m}^{q,-q} \langle \delta m_1^q \delta m_1^{-q} \rangle + \bar{m}_{\rho,\rho}^{q,-q} \langle \delta \rho_1^q \delta \rho_1^{-q} \rangle + 2 \bar{m}_{m,\rho}^{q,-q} \langle \delta m_1^q \delta \rho_1^{-q} \rangle \ . \tag{B.117}$$

So far, the correction $\Delta\mathcal{F}_{\text{topo}}$ in (B.95) together with the expression of the C_i's in (B.114) to (B.117) is valid for any topological field $\bar{m} = \mathcal{G}(x, \{\rho, m\})$ where $\mathcal{G}$ is a functional. We now apply this result for the specific case of the topological field $\bar{m}$ given by (3.75) and (3.74) in main text. For homogeneous ρ_0 and m_0, we can compute the functional derivatives of $\bar{m} = \int_{x-y}^{x+y} m(z)dz/k$ as

$$\frac{\delta\bar{m}(x)}{\delta m(z)} = \frac{\Theta(x+y_0-z)\Theta(z-x+y_0)}{2y_0\rho_0} , \qquad \frac{\delta^2\bar{m}(x)}{\delta m(z)\delta m(s)} = 0 , \tag{B.118}$$

$$\frac{\delta\bar{m}(x)}{\delta\rho(z)} = -\frac{m_0\Theta(x+y_0-z)\Theta(z-x+y_0)}{2y_0\rho_0^2} , \qquad \frac{\delta^2\bar{m}(x)}{\delta\rho(z)\delta\rho(s)} = 0 , \tag{B.119}$$

$$\frac{\delta^2\bar{m}(x)}{\delta\rho(z)\delta m(s)} = -\frac{\Theta(x+y_0-z)\Theta(z-x+y_0)}{4y_0\rho_0^2}\Big[\delta(s-x-y_0)+\delta(s-x+y_0)\Big] , \tag{B.120}$$

where $\Theta(u)$ is the Heaviside function which is equal to 0 if $u<0$ or equal to 1 if $u>0$. Going into Fourier space, we obtain

$$\bar{m}_m^q = -\frac{\text{sinc}(qy_0)}{\rho_0} , \qquad \bar{m}_\rho^q = \frac{m_0}{\rho_0}\,\text{sinc}(qy_0) , \tag{B.121}$$

$$\bar{m}_{\rho,\rho}^{q,q'} = \bar{m}_{m,m}^{q,q'} = 0 , \qquad \bar{m}_{\rho,m}^{q,q'} = \frac{\text{sinc}(qy_0)}{\rho_0}\cos(q'y_0) . \tag{B.122}$$

To compute the C_i's for the topological field $\bar{m}$ studied in section 3.5.1, we still need the expression of the correlators of the fields $\delta\rho_1$ and δm_1. For the specific definition of $\bar{m}$ at hand, the matrix coefficients A_{ij}^q of the linearized dynamics (B.100) are equal to the M_{ij}^q defined in (B.73) to (B.75) and we get

$$\partial_t\begin{pmatrix}\delta\rho_1^q\\ \delta m_1^q\end{pmatrix} = \begin{pmatrix}M_{11}^q & M_{12}^q\\ M_{21}^q & M_{22}^q\end{pmatrix}\begin{pmatrix}\delta\rho_1^q\\ \delta m_1^q\end{pmatrix} + \begin{pmatrix}0\\ \sqrt{2\rho_0}\,\eta^q\end{pmatrix} . \tag{B.123}$$

Using the system (B.101) to (B.103) with $A_{ij}^q = M_{ij}^q$, we obtain the expressions of the steady-state correlators in Fourier space to first order in m_0

$$\langle\delta m_1^q\delta m_1^{-q}\rangle = \rho_0\frac{2D\Gamma - 2D\Gamma\beta\,\text{sinc}(qy_0) + 2D^2q^2 + v^2}{2(\Gamma-\Gamma\beta\,\text{sinc}(qy_0)+Dq^2)\,(2D\Gamma - 2D\Gamma\beta\,\text{sinc}(qy_0) + D^2q^2+v^2)} + \mathcal{O}\left(m_0^2\right) \tag{B.124}$$

$$\langle\delta\rho_1^q\delta\rho_1^{-q}\rangle = \frac{\rho_0 v^2}{2(\Gamma-\Gamma\beta\,\text{sinc}(qy_0)+Dq^2)\,(2D\Gamma - 2D\Gamma\beta\,\text{sinc}(qy_0) + D^2q^2+v^2)} + \mathcal{O}\left(m_0^2\right) \tag{B.125}$$

$$\begin{aligned}\langle\delta m_1^q\delta\rho_1^{-q}\rangle =& \frac{iqDv\rho_0}{2(\Gamma-\Gamma\beta\,\text{sinc}(qy_0)+Dq^2)\,(2D\Gamma - 2D\Gamma\beta\,\text{sinc}(qy_0) + D^2q^2+v^2)}\\ &+ \frac{\beta v^2\Gamma\,(1-\text{sinc}\,(qy_0))\,m_0}{2\,(\Gamma-\Gamma\beta\,\text{sinc}\,(qy_0)+Dq^2)^{\,2}\,(2D\Gamma - 2D\Gamma\beta\,\text{sinc}\,(qy_0) + D^2q^2+v^2)} + \mathcal{O}\left(m_0^2\right) .\end{aligned} \tag{B.126}$$

We now have all the ingredients needed to compute $\Delta\mathcal{F}_{\text{topo}}$ in (B.95). First, we have to inject the correlators (B.124) to (B.126) and the functional derivatives (B.121) to (B.122) into the expressions of the C_i's in (B.114) to (B.117). Once we have the C_i's, we just plug them back into the expression (B.95) for $\Delta\mathcal{F}_{\text{topo}}$. A lengthy but straightforward computation then gives

$$\Delta\mathcal{F}_{\text{topo}} = \frac{m_0}{y_0\rho_0}\left[2\beta(c_1-c_4)+\beta^2(1-\beta)c_2+2\beta^2c_3\right] + \mathcal{O}(m_0^2) . \tag{B.127}$$

Where c_1, c_2, c_3, and c_4 are given by

$$c_1 = \int \frac{d\tilde{q}}{2\pi} \frac{v^2 \operatorname{sinc}(\tilde{q})}{2\left(1-\beta\operatorname{sinc}(\tilde{q})+\frac{D}{\Gamma y_0^2}\tilde{q}^2\right)\left(2D\Gamma-2D\Gamma\beta\operatorname{sinc}(\tilde{q})+D^2\frac{\tilde{q}^2}{y_0^2}+v^2\right)} \tag{B.128}$$

$$c_2 = \int \frac{d\tilde{q}}{2\pi} \frac{\operatorname{sinc}^2(\tilde{q})\left[2D\Gamma-2D\Gamma\beta\operatorname{sinc}(\tilde{q})+2D^2\frac{\tilde{q}^2}{y_0^2}+v^2\right]}{2\left(1-\beta\operatorname{sinc}(\tilde{q})+\frac{D}{\Gamma y_0^2}\tilde{q}^2\right)\left(2D\Gamma-2D\Gamma\beta\operatorname{sinc}(\tilde{q})+D^2\frac{\tilde{q}^2}{y_0^2}+v^2\right)} \tag{B.129}$$

$$c_3 = \int \frac{d\tilde{q}}{2\pi} \frac{\operatorname{sinc}(\tilde{q})\left[2D\Gamma-2D\Gamma\beta\operatorname{sinc}(\tilde{q})+2D^2\frac{\tilde{q}^2}{y_0^2}+v^2\right]}{2\left(1-\beta\operatorname{sinc}(\tilde{q})+\frac{D}{\Gamma y_0^2}\tilde{q}^2\right)\left(2D\Gamma-2D\Gamma\beta\operatorname{sinc}(\tilde{q})+D^2\frac{\tilde{q}^2}{y_0^2}+v^2\right)} \tag{B.130}$$

$$c_4 = \int \frac{d\tilde{q}}{2\pi} \frac{\beta v^2\left(\Gamma-\Gamma\operatorname{sinc}\left(\tilde{q}\right)\right)\operatorname{sinc}(\tilde{q})\left(1-\cos(\tilde{q})\right)}{2\left(1-\beta\operatorname{sinc}\left(\tilde{q}\right)+\frac{D}{\Gamma y_0^2}\tilde{q}^2\right)^2\left(2D\Gamma-2D\Gamma\beta\operatorname{sinc}\left(\tilde{q}\right)+D^2\frac{\tilde{q}^2}{y_0^2}+v^2\right)} \,. \tag{B.131}$$

Note that all the c_i's are dimensionless and only depends on three independent parameters: β, $\Gamma D/v^2$, and $\Gamma k/(v\rho_0)$. Consequently, they all assume the scaling form

$$c_i = \bar{c}_i\left(\beta, \tfrac{\Gamma k}{v\rho_0}, \tfrac{\Gamma D}{v^2}\right) \,. \tag{B.132}$$

For example, we deduce from (B.128) the expression for $\bar{c}_1$

$$\bar{c}_1(\mu,\nu,\omega) = \int \frac{du}{2\pi} \frac{\operatorname{sinc}(u)}{\left(1-\mu\operatorname{sinc}(u)+4u^2\frac{\omega^2}{\nu^2}\right)\left(1+2\omega-2\omega\mu\operatorname{sinc}(u)+4u^2\frac{\omega^2}{\nu^2}\right)} \,. \tag{B.133}$$

Using the scaling forms of (B.132) in (B.127), $\Delta\mathcal{F}_{\text{topo}}$ can be cast into

$$\Delta\mathcal{F}_{\text{topo}} = \frac{2m_0}{k} g\left(\beta, \frac{\Gamma k}{v\rho_0}, \frac{\Gamma D}{v^2}\right) + \mathcal{O}(m_0^2) \,. \tag{B.134}$$

where g, which appears in expression (3.82) of the main text, is given by

$$g\left(\beta, \frac{\Gamma k}{v\rho_0}, \frac{\Gamma D}{v^2}\right) = 2\beta(\bar{c}_1-\bar{c}_4)+\beta^2(1-\beta)\bar{c}_2+2\beta^2\bar{c}_3 \,. \tag{B.135}$$

Note that the convergence of the integrals c_1, c_2, c_3 and c_4 is ensured by assumption AII which is verified in the high temperature phase when $\beta < 1$.

Importantly, the dependence of g on ρ_0 cannot be eliminated, so that the renormalization of the critical-temperature indeed leads to a density-dependent onset of order. Using the fact that $\beta < 1$, $c_1 > c_4$, and that c_1, c_2, c_3 are positive, we deduce that g is a density-dependent positive function in the high temperature phase. Consequently, the incorporation of microscopic noise should lower the critical temperature.

B.4 Extension to generic alignment

This appendix is devoted to the computation of $\Delta\mathcal{F}_{\text{topo}}$ in (3.88) for a generic functional alignment $\bar{m}$ as in (3.85). It is not self-contained and as such we advise a previous reading of appendix B.3.2.

As shown in (B.95) of appendix B.3.2, $\Delta\mathcal{F}_{\text{topo}}$ crucially depends on the functional derivatives of $\bar{m}$ with respect to ρ and m through the C_i's whose expressions are given

in (B.96) to (B.99). Given $\delta\bar{m}/\delta\rho$ and $\delta\bar{m}/\delta m$, we can derive the matrix coefficients A^q_{ij} of (B.100), which in turn yields the correlators $\langle\delta\rho_1^q\delta\rho_1^{-q}\rangle$, $\langle\delta\rho_1^q\delta m_1^{-q}\rangle$ and $\langle\delta m_1^q\delta m_1^{-q}\rangle$ in (B.104) to (B.106). These correlators, together with the second functional derivatives of $\bar{m}$, allow us to compute the C_i's through the use of (B.114) to (B.117). Thus, if the functional derivatives of $\bar{m}$ are constrained to assume some scaling law, such a scaling will also be reflected in $\Delta\mathcal{F}_{\text{topo}}$.

The first and second functional derivatives of $\bar{m}$ at ρ_0, m_0 are defined as

$$\begin{aligned}\bar{m}(x) =&\mathcal{G}(x,\{\rho_0,m_0\}) + \int_0^L \left[\frac{\delta\bar{m}(x)}{\delta\rho(z)}\delta\rho(z) + \frac{\delta\bar{m}(x)}{\delta m(z)}\delta m(z)\right] dz \\ &+ \int_0^L\int_0^L \frac{1}{2}\left[\frac{\delta^2\bar{m}(x)}{\delta\rho(s)\delta\rho(z)}\delta\rho(s)\delta\rho(z) + \frac{\delta^2\bar{m}(x)}{\delta m(s)\delta m(z)}\delta m(s)\delta m(z)\right] dsdz \\ &+ \int_0^L\int_0^L \frac{\delta^2\bar{m}(x)}{\delta\rho(s)\delta m(z)}\delta\rho(s)\delta m(z)dsdz + o(\delta\rho^2,\delta m^2,\delta\rho\delta m)\ . \end{aligned} \tag{B.136}$$

Because $\bar{m}$ is dimensionless, we read on the above equation that all its functional derivatives are dimensionless as well. It entails that, in Fourier space, the first order functional derivatives of $\bar{m}$ scale as lengths $[L]$ while the second order ones scale as lengths squared $[L^2]$:

$$\bar{m}^q_\rho = \int_0^L e^{-iqz}\frac{\delta\bar{m}}{\delta\rho}(z)\ dz \propto [L], \qquad \bar{m}^q_m = \int_0^L e^{-iqz}\frac{\delta\bar{m}}{\delta m}(z)\ dz \propto [L] \tag{B.137}$$

$$\bar{m}^{q,q'}_{m,m} = \int_0^L\int_0^L e^{-iqs-iq'z}\frac{\delta^2\bar{m}}{\delta m\delta m}(s,z)\ dsdz \propto [L]^2 \tag{B.138}$$

$$\bar{m}^{q,q'}_{\rho,\rho} = \int_0^L\int_0^L e^{-iqs-iq'z}\frac{\delta^2\bar{m}}{\delta\rho\delta\rho}(s,z)\ dsdz \propto [L]^2 \tag{B.139}$$

$$\bar{m}^{q,q'}_{m,\rho} = \int_0^L\int_0^L e^{-iqs-iq'z}\frac{\delta^2\bar{m}}{\delta m\delta\rho}(s,z)\ dsdz \propto [L]^2\ . \tag{B.140}$$

We expect $\bar{m}^q_\rho$, $\bar{m}^q_m$, $\bar{m}^{q,-q}_{\rho,\rho}$, $\bar{m}^{q,-q}_{m,m}$, $\bar{m}^{q,-q}_{m,\rho}$ to depend on ρ_0, m_0 and on the wavevector q. Using assumptions AI and AIII, we suppose that ρ_0, m_0, and $\bar{m}_0 = \mathcal{G}(x,\{m_0,\rho_0\})$ remain homogeneous in space throughout the derivation. As $\bar{m}$ is dimensionless, $\bar{m}_0$ will depend on the ratio m_0/ρ_0 by dimensional analysis. Taking into account all these dependences, $\bar{m}^q_\rho$, $\bar{m}^q_m$, $\bar{m}^{q,-q}_{\rho,\rho}$, $\bar{m}^{q,-q}_{m,m}$, $\bar{m}^{q,-q}_{m,\rho}$, and $\bar{m}_0$ will have the following scaling forms

$$\begin{aligned}
\bar{m}^q_\rho =& \frac{1}{\rho_0}\bar{f}_\rho\left(\frac{m_0}{\rho_0},\frac{q}{\rho_0},\dots\right) & \bar{m}^q_m =& \frac{1}{\rho_0}\bar{f}_m\left(\frac{m_0}{\rho_0},\frac{q}{\rho_0},\dots\right)\\
\bar{m}^{q,-q}_{\rho,\rho} =& \frac{1}{\rho_0^2}\bar{f}_{\rho\rho}\left(\frac{m_0}{\rho_0},\frac{q}{\rho_0},\dots\right) & \bar{m}^{q,-q}_{m,m} =& \frac{1}{\rho_0^2}\bar{f}_{mm}\left(\frac{m_0}{\rho_0},\frac{q}{\rho_0},\dots\right)\\
\bar{m}^{q,-q}_{m,\rho} =& \frac{1}{\rho_0^2}\bar{f}_{m\rho}\left(\frac{m_0}{\rho_0},\frac{q}{\rho_0},\dots\right) & \bar{m}_0 =& \bar{f}\left(\frac{m_0}{\rho_0},\dots\right)\ ,
\end{aligned} \tag{B.141}$$

where the dots refer to other dimensionless parameters entering in the definition of $\bar{m}$ (e.g., the number k of nearest neighbours) and are omitted for clarity from now on. Using (B.141), the A^q_{ij} involved in the linearized hydrodynamics (B.100) for $\delta\rho_1$ and δm_1 are

generically given by

$$A^q_{11} = -Dq^2\,, \qquad A^q_{12} = -ivq \tag{B.142}$$

$$\begin{aligned} A^q_{21} =& -iqv + 2\Gamma\beta\bar{f}\left(\tfrac{m_0}{\rho_0}\right)\left[1+\frac{\beta^2}{6}\bar{f}\left(\tfrac{m_0}{\rho_0}\right)^2\right] \\ &+ 2\Gamma\left[\beta\left(1+\frac{\beta^2}{2}\bar{f}\left(\tfrac{m_0}{\rho_0}\right)\right) - \tfrac{m_0}{\rho_0}\beta^2\bar{f}\left(\tfrac{m_0}{\rho_0}\right)\right]\bar{f}_\rho\left(\tfrac{m_0}{\rho_0},\tfrac{q}{\rho_0}\right) \end{aligned} \tag{B.143}$$

$$\begin{aligned} A^q_{22} =& -2\Gamma\left(1+\frac{\beta^2}{2}\bar{f}\left(\tfrac{m_0}{\rho_0}\right)^2\right) - Dq^2 \\ &+ 2\Gamma\left[\beta\left(1+\frac{\beta^2}{2}\bar{f}\left(\tfrac{m_0}{\rho_0}\right)\right) - \tfrac{m_0}{\rho_0}\beta^2\bar{f}\left(\tfrac{m_0}{\rho_0}\right)\right]\bar{f}_m\left(\tfrac{m_0}{\rho_0},\tfrac{q}{\rho_0}\right)\,. \end{aligned} \tag{B.144}$$

From (B.142) to (B.144), we observe that the A^q_{ij}'s all follow the generic scaling form

$$A^q_{ij} = \Gamma\,\bar{g}_{ij}\left(\frac{\Gamma D}{v^2},\frac{\Gamma}{v\rho_0},\frac{q}{\rho_0},\frac{m_0}{\rho_0},\beta\right) \tag{B.145}$$

Because the system (B.101) to (B.103) only involves the A^q_{ij}'s and ρ_0 as coefficients, its solution will assume a scaling form similar to (B.145): a prefactor depending on ρ_0 and Γ multiplied by a function depending on the dimensionless variables entering in $\bar{g}_{ij}$. Noting that $\langle\delta m^q_1\delta m^{-q}_1\rangle$, $\langle\delta\rho^q_1\delta\rho^{-q}_1\rangle$ and $\langle\delta m^q_1\delta\rho^{-q}_1\rangle$ in (B.104) to (B.106) scale as $[T]/[L]$, this prefactor must be ρ_0/Γ and we finally obtain

$$\langle\delta\rho^q_1\delta\rho^{-q}_1\rangle = \frac{\rho_0}{\Gamma}\bar{g}_1\left(\frac{\Gamma D}{v^2},\frac{\Gamma}{v\rho_0},\frac{q}{\rho_0},\frac{m_0}{\rho_0},\beta\right)\,,\quad \langle\delta m^q_1\delta m^{-q}_1\rangle = \frac{\rho_0}{\Gamma}\bar{g}_2\left(\frac{\Gamma D}{v^2},\frac{\Gamma}{v\rho_0},\frac{q}{\rho_0},\frac{m_0}{\rho_0},\beta\right) \tag{B.146}$$

$$\langle\delta m^q_1\delta\rho^{-q}_1\rangle = \frac{\rho_0}{\Gamma}\bar{g}_3\left(\frac{\Gamma D}{v^2},\frac{\Gamma}{v\rho_0},\frac{q}{\rho_0},\frac{m_0}{\rho_0},\beta\right)\,. \tag{B.147}$$

Injecting (B.146)-(B.147) together with (B.141) into (B.114)-(B.117) yields the C_i's as

$$C_1 = \int\frac{dq}{2\pi}\frac{1}{\rho_0\Gamma}\bar{h}_1\left(\frac{\Gamma D}{v^2},\frac{\Gamma}{v\rho_0},\frac{q}{\rho_0},\frac{m_0}{\rho_0},\beta\right)\quad C_2 = \int\frac{dq}{2\pi}\frac{1}{\Gamma}\bar{h}_2\left(\frac{\Gamma D}{v^2},\frac{\Gamma}{v\rho_0},\frac{q}{\rho_0},\frac{m_0}{\rho_0},\beta\right) \tag{B.148}$$

$$C_3 = \int\frac{dq}{2\pi}\frac{1}{\Gamma}\bar{h}_3\left(\frac{\Gamma D}{v^2},\frac{\Gamma}{v\rho_0},\frac{q}{\rho_0},\frac{m_0}{\rho_0},\beta\right)\qquad C_4 = \int\frac{dq}{2\pi}\frac{1}{\rho_0\Gamma}\bar{h}_4\left(\frac{\Gamma D}{v^2},\frac{\Gamma}{v\rho_0},\frac{q}{\rho_0},\frac{m_0}{\rho_0},\beta\right)\,, \tag{B.149}$$

where the $\bar{h}_i$'s are given by

$$\bar{h}_1 = |\bar{f}_m|^2\,\bar{g}_2 + |\bar{f}_\rho|^2\,\bar{g}_1 + \bar{f}_m\bar{f}^\star_\rho\,\bar{g}_3\,,\qquad \bar{h}_2 = \bar{f}_m\,\bar{g}_2 + \bar{f}^\star_\rho\,\bar{g}_3\,, \tag{B.150}$$

$$\bar{h}_3 = \bar{f}_\rho\,\bar{g}_1 + \bar{f}_m\,\bar{g}_3\,,\qquad \bar{h}_4 = \bar{f}_{mm}\,\bar{g}_2 + \bar{f}_{\rho\rho}\,\bar{g}_1 + \bar{f}_{m\rho}\,\bar{g}_3\,. \tag{B.151}$$

Making the integrals dimensionless in (B.148)-(B.149) by changing variable to $\tilde{q} = q/\rho_0$, we obtain the final scaling form of the C_i's as

$$C_1 = \frac{1}{\Gamma}\bar{H}_1\left(\frac{\Gamma D}{v^2},\frac{\Gamma}{v\rho_0},\frac{m_0}{\rho_0},\beta\right)\,,\qquad C_2 = \frac{\rho_0}{\Gamma}\bar{H}_2\left(\frac{\Gamma D}{v^2},\frac{\Gamma}{v\rho_0},\frac{m_0}{\rho_0},\beta\right)\,, \tag{B.152}$$

$$C_3 = \frac{\rho_0}{\Gamma}\bar{H}_3\left(\frac{\Gamma D}{v^2},\frac{\Gamma}{v\rho_0},\frac{m_0}{\rho_0},\beta\right)\,,\qquad C_4 = \frac{1}{\Gamma}\bar{H}_4\left(\frac{\Gamma D}{v^2},\frac{\Gamma}{v\rho_0},\frac{m_0}{\rho_0},\beta\right)\,. \tag{B.153}$$

Finally plugging the above scalings into the expression of $\Delta\mathcal{F}_{\text{topo}}$ (B.95), we obtain

$$\begin{aligned}\Delta\mathcal{F}_{\text{topo}} =& \left(\beta^2 m_0 - \beta^3\rho_0\bar{m}_0\right)\bar{H}_1 + 2\beta^2\bar{m}_0\rho_0\bar{H}_2 - \left(2\beta + \beta^3\bar{m}_0^2\right)\rho_0\bar{H}_3 \\ &+ \left(2\beta^2\bar{m}_0 m_0 - \beta^3\bar{m}_0^2\rho_0 - 2\beta\rho_0\right)\bar{H}_4 \ ,\end{aligned} \tag{B.154}$$

which can be cast into the following scaling form

$$\Delta\mathcal{F}_{\text{topo}} = \rho_0\bar{\mathcal{F}}_1\left(\frac{\Gamma D}{v^2}, \frac{\Gamma}{v\rho_0}, \frac{m_0}{\rho_0}, \beta\right) + m_0\bar{\mathcal{F}}_2\left(\frac{\Gamma D}{v^2}, \frac{\Gamma}{v\rho_0}, \frac{m_0}{\rho_0}, \beta\right) \ . \tag{B.155}$$

As we are interested in the renormalization of the linear Landau term, we can taylor expand $\Delta\mathcal{F}_{\text{topo}}$ up to order m_0

$$\begin{aligned}\Delta\mathcal{F}_{\text{topo}} =& \rho_0\bar{\mathcal{F}}_1\left(\frac{\Gamma D}{v^2}, \frac{\Gamma}{v\rho_0}, 0, \beta\right) + m_0\ \bar{\mathcal{F}}_1^{(0,0,1,0)}\left(\frac{\Gamma D}{v^2}, \frac{\Gamma}{v\rho_0}, 0, \beta\right) \\ &+ m_0\ \bar{\mathcal{F}}_2\left(\frac{\Gamma D}{v^2}, \frac{\Gamma}{v\rho_0}, 0, \beta\right) + \mathcal{O}(m_0^2)\end{aligned} \tag{B.156}$$

The first term on the right hand side of (B.156) is unphysical as it breaks the parity $m_0 \to -m_0$ in the Landau potential. Its presence inconsistently implies that a nonzero magnetization would subsist even in the very high temperature regime: we thus set this term to zero and obtain the final scaling form of $\Delta\mathcal{F}_{\text{topo}}$ as

$$\Delta\mathcal{F}_{\text{topo}} = m_0\ \bar{\mathcal{F}}\left(\frac{\Gamma D}{v^2}, \frac{\Gamma}{v\rho_0}, \beta\right) + \mathcal{O}(m_0^2) \ , \tag{B.157}$$

where $\bar{\mathcal{F}}(u,v,w) = \bar{\mathcal{F}}_1^{(0,0,1,0)}(u,v,0,w) + \bar{\mathcal{F}}_2(u,v,0,w)$. Without changing the zero-th order in the noise strength σ, we can replace m_0 and ρ_0 by $\tilde{m} = \langle m\rangle$ and $\tilde{\rho} = \langle\rho\rangle$ in (B.157). This substitution gives back (3.89) of main text:

$$\Delta\mathcal{F}_{\text{topo}} = \tilde{m}\ \bar{\mathcal{F}}\left(\frac{\Gamma D}{v^2}, \frac{\Gamma}{v\tilde{\rho}}, \beta\right) + \mathcal{O}(\tilde{m}^2) \ , \tag{B.158}$$

B.5 Renormalization for fully connected alignment

This appendix is devoted to the computation of $\Delta\mathcal{F}_{\text{topo}}$ in (3.88) for a fully connected AIM. It is not self-contained and as such we advise a previous reading of appendix B.3.2 and B.4. We first recall the definition (3.90) of the alignment $\bar{m}$ for the fully connected AIM

$$\bar{m} = \frac{\int_0^L m(z)dz}{N}; \qquad \text{where} \qquad N = \int_0^L \rho(z)dz \ . \tag{B.159}$$

For this specific choice of $\bar{m}$, the following simplifications occur in the Fourier transforms of the functional derivatives defined in (B.137) to (B.140)

$$\bar{m}_0 = \frac{m_0}{\rho_0} \ , \quad \bar{m}_m^q = \frac{1}{\rho_0}\delta_{q,0} \ , \qquad \bar{m}_\rho^q = \bar{m}_{\rho,\rho}^{q,q'} = \bar{m}_{m,m}^{q,q'} = \bar{m}_{m,m}^{q,q'} = 0 \ . \tag{B.160}$$

Using the discrete expressions for the C_i's in (B.108), (B.110), (B.111) and (B.112) together with (B.160), we obtain for the fully-connected version

$$C_1 = \frac{1}{N\rho_0}\langle\delta m_1^0\delta m_1^{-0}\rangle, \ C_2 = \frac{1}{N}\langle\delta m_1^0\delta m_1^{-0}\rangle, \ C_3 = \frac{1}{N}\langle\delta m_1^0\delta\rho_1^{-0}\rangle, \ C_4 = 0 \ . \tag{B.161}$$

Note that to obtain (B.161), we have used that $N = L\rho_0$. As mass is conserved in the system, we have that $\delta\rho_1^0 \propto \int_0^L \delta\rho_1(z)dz = 0$. Using (B.106), it first entails that $\langle \delta m_1^0 \delta \rho_1^{-0} \rangle = 0$ and we thus further simplify the C_i's as

$$C_1 = \frac{1}{N\rho_0}\langle \delta m_1^0 \delta m_1^{-0} \rangle,\ C_2 = \frac{1}{N}\langle \delta m_1^0 \delta m_1^{-0} \rangle,\ C_3 = C_4 = 0\ . \tag{B.162}$$

Mass conservation also entails, using (B.100), that δm_1^0 evolves according to the following Langevin equation

$$\dot{\delta m_1^0} = A_{22}^0 \delta m_1^0 + \sqrt{2\rho_0}\,\eta^0\ , \tag{B.163}$$

where η^0 is a Gaussian white noise such that $\langle \eta^0(t)\eta^0(t')\rangle = L^{-1}\delta(t-t')$ and A_{22}^0 is given by (B.144) as

$$A_{22}^0 = -2\Gamma\left(1 + \frac{\beta^2}{2}\frac{m_0^2}{\rho_0^2}\right) + 2\Gamma\left[\beta\left(1 + \frac{\beta^2}{2}\frac{m_0}{\rho_0}\right) - \beta^2\frac{m_0^2}{\rho_0^2}\right]\ . \tag{B.164}$$

Using Itō calculus on (B.163), and taking care of the factor L^{-1} in (B.104), we obtain

$$\langle \delta m_1^0 \delta m_1^{-0} \rangle = \frac{\rho_0}{2\Gamma\left[1 + \frac{\beta^2}{2}\frac{m_0^2}{\rho_0^2} - \beta\left(1 + \frac{\beta^2}{2}\frac{m_0}{\rho_0}\right) + \beta^2\frac{m_0^3}{\rho_0^3}\right]}\ . \tag{B.165}$$

Expanding $\langle \delta m_1^0 \delta m_1^{-0} \rangle$ to first order in m_0, we obtain

$$\langle \delta m_1^0 \delta m_1^{-0} \rangle = \frac{\rho_0}{2\Gamma(1-\beta)}\left(1 + \frac{\beta^2}{2(1-\beta)}\frac{m_0}{\rho_0} + \mathcal{O}(m_0^2)\right) \tag{B.166}$$

Inserting the above expansion into (B.162), and then injecting the resulting C_i's into (B.95) yields $\Delta\mathcal{F}_{\text{topo}}$ for the fully connected model

$$\Delta\mathcal{F}_{\text{topo}} = \frac{m_0}{N}\left(\frac{\beta^2}{2} + \frac{\beta^2}{1-\beta}\right) + \mathcal{O}(m_0^2)\ . \tag{B.167}$$

Without changing the leading order in the noise strength σ of $\Delta\mathcal{F}_{\text{topo}}$, we can replace m_0 and ρ_0 by $\tilde{m} = \langle m \rangle$ and $\tilde{\rho} = \langle \rho \rangle$ in (B.167). This substitution gives back (3.91) of main text

$$\Delta\mathcal{F}_{\text{topo}} = \frac{\tilde{m}}{N}\left(\frac{\beta^2}{2} + \frac{\beta^2}{1-\beta}\right) + \mathcal{O}(\tilde{m}^2)\ . \tag{B.168}$$

B.6 Renormalization of mean-field hydrodynamics of Voronoi-based Vicsek model

This appendix is devoted to the derivation of the renormalized hydrodynamics (3.102)-(3.103) of the main text. Following the scheme developed in section 3.4, we call ρ_0 and W_0 the mean-field solutions of (3.100)-(3.101) without noise (*ie* with $\sigma = 0$) and introduce the perturbative series

$$\rho = \rho_0 + \sqrt{\sigma}\ \delta\rho_1 + \sigma\delta\rho_2 + ..\ , \qquad W = W_0 + \sqrt{\sigma}\ \delta W_1 + \sigma\delta W_2 + ..\ . \tag{B.169}$$

Injecting (B.169) into (3.100)-(3.101) and equating terms of order $\sigma^{k/2}$ yields the evolution equation for $\delta\rho_k$ and δW_k. Further using the definition $\mathcal{F}_{tt} = \alpha W - \gamma W^3/\rho^2$, we obtain, for $k = 1$

$$\partial_t \delta\rho_1 = - v\partial_x \delta W_1 + \partial_x \left(\sqrt{2\epsilon\rho_0}\eta_1\right) \tag{B.170}$$

$$\begin{aligned}\partial_t \delta W_1 =& D\partial_{xx}\delta W_1 - \frac{v}{2}\partial_x\delta\rho_1 - \frac{\lambda}{\rho_0}W_0\partial_x W_1 - \frac{\lambda}{\rho_0}W_1\partial_x W_0 + \frac{\lambda}{\rho_0^2}\delta\rho_1 W_0\partial_x W_0 \\ &+ \frac{\partial\mathcal{F}_{tt}}{\partial\rho}\delta\rho_1 + \frac{\partial\mathcal{F}_{tt}}{\partial W}\delta W_1 + \sqrt{2\rho_0}\,\eta_2 \,.\end{aligned} \tag{B.171}$$

while for $k = 2$ we get

$$\partial_t \delta\rho_2 = - v\partial_x \delta W_2 + \partial_x \left(\frac{\sqrt{\epsilon}\delta\rho_1}{\sqrt{2\rho_0}}\eta_1\right) \tag{B.172}$$

$$\begin{aligned}\partial_t \delta W_2 =& D\partial_{xx}\delta W_2 - \frac{v}{2}\partial_x\delta\rho_2 + \frac{\partial\mathcal{F}_{tt}}{\partial\rho}\delta\rho_2 + \frac{\partial\mathcal{F}_{tt}}{\partial W}\delta W_2 + \frac{\partial^2\mathcal{F}_{tt}}{\partial W^2}\frac{\delta W_1^2}{2} + \frac{\partial^2\mathcal{F}_{tt}}{\partial\rho^2}\frac{\delta\rho_1^2}{2} + \frac{\partial^2\mathcal{F}_{tt}}{\partial W\partial\rho}\delta W_1\delta\rho_1 \\ &- \frac{\lambda}{\rho_0}\delta W_1\partial_x\delta W_1 - \frac{\lambda}{\rho_0^3}W_0\partial_x W_0\delta\rho_1^2 - \frac{\lambda}{\rho_0}\delta W_2\partial_x W_0 - \frac{\lambda}{\rho_0}W_0\partial_x\delta W_2 + \frac{\lambda}{\rho_0^2}\delta\rho_1\delta W_1\partial_x W_0 \\ &+ \frac{\lambda}{\rho_0^2}W_0\delta\rho_1\partial_x\delta W_1 + \frac{\lambda}{\rho_0^2}\delta\rho_2 W_0\partial_x W_0 + \frac{\delta\rho_1}{\sqrt{2\rho_0}}\,\eta_2 \,,\end{aligned} \tag{B.173}$$

Averaging (B.170)-(B.171) over the noise with Itō prescription gives

$$\partial_t\langle\delta\rho_1\rangle = - v\partial_x\langle\delta W_1\rangle \tag{B.174}$$

$$\begin{aligned}\partial_t\langle\delta W_1\rangle =& D\partial_{xx}\langle\delta W_1\rangle - \frac{v}{2}\partial_x\langle\delta\rho_1\rangle - \frac{\lambda}{\rho_0}W_0\partial_x\langle W_1\rangle - \frac{\lambda}{\rho_0}\langle W_1\rangle\partial_x W_0 + \frac{\lambda}{\rho_0^2}\langle\delta\rho_1\rangle W_0\partial_x W_0 \\ &+ \frac{\partial\mathcal{F}_{tt}}{\partial\rho}\langle\delta\rho_1\rangle + \frac{\partial\mathcal{F}_{tt}}{\partial W}\langle\delta W_1\rangle \,.\end{aligned} \tag{B.175}$$

Doing likewise for (B.172)-(B.173) yields

$$\partial_t\langle\delta\rho_2\rangle = - v\partial_x\langle\delta W_2\rangle \tag{B.176}$$

$$\begin{aligned}\partial_t\langle\delta W_2\rangle =& D\partial_{xx}\langle\delta W_2\rangle - \frac{v}{2}\partial_x\langle\delta\rho_2\rangle + \frac{\partial\mathcal{F}_{tt}}{\partial\rho}\langle\delta\rho_2\rangle + \frac{\partial\mathcal{F}_{tt}}{\partial W}\langle\delta W_2\rangle + \frac{\partial^2\mathcal{F}_{tt}}{\partial W^2}\frac{\langle\delta W_1^2\rangle}{2} + \frac{\partial^2\mathcal{F}_{tt}}{\partial\rho^2}\frac{\langle\delta\rho_1^2\rangle}{2} \\ &+ \frac{\partial^2\mathcal{F}_{tt}}{\partial W\partial\rho}\langle\delta W_1\delta\rho_1\rangle - \frac{\lambda}{\rho_0}\langle\delta W_1\partial_x\delta W_1\rangle - \frac{\lambda}{\rho_0^3}W_0\partial_x W_0\langle\delta\rho_1^2\rangle - \frac{\lambda}{\rho_0}\langle\delta W_2\rangle\partial_x W_0 \\ &- \frac{\lambda}{\rho_0}W_0\partial_x\langle\delta W_2\rangle + \frac{\lambda}{\rho_0^2}\langle\delta\rho_1\delta W_1\rangle\partial_x W_0 + \frac{\lambda}{\rho_0^2}W_0\langle\delta\rho_1\partial_x\delta W_1\rangle + \frac{\lambda}{\rho_0^2}\langle\delta\rho_2\rangle W_0\partial_x W_0 \,,\end{aligned} \tag{B.177}$$

Summing together (3.98), $\sqrt{\sigma}$ times (B.174), and σ times (B.176) gives the evolution of $\tilde{\rho}$ up to order σ

$$\partial_t\tilde{\rho} = -v\partial_x\tilde{W} \,, \tag{B.178}$$

while adding (3.99), $\sqrt{\sigma}$ times (B.175), and σ times (B.177) yields the evolution of $\tilde{m}$ up to order σ

$$\begin{aligned}\partial_t\tilde{W} =&D\partial_{xx}\tilde{W} - \frac{\lambda}{\tilde{\rho}}\tilde{W}\partial_x\tilde{W} - \frac{v}{2}\partial_x\tilde{\rho} + \alpha\tilde{W} - \frac{\gamma}{\tilde{\rho}^2}\tilde{W}^3 + \mathcal{F}_{tt}(\tilde{\rho},\tilde{W}) + \sigma\Bigg[\frac{\partial^2\mathcal{F}_{tt}}{\partial W^2}\left(\frac{\langle\delta W_1^2\rangle - \langle\delta W_1\rangle^2}{2}\right)\\ &+ \frac{\partial^2\mathcal{F}_{tt}}{\partial\rho^2}\left(\frac{\langle\delta\rho_1^2\rangle - \langle\delta\rho_1\rangle^2}{2}\right) + \frac{\partial^2\mathcal{F}_{tt}}{\partial W\partial\rho}\left(\langle\delta m_1\delta\rho_1\rangle - \langle\delta W_1\rangle\langle\delta\rho_1\rangle\right)\\ &- \frac{\lambda}{\rho_0}\left(\langle\delta W_1\partial_x\delta W_1\rangle - \langle\delta W_1\rangle\partial_x\langle\delta W_1\rangle\right) - \frac{\lambda}{\rho_0^3}W_0\partial_x W_0\left(\langle\delta\rho_1^2\rangle - \langle\delta\rho_1\rangle^2\right)\\ &+ \frac{\lambda}{\rho_0^2}\partial_x W_0\left(\langle\delta\rho_1\delta W_1\rangle - \langle\delta\rho_1\rangle\langle\delta W_1\rangle\right) + \frac{\lambda}{\rho_0^2}W_0\left(\langle\delta\rho_1\partial_x\delta W_1\rangle - \langle\delta\rho_1\rangle\partial_x\langle W_1\rangle\right)\Bigg] .\end{aligned} \tag{B.179}$$

The terms proportional to $\partial_x W_0$ in (B.179) can only renormalize λ, not $\mathcal{F}_{tt}$ so that we set them to zero and focus on computing

$$\begin{aligned}\Delta\mathcal{F}_{tt} =&\frac{\partial^2\mathcal{F}_{tt}}{\partial W^2}\left(\frac{\langle\delta W_1^2\rangle - \langle\delta W_1\rangle^2}{2}\right) + \frac{\partial^2\mathcal{F}_{tt}}{\partial\rho^2}\left(\frac{\langle\delta\rho_1^2\rangle - \langle\delta\rho_1\rangle^2}{2}\right)\\ &+ \frac{\partial^2\mathcal{F}_{tt}}{\partial W\partial\rho}\left(\langle\delta m_1\delta\rho_1\rangle - \langle\delta W_1\rangle\langle\delta\rho_1\rangle\right) - \frac{\lambda}{\rho_0}\left(\langle\delta W_1\partial_x\delta W_1\rangle - \langle\delta W_1\rangle\partial_x\langle\delta W_1\rangle\right)\\ &+ \frac{\lambda}{\rho_0^2}W_0\left(\langle\delta\rho_1\partial_x\delta W_1\rangle - \langle\delta\rho_1\rangle\partial_x\langle W_1\rangle\right) .\end{aligned} \tag{B.180}$$

As we are solely interested in the renormalization of α, we only have to derive the correlators involving $\delta\rho_1$ and δW_1 in $\Delta\mathcal{F}_{tt}$ to order W_0. To perform this derivation, similarly to AI, we have to assume that $\delta\rho_1$ and δW_1 are fast mode varying on lengthscales much smaller than those of ρ_0 and W_0. Under this assumption, $\rho_0(x,t)$, $W_0(x,t)$ and $\partial_x W_0(x,t)$ entering in the linearized evolution (B.170)-(B.171) for $\delta\rho_1$ and δW_1 can be considered as constants. This adiabatic approximation allows us to compute the correlators in terms of ρ_0, W_0 and $\partial_x W_0$ as constants and to re-establish their dependency on x and t a posteriori. Note that any dependency of the correlators on $\partial_x W_0$ will renormalize λ, not α. Thus, to simplify the derivation of $\hat{\alpha}$ and get rid of any dependency on $\partial_x W_0$ in the correlators, we set $\partial_x W_0 = 0$ in the linearized evolution (B.170)-(B.171)

$$\partial_t\delta\rho_1 = - v\partial_x\delta W_1 + \partial_x\left(\sqrt{2\epsilon\rho_0}\eta_1\right) \tag{B.181}$$

$$\partial_t\delta W_1 =D\partial_{xx}\delta W_1 - \frac{v}{2}\partial_x\delta\rho_1 - \frac{\lambda}{\rho_0}W_0\partial_x W_1 + \frac{\partial\mathcal{F}_{tt}}{\partial\rho}\delta\rho_1 + \frac{\partial\mathcal{F}_{tt}}{\partial W}\delta W_1 + \sqrt{2\rho_0}\,\eta_2 . \tag{B.182}$$

Multiplying (B.181) and (B.182) by e^{iqx}/L and integrating over x yields the time-evolution of the q-th Fourier modes

$$\partial_t\begin{pmatrix}\delta\rho_1^q\\ \delta W_1^q\end{pmatrix} = \begin{pmatrix}T_{11}^q & T_{12}^q\\ T_{21}^q & T_{22}^q\end{pmatrix}\begin{pmatrix}\delta\rho_1^q\\ \delta W_1^q\end{pmatrix} + \begin{pmatrix}\sqrt{2\epsilon\rho_0}\,iq\,\eta_1^q\\ \sqrt{2\rho_0}\,\eta_2^q\end{pmatrix} , \tag{B.183}$$

where the convention for $\delta\rho_1^q$ and δW_1^q is given in (B.24). Note that η_1^q and η_2^q are the q-th Fourier modes of the two uncorrelated Gaussian white noises η_1 and η_2. Their correlations reads $\langle\eta_k^q\eta_l^{q'}\rangle = L^{-1}\delta_{k,l}\delta(t-t')\delta_{q+q',0}$. Finally, the matrix coefficients T_{kl}^q are given by

$$T_{11}^q = 0 , \quad T_{12}^q = - ivq , \quad T_{21}^q = - iq\frac{v}{2} + 2\gamma\frac{W_0^3}{\rho_0^3} , \quad T_{22}^q = - \lambda iq\frac{W_0}{\rho_0} - Dq^2 + \alpha - 3\gamma\frac{W_0^2}{\rho_0^2} . \tag{B.184}$$

To compute the correlators involved in $\Delta\mathcal{F}_{tt}$, we use Itō calculus on the stochastic system (B.183) to get the following closed system of equations

$$\frac{d}{dt}\langle\delta\rho_1^q\delta\rho_1^{q'}\rangle = (T_{11}^q + T_{11}^{q'})\langle\delta\rho_1^q\delta\rho_1^{q'}\rangle + T_{12}^q\langle\delta W_1^q\delta\rho_1^{q'}\rangle + T_{12}^{q'}\langle\delta\rho_1^q\delta W_1^{q'}\rangle - \frac{2\epsilon\rho_0 q^2}{L}\delta_{q+q',0} = 0 \tag{B.185}$$

$$\frac{d}{dt}\langle\delta W_1^q\delta\rho_1^{q'}\rangle = (T_{22}^q + T_{11}^{q'})\langle\delta W_1^q\delta\rho_1^{q'}\rangle + T_{21}^q\langle\delta\rho_1^q\delta\rho_1^{q'}\rangle + T_{12}^{q'}\langle\delta W_1^q\delta W_1^{q'}\rangle = 0 \tag{B.186}$$

$$\frac{d}{dt}\langle\delta W_1^q\delta W_1^{q'}\rangle = (T_{22}^q + T_{22}^{q'})\langle\delta W_1^q\delta W_1^{q'}\rangle + T_{21}^q\langle\delta\rho_1^q\delta W_1^{q'}\rangle + T_{21}^{q'}\langle\delta W_1^q\delta\rho_1^{q'}\rangle + \frac{2\rho_0}{L}\delta_{q+q',0} = 0\ , \tag{B.187}$$

where the last equality once again stems from working in the steady state. Inverting this system yields

$$\langle\delta W_1^q\delta W_1^{q'}\rangle = g_{ww}(q)\frac{\delta_{q+q',0}}{L}\ ,\quad \langle\delta\rho_1^q\delta\rho_1^{q'}\rangle = g_{\rho\rho}(q)\frac{\delta_{q+q',0}}{L}\ ,\quad \langle\delta W_1^q\delta\rho_1^{q'}\rangle = g_{w\rho}(q)\frac{\delta_{q+q',0}}{L}\ , \tag{B.188}$$

where, to first order in W_0, the functions $g_{ww}(q)$, $g_{\rho\rho}(q)$ and $g_{w\rho}(q)$ are given by

$$g_{ww}(q) = \frac{\rho_0}{2D}\left[-\epsilon + \frac{2D - \epsilon\alpha}{Dq^2 - \alpha}\right] + \mathcal{O}\left(W_0^2\right) \tag{B.189}$$

$$g_{\rho\rho}(q) = \frac{\rho_0}{D}\left[-2\frac{D^2q^2\epsilon}{v^2} + 2\frac{D\epsilon\alpha}{v^2} - \epsilon + \frac{2D - \alpha\epsilon}{Dq^2 - \alpha}\right] + \mathcal{O}\left(W_0^2\right) \tag{B.190}$$

$$g_{w\rho}(q) = \frac{\epsilon}{Dv}\left[iqD\rho_0 + W_0\lambda + W_0\frac{\lambda\alpha}{Dq^2 - \alpha}\right] + \mathcal{O}\left(W_0^2\right)\ . \tag{B.191}$$

At this point we note that $g_{ww}(q)$, $g_{\rho\rho}(q)$ and $g_{w\rho}(q)$ contains a polynomial part and a rational part in the wave-vector q. Upon Fourier transforming back in real space using (B.25), these polynomial parts will yield terms proportional to $\delta(x-y)$ in the two-point functions $\langle\delta\rho_1(x)\delta\rho_1(y)\rangle$, $\langle\delta W_1(x)\delta W_1(y)\rangle$ and $\langle\delta W_1(x)\delta\rho_1(y)\rangle$. These delta peaks are unphysical and to regularize the correlators taken at $x = y$ we hereafter neglect the polynomial parts to consider only that

$$g_{ww}(q) = \frac{\rho_0}{2D}\frac{2D - \epsilon\alpha}{Dq^2 - \alpha}\ ,\qquad g_{\rho\rho}(q) = \frac{\rho_0}{D}\frac{2D - \alpha\epsilon}{Dq^2 - \alpha}\ ,\qquad g_{w\rho}(q) = \frac{\epsilon W_0}{Dv}\frac{\lambda\alpha}{Dq^2 - \alpha}\ . \tag{B.192}$$

We note that we can integrate $g_{ww}(q)$, $g_{\rho\rho}(q)$ and $g_{w\rho}(q)$ over q only if $\alpha < 0$, which means that we have to restrict our study to the high temperature phase where such a condition is respected (this is equivalent to assumption AII). We finally obtain

$$\langle\delta\rho_1^2\rangle = \int\frac{dq}{2\pi}g_{\rho\rho}(q) = \frac{\rho_0(2D - \alpha\epsilon)}{2D\sqrt{D|\alpha|}}\ ,\quad \langle\delta W_1^2\rangle = \int\frac{dq}{2\pi}g_{ww}(q) = \frac{\rho_0(2D - \alpha\epsilon)}{4D\sqrt{D|\alpha|}}$$
$$\langle\delta W_1\delta\rho_1\rangle = \int\frac{dq}{2\pi}g_{w\rho}(q) = W_0\frac{\epsilon\lambda\alpha}{2Dv\sqrt{D|\alpha|}}\ ,\quad \langle\delta W_1\partial_x\delta W_1\rangle = \int\frac{dq}{2\pi}iqg_{ww}(q) = 0\ . \tag{B.193}$$

Injecting the above expression of the correlators in (B.180) yields the final expression for $\Delta\mathcal{F}_{tt}$ as

$$\Delta\mathcal{F}_{tt} = \frac{1}{2}\frac{\partial^2\mathcal{F}_{tt}}{\partial W^2}\langle\delta W_1^2\rangle + \mathcal{O}(W_0^2) = -\frac{3\gamma}{\rho_0}\frac{2D - \alpha\epsilon}{4D\sqrt{D|\alpha|}}W_0 + \mathcal{O}(W_0^2)\ . \tag{B.194}$$

We readily deduce from the above expression the formula (3.104) of main text

$$\hat{\alpha} = \alpha - \sigma \frac{3\gamma}{\tilde{\rho}} \frac{2D - \alpha\epsilon}{4D\sqrt{D|\alpha|}} \tag{B.195}$$

C. Lattice gas model for active solidification

C.1 Derivation of the hydrodynamic equations

In this appendix, we derive the hydrodynamic equations (4.34) and (4.35) of the main text. To this aim, we follow and adapt [148, 172–174]. We consider a lattice with L different sites and a discretized time t_j with $j \in \{1, .., N\}$. In a time $dt = t_{j+1} - t_j$, a unique spin makes one of the three moves described in RI, RII and RIII. A trajectory of the spins is completely determined by the set $\{\eta\}$ containing all the $\eta_i^\pm(t_j)$'s

$$\{\eta\} = \left\{\eta_i^\pm(t_j) \quad \text{for} \quad i \in \{1, .., L\},\ j \in \{1, .., N\}\right\} . \tag{C.1}$$

More particularly, at time t_j, a configuration of the spins is entirely described by the set $\{\eta^j\}$ defined as

$$\{\eta^j\} = \left\{\eta_i^\pm(t_j) \quad \text{for} \quad i \in \{1, .., L\}\right\} . \tag{C.2}$$

Let us define $J_i^\pm(t_j)$ as the variation of the number of $\pm$ spins at site i between time t_j and t_{j+1}. For a fixed trajectory of the spins, we have $J_i^\pm(t_j) = \eta_i^\pm(t_{j+1}) - \eta_i^\pm(t_j)$. Note that because a unique spin moves during dt, each $J_i^\pm(t_j)$ takes values in $\{-1, 0, 1\}$ and only two of them are nonzero at the same time t_j.

For example, when a spin + at site i hops to the right at time t_j, we have $J_i^+(t_j) = -1$ and $J_{i+1}^+(t_j) = 1$ while all other $J_k^\pm(t_j)$ are zero. Let us finally introduce the set $\{J\}$ containing all the $J_i^\pm(t_j)$'s

$$\{J\} = \left\{J_i^\pm(t_j) \quad \text{for} \quad i \in \{1, .., L\},\ j \in \{1, .., N\}\right\} , \tag{C.3}$$

and the set $\{J^j\}$ containing the $J_i^\pm(t_j)$'s at a given time

$$\{J^j\} = \left\{J_i^\pm(t_j) \quad \text{for} \quad i \in \{1, .., L\}\right\} . \tag{C.4}$$

We start by establishing a path integral formulation for the probability $P[\{\eta\}]$ to observe a given trajectory $\{\eta\}$ of the spins. Using a standard path integral formalism for on-lattice particle models [172, 173], we obtain

$$P[\{\eta\}] = \Big\langle \prod_{i=1}^{L} \prod_{j=1}^{N} \delta\left(\eta_i^+(t_{j+1}) - \eta_i^+(t_j) - J_i^+(t_j)\right) \delta\left(\eta_i^-(t_{j+1}) - \eta_i^-(t_j) - J_i^-(t_j)\right) \Big\rangle_{\{J\}} , \tag{C.5}$$

where $\langle\cdot\rangle_{\{J\}}$ indicates averaging over all the configurations in $\{J\}$. Note that in (C.5), the $\eta_i^+(t_j)$'s and $\eta_i^-(t_j)$'s correspond to the fixed trajectory $\{\eta\}$ while the $J_i^\pm(t_j)$'s are stochastic variables over which we average. Using the integral expression of the Dirac function $\delta(s) = \int \exp(is\hat{s})d\hat{s}/(2\pi)$ into (C.5), we introduce the fields $\hat{\eta}_i^+(t_j)$ and $\hat{\eta}_i^-(t_j)$ which are conjugated to $\eta_i^+(t_j)$ and $\eta_i^-(t_j)$, respectively. We obtain

$$P[\{\eta\}] = \int \prod_{j=1}^{N} \Bigg[\prod_{i=1}^{L} \left[d\hat{\eta}_i^+(t_j) d\hat{\eta}_i^-(t_j) e^{\hat{\eta}_i^+(t_j)\left[\eta_i^+(t_{j+1}) - \eta_i^+(t_j)\right]} e^{\hat{\eta}_i^-(t_j)\left[\eta_i^-(t_{j+1}) - \eta_i^-(t_j)\right]} \right] \Big\langle \prod_{i=1}^{L} \left[e^{-\hat{\eta}_i^+(t_j) J_i^+(t_j) - \hat{\eta}_i^-(t_j) J_i^-(t_j)} \right] \Big\rangle_{\{J^j\}} \Bigg] , \tag{C.6}$$

where $\langle\cdot\rangle_{\{J^j\}}$ is the average over all configurations $\mathcal{C}$ in $\{J^j\}$.

Denoting $f(\mathcal{C}) = \prod_{i=1}^{L} e^{-\hat{\eta}_i^+(t_j)J_i^+(t_j)-\hat{\eta}_i^-(t_j)J_i^-(t_j)}$, we thus have

$$\langle\prod_{i=1}^{L}\left[e^{-\hat{\eta}_i^+(t_j)J_i^+(t_j)-\hat{\eta}_i^-(t_j)J_i^-(t_j)}\right]\rangle_{\{J^j\}} = \sum_{\mathcal{C}\in\{J^j\}} f(\mathcal{C})P\left(\mathcal{C}|\{\eta^j\}\right) \ , \tag{C.7}$$

with $P\left(\mathcal{C}|\{\eta^j\}\right)$ the probability to observe the set of configuration $\mathcal{C}$ given the positions of the spins $\{\eta^j\}$ at the previous time t_j. We now separate the possible configurations $\mathcal{C}$ in $\{J^j\}$ according to the microscopic move they relate to. We define the subset $\mathcal{N}_d^j$, $\mathcal{N}_h^j$, and $\mathcal{N}_s^j$ of $\{J^j\}$ as

$$\mathcal{N}_d^j = \left\{J_i^\pm(t_j) \text{ for } i \in \{1,..,L\} \text{ generated by a diffusive move}\right\} \tag{C.8}$$

$$\mathcal{N}_h^j = \left\{J_i^\pm(t_j) \text{ for } i \in \{1,..,L\} \text{ generated by a hopping move}\right\} \tag{C.9}$$

$$\mathcal{N}_s^j = \left\{J_i^\pm(t_j) \text{ for } i \in \{1,..,L\} \text{ generated by a flipping move}\right\} \ . \tag{C.10}$$

We further define $\mathcal{C}_0$ as the configuration where all the $J_i^\pm(t_j)$ for $i \in \{1,..,L\}$ vanish: it corresponds to the case when no move is performed at time t_j. We can now dispatch the sum over the configurations in (C.7) on the subsets $\mathcal{N}_d^j$, $\mathcal{N}_h^j$, $\mathcal{N}_s^j$ and obtain

$$\begin{aligned}\langle f\rangle_{\{J^j\}} =& f(\mathcal{C}_0)P\left(\mathcal{C}_0|\{\eta^j\}\right) + \sum_{\mathcal{C}\in\mathcal{N}_d^j} f(\mathcal{C})P\left(\mathcal{C}|\{\eta^j\}\right) + \sum_{\mathcal{C}\in\mathcal{N}_h^j} f(\mathcal{C})P\left(\mathcal{C}|\{\eta^j\}\right) \\ &+ \sum_{\mathcal{C}\in\mathcal{N}_s^j} f(\mathcal{C})P\left(\mathcal{C}|\{\eta^j\}\right) \ .\end{aligned} \tag{C.11}$$

Because $\mathcal{C}_0$ is the zero move configuration, we have $f(\mathcal{C}_0) = 1$ and

$$P\left(\mathcal{C}_0|\{\eta^j\}\right) = 1 - \sum_{\mathcal{C}\in\mathcal{N}_d^j} P\left(\mathcal{C}|\{\eta^j\}\right) - \sum_{\mathcal{C}\in\mathcal{N}_h^j} P\left(\mathcal{C}|\{\eta^j\}\right) - \sum_{\mathcal{C}\in\mathcal{N}_s^j} P\left(\mathcal{C}|\{\eta^j\}\right) \ . \tag{C.12}$$

Injecting (C.12) into (C.11), we get

$$\langle f\rangle_{\{J^j\}} = 1 + T_d + T_h + T_s \ , \tag{C.13}$$

with T_d, T_h and T_s given by

$$T_d = \sum_{\mathcal{C}\in\mathcal{N}_d^j} \left(f(\mathcal{C}) - 1\right) P\left(\mathcal{C}|\{\eta^j\}\right), \qquad T_h = \sum_{\mathcal{C}\in\mathcal{N}_h^j} \left(f(\mathcal{C}) - 1\right) P\left(\mathcal{C}|\{\eta^j\}\right) \tag{C.14}$$

$$T_s = \sum_{\mathcal{C}\in\mathcal{N}_s^j} \left(f(\mathcal{C}) - 1\right) P\left(\mathcal{C}|\{\eta^j\}\right) \ . \tag{C.15}$$

We note that T_d, T_h and T_s are proportional to dt through the probability $P\left(\mathcal{C}|\{\eta^j\}\right)$ that a move occurred. To order dt, we can thus reexponentiate (C.13) and obtain

$$\langle f\rangle_{\{J^j\}} = \exp(T_d + T_h + T_s) + \mathcal{O}(dt^2) \, . \tag{C.16}$$

Hereafter, terms of order $\mathcal{O}(dt^2)$ will be omitted for clarity. We now determine the terms T_d, T_h and T_s through a detailed analysis of the subsets $\mathcal{N}_d^j$, $\mathcal{N}_h^j$ and $\mathcal{N}_s^j$ respectively. Let us start with $\mathcal{N}_d^j$: it contains four typical configurations

- $\mathcal{C}_d^{i,1}$, when a + spin diffuses from site i to site $i+1$. In this case, $J_i^+(t_j) = -1$ and $J_{i+1}^+(t_j) = 1$ while the remaining $J_k^\pm(t_j)$ are zero. We thus obtain $f(\mathcal{C}_d^{i,1}) = e^{\hat{\eta}_i^+(t_j) - \hat{\eta}_{i+1}^+(t_j)}$. The microscopic rules further gives $P\left(\mathcal{C}_d^{i,1}|\{\eta^j\}\right) = Da^{-2}\eta_i^+(t_j)dt$.

- $\mathcal{C}_d^{i,2}$, when a + spin diffuses from site $i+1$ to site i. In this case, $J_i^+(t_j) = 1$ and $J_{i+1}^+(t_j) = -1$ while the remaining $J_k^\pm(t_j)$ are zero. We thus obtain $f(\mathcal{C}_d^{i,2}) = e^{-\hat{\eta}_i^+(t_j) + \hat{\eta}_{i+1}^+(t_j)}$. The microscopic rules further gives $P\left(\mathcal{C}_d^{i,2}|\{\eta^j\}\right) = Da^{-2}\eta_{i+1}^+(t_j)dt$.

- $\mathcal{C}_d^{i,3}$, when a − spin diffuses from site i to site $i+1$. In this case, $J_i^-(t_j) = -1$ and $J_{i+1}^-(t_j) = 1$ while the remaining $J_k^\pm(t_j)$ are zero. We thus obtain $f(\mathcal{C}_d^{i,3}) = e^{\hat{\eta}_i^-(t_j) - \hat{\eta}_{i+1}^-(t_j)}$. The microscopic rules further gives $P\left(\mathcal{C}_d^{i,3}|\{\eta^j\}\right) = Da^{-2}\eta_i^-(t_j)dt$.

- $\mathcal{C}_d^{i,4}$, when a − spin diffuses from site $i+1$ to site i. In this case, $J_i^-(t_j) = 1$ and $J_{i+1}^-(t_j) = -1$ while the remaining $J_k^\pm(t_j)$ are zero. We thus obtain $f(\mathcal{C}_d^{i,4}) = e^{-\hat{\eta}_i^-(t_j) + \hat{\eta}_{i+1}^-(t_j)}$. The microscopic rules further gives $P\left(\mathcal{C}_d^{i,4}|\{\eta^j\}\right) = Da^{-2}\eta_{i+1}^-(t_j)dt$.

Using translational invariance, T_d in (C.14) can be expressed in terms of these typical configurations $\mathcal{C}_d^{i,k}$ for $k \in \{1,2,3,4\}$ as

$$T_d = \sum_i \sum_{k=1}^{4} \left(f(\mathcal{C}_d^{i,k}) - 1\right) P\left(\mathcal{C}_d^{i,k}|\{\eta^j\}\right) \tag{C.17}$$

In a similar way, we now describe the two typical configurations in $\mathcal{N}_h^i$

- $\mathcal{C}_h^{i,1}$, when a + spin at site i hops to site $i+1$. In this case, $J_i^+(t_j) = -1$ and $J_{i+1}^+(t_j) = 1$ while the remaining $J_k^\pm(t_j)$ are zero. We thus obtain $f(\mathcal{C}_h^{i,1}) = e^{\hat{\eta}_i^+(t_j) - \hat{\eta}_{i+1}^+(t_j)}$. The microscopic rules gives $P\left(\mathcal{C}_h^{i,1}|\{\eta^j\}\right) = \eta_i^+(t_j)e^{-\lambda\left[\eta_i^+(t_j) + \eta_i^-(t_j)\right]} v\, a^{-1}\, dt$.

- $\mathcal{C}_h^{i,2}$, when a − spin at site $i+1$ hops to site i. In this case, $J_i^-(t_j) = 1$ and $J_{i+1}^-(t_j) = -1$ while the remaining $J_k^\pm(t_j)$ are zero. We thus obtain $f(\mathcal{C}_h^{i,2}) = e^{-\hat{\eta}_i^-(t_j) + \hat{\eta}_{i+1}^-(t_j)}$. The microscopic rules gives $P\left(\mathcal{C}_h^{i,2}|\{\eta^j\}\right) = \eta_{i+1}^-(t_j)e^{-\lambda\left[\eta_{i+1}^+(t_j) + \eta_{i+1}^-(t_j)\right]} v\, a^{-1}\, dt$.

Using translational invariance, T_h in (C.14) can be expressed in terms of these typical configurations $\mathcal{C}_h^{i,1}$ and $\mathcal{C}_h^{i,2}$ as

$$T_h = \sum_i \sum_{k=1}^{2} \left(f(\mathcal{C}_h^{i,k}) - 1\right) P\left(\mathcal{C}_h^{i,k}|\{\eta^j\}\right) \tag{C.18}$$

Finally, there are two typical configurations in $\mathcal{N}_s^i$

- $\mathcal{C}_s^{i,1}$, when a + spin at site i flips into a − spin. In this case, $J_i^+(t_j) = -1$ and $J_i^-(t_j) = 1$ while the remaining $J_k^\pm(t_j)$ are zero. We thus obtain $f(\mathcal{C}_h^{i,1}) = e^{\hat{\eta}_i^+(t_j) - \hat{\eta}_i^-(t_j)}$. The microscopic rules further gives

$$\begin{aligned} P\left(\mathcal{C}_s^{i,1}|\{\eta^j\}\right) =& \eta_i^+(t_j)\gamma\, dt\Big[\Theta\left(3 - \eta_i^+(t_j) - \eta_i^-(t_j)\right) e^{-\beta\left[\eta_i^+(t_j) - \eta_i^-(t_j)\right]} \\ &+ \Theta\left(\eta_i^+(t_j) + \eta_i^-(t_j) - 4\right)\Big]\,. \end{aligned} \tag{C.19}$$

- $\mathcal{C}_s^{i,2}$, when a $-$ spin at site i flips into a $+$ spin. In this case, $J_i^+(t_j)=1$ and $J_i^-(t_j)=-1$ while the remaining $J_k^\pm(t_j)$ are zero. We thus obtain $f(\mathcal{C}_h^{i,2})=e^{-\hat{\eta}_i^+(t_j)+\hat{\eta}_i^-(t_j)}$. The microscopic rules further gives

$$P\left(\mathcal{C}_s^{i,2}|\{\eta^j\}\right)=\eta_i^-(t_j)\gamma\,dt\Big[\Theta\left(3-\eta_i^+(t_j)-\eta_i^-(t_j)\right)e^{\beta\left[\eta_i^+(t_j)-\eta_i^-(t_j)\right]} + \Theta\left(\eta_i^+(t_j)+\eta_i^-(t_j)-4\right)\Big]\,. \tag{C.20}$$

Using translational invariance, T_s in (C.15) can be expressed in terms of these typical configurations $\mathcal{C}_s^{i,1}$ and $\mathcal{C}_s^{i,2}$ as

$$T_s=\sum_i\sum_{k=1}^{2}\left(f(\mathcal{C}_s^{i,k})-1\right)P\left(\mathcal{C}_s^{i,k}|\{\eta^j\}\right)\,. \tag{C.21}$$

Injecting (C.17),(C.18),(C.21) into the expression (C.16) to get $\langle f\rangle_{\{J^j\}}$, we can then evaluate $P[\{\eta\}]$ in (C.6) as

$$P[\{\eta\}]=\int\prod_{i=1}^{L}\prod_{j=1}^{N}d\hat{\eta}_i^+(t_j)d\hat{\eta}_i^-(t_j)\,e^{\mathcal{S}}\,, \tag{C.22}$$

where the action $\mathcal{S}$ reads

$$\begin{aligned}\mathcal{S}=\sum_{i,j}\Bigg[&\hat{\eta}_i^+(t_j)\left(\eta_i^+(t_{j+1})-\eta_i^+(t_j)\right)+\hat{\eta}_i^-(t_j)\left(\eta_i^-(t_{j+1})-\eta_i^-(t_j)\right)\\
&+\frac{Ddt}{a^2}\Big[\eta_i^+(t_j)(e^{\hat{\eta}_i^+(t_j)-\hat{\eta}_{i+1}^+(t_j)}-1)+\eta_{i+1}^+(t_j)(e^{-\hat{\eta}_i^+(t_j)+\hat{\eta}_{i+1}^+(t_j)}-1)\\
&+\eta_i^-(t_j)(e^{\hat{\eta}_i^-(t_j)-\hat{\eta}_{i+1}^-(t_j)}-1)+\eta_{i+1}^-(t_j)(e^{-\hat{\eta}_i^-(t_j)+\hat{\eta}_{i+1}^-(t_j)}-1)\Big]\\
&+\frac{vdt}{a}\Big[f_h^+(e^{\hat{\eta}_i^+(t_j)-\hat{\eta}_{i+1}^+(t_j)}-1)+f_h^-(e^{-\hat{\eta}_i^-(t_j)+\hat{\eta}_{i+1}^-(t_j)}-1)\Big]\\
&+\gamma dt\Big[f_s^+(e^{\hat{\eta}_i^+(t_j)-\hat{\eta}_i^-(t_j)}-1)+\gamma f_s^-(e^{-\hat{\eta}_i^+(t_j)+\hat{\eta}_i^-(t_j)}-1)\Big]\Bigg]\,,\end{aligned} \tag{C.23}$$

with f_h^+ and f_h^- given by

$$f_h^+=e^{-\lambda\eta_i^+(t_j)-\lambda\eta_i^-(t_j)}\eta_i^+(t_j)\qquad f_h^-=e^{-\lambda\eta_{i+1}^+(t_j)-\lambda\eta_{i+1}^-(t_j)}\eta_{i+1}^-(t_j)\,, \tag{C.24}$$

while f_s^+ and f_s^- reads

$$f_s^+=\eta_i^+(t_j)\left[\Theta\left(3-\eta_i^+(t_j)-\eta_i^-(t_j)\right)e^{-\beta(\eta_i^+(t_j)-\eta_i^-(t_j))}+\Theta\left(\eta_i^+(t_j)+\eta_i^-(t_j)-4\right)\right] \tag{C.25}$$

$$f_s^-=f_s^+\left(\eta_i^+(t_j)\to\eta_i^-(t_j),\,\eta_i^-(t_j)\to\eta_i^+(t_j)\right)\,. \tag{C.26}$$

At this point, while we would like to perform a Taylor expansion of the action at order $o(a)$ and $o(dt)$, we can not do it because $\eta_i^\pm(t_j)$ is an integer and therefore the expressions $\eta_{i+1}^\pm=\eta_i^\pm+\partial_x\eta_i^\pm a$ or $\eta_i^\pm(t_{j+1})=\eta_i^\pm(t_j)+\partial_t\eta_i^\pm dt$ makes no sense. We have to find a way to go to smooth real variables, and to this aim we introduce the Poisson parameters $\rho_i^+(t_j)$ and $\rho_i^-(t_j)$ for $(i,j)\in\{1,..,L\}\times\{1,..,N\}$. In the limit $a\to 0$, we know that the diffusion dominates microscopically, and in this regime the stochastic variables $\eta_i^+(t_j)$ and $\eta_i^-(t_j)$ thus follow a Poisson law whose average we parametrize by $\rho_i^+(t_j)$ and $\rho_i^-(t_j)$.

We now take the mean value of $\mathcal{S}$ with respect to this factorized Poissonian law on the $\eta_i(t_j)$'s

$$\begin{aligned}\langle\mathcal{S}\rangle =&\sum_{i,j}\Bigg[\hat{\eta}_i^+(t_j)\left(\langle\eta_i^+(t_{j+1})-\eta_i^+(t_j)\rangle\right)+\hat{\eta}_i^-(t_j)\left(\langle\eta_i^-(t_{j+1})-\eta_i^-(t_j)\rangle\right)\\&+\frac{Ddt}{a^2}\Big[\langle\eta_i^+(t_j)\rangle(e^{\hat{\eta}_i^+(t_j)-\hat{\eta}_{i+1}^+(t_j)}-1)+\langle\eta_{i+1}^+(t_j)\rangle(e^{-\hat{\eta}_i^+(t_j)+\hat{\eta}_{i+1}^+(t_j)}-1)\\&+\langle\eta_i^-(t_j)\rangle(e^{\hat{\eta}_i^-(t_j)-\hat{\eta}_{i+1}^-(t_j)}-1)+\langle\eta_{i+1}^-(t_j)\rangle(e^{-\hat{\eta}_i^-(t_j)+\hat{\eta}_{i+1}^-(t_j)}-1)\Big]\\&+\frac{vdt}{a}\Big[\langle f_h^+\rangle(e^{\hat{\eta}_i^+(t_j)-\hat{\eta}_{i+1}^+(t_j)}-1)+\langle f_h^-\rangle(e^{-\hat{\eta}_i^-(t_j)+\hat{\eta}_{i+1}^-(t_j)}-1)\Big]\\&+\gamma dt\Big[\langle f_s^+\rangle(e^{\hat{\eta}_i^+(t_j)-\hat{\eta}_i^-(t_j)}-1)+\langle f_s^-\rangle(e^{-\hat{\eta}_i^+(t_j)+\hat{\eta}_i^-(t_j)}-1)\Big]\Bigg]\,. \end{aligned}\tag{C.27}$$

Let us now evaluate the averages appearing in (C.27). For terms linear in η, the average is given by the corresponding Poissonian parameter and we obtain

$$\langle\eta_i^\pm(t_j)\rangle=\rho_i^\pm(t_j)\,,\quad \langle\eta_i^\pm(t_{j+1})\rangle=\rho_i^\pm(t_{j+1})\,,\quad \langle\eta_{i+1}^\pm(t_j)\rangle=\rho_{i+1}^\pm(t_j)\,.\tag{C.28}$$

For $\langle f_h^+\rangle$, we get

$$\langle f_h^+\rangle =\langle\eta_i^+(t_j)e^{-\lambda(\eta_i^-(t_j)+\eta_i^+(t_j))}\rangle\tag{C.29}$$

$$\langle f_h^+\rangle =\sum_{n,k=0}^{\infty}\frac{n\left[\rho_i^+(t_j)\right]^n\left[\rho_i^-(t_j)\right]^k}{n!k!}e^{-\rho_i^+(t_j)-\rho_i^-(t_j)-\lambda(n+k)}\tag{C.30}$$

$$\langle f_h^+\rangle =\rho_i^+(t_j)e^{-\left(\rho_i^+(t_j)+\rho_i^-(t_j)\right)\left(1-e^{-\lambda}\right)-\lambda}=\mathcal{V}(\rho_i^+(t_j),\rho_i^-(t_j))\,,\tag{C.31}$$

where we have defined the function $\mathcal{V}(x,y)=xe^{-(x+y)\left(1-e^{-\lambda}\right)-\lambda}$. Performing a similar computation for $\langle f_h^-\rangle$, we deduce

$$\langle f_h^-\rangle =\mathcal{V}(\rho_{i+1}^-(t_j),\rho_{i+1}^+(t_j))\,.\tag{C.32}$$

Finally, for $\langle f_s^+\rangle$ we compute that

$$\begin{aligned}\langle f_s^+\rangle =&\left\langle\eta_i^+(\tau)\left[\Theta\left[3-\eta_i^+(\tau)-\eta_i^-(\tau)\right]e^{-\beta(\eta_i^+(\tau)-\eta_i^-(\tau))}+\Theta\left[\eta_i^+(\tau)+\eta_i^-(\tau)-4\right]\right]\right\rangle\\=&\sum_{n,k=0}^{n+k\leq 3}\frac{n\left[\rho_i^+(\tau)\right]^n\left[\rho_i^-(\tau)\right]^k}{n!k!}e^{-\rho_i^+(\tau)-\rho_i^-(\tau)-\beta(n-k)}+\sum_{n+k>3}^{\infty}\frac{n\left[\rho_i^+(\tau)\right]^n\left[\rho_i^-(\tau)\right]^k}{k!n!}e^{-\rho_i^+(\tau)-\rho_i^-(\tau)}\\=&\mathcal{U}(\rho_i^+(t_j),\rho_i^-(t_j))\,,\end{aligned}\tag{C.33}$$

where the function $\mathcal{U}(x,y)$ is defined by

$$\mathcal{U}(x,y)=e^{-x-y}\left((e^{-\beta}-1)x+(e^{-2\beta}-1)x^2+\frac{e^{-3\beta}-1}{2}x^3+(e^{-\beta}-1)x^2y+\frac{e^{\beta}-1}{2}xy^2\right)+x\,.$$

The symmetry $+\leftrightarrow-$ then yields $\langle f_s^-\rangle$ as

$$\langle f_s^-\rangle =\mathcal{U}(\rho_i^-(t_j),\rho_i^+(t_j))\tag{C.34}$$

Plugging the averages computed in (C.28) (C.31) (C.32) (C.33) (C.34) into expression (C.27) for $\langle \mathcal{S} \rangle$, we get an action depending on the smooth, real variables $\rho_i^{\pm}(t_j)$

$$\begin{aligned}\langle \mathcal{S} \rangle =& \sum_{i,j} \Big[\hat{\eta}_i^+(t_j) \left(\rho_i^+(t_{j+1}) - \rho_i^+(t_j) \right) + \hat{\eta}_i^-(t_j) \left(\rho_i^-(t_{j+1}) - \rho_i^-(t_j) \right) \\ &+ \frac{Ddt}{a^2} \Big[\rho_i^+(t_j)(e^{\hat{\eta}_i^+(t_j) - \hat{\eta}_{i+1}^+(t_j)} - 1) + \rho_{i+1}^+(t_j)(e^{-\hat{\eta}_i^+(t_j) + \hat{\eta}_{i+1}^+(t_j)} - 1) \\ &+ \rho_i^-(t_j)(e^{\hat{\eta}_i^-(t_j) - \hat{\eta}_{i+1}^-(t_j)} - 1) + \rho_{i+1}^-(t_j)(e^{-\hat{\eta}_i^-(t_j) + \hat{\eta}_{i+1}^-(t_j)} - 1) \Big] \\ &+ \frac{vdt}{a} \Big[\mathcal{V}\left(\rho_i^+(t_j), \rho_i^-(t_j) \right) (e^{\hat{\eta}_i^+(t_j) - \hat{\eta}_{i+1}^+(t_j)} - 1) + \mathcal{V}\left(\rho_{i+1}^-(t_j), \rho_{i+1}^+(t_j) \right) (e^{-\hat{\eta}_i^-(t_j) + \hat{\eta}_{i+1}^-(t_j)} - 1) \Big] \\ &+ \gamma dt \Big[\mathcal{U}\left(\rho_i^+(t_j), \rho_i^-(t_j) \right) (e^{\hat{\eta}_i^+(t_j) - \hat{\eta}_i^-(t_j)} - 1) + \mathcal{U}\left(\rho_i^-(t_j), \rho_i^+(t_j) \right) (e^{-\hat{\eta}_i^+(t_j) + \hat{\eta}_i^-(t_j)} - 1) \Big] \Big] \, . \end{aligned} \tag{C.35}$$

We can now take the limit of continuous time using $\rho_i^{\pm}(t_{j+1}) - \rho_i^{\pm}(t_j) = \dot{\rho}_i^{\pm}(t) dt$ in the above expression. Dropping the time dependence for now on, we assume that the quantities $\rho_i^{\pm}$, $\hat{\eta}_i^{\pm}$ are taken at time t

$$\begin{aligned}\langle \mathcal{S} \rangle =& \int dt \sum_i \Big[\hat{\eta}_i^+ \dot{\rho}_i^+ + \hat{\eta}_i^- \dot{\rho}_i^- + \frac{D}{a^2} \Big[\rho_i^+(e^{\hat{\eta}_i^+ - \hat{\eta}_{i+1}^+} - 1) + \rho_{i+1}^+(e^{-\hat{\eta}_i^+ + \hat{\eta}_{i+1}^+} - 1) \\ &+ \rho_i^-(e^{\hat{\eta}_i^- - \hat{\eta}_{i+1}^-} - 1) + \rho_{i+1}^-(e^{-\hat{\eta}_i^- + \hat{\eta}_{i+1}^-} - 1) \Big] \\ &+ \frac{v}{a} \Big[\mathcal{V}\left(\rho_i^+, \rho_i^- \right) (e^{\hat{\eta}_i^+ - \hat{\eta}_{i+1}^+} - 1) + \mathcal{V}\left(\rho_{i+1}^-, \rho_{i+1}^+ \right) (e^{-\hat{\eta}_i^- + \hat{\eta}_{i+1}^-} - 1) \Big] \\ &+ \gamma \Big[\mathcal{U}\left(\rho_i^+, \rho_i^- \right) (e^{\hat{\eta}_i^+ - \hat{\eta}_i^-} - 1) + \mathcal{U}\left(\rho_i^-, \rho_i^+ \right) (e^{-\hat{\eta}_i^+ + \hat{\eta}_i^-} - 1) \Big] \Big] \, . \end{aligned} \tag{C.36}$$

We can now make the following change of variables

$$\rho_i = \rho_i^+ + \rho_i^- \qquad m_i = \rho_i^+ - \rho_i^- \qquad \hat{\rho}_i = \frac{\hat{\eta}_i^+ + \hat{\eta}_i^-}{2} \qquad \hat{m}_i = \frac{\hat{\eta}_i^+ - \hat{\eta}_i^-}{2} \, . \tag{C.37}$$

In these new set of variables the actions $\mathcal{S}$ reads

$$\begin{aligned}\langle \mathcal{S} \rangle =& \int_0^T dt \sum_i \Big[\hat{\rho}_i \dot{\rho}_i + \hat{m}_i \dot{m}_i + \frac{D}{a^2} \rho_{i+1} (e^{-\hat{\rho}_i - \hat{m}_i + \hat{\rho}_{i+1} + \hat{m}_{i+1}} + e^{-\hat{\rho}_i + \hat{m}_i + \hat{\rho}_{i+1} - \hat{m}_{i+1}} - 2) \\ &+ \frac{D}{a^2} \rho_i (e^{\hat{\rho}_i + \hat{m}_i - \hat{\rho}_{i+1} - \hat{m}_{i+1}} + e^{\hat{\rho}_i - \hat{m}_i - \hat{\rho}_{i+1} + \hat{m}_{i+1}} - 2) + \frac{D}{a^2} m_i (e^{\hat{\rho}_i + \hat{m}_i - \hat{\rho}_{i+1} - \hat{m}_{i+1}} - e^{\hat{\rho}_i - \hat{m}_i - \hat{\rho}_{i+1} + \hat{m}_{i+1}}) \\ &+ \frac{D}{a^2} m_{i+1} (e^{-\hat{\rho}_i - \hat{m}_i + \hat{\rho}_{i+1} + \hat{m}_{i+1}} - e^{-\hat{\rho}_i + \hat{m}_i + \hat{\rho}_{i+1} - \hat{m}_{i+1}}) + \frac{v}{a} \mathcal{V}\left(\frac{\rho_i + m_i}{2}, \frac{\rho_i - m_i}{2} \right) (e^{\hat{\rho}_i + \hat{m}_i - \hat{\rho}_{i+1} - \hat{m}_{i+1}} - 1) \\ &+ \frac{v}{a} \mathcal{V}\left(\frac{\rho_{i+1} - m_{i+1}}{2}, \frac{\rho_{i+1} + m_{i+1}}{2} \right) (e^{\hat{\rho}_{i+1} - \hat{m}_{i+1} - \hat{\rho}_i + \hat{m}_i} - 1) \\ &+ \gamma \, \mathcal{U}\left(\frac{\rho_i + m_i}{2}, \frac{\rho_i - m_i}{2} \right) (e^{\hat{m}_i} - 1) + \gamma \, \mathcal{U}\left(\frac{\rho_i - m_i}{2}, \frac{\rho_i + m_i}{2} \right) (e^{-\hat{m}_i} - 1) \, . \end{aligned} \tag{C.38}$$

Before taking the limit of continuous space in the action $\langle \mathcal{S} \rangle$, we need to perform a Taylor expansion of the fields using

$$\begin{aligned} \rho_{i+i} =& \rho_i + a\partial_x \rho_i + \frac{a^2}{2} \partial_{xx} \rho_i + o(a^2) \qquad & m_{i+i} =& m_i + a\partial_x m_i + \frac{a^2}{2} \partial_{xx} m_i + o(a^2) \\ \hat{\rho}_{i+i} =& \hat{\rho}_i + a\partial_x \hat{\rho}_i + \frac{a^2}{2} \partial_{xx} \hat{\rho}_i + o(a^2) \qquad & \hat{m}_{i+i} =& \hat{m}_i + a\partial_x \hat{m}_i + \frac{a^2}{2} \partial_{xx} \hat{m}_i + o(a^2) \, . \end{aligned}$$

Plugging the above expansions into (C.38), we are now ready to take the limit $a \to 0$. We obtain

$$\langle \mathcal{S} \rangle = \frac{1}{a} \int_0^L \int_0^T S[\rho, m, \hat{\rho}, \hat{m}] dt dx + o(a^{-1}) \ , \tag{C.39}$$

where $S[\rho, m, \hat{\rho}, \hat{m}]$ is given by

$$\begin{aligned} S = {} & \hat{\rho}\dot{\rho} + \hat{m}\dot{m} + D\nabla\hat{\rho}\nabla\rho + D\nabla\hat{m}\nabla m + \frac{D}{2}\rho\left[(\nabla\hat{\rho} + \nabla\hat{m})^2 + (\nabla\hat{\rho} - \nabla\hat{m})^2\right] \\ & + \frac{D}{2}m\left[(\nabla\hat{\rho} + \nabla\hat{m}))^2 - (\nabla\hat{\rho} - \nabla\hat{m})^2\right] + \gamma\,\mathcal{U}\left(\frac{\rho+m}{2}, \frac{\rho-m}{2}\right)(e^{\hat{m}} - 1) \\ & - v\nabla\hat{m}\left[\mathcal{V}\left(\frac{\rho+m}{2}, \frac{\rho-m}{2}\right) + \mathcal{V}\left(\frac{\rho-m}{2}, \frac{\rho+m}{2}\right)\right] + \gamma\,\mathcal{U}\left(\frac{\rho-m}{2}, \frac{\rho+m}{2}\right)(e^{-\hat{m}} - 1) \\ & - v\nabla\hat{\rho}\left[\mathcal{V}\left(\frac{\rho+m}{2}, \frac{\rho-m}{2}\right) - \mathcal{V}\left(\frac{\rho-m}{2}, \frac{\rho+m}{2}\right)\right] \ . \end{aligned} \tag{C.40}$$

We can further simplify the integrand S by using the expression of $\mathcal{V}$

$$\begin{aligned} S = {} & \hat{\rho}\dot{\rho} + \hat{m}\dot{m} + D\nabla\hat{\rho}\nabla\rho + D\nabla\hat{m}\nabla m + \frac{D}{2}\rho\left[(\nabla\hat{\rho} + \nabla\hat{m})^2 + (\nabla\hat{\rho} - \nabla\hat{m})^2\right] \\ & + \frac{D}{2}m\left[(\nabla\hat{\rho} + \nabla\hat{m}))^2 - (\nabla\hat{\rho} - \nabla\hat{m})^2\right] - v\rho\ e^{-\rho(1-e^{-\lambda})-\lambda}\nabla\hat{m} - vm\ e^{-\rho(1-e^{-\lambda})-\lambda}\nabla\hat{\rho} \\ & + \gamma\,\mathcal{U}\left(\frac{\rho+m}{2}, \frac{\rho-m}{2}\right)(e^{\hat{m}} - 1) + \gamma\,\mathcal{U}\left(\frac{\rho-m}{2}, \frac{\rho+m}{2}\right)(e^{-\hat{m}} - 1) \ . \end{aligned} \tag{C.41}$$

We are now ready to deduce the hydrodynamics of our microscopic model. Because we took the regime $a \to 0$, we just have to do a saddle-point of the above integrand S to get the evolution equations for ρ and m. The hydrodynamics is obtained from minimizing (C.41) with respect to $\hat{m}$ and $\hat{\rho}$

$$\frac{\delta S}{\delta\hat{\rho}} = 0 \qquad \frac{\delta S}{\delta\hat{m}} = 0 \qquad \frac{\delta S}{\delta\rho} = 0 \qquad \frac{\delta S}{\delta m} = 0 \ . \tag{C.42}$$

Conditions $\delta S/\delta\rho = \delta S/\delta m = 0$ are met for constant homogeneous fields $\hat{\rho} = \hat{m} = 0$ while, for such fields, $\delta S/\delta\hat{\rho} = 0$ and $\delta S/\delta\hat{m} = 0$ yields the sought after hydrodynamics for ρ and m

$$\partial_t\rho = D\nabla^2\rho - \nabla(vm\ e^{-\rho(1-e^{-\lambda})-\lambda}) \tag{C.43}$$

$$\begin{aligned} \partial_t m = {} & D\nabla^2 m - \nabla(v\rho\ e^{-\rho(1-e^{-\lambda})-\lambda}) - \gamma m\ e^{-\rho}\Big[\left(e^{-\beta} - 1\right) + \left(e^{-2\beta} - 1\right)\rho \\ & + \left(3e^{-3\beta} + 2e^{-\beta} - e^{\beta} - 4\right)\frac{\rho^2}{8}\Big] - \gamma\ m^3 e^{-\rho}\ \frac{e^{-3\beta}}{8}\left(e^{2\beta} - 1\right)^2 - \gamma m \ , \end{aligned} \tag{C.44}$$

which correspond to (4.34) and (4.35) of main text. Note that the coarse-graining method employed in this section is very generic and can be applied to a very broad class of lattice models. The key assumption is the existence of a stochastic process which dominates the dynamics as $a \to 0$: in our case, the diffusion dominate. As long as the measure associated to this dominant stochastic process is factorized and parametrized by on-site real variables, the coarse-graining can be performed. In our case, this measure is the poisson law parametrized by $\rho_i^{\pm}$ the averaged number of particles at site i. For example, we could apply this coarse-graining procedure to exclusion processes, in which

exchanging neighboring particles replaces diffusion as the dominant stochastic dynamics in the limit $a \to 0$. In this case, the associated dominant measure is a product of Bernoulli distributions indexed by real parameters representing the averaged number of particles at site i. Using the procedure presented in this section, we could then rederive the results of [148] for the exclusion process. Note also that, from (C.38), we could derive the microscopic Gaussian fluctuations of the field ρ and m by developing $\langle \mathcal{S} \rangle$ to the next order in a.

C.2 Numerical methods for lattice gas

In this appendix, we detail the simulations of the active lattice gas dynamics RI-RII-RIII which were used to obtain Fig. 4.14. We used a random sequential update with discretized time and $N \sim 2 \times 10^5$ particles. At each time step dt, we repeat N times the following chain of instructions

LI Draw a particle uniformly

LII Draw a float uniformly between 0 and 1

LIII Update the position and spin of the particle according to the stochastic dynamic RI-RII-RIII

Note that, in Fig. 4.14, the lattice size is of order $a \sim 0.0025$ while the total length is $L = 400$: there is thus a high number of sites $N_{sites} \sim 2 \times 10^5$. Furthermore, we had to impose very small time step $dt \sim 10^{-6}$ in order to keep the probabilty $Da^{-2}dt$ of a diffusive move RI of order 1. As the diffusion rate $Da^{-2} \sim 1.6 \times 10^5$ dominates the flipping rate $\gamma \sim 1$ by five orders of magnitude, we are close to the limit where the random float drawn in LII never triggers a spin flip in LIII due to lack of numerical precision. The issue is the following: the generator of random numbers cannot accurately restitute a binary distribution of probability p_1 and $1 - p_1$ when $p_1/(1 - p_1) \lesssim 10^{-10}$. Therefore, drawing two random numbers, one for selecting a particle LI and one for choosing its move LII is crucial in this algorithm. If instead we draw a unique random float, and extract its first $N \sim 2 \times 10^5$ decimals for selecting a particle before using its remaining part to choose a move in LIII, the algorithm is inconsistently producing a dynamics without spin flips.

D. Scale-free correlations in anisotropic systems

D.1 Derivation of the density correlations under confinement

This appendix is devoted to the computation of the density correlation $\langle \delta\rho(\mathbf{x},t)\delta\rho(0,t)\rangle$ induced by the dynamics

$$\partial_t \delta\rho = \boldsymbol{\nabla}\cdot[\boldsymbol{\Lambda}] + \frac{D}{2}\boldsymbol{\nabla}^2\delta\rho \,, \tag{D.1}$$

with no-flux boundary conditions in the $\perp$ direction and periodic boundary conditions in the $\parallel$ direction. We recall that the Gaussian noise $\boldsymbol{\Lambda}$ in (D.1) satisifies

$$\langle \Lambda^\alpha(\mathbf{r},t)\Lambda^\beta(\mathbf{r}',t')\rangle = \left[D\delta^{\alpha\beta}\rho_b\delta(\mathbf{r}-\mathbf{r}') + h_\alpha h_0(\mathbf{r}-\mathbf{r}')\delta^{\alpha\beta}\rho_b^2\right]\delta(t-t') \,. \tag{D.2}$$

We consider a domain of size $L_\perp \times L_\parallel$ with $L_\parallel \gg L_\perp$ and decompose $\delta\rho(\mathbf{x},t)$ on its discrete and continuous Fourier modes in the $\perp$ direction and $\parallel$ directions, respectively. The boundary conditions on the field ρ are $\delta\rho(x_\perp,0,t) = \delta\rho(x_\perp,L_\parallel,t)$ and $\partial_\perp\delta\rho(0,x_\parallel,t) = \partial_\perp\delta\rho(L_\perp,x_\parallel,t) = 0$. Since $\delta\rho$ need not be a periodic function of $x_\perp$, we formally extend its definition by parity as $\delta\rho(-x_\perp,x_\parallel,t) = \delta\rho(x_\perp,x_\parallel,t)$. $\delta\rho$ then becomes a periodic function on the domain $[-L_\perp,L_\perp]\times[0,L_\parallel]$ and we decompose it as

$$\delta\rho(\mathbf{x},t) = \int \frac{e^{ikx_\parallel}dk}{2\pi}\int\frac{e^{-iwt}dw}{2\pi}\sum_{n=0}^{\infty}\mathcal{N}_n\, A_{q_n,k,w}\cos(q_n x_\perp) \,, \tag{D.3}$$

where $q_n = n\pi/L_\perp$, $\mathcal{N}_n = 1-\delta_{n,0}/2$ and $A_{q_n,k,w}$ is given by

$$A_{q_n,k,w} = \int e^{-ikx_\parallel}dx_\parallel \int e^{iwt}dt\,\frac{1}{L_\perp}\int_{-L_\perp}^{L_\perp}\cos(q_n x_\perp)\delta\rho(x_\perp,x_\parallel,t)dx_\perp \,. \tag{D.4}$$

Note that only the cosine modes enter (D.3) to ensure the no-flux boundary conditions $\partial_\perp\delta\rho(0,x_\parallel,t) = \partial_\perp\delta\rho(L_\perp,x_\parallel,t) = 0$. Outside (D.3), we will consider the restriction of $\delta\rho$ to the domain $[0,L_\perp]$: our results will be unaffected by this formal extension.

Similarly, we project $\boldsymbol{\nabla}\cdot\boldsymbol{\Lambda}$ on its Fourier modes as

$$\boldsymbol{\nabla}\cdot\boldsymbol{\Lambda}(\mathbf{x},t) = \int \frac{e^{ikx_\parallel}dk}{2\pi}\int\frac{e^{-iwt}dw}{2\pi}\sum_{n=0}^{\infty}\mathcal{N}_n\,\Lambda_{q_n,k,w}\cos(q_n x_\perp) \,, \tag{D.5}$$

where $\Lambda_{q_n,k,w}$ is given by

$$\Lambda_{q_n,k,w} = \int e^{-ikx_\parallel}dx_\parallel \int e^{iwt}dt\,\frac{1}{L_\perp}\int_{-L_\perp}^{L_\perp}\cos(q_n x_\perp)\boldsymbol{\nabla}\cdot\boldsymbol{\Lambda}(x_\perp,x_\parallel,t)dx_\perp \,. \tag{D.6}$$

As for $A_{q_n,k,w}$ in (D.4), note that the integral over $x_\perp$ in (D.6) runs from $-L_\perp$ to $L_\perp$: we have formally extended $\boldsymbol{\nabla}\cdot\boldsymbol{\Lambda}$ to the domain $[-L_\perp,0]$ by parity taking $\boldsymbol{\Lambda}(x_\parallel,-x_\perp,t) =$

$\mathbf{\Lambda}(x_\parallel, x_\perp, t)$. Inserting (D.3) and (D.5) into the time-evolution for $\delta\rho$ (D.1), we obtain the $A_{q_n,k,w}$ as a function of the $\Lambda_{q_n,k,w}$

$$A_{q_n,k,w} = \frac{\Lambda_{q_n,k,w}}{-iw + \frac{D}{2}(k^2+q_n^2)} \,. \tag{D.7}$$

Using (D.7) into (D.3), we express the correlator $\langle \delta\rho(\mathbf{x},t)\delta\rho(0,t)\rangle$ as

$$\langle \delta\rho(\mathbf{x},t)\delta\rho(0,t)\rangle = \int e^{ikx_\parallel}\frac{dkdk'}{(2\pi)^2}\int e^{-iwt-iw't}\frac{dwdw'}{(2\pi)^2}\sum_{n,n'=0}^{\infty} \mathcal{N}_n\mathcal{N}_{n'}\cos(q_n x_\perp)\frac{\langle \Lambda_{q_n,k,w}\Lambda_{q_{n'},k',w'}\rangle}{\left(-iw+\frac{D}{2}(k^2+q_n^2)\right)\left(-iw'+\frac{D}{2}(k'^2+q_{n'}^2)\right)} \,. \tag{D.8}$$

To close the above expression, we need to compute $\langle \Lambda_{q_n,k,w}\Lambda_{q_{n'},k',w'}\rangle$. As a starting point, we perform an integration by parts in (D.6) to obtain

$$\Lambda_{q_n,k,w} = \int dx_\parallel dt \frac{e^{iwt-ikx_\parallel}}{L_\perp}\int_{-L_\perp}^{L_\perp}\left[ik\cos(q_n x_\perp)\Lambda^\parallel(x_\perp,x_\parallel,t) + q_n\sin(q_n x_\perp)\Lambda^\perp(x_\perp,x_\parallel,t)\right]dx_\perp \,. \tag{D.9}$$

We now multiply $\Lambda_{q_n,k,w}$ by $\Lambda_{q_{n'},k',w'}$, use (D.9), and take the average by inserting (D.2). This tedious but straightforward computation leads to

$$\langle \Lambda_{q_n,k,w}\Lambda_{q_{n'},k',w'}\rangle = (2\pi)^2\delta(k+k')\delta(w+w')\delta_{n,n'}\mathcal{N}_n \left[\frac{\rho_b D}{L_\perp}(k^2+q_n^2) + \rho_b^2\sigma^3 c_n(h_\parallel k^2 + h_\perp q_n^2)e^{-\frac{k^2\sigma^2}{2}}\right] \,, \tag{D.10}$$

where c_n is the n-th Fourier coefficient of the function $h_0(x_\perp)$:

$$c_n = \frac{1}{L_\perp}\int_{-L_\perp}^{L_\perp}\cos(q_n x_\perp)\frac{1}{\sqrt{2\pi}}e^{-\frac{x_\perp^2}{2\sigma^2}}dx_\perp \,. \tag{D.11}$$

In the limit $L_\perp \gg \sigma$, the bound in the above integral can be extended to $\pm\infty$ and we obtain $c_n \simeq \sigma\exp(-q_n^2\sigma^2/2)/L_\perp$. Injecting this approximation in (D.10), we obtain

$$\langle \Lambda_{q_n,k,w}\Lambda_{q_{n'},k',w'}\rangle = (2\pi)^2\delta(k+k')\delta(w+w')\frac{\delta_{n,n'}\mathcal{N}_n}{L_\perp} \left[\rho_b D(k^2+q_n^2) + \rho_b^2(h_\parallel k^2 + h_\perp q_n^2)h_0(k,q_n)\right] \,, \tag{D.12}$$

where we have used the definition of the function $h_0(\mathbf{k})$, *ie* $h_0(k,q) = \sigma^4 e^{-\frac{(k^2+q^2)\sigma^2}{2}}$. Inserting expression (D.12) into (D.8) gives the correlator as

$$\langle \delta\rho(\mathbf{x},t)\delta\rho(0,t)\rangle = \int\frac{dk}{2\pi}\int\frac{dw}{2\pi}\frac{e^{ikx_\parallel}}{L_\perp}\sum_{n=0}^{\infty} \mathcal{N}_n\cos(q_n x_\perp)\frac{\rho_b D(k^2+q_n^2) + \rho_b^2(h_\parallel k^2+h_\perp q_n^2)h_0(k,q_n)}{\left[w - i\frac{D}{2}(k^2+q_n^2)\right]\left[w + i\frac{D}{2}(k^2+q_n^2)\right]} \,.$$

Performing the integral over w using Cauchy residu theorem yields

$$\langle \delta\rho(\mathbf{x},t)\delta\rho(0,t)\rangle = \int \frac{dk}{2\pi}\frac{e^{ikx_\parallel}}{L_\perp}\sum_{n=0}^{\infty}\mathcal{N}_n\cos(q_n x_\perp)\left[\rho_b + \frac{\rho_b^2}{D}\frac{(h_\parallel k^2 + h_\perp q_n^2)h_0(k,q_n)}{k^2+q_n^2}\right] . \tag{D.13}$$

As described in section 5.1, we must take into account a volume-dependent correction for finite-size systems. In this appendix, we follow a path different from the one in section 5.1 and determine this correction by enforcing mass conservation. To this aim, we will check mass conservation in (D.13) by integrating $\langle \delta\rho(\mathbf{x},t)\delta\rho(0,t)\rangle$. As we have extended $\delta\rho$ to the domain $[-L_\perp, 0]$ by parity, we can perform this integration in the whole domain $[-L_\perp, L_\perp]\times[0, L_\parallel]$. Mass conservation thus reads

$$\int_{-L_\perp}^{L_\perp}\int_0^{L_\parallel}\langle \delta\rho(\mathbf{x},t)\delta\rho(0,t)\rangle dx_\perp dx_\parallel = 0 . \tag{D.14}$$

The second term on the right-hand side of (D.13) can be written as a full derivative

$$\int \frac{dk}{2\pi}\frac{e^{ikx_\parallel}}{L_\perp}\sum_{n=0}^{\infty}\mathcal{N}_n\cos(q_n x_\perp)\frac{\rho_b^2}{D}\frac{h_\parallel k^2 + h_\perp q_n^2}{k^2+q_n^2}h_0(k,q_n) = -(h_\parallel\partial_\parallel^2 + h_\perp\partial_\perp^2)f(x_\parallel, x_\perp) ,$$

where $f(x_\parallel, x_\perp)$ is given by

$$f(x_\parallel, x_\perp) = \int \frac{dk}{2\pi}\frac{e^{ikx_\parallel}}{L_\perp}\sum_{n=0}^{\infty}\mathcal{N}_n\cos(q_n x_\perp)\frac{\rho_b^2}{D}\frac{h_0(k,q_n)}{k^2+q_n^2} . \tag{D.15}$$

As the function f is periodic on the domain $[-L_\perp, L_\perp]\times[0, L_\parallel]$, its integral will vanish. The integral of $\langle \delta\rho(\mathbf{x})\delta\rho(0)\rangle$ is thus given by

$$\int_{-L_\perp}^{L_\perp}\int_0^{L_\parallel}\langle \delta\rho(\mathbf{x},t)\delta\rho(0,t)\rangle dx_\perp dx_\parallel = \int_{-L_\perp}^{L_\perp}\int_0^{L_\parallel}\int \frac{dk}{2\pi}\frac{e^{ikx_\parallel}}{L_\perp}\sum_{n=0}^{\infty}\mathcal{N}_n\cos(q_n x_\perp)\rho_b \tag{D.16}$$

$$= \rho_b . \tag{D.17}$$

Comparing (D.17) to (D.14), we note that we have to subtract $\rho_b/(2L_\parallel L_\perp)$ from $\langle \delta\rho(\mathbf{x})\delta\rho(0)\rangle$ as expressed in (D.13) to ensure mass conservation. We thus deduce the expression of the density correlator as

$$\langle \delta\rho(\mathbf{x},t)\delta\rho(0,t)\rangle = \int \frac{dk}{2\pi}\frac{e^{ikx_\parallel}}{L_\perp}\sum_{n=0}^{\infty}\mathcal{N}_n\cos(q_n x_\perp)\left[\rho_b + \frac{\rho_b^2}{D}\frac{(h_\parallel k^2 + h_\perp q_n^2)h_0(k,q_n)}{k^2+q_n^2}\right] - \frac{\rho_b}{2L_\perp L_\parallel} . \tag{D.18}$$

Finally, we note that the Fourier transform $c_{n,k}$ of a Dirac distribution is given by

$$c_{n,k} = \int dx_\parallel e^{-ikx_\parallel}\int_{-L_\perp}^{L_\perp}\frac{\mathcal{N}_n}{L_\perp}\cos(q_n x_\perp)\delta(x_\parallel)\delta(x_\perp) = \frac{\mathcal{N}_n}{L_\perp} , \tag{D.19}$$

so that

$$\delta(x_\parallel)\delta(x_\perp) = \int \frac{dk}{2\pi}\frac{e^{ikx_\parallel}}{L_\perp}\sum_{n=0}^{\infty}\mathcal{N}_n\cos(q_n x_\perp) . \tag{D.20}$$

Inserting (D.20) in (D.18), we obtain the final form of the two-point function as

$$\langle \delta\rho(\mathbf{x},t)\delta\rho(0,t)\rangle = \int \frac{dk}{2\pi}\frac{e^{ikx_\parallel}}{L_\perp}\sum_{n=0}^{\infty}\mathcal{N}_n\cos(q_n x_\perp)\left[\frac{\rho_b^2}{D}\frac{(h_\parallel k^2 + h_\perp q_n^2)h_0(k,q_n)}{k^2+q_n^2}\right]$$
$$+ \rho_b\,\delta(\mathbf{x}) - \frac{\rho_b}{2L_\perp L_\parallel} . \tag{D.21}$$

D.2 Derivation of the sum involved in the local pressure

In this appendix, we derive (5.99) of main text. To this aim, we will use the Poisson summation formula which state that

$$\sum_{n\in\mathbb{Z}} f(na) = \frac{1}{a}\sum_{n\in\mathbb{Z}}\int_{-\infty}^{\infty} dx f(x) e^{-i\frac{2\pi n}{a}x} , \tag{D.22}$$

for any function f and scalar a. We want to compute $\sum_{n\geq 1} 2\mathcal{N}_n(-1)^n b_n$ where the sequence b_n is given by

$$b_n = \int \frac{dk}{2\pi}\frac{1}{2L_\perp}\left[\frac{(h_\parallel k^2 + h_\perp q_n^2)h_0(k,q_n)}{k^2+q_n^2}\right] , \tag{D.23}$$

with $q_n = n\pi/L_\perp$ and $h_0(k,q) = \sigma^4 e^{-\frac{(k^2+q^2)\sigma^2}{2}}$. We first note that b_n is a sequence of positive terms such that $b_n = b_{-n}$. Using the definition $\mathcal{N}_n = 1-\delta_{n,0}/2$, we can recast the sum over $n\geq 1$ into a sum over $n\in\mathbb{Z}$:

$$\sum_{n\geq 1}^{\infty} 2\mathcal{N}_n(-1)^n b_n = \sum_{n\in\mathbb{Z}}(-1)^n b_n . \tag{D.24}$$

We can further express the alternating series in terms of series of constant sign as

$$\sum_{n\in\mathbb{Z}}(-1)^n b_n = \sum_{n\in\text{even}} b_n - \sum_{n\in\text{odd}} b_n = 2\sum_{n\in\mathbb{Z}} b_{2n} - \sum_{n\in\mathbb{Z}} b_n . \tag{D.25}$$

Inserting (D.25) into (D.24), we obtain

$$\sum_{n\geq 1} 2\mathcal{N}_n(-1)^n b_n = 2\sum_{n\in\mathbb{Z}} b_{2n} - \sum_{n\in\mathbb{Z}} b_n . \tag{D.26}$$

Let us now apply the Poisson summation formula (D.22) with $a=\pi/L_\perp$ to the second term on the right-hand side of (D.26). We obtain

$$\sum_{n\in\mathbb{Z}} b_n = \sum_{n\in\mathbb{Z}}\int \frac{dk}{2\pi}\frac{dq}{2\pi} e^{-2iL_\perp nq}\left[\frac{(h_\parallel k^2 + h_\perp q^2)h_0(k,q)}{k^2+q^2}\right] . \tag{D.27}$$

We note that we have already computed the integral on the right-hand side of (D.27) in expression (5.62) of main text. Using this result, we get

$$\sum_{n\in\mathbb{Z}} b_n = \sum_{n\in\mathbb{Z}}\frac{\sigma^2}{2\pi}\left[\frac{\sigma^2(h_\parallel - h_\perp)}{4L_\perp^2 n^2}\left(1-e^{-\frac{2L_\perp^2 n^2}{\sigma^2}}\right) + h_\perp e^{-\frac{2L_\perp^2 n^2}{\sigma^2}}\right] . \tag{D.28}$$

Similar arguments allow us to compute the first term on the right-hand side of (D.26) as

$$2\sum_{n\in\mathbb{Z}} b_{2n} = \sum_{n\in\mathbb{Z}}\frac{\sigma^2}{2\pi}\left[\frac{\sigma^2(h_\parallel - h_\perp)}{L_\perp^2 n^2}\left(1-e^{-\frac{L_\perp^2 n^2}{2\sigma^2}}\right) + h_\perp e^{-\frac{L_\perp^2 n^2}{2\sigma^2}}\right] . \tag{D.29}$$

Inserting (D.28) and (D.29) in (D.26), we obtain

$$\sum_{n\geq 1} 2\mathcal{N}_n(-1)^n b_n = \sum_{n\in\mathbb{Z}}\frac{\sigma^4}{2\pi}\left[\frac{h_\parallel - h_\perp}{4L_\perp^2 n^2}\left(3-4e^{-\frac{L_\perp^2 n^2}{2\sigma^2}} - e^{-\frac{2L_\perp^2 n^2}{\sigma^2}}\right) + \frac{h_\perp}{\sigma^2}\left(e^{-\frac{L_\perp^2 n^2}{2\sigma^2}} - e^{-\frac{2L_\perp^2 n^2}{\sigma^2}}\right)\right] . \tag{D.30}$$

In the above expression, the only divergent term in the series on the right-hand side is the term $n = 0$. To regularize (D.30), we neglect this term and recast the sum in the positive integers:

$$\sum_{n\geq 1} 2\mathcal{N}_n(-1)^n b_n = \sum_{n=1}^{\infty} \frac{\sigma^4}{\pi}\left[\frac{h_\parallel - h_\perp}{4L_\perp^2 n^2}\left(3 - 4e^{-\frac{L_\perp^2 n^2}{2\sigma^2}} + e^{-\frac{2L_\perp^2 n^2}{\sigma^2}}\right) + \frac{h_\perp}{\sigma^2}\left(e^{-\frac{L_\perp^2 n^2}{2\sigma^2}} - e^{-\frac{2L_\perp^2 n^2}{\sigma^2}}\right)\right].$$

Using that $\sum_{n=1}^{\infty} 1/n^2 = \pi^2/6$, we finally obtain (5.99) of main text:

$$\begin{aligned}\sum_{n\geq 1} 2\mathcal{N}_n(-1)^n b_n =& \frac{\sigma^4(h_\parallel - h_\perp)\pi}{8L_\perp^2} + \frac{\sigma^4(h_\parallel - h_\perp)}{4\pi L_\perp^2}\sum_{n=1}^{\infty}\frac{1}{n^2}\left[e^{-\frac{2L_\perp^2 n^2}{\sigma^2}} - 4e^{-\frac{L_\perp^2 n^2}{2\sigma^2}}\right] \\ &+ \frac{\sigma^2 h_\perp}{\pi}\left[\Theta_3\left(0, e^{-\frac{L_\perp^2}{2\sigma^2}}\right) - \Theta_3\left(0, e^{-\frac{2L_\perp^2}{\sigma^2}}\right)\right], \end{aligned} \tag{D.31}$$

where $\Theta_3(u, v) = 1 + 2\sum_{n\geq 1} v^{n^2}\cos(2nu)$ is the third elliptic function.

Bibliography

[1] Gatien Verley, K Mallick, and D Lacoste. Modified fluctuation-dissipation theorem for non-equilibrium steady states and applications to molecular motors. EPL (Europhysics Letters), 93(1):10002, 2011.

[2] David Andrieux and Pierre Gaspard. Fluctuation theorems and the nonequilibrium thermodynamics of molecular motors. Physical Review E, 74(1):011906, 2006.

[3] Frank Jülicher, Armand Ajdari, and Jacques Prost. Modeling molecular motors. Reviews of Modern Physics, 69(4):1269, 1997.

[4] Volker Schaller, Christoph Weber, Christine Semmrich, Erwin Frey, and Andreas R Bausch. Polar patterns of driven filaments. Nature, 467(7311):73–77, 2010.

[5] É Fodor, M Guo, NS Gov, P Visco, DA Weitz, and F van Wijland. Activity-driven fluctuations in living cells. EPL (Europhysics Letters), 110(4):48005, 2015.

[6] FS Gnesotto, Federica Mura, Jannes Gladrow, and Chase P Broedersz. Broken detailed balance and non-equilibrium dynamics in living systems: a review. Reports on Progress in Physics, 81(6):066601, 2018.

[7] Daisuke Mizuno, Catherine Tardin, C. F. Schmidt, and F. C. MacKintosh. Nonequilibrium mechanics of active cytoskeletal networks. Science, 315(5810):370–373, 2007.

[8] Andrea Cavagna and Irene Giardina. Bird flocks as condensed matter. Annual Review of Condensed Matter Physics, 5(1):183–207, 2014.

[9] M. Ballerini, N. Cabibbo, R. Candelier, A. Cavagna, E. Cisbani, I. Giardina, V. Lecomte, A. Orlandi, G. Parisi, A. Procaccini, M. Viale, and V. Zdravkovic. Interaction ruling animal collective behavior depends on topological rather than metric distance: Evidence from a field study. Proceedings of the National Academy of Sciences, 105(4):1232–1237, 2008.

[10] Rama Cont and Jean-Philipe Bouchaud. Herd behavior and aggregate fluctuations in financial markets. Macroeconomic dynamics, 4(2):170–196, 2000.

[11] Jean-Philippe Bouchaud, Yuval Gefen, Marc Potters, and Matthieu Wyart. Fluctuations and response in financial markets: the subtle nature ofrandom'price changes. Quantitative finance, 4(2):176, 2003.

[12] Giovanni Gallavotti and Ezechiel Godert David Cohen. Dynamical ensembles in nonequilibrium statistical mechanics. Physical review letters, 74(14):2694, 1995.

[13] Jorge Kurchan. Fluctuation theorem for stochastic dynamics. Journal of Physics A: Mathematical and General, 31(16):3719, 1998.

[14] Christopher Jarzynski. Nonequilibrium equality for free energy differences. Physical Review Letters, 78(14):2690, 1997.

[15] Gianmaria Falasco and Marco Baiesi. Temperature response in nonequilibrium stochastic systems. EPL, 113(2):20005, 2016.

[16] C. Maes, S. Safaverdi, P. Visco, and F. van Wijland. Fluctuation-response relations for nonequilibrium diffusions with memory. Phys. Rev. E, 87:022125, 2013.

[17] J. Prost, J.-F. Joanny, and J. M. R. Parrondo. Generalized fluctuation-dissipation theorem for steady-state systems. Phys. Rev. Lett., 103:090601, 2009.

[18] GS Agarwal. Fluctuation-dissipation theorems for systems in non-thermal equilibrium and applications. Zeitschrift für Physik, 252(1):25–38, 1972.

[19] M Cristina Marchetti, Jean-François Joanny, Sriram Ramaswamy, Tanniemola B Liverpool, Jacques Prost, Madan Rao, and R Aditi Simha. Hydrodynamics of soft active matter. Reviews of Modern Physics, 85(3):1143, 2013.

[20] Sriram Ramaswamy. The mechanics and statistics of active matter. Annu. Rev. Condens. Matter Phys., 1(1):323–345, 2010.

[21] Étienne Fodor and M. C Marchetti. The statistical physics of active matter: From self-catalytic colloids to living cells. Physica A, 504:106–120, 2018.

[22] AI Curatolo, N Zhou, Y Zhao, C Liu, A Daerr, J Tailleur, and J Huang. Cooperative pattern formation in multi-component bacterial systems through reciprocal motility regulation. Nature Physics, 16(11):1152–1157, 2020.

[23] Guannan Liu, Adam Patch, Fatmagul Bahar, David Yllanes, Roy D Welch, M Cristina Marchetti, Shashi Thutupalli, and Joshua W Shaevitz. A motility-induced phase transition drives myxococcus xanthus aggregation. arXiv preprint arXiv:1709.06012, 2017.

[24] Hervé Turlier, Dmitry A Fedosov, Basile Audoly, Thorsten Auth, Nir S Gov, Cécile Sykes, J-F Joanny, Gerhard Gompper, and Timo Betz. Equilibrium physics breakdown reveals the active nature of red blood cell flickering. Nature physics, 12(5):513–519, 2016.

[25] Claudio Maggi, Matteo Paoluzzi, Nicola Pellicciotta, Alessia Lepore, Luca Angelani, and Roberto Di Leonardo. Generalized energy equipartition in harmonic oscillators driven by active baths. Physical review letters, 113(23):238303, 2014.

[26] Andrea Cavagna, Daniele Conti, Chiara Creato, Lorenzo Del Castello, Irene Giardina, Tomas S Grigera, Stefania Melillo, Leonardo Parisi, and Massimiliano Viale. Dynamic scaling in natural swarms. Nature Physics, 13(June), 2017.

[27] He-Peng Zhang, Avraham Be'er, E-L Florin, and Harry L Swinney. Collective motion and density fluctuations in bacterial colonies. Proceedings of the National Academy of Sciences, 107(31):13626–13630, 2010.

[28] Antoine Bricard, Jean-Baptiste Caussin, Nicolas Desreumaux, Olivier Dauchot, and Denis Bartolo. Emergence of macroscopic directed motion in populations of motile colloids. Nature, 503(7474):95–98, 2013.

[29] Delphine Geyer, Alexandre Morin, and Denis Bartolo. Sounds and hydrodynamics of polar active fluids. Nature materials, 17(9):789, 2018.

[30] Daiki Nishiguchi and Masaki Sano. Mesoscopic turbulence and local order in janus particles self-propelling under an ac electric field. Phys. Rev. E, 92:052309, Nov 2015.

[31] Junichiro Iwasawa, Daiki Nishiguchi, and Masaki Sano. Algebraic correlations and anomalous fluctuations in ordered flocks of janus particles fueled by an ac electric field. arXiv preprint arXiv:2011.14548, 2020.

[32] Juan Ruben Gomez-Solano, Alex Blokhuis, and Clemens Bechinger. Dynamics of self-propelled janus particles in viscoelastic fluids. Physical review letters, 116(13):138301, 2016.

[33] Ivo Buttinoni, Giovanni Volpe, Felix Kümmel, Giorgio Volpe, and Clemens Bechinger. Active brownian motion tunable by light. Journal of Physics: Condensed Matter, 24(28):284129, 2012.

[34] Julien Deseigne, Olivier Dauchot, and Hugues Chaté. Collective motion of vibrated polar disks. Physical Review Letters, 105(9):098001, 2010.

[35] G Junot, G Briand, R Ledesma-Alonso, and Olivier Dauchot. Active versus passive hard disks against a membrane: mechanical pressure and instability. Physical review letters, 119(2):028002, 2017.

[36] Olivier Dauchot and Vincent Démery. Dynamics of a self-propelled particle in a harmonic trap. Physical review letters, 122(6):068002, 2019.

[37] G. Quincke. Uber rotationen im constanten electrischen felde. Annalen der Physik, (295):417–486, 1896.

[38] Ziane Izri, Marjolein N Van Der Linden, Sébastien Michelin, and Olivier Dauchot. Self-propulsion of pure water droplets by spontaneous marangoni-stress-driven motion. Physical review letters, 113(24):248302, 2014.

[39] Julien Deseigne, Sébastien Léonard, Olivier Dauchot, and Hugues Chaté. Vibrated polar disks: spontaneous motion, binary collisions, and collective dynamics. Soft Matter, 8(20):5629–5639, 2012.

[40] Dmitri Volfson, Arshad Kudrolli, and Lev S Tsimring. Anisotropy-driven dynamics in vibrated granular rods. Physical Review E, 70(5):051312, 2004.

[41] Sela Samin and René Van Roij. Self-propulsion mechanism of active janus particles in near-critical binary mixtures. Physical review letters, 115(18):188305, 2015.

[42] Gerhard Gompper, Roland G Winkler, Thomas Speck, Alexandre Solon, Cesare Nardini, Fernando Peruani, Hartmut Löwen, Ramin Golestanian, U Benjamin Kaupp, Luis Alvarez, et al. The 2020 motile active matter roadmap. Journal of Physics: Condensed Matter, 32(19):193001, 2020.

[43] Qian Chen, Sung Chul Bae, and Steve Granick. Directed self-assembly of a colloidal kagome lattice. Nature, 469(7330):381, 2011.

[44] Jie Zhang, Erik Luijten, Bartosz A. Grzybowski, and Steve Granick. Active colloids with collective mobility status and research opportunities. Chem. Soc. Rev., 46:5551–5569, 2017.

[45] Lokrshi Prawar Dadhichi, Ananyo Maitra, and Sriram Ramaswamy. Origins and diagnostics of the nonequilibrium character of active systems. Journal of Statistical Mechanics: Theory and Experiment, 2018(12):123201, 2018.

[46] Pawel Romanczuk, Markus Bär, Werner Ebeling, Benjamin Lindner, and Lutz Schimansky-Geier. Active brownian particles. The European Physical Journal Special Topics, 202(1):1–162, 2012.

[47] Alexandre P Solon, Michael E Cates, and Julien Tailleur. Active brownian particles and run-and-tumble particles: A comparative study. The European Physical Journal Special Topics, 224(7):1231–1262, 2015.

[48] Marco Bianucci and Riccardo Mannella. Optimal fpe for non-linear 1d-sde. i: Additive gaussian colored noise. Journal of Physics Communications, 4(10):105019, 2020.

[49] Grzegorz Szamel. Self-propelled particle in an external potential: Existence of an effective temperature. Physical Review E, 90(1):012111, 2014.

[50] Urna Basu, Satya N Majumdar, Alberto Rosso, and Grégory Schehr. Long-time position distribution of an active brownian particle in two dimensions. Physical Review E, 100(6):062116, 2019.

[51] Urna Basu, Satya N Majumdar, Alberto Rosso, Sanjib Sabhapandit, and Grégory Schehr. Exact stationary state of a run-and-tumble particle with three internal states in a harmonic trap. Journal of Physics A: Mathematical and Theoretical, 53(9):09LT01, 2020.

[52] Alexander K Hartmann, Satya N Majumdar, Hendrik Schawe, and Grégory Schehr. The convex hull of the run-and-tumble particle in a plane. Journal of Statistical Mechanics: Theory and Experiment, 2020(5):053401, 2020.

[53] Amir Shee, Abhishek Dhar, and Debasish Chaudhuri. Active brownian particles: mapping to equilibrium polymers and exact computation of moments. Soft Matter, 16(20):4776–4787, 2020.

[54] Lorenzo Caprini, Umberto Marini Bettolo Marconi, and Andrea Puglisi. Activity induced delocalization and freezing in self-propelled systems. Scientific reports, 9(1):1386, 2019.

[55] Benjamin Walter, Gunnar Pruessner, and Guillaume Salbreux. First passage time distribution of active thermal particles in potentials. Physical Review Research, 3(1):013075, 2021.

[56] Étienne Fodor, Cesare Nardini, Michael E. Cates, Julien Tailleur, Paolo Visco, and Frédéric van Wijland. How far from equilibrium is active matter? Phys. Rev. Lett., 117:038103, 2016.

[57] David Martin, Jérŕmy O'byrne, Michael E Cates, Étienne Fodor, Cesare Nardini, Julien Tailleur, and Frédéric van Wijland. Statistical Mechanics of Active Ornstein Uhlenbeck Particles. arXiv preprint arXiv:2008.12972v1, 2020.

[58] David Martin and Thibaut Arnoulx de Pirey. Aoup in the presence of brownian noise: a perturbative approach. Journal of Statistical Mechanics: Theory and Experiment, 2021(4):043205, 2021.

[59] Tamás Vicsek, András Czirók, Eshel Ben-Jacob, Inon Cohen, and Ofer Shochet. Novel type of phase transition in a system of self-driven particles. Physical Review Letters, 75(6):1226, 1995.

[60] Gabriel Baglietto and Ezequiel V Albano. Nature of the order-disorder transition in the vicsek model for the collective motion of self-propelled particles. Physical Review E, 80(5):050103, 2009.

[61] Hugues Chaté, Francesco Ginelli, Guillaume Grégoire, and Franck Raynaud. Collective motion of self-propelled particles interacting without cohesion. Phys. Rev. E, 77:046113, Apr 2008.

[62] Guillaume Grégoire and Hugues Chaté. Onset of collective and cohesive motion. Physical review letters, 92(2):025702, 2004.

[63] Francesco Ginelli and Hugues Chaté. Relevance of metric-free interactions in flocking phenomena. Physical Review Letters, 105(16):168103, 2010.

[64] Yen-Liang Chou, Rylan Wolfe, and Thomas Ihle. Kinetic theory for systems of self-propelled particles with metric-free interactions. Physical Review E, 86(2):021120, 2012.

[65] Parisa Rahmani, Fernando Peruani, and Pawel Romanczuk. Topological active matter in complex environments. arXiv preprint arXiv:2010.05902, 2020.

[66] David Martin, Hugues Chaté, Cesare Nardini, Alexandre Solon, Julien Tailleur, and Frédéric Van Wijland. Fluctuation-induced phase separation in metric and topological models of collective motion. Physical Review Letters, 126(14):148001, 2021.

[67] Michael E Cates and Julien Tailleur. Motility-induced phase separation. Annu. Rev. Condens. Matter Phys., 6(1):219–244, 2015.

[68] M. E. Cates and J. Tailleur. When are active brownian particles and run-and-tumble particles equivalent? consequences for motility-induced phase separation. EPL, 101(2):20010, 2013.

[69] Alexandre P Solon, Joakim Stenhammar, Michael E Cates, Yariv Kafri, and Julien Tailleur. Generalized thermodynamics of motility-induced phase separation: phase equilibria, laplace pressure, and change of ensembles. New Journal of Physics, 20(7):075001, 2018.

[70] Giuseppe Gonnella, Davide Marenduzzo, Antonio Suma, and Adriano Tiribocchi. Motility-induced phase separation and coarsening in active matter. Comptes Rendus Physique, 16(3):316–331, 2015.

[71] Claudio B Caporusso, Pasquale Digregorio, Demian Levis, Leticia F Cugliandolo, and Giuseppe Gonnella. Micro and macro motility-induced phase separation in a two-dimensional active brownian particle system. arXiv preprint arXiv:2005.06893, 2020.

[72] Hugues Chaté, Francesco Ginelli, Guillaume Grégoire, Fernando Peruani, and Franck Raynaud. Modeling collective motion: variations on the vicsek model. The European Physical Journal B, 64(3):451–456, 2008.

[73] Tamás Vicsek and Anna Zafeiris. Collective motion. Physics reports, 517(3-4):71–140, 2012.

[74] Aitor Martín-Gómez, Demian Levis, Albert Díaz-Guilera, and Ignacio Pagonabarraga. Collective motion of active brownian particles with polar alignment. Soft matter, 14(14):2610–2618, 2018.

[75] Julien Barré, Raphaël Chétrite, Massimiliano Muratori, and Fernando Peruani. Motility-induced phase separation of active particles in the presence of velocity alignment. Journal of Statistical Physics, 158(3):589–600, 2015.

[76] F. D. C. Farrell, M. C. Marchetti, D. Marenduzzo, and J. Tailleur. Pattern formation in self-propelled particles with density-dependent motility. Phys. Rev. Lett., 108:248101, Jun 2012.

[77] Fernando Peruani, Tobias Klauss, Andreas Deutsch, and Anja Voss-Boehme. Traffic jams, gliders, and bands in the quest for collective motion of self-propelled particles. Physical Review Letters, 106(12):128101, 2011.

[78] Elena Sese-Sansa, Ignacio Pagonabarraga, and Demian Levis. Velocity alignment promotes motility-induced phase separation. EPL (Europhysics Letters), 124(3):30004, 2018.

[79] Delphine Geyer, David Martin, Julien Tailleur, and Denis Bartolo. Freezing a flock: Motility-induced phase separation in polar active liquids. Physical Review X, 9(3):031043, 2019.

[80] Jeremie Palacci, Stefano Sacanna, Asher Preska Steinberg, David J. Pine, and Paul M. Chaikin. Living crystals of light-activated colloidal surfers. Science, 339(6122):936–940, 2013.

[81] VN Bondarev. Long-range correlations in the statistical theory of fluid criticality. Fluid Phase Equilibria, 506:112417, 2020.

[82] Marshall Fixman. Correlations at the critical point. The Journal of Chemical Physics, 36(8):1965–1968, 1962.

[83] David S Cannell. Measurement of the long-range correlation length of s f 6 very near the critical point. Physical Review A, 12(1):225, 1975.

[84] JR Dorfman, TR Kirkpatrick, and JV Sengers. Generic long-range correlations in molecular fluids. Annual Review of Physical Chemistry, 45(1):213–239, 1994.

[85] IW Smith, M Giglio, and GB Benedek. Correlation range and compressibility of xenon near the critical point. Physical review letters, 27(23):1556, 1971.

[86] TR Kirkpatrick, JM Ortiz de Zárate, and Jan V Sengers. Nonequilibrium fluctuation-induced casimir pressures in liquid mixtures. Physical Review E, 93(3):032117, 2016.

[87] MR Evans, Y Kafri, HM Koduvely, and D Mukamel. Phase separation in one-dimensional driven diffusive systems. Physical review letters, 80(3):425, 1998.

[88] Ricardo Brito, U Marini Bettolo Marconi, and R Soto. Generalized casimir forces in nonequilibrium systems. Physical Review E, 76(1):011113, 2007.

[89] Avi Aminov, Yariv Kafri, and Mehran Kardar. Fluctuation-induced forces in nonequilibrium diffusive dynamics. Physical review letters, 114(23):230602, 2015.

[90] Ali Najafi and Ramin Golestanian. Forces induced by nonequilibrium fluctuations: The soret-casimir effect. EPL (Europhysics Letters), 68(6):776, 2004.

[91] Pedro L Garrido, Joel L Lebowitz, Christian Maes, and Herbert Spohn. Long-range correlations for conservative dynamics. Physical Review A, 42(4):1954, 1990.

[92] Herbert Spohn. Long range correlations for stochastic lattice gases in a non-equilibrium steady state. Journal of Physics A: Mathematical and General, 16(18):4275, 1983.

[93] A Lederhendler and D Mukamel. Long-range correlations and ensemble inequivalence in a generalized a b c model. Physical review letters, 105(15):150602, 2010.

[94] Vivien Lecomte, Alberto Imparato, and Frédéric van Wijland. Current fluctuations in systems with diffusive dynamics, in and out of equilibrium. Progress of Theoretical Physics Supplement, 184:276–289, 2010.

[95] Christian M Rohwer, Alexandre Solon, Mehran Kardar, and Matthias Krüger. Nonequilibrium forces following quenches in active and thermal matter. Physical Review E, 97(3):032125, 2018.

[96] Andrea Cavagna, Alessio Cimarelli, Irene Giardina, Giorgio Parisi, Raffaele Santagati, Fabio Stefanini, and Massimiliano Viale. Scale-free correlations in starling flocks. Proceedings of the National Academy of Sciences, 107(26):11865–11870, 2010.

[97] Alexis Poncet, Olivier Bénichou, Vincent Démery, and Gleb Oshanin. Universal long ranged correlations in driven binary mixtures. Physical review letters, 118(11):118002, 2017.

[98] Sunghan Ro, Yariv Kafri, Mehran Kardar, and Julien Tailleur. Disorder-induced long-ranged correlations in scalar active matter. Physical Review Letters, 126(4):048003, 2021.

[99] G Grinstein, D-H Lee, and Subir Sachdev. Conservation laws, anisotropy, and "self-organized criticality"in noisy nonequilibrium systems. Physical review letters, 64(16):1927, 1990.

[100] Udo Seifert. Stochastic thermodynamics, fluctuation theorems and molecular machines. Rep. Prog. Phys., 75(12):126001, 2012.

[101] Jérémy O'Byrne, Yariv Kafri, Julien Tailleur, and Frédéric van Wijland. Time-(ir) reversibility in active matter: from micro to macro. arXiv preprint arXiv:2104.03030, 2021.

[102] Wolfram Research, Inc. Mathematica, Version 12.1. Champaign, IL, 2020.

[103] Charles Doering, Werner Horsthemke, and Jason Riordan. Non equilibrium fluctuation-induced transport. Physical Review Letters, 72(19), may 1994.

[104] T.E. Dialynas, Katja Lindenberg, and G.P. Tsironis. Ratchet motion induced by deterministic and correlated stochastic forces. Physical Review E, 56(4), october 1997.

[105] B Lindner, Lutz Schimansky-Geier, Peter Reimann, Peter Hänggi, and M Nagaoka. Inertia ratchets: A numerical study versus theory. Physical Review E, 59(2):1417, 1999.

[106] Mark M. Millonas and Mark I. Dykman. Transport and current reversal in stochastically driven ratchets. Phys. Lett. A, 185(1):65 – 69, 1994.

[107] Lennart Dabelow, Stefano Bo, and Ralf Eichhorn. Irreversibility in active matter systems: Fluctuation theorem and mutual information. Physical Review X, 9(2):021009, 2019.

[108] Lorenzo Caprini, Umberto Marini Bettolo Marconi, Andrea Puglisi, and Angelo Vulpiani. The entropy production of ornstein–uhlenbeck active particles: a path integral method for correlations. Journal of Statistical Mechanics: Theory and Experiment, 2019(5):053203, 2019.

[109] Elijah Flenner and Grzegorz Szamel. Active matter: quantifying the departure from equilibrium. Physical Review E, 102(2):022607, 2020.

[110] Lorenzo Caprini, Umberto Marini Bettolo Marconi, Andrea Puglisi, and Angelo Vulpiani. Comment on "entropy production and fluctuation theorems for active matter". Physical review letters, 121(13):139801, 2018.

[111] Claire Wilhelm. Out-of-equilibrium microrheology inside living cells. Physical review letters, 101(2):028101, 2008.

[112] Wylie W Ahmed, Etienne Fodor, Maria Almonacid, Matthias Bussonnier, Marie-Hélène Verlhac, Nir Gov, Paolo Visco, Frédéric van Wijland, and Timo Betz. Active mechanics reveal molecular-scale force kinetics in living oocytes. Biophysical journal, 114(7):1667–1679, 2018.

[113] Eyal Ben-Isaac, YongKeun Park, Gabriel Popescu, Frank LH Brown, Nir S Gov, and Yair Shokef. Effective temperature of red-blood-cell membrane fluctuations. Physical review letters, 106(23):238103, 2011.

[114] Eric Bertin, Michel Droz, and Guillaume Grégoire. Boltzmann and hydrodynamic description for self-propelled particles. Physical Review E, 74(2):022101, 2006.

[115] John Toner. Reanalysis of the hydrodynamic theory of fluid, polar-ordered flocks. Physical Review E, 86(3):031918, 2012.

[116] John Toner, Yuhai Tu, and Sriram Ramaswamy. Hydrodynamics and phases of flocks. Annals of Physics, 318(1):170 – 244, 2005. Special Issue.

[117] John Toner and Yuhai Tu. Flocks, herds, and schools: A quantitative theory of flocking. Physical review E, 58(4):4828, 1998.

[118] John Toner and Yuhai Tu. Long-range order in a two-dimensional dynamical xy model: how birds fly together. Physical Review Letters, 75(23):4326, 1995.

[119] Alexandre P Solon, Hugues Chaté, and Julien Tailleur. From phase to microphase separation in flocking models: The essential role of nonequilibrium fluctuations. Physical review letters, 114(6):068101, 2015.

[120] Eric Bertin, Michel Droz, and Guillaume Grégoire. Hydrodynamic equations for self-propelled particles: microscopic derivation and stability analysis. Journal of Physics A: Mathematical and Theoretical, 42(44):445001, 2009.

[121] Alexandre P Solon, Jean-Baptiste Caussin, Denis Bartolo, Hugues Chaté, and Julien Tailleur. Pattern formation in flocking models: A hydrodynamic description. Physical Review E, 92(6):062111, 2015.

[122] Jean-Baptiste Caussin, Alexandre Solon, Anton Peshkov, Hugues Chaté, Thierry Dauxois, Julien Tailleur, Vincenzo Vitelli, and Denis Bartolo. Emergent spatial structures in flocking models: a dynamical system insight. Physical Review Letters, 112(14):148102, 2014.

[123] Takayuki Niizato and Yukio-Pegio Gunji. Metric–topological interaction model of collective behavior. Ecological Modelling, 222(17):3041–3049, 2011.

[124] Jacques Gautrais, Francesco Ginelli, Richard Fournier, Stéphane Blanco, Marc Soria, Hugues Chaté, and Guy Theraulaz. Deciphering interactions in moving animal groups. PLoS Comput Bio, 8, 2012.

[125] Marcelo Camperi, Andrea Cavagna, Irene Giardina, Giorgio Parisi, and Edmondo Silvestri. Spatially balanced topological interaction grants optimal cohesion in flocking models. Interface Focus, 2, 2012.

[126] Francesco Ginelli, Fernando Peruani, Marie-Helène Pillot, Hugues Chaté, Guy Theraulaz, and Richard Bon. Intermittent collective dynamics emerge from conflicting imperatives in sheep herds. Proceedings of the National Academy of Sciences, 112(41):12729–12734, 2015.

[127] Daniel L Barton, Silke Henkes, Cornelis J Weijer, and Rastko Sknepnek. Active vertex model for cell-resolution description of epithelial tissue mechanics. PLoS computational biology, 13(6):e1005569, 2017.

[128] Anton Peshkov, Sandrine Ngo, Eric Bertin, Hugues Chaté, and Francesco Ginelli. Continuous theory of active matter systems with metric-free interactions. Physical Review Letters, 109(9):098101, 2012.

[129] Parisa Rahmani, Fernando Peruani, and Pawel Romanczuk. Flocking in complex environments—attention trade-offs in collective information processing. PLOS Computational Biology, 16(4):e1007697, 2020.

[130] Mehdi Moussaïd, Dirk Helbing, and Guy Theraulaz. How simple rules determine pedestrian behavior and crowd disasters. Proceedings of the National Academy of Sciences, 108(17):6884–6888, 2011.

[131] Hisao Honda, Masaharu Tanemura, and Akihiro Yoshida. Differentiation of wing epidermal scale cells in a butterfly under the lateral inhibition model-appearance of large cells in a polygonal pattern. Acta biotheoretica, 48(2):121–136, 2000.

[132] Gernot Schaller and Michael Meyer-Hermann. Multicellular tumor spheroid in an off-lattice voronoi-delaunay cell model. Physical Review E, 71(5):051910, 2005.

[133] Martin Bock, Amit Kumar Tyagi, Jan-Ulrich Kreft, and Wolfgang Alt. Generalized voronoi tessellation as a model of two-dimensional cell tissue dynamics. Bulletin of mathematical biology, 72(7):1696–1731, 2010.

[134] Dapeng Bi, Xingbo Yang, M Cristina Marchetti, and M Lisa Manning. Motility-driven glass and jamming transitions in biological tissues. Physical Review X, 6(2):021011, 2016.

[135] AP Solon and Julien Tailleur. Revisiting the flocking transition using active spins. Physical Review Letters, 111(7):078101, 2013.

[136] Alexandre P Solon and Julien Tailleur. Flocking with discrete symmetry: The two-dimensional active ising model. Physical Review E, 92(4):042119, 2015.

[137] Pau Clusella and Romualdo Pastor-Satorras. Phase transitions on a class of generalized vicsek-like models of collective motion. Chaos: An Interdisciplinary Journal of Nonlinear Science, 31(4):043116, 2021.

[138] J. R. Melcher and G. I. Taylor. Electrohydrodynamics: A review of the role of interfacial shear stresses. Annual Review of Fluid Mechanics, 1(1):111–146, 1969.

[139] J Palacci, S Sacanna, S-H Kim, G-R Yi, DJ Pine, and PM Chaikin. Light-activated self-propelled colloids. Phil. Trans. R. Soc. A, 372(2029):20130372, 2014.

[140] J Tailleur and ME Cates. Sedimentation, trapping, and rectification of dilute bacteria. EPL (Europhysics Letters), 86(6):60002, 2009.

[141] Elsen Tjhung, Cesare Nardini, and Michael E. Cates. Cluster phases and bubbly phase separation in active fluids: Reversal of the ostwald process. Phys. Rev. X, 8:031080, Sep 2018.

[142] Cesare Nardini, Étienne Fodor, Elsen Tjhung, Frédéric van Wijland, Julien Tailleur, and Michael E. Cates. Entropy production in field theories without time-reversal symmetry: Quantifying the non-equilibrium character of active matter. Phys. Rev. X, 7:021007, 2017.

[143] Mark J Schnitzer. Theory of continuum random walks and application to chemotaxis. Physical Review E, 48(4):2553, 1993.

[144] Yaouen Fily and M. Cristina Marchetti. Athermal phase separation of self-propelled particles with no alignment. Phys. Rev. Lett., 108:235702, 2012.

[145] Gabriel S Redner, Michael F Hagan, and Aparna Baskaran. Structure and dynamics of a phase-separating active colloidal fluid. Physical review letters, 110(5):055701, 2013.

[146] Julian Bialké, Hartmut Löwen, and Thomas Speck. Microscopic theory for the phase separation of self-propelled repulsive disks. EPL (Europhysics Letters), 103(3):30008, 2013.

[147] Thibaut Arnoulx de Pirey, Gustavo Lozano, and Frédéric van Wijland. Active hard spheres in infinitely many dimensions. Phys. Rev. Lett., 123:260602, 2019.

[148] Mourtaza Kourbane-Houssene, Clément Erignoux, Thierry Bodineau, and Julien Tailleur. Exact hydrodynamic description of active lattice gases. Physical review letters, 120(26):268003, 2018.

[149] Jérémy O'Byrne and Julien Tailleur. Lamellar to micellar phases and beyond: When tactic active systems admit free energy functionals. Physical Review Letters, 125(20):208003, 2020.

[150] Antoine Bricard, Jean-Baptiste Caussin, Debasish Das, Charles Savoie, Vijayakumar Chikkadi, Kyohei Shitara, Oleksandr Chepizhko, Fernando Peruani, David Saintillan, and Denis Bartolo. Emergent vortices in populations of colloidal rollers. Nature communications, 6:7470, 2015.

[151] Alexandre Morin, Nicolas Desreumaux, Jean-Baptiste Caussin, and Denis Bartolo. Distortion and destruction of colloidal flocks in disordered environments. Nature Physics, 13(1):63–67, 2017.

[152] Alexandre Morin, David Lopes Cardozo, Vijayakumar Chikkadi, and Denis Bartolo. Diffusion, subdiffusion, and localization of active colloids in random post lattices. Phys. Rev. E, 96:042611, Oct 2017.

[153] G Briand and Olivier Dauchot. Crystallization of self-propelled hard discs. Physical review letters, 117(9):098004, 2016.

[154] Alexandre P Solon, Joakim Stenhammar, Raphael Wittkowski, Mehran Kardar, Yariv Kafri, Michael E Cates, and Julien Tailleur. Pressure and phase equilibria in interacting active brownian spheres. Physical review letters, 114(19):198301, 2015.

[155] Takahiro Nemoto, Étienne Fodor, Michael E Cates, Robert L Jack, and Julien Tailleur. Optimizing active work: Dynamical phase transitions, collective motion, and jamming. Physical Review E, 99(2):022605, 2019.

[156] Shradha Mishra, Aparna Baskaran, and M. Cristina Marchetti. Fluctuations and pattern formation in self-propelled particles. Phys. Rev. E, 81:061916, Jun 2010.

[157] Clément Erignoux. Hydrodynamic limit for an active exclusion process. arXiv preprint arXiv:1608.04937, 2016.

[158] Benoît Mahault, Francesco Ginelli, and Hugues Chaté. Quantitative assessment of the toner and tu theory of polar flocks. Physical review letters, 123(21):218001, 2019.

[159] David S Dean. Langevin equation for the density of a system of interacting langevin processes. Journal of Physics A: Mathematical and General, 29(24):L613, 1996.

[160] Crispin W Gardiner et al. Handbook of stochastic methods, volume 3. Springer Berlin, 1985.

[161] Christian M Rohwer, Mehran Kardar, and Matthias Krüger. Transient casimir forces from quenches in thermal and active matter. Physical review letters, 118(1):015702, 2017.

[162] M. Kardar. Fluctuation induced forces in and out of equilibrium. http://www.mit.edu/~kardar/teaching/LesHouches18/lectures/index.html, 2018.

[163] Vincent Démery, Olivier Bénichou, and Hugo Jacquin. Generalized langevin equations for a driven tracer in dense soft colloids: construction and applications. New Journal of Physics, 16(5):053032, 2014.

[164] D. Martin, C. Nardini, M. E. Cates, and É. Fodor. Extracting maximum power from active colloidal heat engines. EPL (Europhys. Lett.), 121(6):60005, 2018.

[165] Charles R. Doering, Patrick S. Hagan, and C. David Levermore. Bistability driven by weakly colored gaussian noise: The fokker-planck boundary layer and mean first-passage times. Phys. Rev. Lett., 59:2129–2132, 1987.

[166] Peter Jung and Peter Hänggi. Dynamical systems: a unified colored-noise approximation. Physical review A, 35(10):4464, 1987.

[167] Ivar Fredholm. Sur une classe d'équations fonctionnelles. Acta mathematica, 27(1):365–390, 1903.

[168] Freddy Bouchet, Krzysztof Gawedzki, and Cesare Nardini. Perturbative calculation of quasi-potential in non-equilibrium diffusions: A mean-field example. Journal of Statistical Physics, 163(5):1157, 2016.

[169] L.D. LANDAU and E.M. LIFSHITZ. Chapter iii - the gibbs distribution. In L.D. LANDAU and E.M. LIFSHITZ, editors, Course of Theoretical Physics (Third Edition), pages 79 – 110. Pergamon, third edition edition, 1980.

[170] Nicolaas Godfried Van Kampen. Stochastic processes in physics and chemistry, volume 1. Elsevier, 1992.

[171] Daniel T Gillespie. Exact numerical simulation of the ornstein-uhlenbeck process and its integral. Physical review E, 54(2):2084, 1996.

[172] Alexei Andreanov, Giulio Biroli, Jean-Philippe Bouchaud, and Alexandre Lefevre. Field theories and exact stochastic equations for interacting particle systems. Physical Review E, 74(3):030101, 2006.

[173] Alexandre Lefevre and Giulio Biroli. Dynamics of interacting particle systems: stochastic process and field theory. Journal of Statistical Mechanics: Theory and Experiment, 2007(07):P07024, 2007.

[174] AG Thompson, J Tailleur, ME Cates, and RA Blythe. Lattice models of nonequilibrium bacterial dynamics. Journal of Statistical Mechanics: Theory and Experiment, 2011(02):P02029, 2011.

Résumé

La matière active regroupe l'étude des systèmes comprenant un grand nombre d'agents capables d'exercer des forces d'auto-propulsion sur leur environement. La motivation première de la matière active est de fournir un cadre théorique simplifié décrivant des ensembles d'entités vivantes en interaction. Cette approche spécifique est déjà à l'origine de plusieurs percées dans la compréhension des systèmes vivants, dans l'étude du mouvement bactérien et dans celle des nuées d'oiseaux par exemple. Par ailleurs, les succès de la matière active se sont récemment étendus au delà du vivant. Le domaine a notamment inspiré toute une panoplie d'expériences basées sur des matériaux artificiels : des rollers de Quincke aux colloïdes de Janus en passant par les grains vibrés. Dans ces montages, les entités actives sont synthétiques et leur moyen de propulsion repose sur un mécanisme physique plutôt que biologique.

Ce manuscrit de thèse contribue au développement de la matière active suivant 4 axes : l'étude exacte d'un modèle de dynamique active, la caractérisation de l'ordre dans la transition vers le mouvement collectif, l'étude de l'émergence d'embouteillages au sein d'un liquide polaire et l'apparition de corrélations longue portée dues à l'anisotropie.

Pour commencer, dans le chapitre 2, je présente une analyse perturbative exacte du modèle hors équilibre Active Ornstein Uhlenbeck Particles (AOUPs). J'y calcule analytiquement la distribution stationnaire d'une AOUP et quantifie son irréversibilité temporelle grâce à 3 signatures : la déviation au poids de Boltzmann, le courant "de cliquet" et la production d'entropie. Je généralise ensuite ces résultats au cas d'une particule soumise à un bruit thermique supplémentaire en sus du bruit actif. L'interaction entre les deux types de fluctuations mène à une riche phénoménologie lorsque la température varie : le courant "de cliquet" peut décroître ou être non monotone alors que la production d'entropie peut décliner ou diverger à haute T. Finalement, je discute de l'extension de ces résultats au cas de N particules actives en dimension d.

Dans le chapitre 3, je revisite la transition vers le mouvement collectif selon le type d'alignement microscopique en jeu. Qu'il s'agisse d'interactions dites "métriques" ou "topologiques", je montre que l'émergence de l'ordre reste généralement discontinue. Pour y parvenir, je présente la notion de transition de premier ordre induite par les fluctuations (FIFOT) et l'applique aux modèles de mouvement collectif.

Dans le chapitre 4, j'étudie l'apparition de séparation de phase induite par la motilité (MIPS) dans les modèles de mouvement collectif. Dans ce but, je reporte l'existence d'embouteillages au sein de denses asssemblées de rollers de Quincke. Lors de cette transition, que nous avons nommée solidification active, les embouteillages se propagent dans la direction opposée à celle du flux de rollers. J'établis ensuite un modèle théorique de la solidification active permettant d'explorer la riche phénoménologie de l'interaction entre MIPS et le mouvement collectif. En faisant varier les paramètres de ce modèle, je prédis l'existence d'une phase où des nuées de taille finie coexistent avec des embouteillages.

Dans le chapitre 5, j'étudie les fluctuations invariantes d'échelles d'un système actif. Partant d'une dynamique microscopique dotée d'interactions anisotropiques à courte portée, je montre l'existence de corrélations de densité macroscopiques à longue portée. J'évalue ensuite l'effet de ces corrélations sur la pression exercée par le système dans le but de dénicher un comportement similaire à la pression de Casimir.

Finalement, dans le dernier chapitre, je conclus ce manuscrit en résumant les contributions développées dans les 4 chapitres précedents. Pour chacun de ces travaux, je propose une possible direction de recherche future.

Mots-clés : physique statistique, matière active, physique hors de l'équilibre, transitions de phase, mouvement collectif, corrélations longue portée, séparation de phase induite par la motilité (MIPS).

Summary

Active Matter deals with the study of colloidal systems for which Brownian motion is replaced by a persistent self-propulsion. The main motivation of Active Matter is to provide a theoretical framework describing ensembles of interacting living entities. Such an approach has already led to breakthroughs in our understanding of living systems, be it in bacterial dynamics or for the analysis of bird flocks. But the successes of active matter now extend beyond living matter. The field has inspired a wealth of experiments dealing with artificial materials: Quincke rollers, Janus colloids, or shaken grains among other examples. In these setups, the active entities are synthetic units whose self-propulsion relies on a physical rather than biological mechanism.

This manuscript contributes to the active matter roadmap along four axes: the exact study of a workhorse model of active dynamics, the characterization of the order in the flocking transition, the study of the interplay between flocks and jams, and the presentation of anisotropy-induced long-ranged correlations.

As a starting point, I present in chapter 2 an exact perturbative analysis of the nonequilibrium model called Active Ornstein Uhlenbeck Particles (AOUPs). Using it, I derive analytically the steady-state distribution of an AOUP and quantify its departure from equilibrium through the characterization of three signatures: the deviation from Boltzmann distribution, the ratchet current, and the entropy production rate. I then generalize these results to the case of a particle experiencing both active and passive noises. The interplay between the two types of fluctuations leads to a rich phenomenology for the ratchet current and the entropy production rate when the temperature is varied: decline or non-monotonicity, divergence or decay at high T. Finally, I discuss the extension of these results to the case of N active particles in dimension d.

In the third chapter, I revisit the transition to collective motion according to the type of microscopic alignment at play. Be it so-called metric or topological interactions, I show that the emergence of flocking generically remains discontinuous. To achieve this result, I present the notion of Fluctuation-Induced First Order Phase Transition (FIFOT) and apply it to models of collective motion.

In the fourth chapter, I study the outbreak of Motility-Induced Phase Separation (MIPS) in flocking models. To this aim, I report the appearance of jams in dense assemblies of Quincke rollers. At the transition, which we dubbed active solidification, the jams propagate upstream the homogeneous flock of rollers. I then establish a theoretical model for active solidification which allows me to explore the rich phenomenology emerging from the interplay between MIPS and collective motion. By varying relevant parameters, I predict the existence of a phase where flocking bands coexist with active jams.

In the fifth chapter, I study long-ranged fluctuations in an active system. Starting from a microscopic dynamics only endowed with short-ranged anisotropic interactions, I show the emergence of macroscopic long-ranged density correlations. I then assess the effect of these correlations on the pressure exerted by the system in order to probe for a possible Casimir-like behaviour.

Finally, in the last chapter, I conclude this manuscript by summarizing the contributions developed in the four previous chapters. For each of these works, I propose a possible future research direction.

Keywords : statistical physics, active matter, nonequilibrium physics, phase transitions, collective motion, long-ranged correlations, Motility-Induced Phase Separation (MIPS).